LOUGHBOROUGH UNIVERSITY

Modelling of driven free surface liquid films

by

Mariano Galvagno

A thesis submitted in partial fulfilment for the degree of Doctor of Philosophy

in the
School of Science
Department of Mathematical Sciences

Declaration of Authorship

I, Mariano Galvagno , declare that this thesis titled, *'Modelling of driven free surface liquid films'* and the work presented in it are my own. I confirm that:

- This work was done wholly or mainly while in candidature for a research degree at Loughborough University.
- Where any part of this thesis has previously been submitted for a degree or any other qualification at Loughborough University or any other institution, this has been clearly stated.
- Where I have consulted the published work of others, this is always clearly attributed.
- Where I have quoted from the work of others, the source is always given. With the exception of such quotations, this thesis is entirely my own work.
- I have acknowledged all main sources of help.
- Where the thesis is based on work done by myself jointly with others, I have made clear exactly what was done by others and what I have contributed myself.

Signed:

Date:

"Er ist also auf doppelte Weise,
einmal mit dem Lernen selbst,
dann mit dem Lernen des Lernens beschäftigt ...
Der Schüler ist reif, wenn er so viel bei andern gelernt hat,
daß er nun für sich selbst zu lernen im Stande ist."

Wilhelm von Humbolt
Der Königsberger Schulplan

"El que no llora, no mama."

Enrique Santos Discépolo

Summary

In several types of coating processes a solid substrate is removed at a controlled velocity U from a liquid bath. The shape of the liquid meniscus and the thickness of the coating layer depend on U. These dependencies have to be understood in detail for non-volatile liquids to control the deposition of such a liquid and to lay the basis for the control in more complicated cases (volatile pure liquid, solution with volatile solvent). We study the case of non-volatile liquids employing a precursor film model that describes partial wettability with a Derjaguin (or disjoining) pressure. In particular, we focus on the relation of the deposition of (i) an ultrathin precursor film at small velocities and (ii) a macroscopic film of thickness $h \propto U^{2/3}$ (corresponding to the classical Landau–Levich film). Depending on the plate inclination, four regimes are found for the change from case (i) to (ii). The different regimes and the transitions between them are analysed employing numerical continuation of steady states and saddle-node bifurcations and simulations in time. We discuss the relation of our results to results obtained with a slip model.

In connection with evaporative processes, we will study the pinning of a droplet due to a sharp corner. The approach employs an evolution equation for the height profile of an evaporating thin film (small contact angle droplet) on a substrate with a rounded edge, and enables one to predict the dependence of the apparent contact angle on the position of the contact line. The calculations confirm experimental observations, namely that there exists a dynamically produced critical angle for depinning that increases with the evaporation rate. This suggests that one may introduce a simple modification of the Gibbs criterion for pinning that accounts for the non-equilibrium effect of evaporation.

Acknowledgements

> "They should have that in a big billboard across Times Square. Without people you're nothing. That's my spiel."
>
> John Graham Mellor

First and foremost, I would like to thank Prof Dr Uwe Thiele for giving me this unique opportunity. In particular, I thank him for his constant guidance and support. His enthusiastic and deep approach to science has helped me to gain invaluable experience in understanding and carrying out scientific research. I also thank him for teaching me how to be a successful scientific *entrepreneur*.

I am grateful to Dr Dmitri Tseluiko for his useful comments and guidance in our productive collaborative projects. To Dr Hender López for our collaboration. To Dr Andy Archer, Dr Te–Sheng Lin, Dr Desislava Todorova and Dr Veronika Schreiber for their helping comments, interesting discussions and camraderie.
I also thank heartily Prof Pierre Colinet, Dr Benoit Scheid and Dr Yannis Tsoumpas for their hospitality during my visit to TIPs – Fluid Physics at the Université Libre de Bruxelles. We held interesting scientific discussions which helped me to gain valuable insights into experimental techniques and into Physics of Liquids.
My gratitude goes as well to Prof Willy Dussel, Prof Daniel Laría and Dr Marc Thibeault for their encouragement and support during my studies at the University of Buenos Aires. I also thank Prof Gastón Giribet, Dr Mauricio Leston, Lic Bernardo P R Súarez and Min José Flores for extremely *useful* discussions. I am particularly thankful to Prof Fernando Peruani for connecting me back with science.
At this point, I would like to mention my fellow comrades, Dr Totò Di Martino, Dr Vicente Azorín – Peris, Dr Lollotte Sloper, Dr William P. Toyos, Lic Antonio Lafuente and Dr Pablo Ruíz for making Loughborough a nicer place to be.

To my parents and all my family back in Buenos Aires and to Carolina for their constant support and encouragement.

Finally, my thanks to all my peers – past and present – in office W2.41 and to all of those who supported me in any respect during the completion of this project.

The research was mainly carried out at Pilkington Library – Café 641– and at the Department of Mathematical Sciences of Loughborough University, Loughborough, Kingdom of Mercia.

ΠΛΕΩΝ ΕΠΙ ΟΙΝΟΠΑ ΠΟΝΤΟΝ ΕΠ ΑΛΛΟΘΡΟΟΥΣ ΑΝΘΡΩΠΟΥΣ

``‘‘Now, as you see, with my ship and crew I beach here, in my journey over the wine-dark sea to foreign-speaking people"``[1]

Loughborough, respectfully borrowing the hexameter verses of Homer, became the port of departure for setting sail to one of the fundamental pillars of Marie Curie Actions and ITN - MULTIFLOW[2]: interaction and exchange of interdisciplinary scientific research within an international, multicultural academic and industrial community. This collaborative network across Europe and Middle-East gathered Experienced Scientists and Early Stage Researchers from diverse academical backgrounds for constructive, amicable discussions. It enabled us to produce state-of-the-art and avant-garde scientific research, and at the same time, it strengthened cultural and international bonds resulting in better understanding and communication. This program helped me to broaden my personal and academic horizon tremendously. I thank Marie Curie Actions and ITN-MULTIFLOW, not only for the financial support, but in particular for the extraordinary experience of scientific and cultural exchange.

[1] Homer, Odyssey, 1 – 183.

[2] Support by the EU via the FP7 Marie Curie scheme (ITN MULTIFLOW, PITN-GA-2008-214919).

List of Publications

Chapters 2, 3 and 4 resulted in the following publications:

(1) "*Continuous and discontinuous dynamic unbinding transitions in a drawn film flow*"; M. Galvagno, D. Tseluiko, H. López and U. Thiele; *Phys. Rev. Lett.* 112, 2014.

(2) "*Collapsed heteroclinic snaking near a heteroclinic chain in dragged meniscus problems*"; D. Tseluiko, M. Galvagno and U. Thiele, *Eur. Phys. J. E* 37, 2014.

(3) "*Nonequilibrium Gibbs' Criterion for Competely Wetting Volatile Liquids*"; Y. Tsoumpas, S. Dehaeck, M. Galvagno, A. Rednikov, H. Ottevaere, U. Thiele, and P. Colinet; *Langmuir*, 30(40), 2014.

Contents

List of Figures

List of Tables

Chapter 1

Introduction

"But, if your award is against us,
don't fail to have metal covers
fashioned for yourselves, like those
they place over statues; else,
watch out!"

Chorus, *Birds*, Aristophanes

In this Thesis we investigate an apparently simple, but subtle process: the spreading and the deposition of a liquid on a surface. This phenomenon is of great importance in natural processes, e.g. some water birds, like ducks or cormorants, preen their feathers not only to align each feather or remove dirt and dust, but also to spread preening oil produced in the uropygial gland to keep the feathers flexible and improve their water repellency[1] [1], or probably more important in our daily life, is the spreading of tears to protect the cornea [4]. An example from Geology is when a lava stream flows over a terrain or mountain slope [2, 3].

Spreading or coating is also an important process in industry, e.g. in immersion lithography processes [5] or in several industrial film coating processes [6], such as automotive coatings for protecting the carrosserie and for the production of photographic paper and film.

A simple way of coating a surface is when a solid flat plate is drawn out of a liquid bath, and a film of fluid may be deposited onto the plate. This has been extensively studied theoretically (e.g. [7–10]) and experimentally (e.g. [11–15])

[1] Waterproofness depends also strongly on the feather structure.

over the years. A key point is to gain control of the deposition process and to develop a detailed understanding of the velocity-dependent shape of the meniscus.

The meniscus, which will be our main object of study, is the curved upper surface of a liquid, e.g. in a tube, produced by surface tension and wettability, see Fig. 1.1. As an interesting remark, the origin of the word meniscus can be traced back to the ancient greek word *μήνη*, meaning *Moon*, which in turn became the root of the diminutive of moon, *μηνίσκος*, meaning as well *crescent moon*, and therefore associated with the shape that the free surface of a partially wetting liquid takes close to a solid [16, 17].

Figure 1.1: Pictorial etymology of *meniscus*: in the left panel a Waxing crescent Moon and in the right panel a water meniscus in a burette.

We start discussing liquid thin films, applications – such as coating for example – and general basics of wettability. Then, we investigate similar physical systems e.g. refs. [14, 18–20] employing a precursor film model to describe the contact line region. This allows us to extend the understanding of the occurring qualitative transitions. In this Chapter we describe briefly some models employed in the literature and the types of surface profiles and flow patterns found. This includes a brief discussion of the used analytical and numerical solution techniques. In Chapter 2 we derive the film thickness evolution equation using a long-wave approximation from the Navier – Stokes equations, we discuss the boundary conditions and analyse the linear stability. Chapter 3 presents our results for drawn menisci for a non–volatile partially wetting liquid, and we gain a deeper understanding of the transitions occurring from the deposition of an ultra–thin precursor film at small velocities to a macroscopic film of thickness $h_\infty \propto U^{2/3}$ (corresponding to the classical Landau–Levich film) at larger velocities. Next, in Chapter 4 we investigate the pinning of evaporating completely wetting droplets at sharp corners. The final Chapter gives our conclusions and an outlook.

1.1 Behaviour of drawn meniscus

A variety of solution behaviours has been described in the literature: Starting with the seminal work of Landau and Levich (1942) [8] studying liquid films on vertical drawn plates, via the extension to inclined plates by Wilson (1982) [9], up to recent work by Snoeijer et al. [14, 18–20]. The discussed solutions mainly fall into two groups: *film* solutions and *meniscus* solutions, see Fig. 1.2. There, we see from left to right, a *meniscus*, a protruding meniscus or *foot* and a *film* solution.

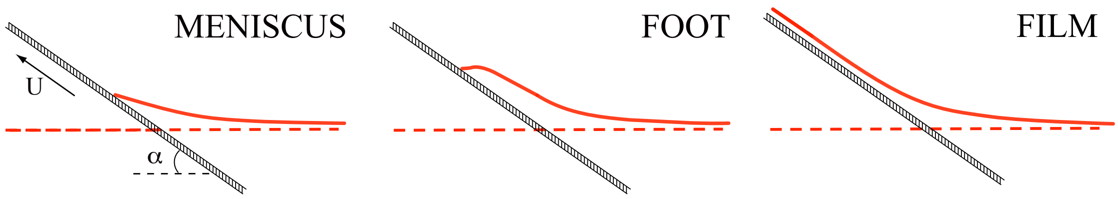

FIGURE 1.2: Three types of profiles connecting a bath to a plate moving with velocity U at an inclination angle α: (right) *meniscus* solution, (middle) *foot* and (left) *film* solution.

These solutions depend on the plate velocity U: at low plate velocities U, meniscus solutions and protruding meniscus exist, for larger plate velocity the film thickness scales with $U^{2/3}$, the so called Landau–Levich law, and at large velocities the film thickness scales with $U^{1/2}$. These solutions can be characterised as follows: The film solutions feature a film that is drawn from the bath and coats the entire plate, while the meniscus solutions exhibit another behaviour: a meniscus rises from the bath due to capillarity, and as the plate velocity increases, due to the drawing force as well, partially coating the plate. In the middle panel of Fig. 1.2 we observe as well a *foot*–like solution. It can be classified as a protruding meniscus only partially coating the plate (a type of meniscus solution) or as a finite length film in case the protuberance is long enough to coat large part of the plate. These solutions were first observed analytically for a liquid drawn out by Marangoni stress produced by a temperature gradient along the substrate [10, 21]. Note that this solution can evolve into a film solution, this matter will be addressed later in the text.

1.1.1 Film solution

Film solutions are of important industrial interest and have been and are still studied from an experimental and analytical point of view (e.g. [11, 22, 23]), but Landau and Levich [8] were the first who accurately determined an analytical solution for the film thickness at large(r) plate velocities. The solution is a function of the control parameters, i.e. the plate speed, the plate inclination and the characteristic properties of the fluid, such as viscosity η and density ρ. To solve the problem, they divided the surface of the liquid in two independent regions: one region located high above the meniscus and the bath, where the drawn film is nearly parallel to the plate, and a second region where the liquid in entrained onto the plate - the meniscus region - in which a slightly deformed shape of the liquid due to the movement of the plate will nearly fit the static meniscus shape. The key point of their solution is the choice of appropriate boundary conditions for the two regions, and the connection of the solutions in the two regions with each other employing asymptotic matching techniques. As matching condition, the continuity of the surface curvature in the overlap zone is requested. Landau–

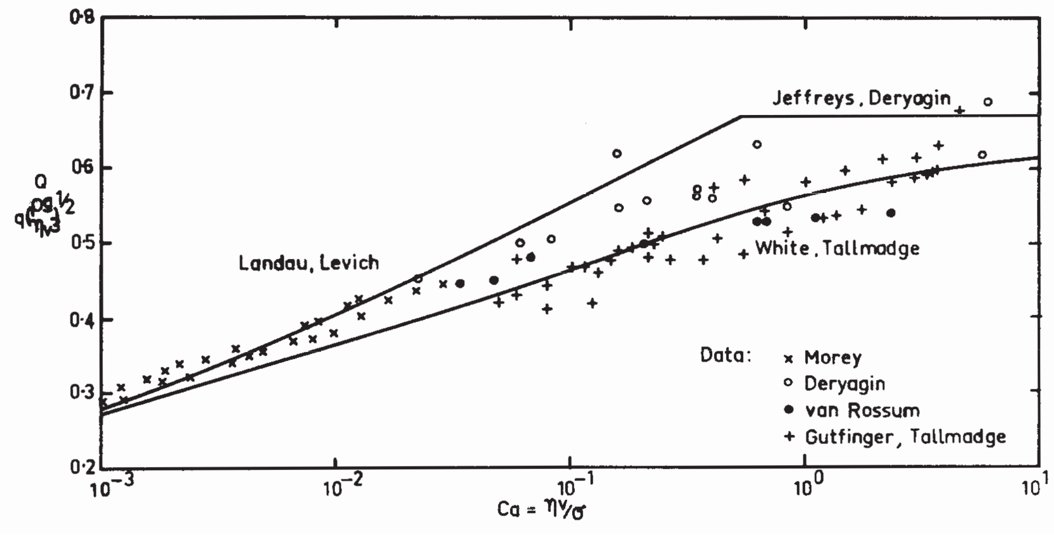

FIGURE 1.3: Shown is comparison of the dimensionless flux in dependance on the capillary number Ca for theory and experiment as shown in the figure. Reprinted from [15], with permission from Elsevier.

Levich's model is valid for small capillary numbers, i.e. for a capillary numbers up to $O(1)$.

For small drawing velocities no macroscopic film is deposited. The macroscopic film deposition of thickness $h \propto \mathrm{Ca}^{\frac{2}{3}}$ occurs above a critical capillary number Ca_c, where $\mathrm{Ca} = U\eta/\gamma$. The model is also in good agreement with experimental results [11] and models with corrections for higher capillary numbers [13, 15, 24].

In Fig. 1.3 we see how the low capillary number theory of Landau and Levich and the high capillary number theory of Derjaguin [25] were matched in the intermediate region by White and Tallmadge [13]. Superposed we see the experimental results of Morey [11], Tallmadge and Gutfinger [26], Rossum [24] and Derjaguin [27].

Further theoretical models with corrections to the Landau–Levich problem have been developed: for small capillary numbers withdrawal, see refs. [9, 28, 29], for plates with small inclination angles see refs. [9, 30], using a contact line with slip model see refs. [28, 29] and for solutions with an imposed precursor film see ref. [30].

1.1.2 Meniscus and foot solutions

Meniscus solutions were studied for different physical and mathematical models: for a contact line using a slip model in a vertical plate geometry, see refs. [18, 19] and for an inclined plate at small angles see refs. [14, 20], in the non-isothermal-case dragging by a temperature gradient see refs. [10, 21], and for a the assumption of a pre-wetted surface for small inclination angles see ref. [30]. In particular, Snoeijer et al. [14, 18, 20] show that above a critical capillary number Ca_c a steady contact line can no longer exist and the solid will eventually be coated completely by a liquid thick film. The bifurcation diagram of this coating transition changes qualitatively, from continuous to discontinuous, when increasing the inclination angle of the plate [20], see Fig. 1.4. A recent experimental study by Snoiejer et al. [19] probes the dynamics of receding contact lines through controlled perturbations of a meniscus. This has provided an experimental access to the entire bifurcation diagram of dynamical wetting, and confirms the hydrodynamic theory they have developed using a slip model [18], see Fig. 1.5. In the left panel of Fig. 1.5 a sketch

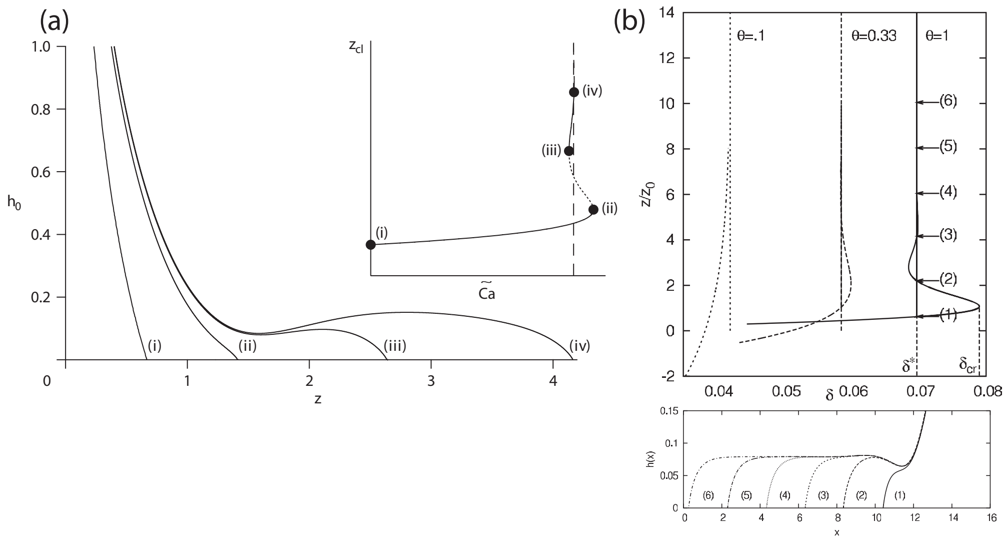

FIGURE 1.4: Relaxation of a dewetting contact line. Theory: (a) film profiles for a vertical drawn plate at Capillary number $\widetilde{Ca}$. Number correspond to the bifurcation diagram in the inset, where the contact line position z_{cl} is represented as function of Capillary number $\widetilde{Ca}$. Reprinted from [18], Fig. (5), reproduced with permission. (b) Upper panel corresponds to the bifurcation diagram contact line position as a function of the capillary number δ, lower panel to the numbered film profiles. Reprinted from [20], Fig. (2). Reproduction with kind permission from Springer Science and Business Media.

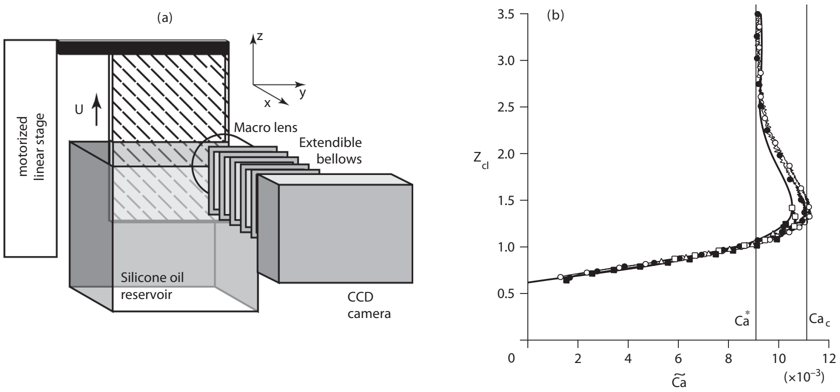

FIGURE 1.5: Relaxation of a dewetting contact line. Sketch of the experimental setup and experimental access to the entire bifurcation diagram of dynamical wetting. Reprinted from [19], Fig. (1) and Fig. (4), reproduced with permission.

of the experimental setup is shown. On the right panel we see the experimental bifurcation diagram, contact line position z_{cl} versus capillary number.

1.1.3 Physical models

The Landau–Levich problem was the corner stone for further systematic extensions of withdrawn plate and coating problems. In these theoretical extensions different physical models and solution techniques were proposed. Next, we list a few of them, followed by a more detailed description.

1. **Models**
    (a) Lubrication theory
    - Extension of Landau–Levich's problem for vertical plates to *small* plate inclination [9]
    - Inclined falling film [7]
    - Contact line with slip model (fixed microscopic angle) [18, 20, 28, 29]
    - Pre-wetted surface (precursor film of imposed thickness) [30]
    - Non–isothermal case - dragging by temperature gradient [10]

    (b) Full Navier–Stokes equations
    - Steady–state calculations [21]
    - Marangoni force driven meniscus [31]

2. **Analytical solution techniques and numerical approaches**
    (a) Asymptotical matched expansions [9, 29, 30]
    (b) Full time simulation of film / meniscus profile equation [10]
    (c) Full time simulation of Navier–Stokes equation [31]
    (d) Numerical determination of steady states of Navier–Stokes equation [21]
    (e) Numerical and asymptotical description [20, 29, 30]

We briefly review in the following paragraphs the main results and differences of the enumerated models:

Derjaguin [7] presents a derivation for a liquid layer which remains on the wall of a vessel, inclined at an angle α with respect to the horizon without capillarity pressure in the framework of lubrication theory. This problem is tackled by Benilov et al. [29] using a co-moving frame whilst describing the drawn-out plate problem.

Wilson [9] extends Landau–Levich 's model introducing new features from asymptotical analysis: he works out the drawn meniscus problem for a vertical infinite plate in the lubrication theory framework and showed that the Landau–Levich result is an asymptotic solution valid as the capillary number tends to zero in his model. He also showed how correction terms may be obtained by the method of matched expansions. This technique is very useful for describing the behaviour in the overlap region, i.e. between the meniscus region and the fully-developed region. He uses this technique for describing the film height for a withdrawn plate inclined at an arbitrary angle α as well.

Hocking [28] encounters employing a slip-model two possible states of the meniscus in the drawn meniscus problem: At the edge of the fluid a foot–like structure may be raised up to a finite distance above the bath, with its edge slipping on the plate. The second state is a continuous film of a certain thickness that is drawn up with the moving plate. The first state occurs for plates inclined at small angles for a sufficiently small plate speed. When a critical speed is reached and exceeded, the height of the edge starts to increase with time. Hocking's model confirms, except at small withdrawal plate velocities, Wilson's findings for the film thickness in the drawn meniscus problem.

Jin, Acrivos and Münch [21] determine the asymptotic film thickness on a plate that is withdrawn vertically, or at small angles from a bath. They numerically solve the steady–state Navier–Stokes equations and find that for creeping flow conditions the load agrees with Wilson's result given above. They also find that for an inclined plate, the corresponding dimensionless flow rate depends on the inclination angle α and on the capillary number Ca.

In a further extension of the model, Münch and Evans [10] study the coating flow on a heated substrate for a Marangoni-driven liquid film rising out of a meniscus onto a slightly inclined substrate. There the thermally induced Marangoni shear stress opposes the component of gravity parallel to the substrate. The numerical simulations show that the time-dependent lubrication model for the film profile can reach a steady state in the meniscus region. Furthermore, they investigate the steady state solutions of the lubrication model by studying the phase space of the corresponding third-order ODE for the dimensionless film equation. The resulting outcome is a copious and rich structure of the phase space with multiple non-monotonic solutions.

Benilov et al. [29] consider an infinite inclined plate being withdrawn at constant velocity U from a bath of viscous liquid. They derive Derjaguin's conjecture [7] as a steady-state solution from their model with the use of a co-moving frame. The conjecture is that for weak effects of inertia and surface tension, the load l, i.e. the thickness of the liquid film clinging to the plate, is $l = \sqrt{\frac{\mu U}{\rho g \sin\alpha}}$, where ρ and μ are the liquids density and viscosity, and g is the acceleration due to gravity. To derive the relation they use the Stokes equations in the limit of small plate inclination. As a result, an infinite set of stable steady-state solutions is obtained, but only one of the solutions corresponds to Derjaguin's solution. This particular special steady solution can only be singled out by matching it to a self-similar solution describing the non-steady part of the film between the bath and the film's front tip. They also carry out direct simulations of the Stokes equations and show that the small-slope approximation is valid when the inclination angle of the plate is less than approximately 35°. Finally they suggest to extend the present methodology to include capillary effects and to compare the results with the drawn meniscus flows with surface tension, i.e. the Landau–Levich film [8].

Benilov et al. [30] also examine two classical problems from the liquid-film theory: first, a liquid layer flowing down an inclined plate, under the condition that the main film is preceded by a thin precursor film. For this first problem they obtain a full asymptotic description of the flow, revealing aspects such as the infinite number of asymptotic zones. They also demonstrate that the solution describing the film is of a smoothed-shock type, with a bulge at the front.

Secondly, they describe the well known drawn meniscus problem, concentrating on solutions with a load larger than that of the Landau–Levich solution. Numerically they show regions in the problem's parameter space where non–Landau–Levich solutions exist, and distinguish subregions with multiple non–Landau–Levich solutions. In the asymptotic limit of strong surface tension, the multiplicity of non–Landau–Levich solutions is a result of non-uniqueness of the solution to the asymptotic boundary-value problem, which describes the film near the edge of the pool. Finally they point out, that the case of non–Landau–Levich solutions of the drawn meniscus problem includes an infinite number of asymptotic zones and from this point of view, the problem is similar to the advancing front problem.

We start our investigations with the study of the drawn meniscus deriving in the next Chapter a long-wave equation employing a precursor film model for the isothermal case. The interaction between the substrate and the plate is modelled for a non-volatile partially wetting liquid using a Derjaguin or disjoining pressure.

Chapter 2

Governing equations and underlying concepts

"That's amazing. What is it?"

E. Ripley

2.1 Governing equations

In this chapter we focus on the derivation of the non-dimensional long-wave equation that describes the drawn meniscus problem. We introduce the scaling, the Derjaguin pressure (disjoining pressure) to model wettability, Laplace pressure (capillary pressure) and hydrostatic pressure, and further on, we will define the boundary conditions, discuss linear stability and have a digression about the streamlines of the film profiles.

2.1.1 Problem and derivation

The starting point for the derivation of the two dimensional thin film equation for the drawn meniscus problem in the laboratory reference frame, see Fig. 2.1, is the hydrodynamic transport equation for the momentum density, the well known Navier – Stokes equation [32–34]. Restricting ourselves to two dimensions, it writes

$$\rho \frac{d\vec{v}}{dt} = \nabla \cdot \underline{\tau} + \vec{f} \qquad (2.1)$$

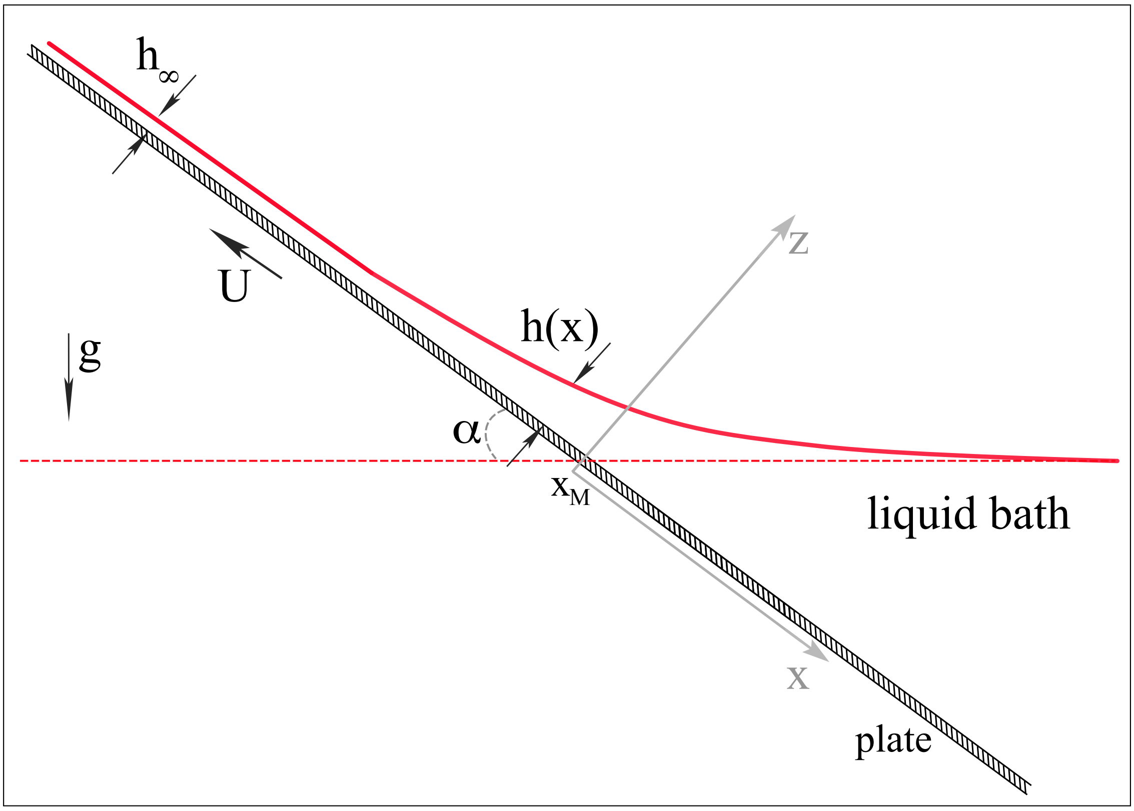

FIGURE 2.1: Sketch of the geometry: An infinite inclined flat plate is withdrawn from a liquid bath with constant speed U and at constant angle α.

where $d/dt = \partial_t + (\vec{v} \cdot \nabla)$ is the material time derivative, $\vec{v} = \binom{u}{w}$ is the velocity field, $\vec{f} = \binom{f_1}{f_2}$ is a body force, ∇ is the Nabla-operator $\nabla = \binom{\partial_x}{\partial_z}$ and $\underline{\tau}$ is the stress tensor defined as

$$\underline{\tau} = -p\underline{I} + \eta \left(\nabla\vec{v} + (\nabla\vec{v})^{\mathrm{T}} \right) \tag{2.2}$$

where $p(x,z)$ denotes the pressure field, I the identity tensor, ρ and η are the density and the dynamic viscosity of the liquid, respectively. For an incompressible fluid the continuity equation states

$$\nabla \cdot \vec{v} = 0. \tag{2.3}$$

We are studying a thin liquid film flowing on a solid flat substrate moving with speed U along the x-direction, thus the resulting boundary conditions are:

1. *No-slip* and *no-penetration* condition, $\vec{v} = \binom{-U}{0}$, at the solid flat substrate ($z = 0$). This condition implies zero relative velocity at the solid boundary and no penetration into the solid substrate.

2. Kinematic condition, $\partial_t h = w - u\partial_x h$ at the free surface $z = h(t, x)$, i.e. the free surface follows the flow field.

3. Force equilibrium condition at the free surface $z = h(t, x)$,

$$(\underline{\tau} - \underline{\tau}_{air}) \cdot \vec{n} = K\gamma\vec{n} + (\partial_s\gamma)\vec{t}. \tag{2.4}$$

It is assumed that the surrounding air does not exert forces on the fluid, i.e. $\underline{\tau}_{air} = 0$. The surface derivative is defined as $\partial_s = \vec{t} \cdot \nabla$. The Laplace or curvature pressure is $p_L = -\frac{\gamma}{2}\nabla \cdot \vec{n}$, while the variation of the surface tension γ along the surfaceis given by $\partial_s\gamma$. Such a variation can be caused, for example, by thermal Marangoni effects. The simplest model is assuming a linear dependence of the surface tension on temperature, i.e. $\gamma = \gamma_0 + \gamma_T(T_0 - T)$. Note that γ_0 is the reference surface tension at reference temperature T_0 and $\gamma_T = d\gamma/dT$ at T_0. In this case the variation is $\partial_s\gamma = \mathrm{Ma}(T_x + \partial_x h T_z)/[1 + (\partial_x h)^2]^{1/2}$ where Ma is the *Marangoni* number defined as $\mathrm{Ma} = l\rho\gamma_T\Delta T/\eta^2$ [39].

The surface's normal vector $\vec{n}$, tangent vector $\vec{t}$ and curvature K are

$$\begin{aligned} \vec{n} &= \frac{(-\partial_x h, 1)}{[1 + (\partial_x h)^2]^{\frac{1}{2}}}, \\ \vec{t} &= \frac{(1, \partial_x h)}{[1 + (\partial_x h)^2]^{\frac{1}{2}}}, \\ K &= \frac{\partial_{xx} h}{[1 + (\partial_x h)^2]^{\frac{3}{2}}}, \end{aligned} \tag{2.5}$$

respectively. The vectorial boundary condition (2.4) can also be expressed as two scalar conditions by projecting it onto the normal and the tangent surface vectors, $\vec{n}$ and $\vec{t}$. One obtains the tangential

$$\eta\left[(\partial_z u + \partial_x w)\left(1 - (\partial_x h)^2\right) + 2\left(\partial_z w - \partial_x u\right)\partial_x h\right] = \partial_s\gamma\left[1 + (\partial_x h)^2\right] \tag{2.6}$$

and normal

$$p + \frac{2\eta}{1+(\partial_x h)^2}\left[-\partial_x u(\partial_x h)^2 - \partial_z w + \partial_x h(\partial_z u + \partial_x w)\right] = -\frac{\gamma \partial_{xx} h}{[1+(\partial_x h)^2]^{\frac{3}{2}}} \quad (2.7)$$

stress condition, respectively.

2.1.2 Wettability: Macroscopic approach

To include the interaction with the substrate, or to understand how a simple liquid wets the substrate, it is necessary to incorporate a condition at the three-phase contact line, i.e., at points where the film height tends to zero, i.e. $h \to 0$. From a macroscopic point of view, this condition is known as the *Young–Laplace* law [35, 36]:

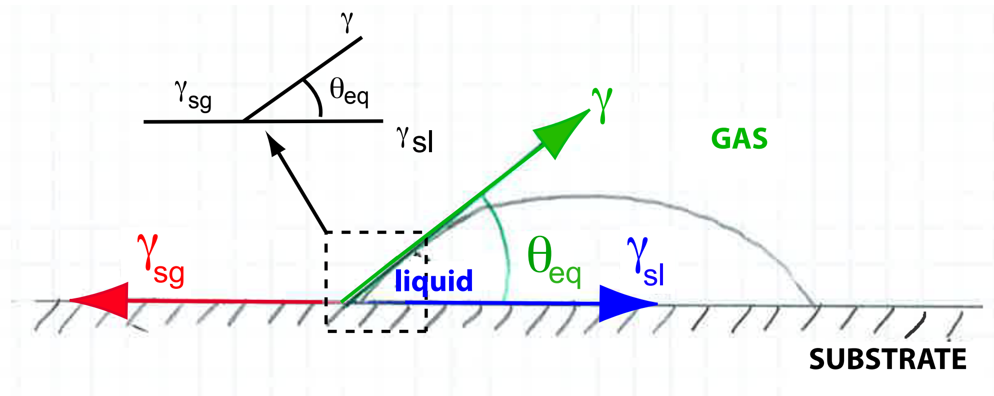

FIGURE 2.2: A sketch of a spherical cap-like droplet sitting on a solid substrate: The static three-phase contact line is approximated as a triangular section (see inset) indicating the solid-liquid ($\gamma_{\rm SL}$), solid-gas ($\gamma_{\rm SG}$) and liquid-gas (γ) interfacial energies. The static equilibrium angle $\theta_{\rm eq}$ is also shown.

$$\gamma \cos\theta_{\rm eq} = \gamma_{\rm SG} - \gamma_{\rm SL}, \quad (2.8)$$

where $\gamma_{\rm SL}$, $\gamma_{\rm SG}$ and γ are the solid-liquid, solid-gas and liquid-gas interfacial tensions respectively and $\theta_{\rm eq}$ is the static equilibrium angle, see Fig. 2.2. The surface tensions are defined as energy per unit of area, equivalent to a force per unit of length (area) acting on the contact point (line).

The three-phase contact line region can be approximated by a macroscopic triangular section. We can also think of the Young–Laplace law as the mechanical force equilibrium at the three-phase contact line between these tensions.

When a simple liquid comes into contact with a flat substrate in absence of gravity, the liquid either [34, 38, 39]:

(a) spreads all over the solid, i.e. the liquid forms a flat film. One may say the static contact angle $\theta_{\text{eq}} = 0$. This is known as *complete wetting*,

(b) or forms droplets on the substrate with a finite static contact angle, $0 < \theta_{\text{eq}} < \pi$. This is known as *partially wetting*,

(c) or forms ideally spherical droplets that have only one contact point with the substrate, i.e. a static contact angle of $\theta_{\text{eq}} = \pi$. This is the case of *non-wetting*.

In Fig. 2.3 we sketch the three described situations. For the case of partial wetting, (b), the border between the liquid and the gas at the substrate is the *static contact line*. Note that Fig. 2.4 shows the experimental images depicting the three different wetting states for the change of the contact angle of water on sapphire from complete wetting to almost non-wetting case [40].

Note that Eq. (2.8) can also be derived using translational invariance / variational arguments from the total interface energy [38]. Note that the macroscopic picture does not consider the particular nature of the contact line region over which intermolecular forces are acting. Accordingly, θ_{eq} is understood to be measured macroscopically on the scale above that of long-ranged intermolecular forces.

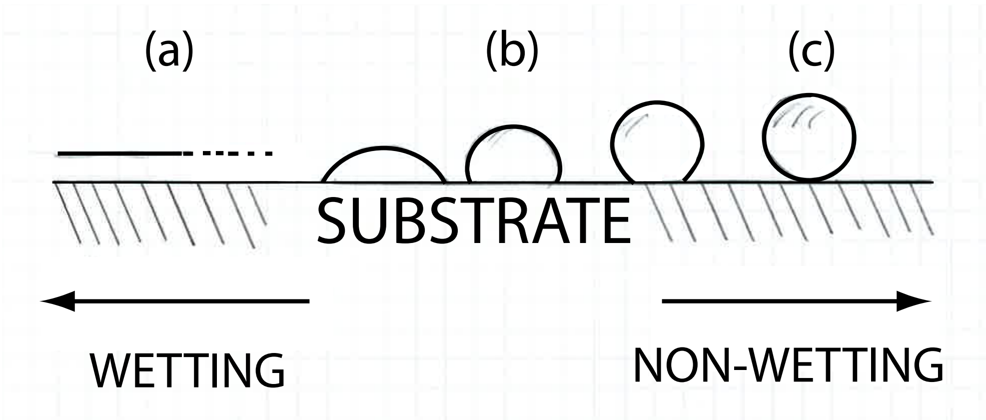

FIGURE 2.3: Sketch of the three qualitatively different wetting behaviours of a simple liquid on a solid substrate: (a) wetting, (b) partial wetting and (c) non-wetting.

FIGURE 2.4: Shown is from right to left a series of experimental images showing the change of the contact angle of water on sapphire (complete wetting to almost non-wetting case). Reproduced with permission of the authors from [40].

The Young–Laplace law models accurately partial wetting situations for static contact angles $\theta_{\mathrm{eq}} \in (0, \pi)$ or where $\cos\theta_{\mathrm{eq}} = (\gamma_{\mathrm{SG}} - \gamma_{\mathrm{SL}})/\gamma$ fulfils

$$-1 < \frac{\gamma_{\mathrm{SG}} - \gamma_{\mathrm{SL}}}{\gamma} < 1. \tag{2.9}$$

However, for the remaining situations - non-wetting and complete wetting - it is necessary to define and use the *spreading coefficient* [38]

$$S = \gamma_{\mathrm{SG}} - (\gamma + \gamma_{\mathrm{SL}}). \tag{2.10}$$

It evaluates the energy difference between a dry substrate and a substrate covered by a liquid. Combining it with the Young–Laplace law (Eq. (2.8)), S can be written in terms of the static contact angle,

$$S = \gamma(\cos\theta_{\mathrm{eq}} - 1). \tag{2.11}$$

Note that for small contact angles $\theta_{\mathrm{eq}} \ll 1$, i.e. in a long-wave approximation, in the partially wetting case we can write,

$$\cos\theta_{\mathrm{eq}} \simeq 1 - \frac{\theta_{\mathrm{eq}}^2}{2}, \tag{2.12}$$

i.e.

$$S \simeq -\gamma\frac{\theta_{\mathrm{eq}}^2}{2} \tag{2.13}$$

and

$$\theta_{\mathrm{eq}} \simeq \sqrt{\frac{-2S}{\gamma}}. \tag{2.14}$$

We can employ Eq. (2.11) to give conditions for complete wetting and non-wetting situations in terms of S as well, without knowing the static contact angle θ_{eq}: For complete wetting, the static contact angle is $\theta_{\text{eq}} = 0$, but the spreading coefficient satisfies $S \geq 0$, while for non-wetting situations, $\theta_{\text{eq}} = \pi$, and $S \leq -2\gamma$. If we know the interfacial energies, we can now infer what type of wetting situation will be described, see Fig. 2.5. However, for situations where the contact line is moving – a dynamic contact line (dynamic contact angle) – e.g. liquid spreading on a surface, a sliding drop on an inclined plate, dip-coating [41, 42], or in immersion lithography processes [5]– causes problems in the hydrodynamical description. If a moving liquid–air interface is in contact with the substrate at the contact line, the no–slip condition results in the divergence of the viscous dissipation at the contact line implying that contact line motion is *not* possible under these conditions [34, 38, 41].

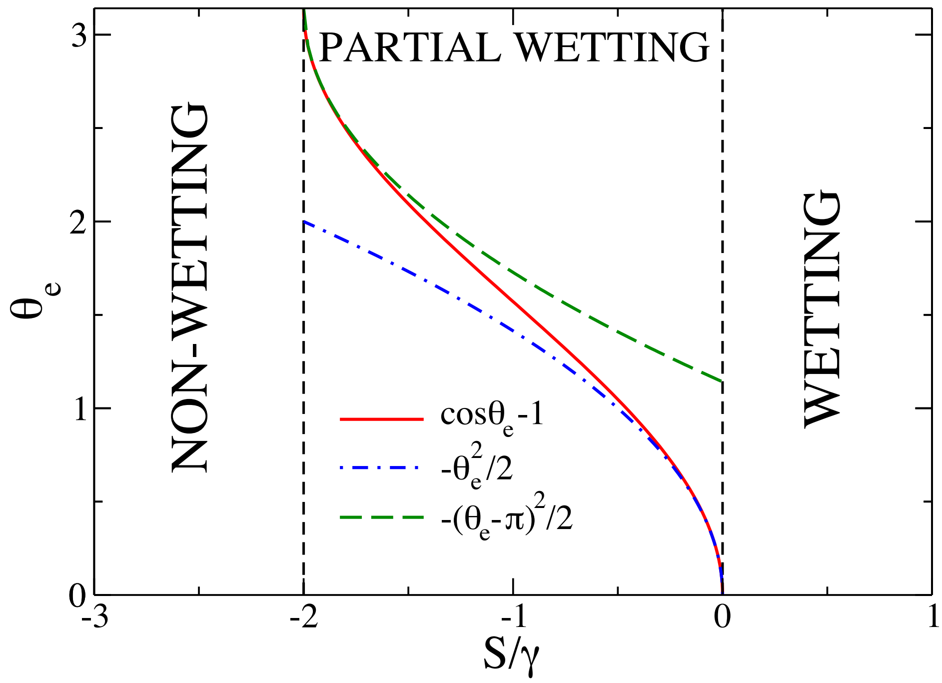

FIGURE 2.5: Scheme of wetting behaviour in terms of the spreading coefficient S. Note the three well defined regions corresponding to non-wetting, partial wetting and wetting situations in terms of S. Red solid line corresponds to the full expression of $S(\theta_{\text{eq}})$, while blue dash-pointed line corresponds to the small angle approximation, see Eq. (2.13) and green dashed line to the large angle approximation, i.e. for $\theta_{\text{eq}} \approx \pi$.

2.1.3 Wetting: Mesoscopic approach

We have to take into account that for thin and ultrathin films (film thickness below 100nm) another thickness dependent force term must be introduced. It has to be done in order to model the transition from a bulk film, where the overall interfacial energy is the sum of the solid-liquid and solid-gas interfacial energies, to a no-film situation, where the system only has liquid-gas interfacial energy. For partially wetting liquids, it has been shown [43–47] that in thermodynamic equilibrium droplets coexist with a microscopic adsorbed thin film at the solid substrate, this thin film is known as *precursor film*, h_p, see Fig. 2.6. The immediate neighbouring area of the droplet is never completely dry due to the adsorbed liquid layer. Derjaguin et al. [43, 44] measured for free films with thickness below 100 nm wetting or adhesion energy $V(h)$ that depends on the thickness of the film. It produces an additional attractive / repulsive force between the two film interfaces, that can be included into the hydrodynamical equations via a supplementary pressure term $\Pi(h) = -\partial_h V(h)$. It may be introduced either:

(i) into the normal force boundary condition as an addition to the Laplace pressure term [38, 39]: $p_L \to p_L - \Pi(h)$

(ii) or as a body force into the Navier–Stokes transport equations [38]: $\vec{f}_{\mathrm{Disj}} = -\nabla\phi_{\mathrm{Disj}}$, where $\phi_{\mathrm{Disj}} = \Pi(z) - \Pi(h)$.

Both approaches lead to the same final result. This additional pressure $\Pi(h)$ is called *disjoining* or *conjoining pressure* [38]. Sometimes it is referred to as *Derjaguin pressure* [48]. The disjoining pressure $\Pi(h)$ used here is a combination of a destabilising long-range van der Waals, $\Pi_{\mathrm{vdW}}(h) = -A/h^3$ (for $A > 0$) , and a short-range stabilising interaction, $\Pi_{\mathrm{sr}} = B/h^6$ (for $B > 0$), i.e.

$$\Pi(h) = \Pi_{\mathrm{vdW}}(h) + \Pi_{\mathrm{sr}}(h) = -\frac{A}{h^3} + \frac{B}{h^6}, \tag{2.15}$$

where A is the Hamaker constant and B the interaction strength of the short–range interaction. For $A > 0$ and $B > 0$ it describes partial wetting where a stable precursor film h_p may coexist with a meniscus of finite contact angle θ_{eq}. In Fig. 2.7 we show disjoining pressures describing three different cases: non-wetting ($B = 0$, $A > 0$), wetting ($A = 0$, $B > 0$) and partial wetting ($A > 0$ and $B > 0$).

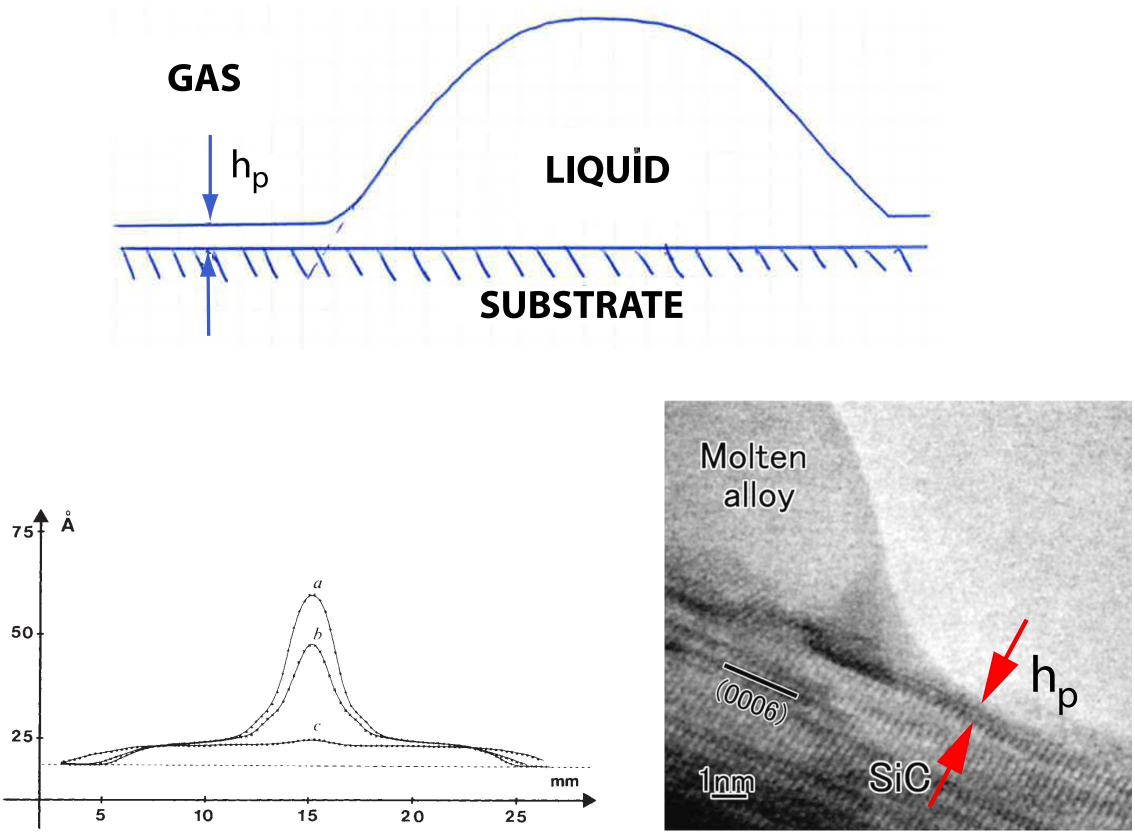

FIGURE 2.6: Precursor Film: Upper panel: Sketch of droplet with the adsorbed precursor fim h_p. Lower panels: Some experiments: Left panel: Ellipsometric thickness profile of a PDMS droplet spreading on a silicon wafer for different times τ after deposition: a - $\tau = 47h$, b - $\tau = 56h$ and c - $\tau = 96h$. y-axis corresponds to droplet height, x-axis corresponds to witdth. Note that the thickness far from the drop is non-zero due to a ultrathin film layer of silicon oxide, it corresponds to the baseline (dashed line) on which the liquid spreads. Note also the preceding precursor film $h_\mathrm{p} \lesssim 10$Å. Reprinted by permission from Macmillan Publishers Ltd: *Nature*, [47], copyright (1989). Right panel: High resolution image of SiC molten alloy spreading at $T \approx 1073K$. A precursor film is extending out of the molten alloy droplet. Reprinted from [46], with permission from Elsevier.

Note that we can define in an analogous way a mesoscopic spreading coefficient $\tilde{S}$ in terms of the wetting (adhesion) energy $V(h)$ for a wetted / non-wetted surface,

$$\tilde{S} = V(\infty) - V(h_0), \tag{2.16}$$

where $V(\infty)$ represents the energy of a very thick film ($V(\infty) = 0$) and $V(h_0)$ the energy corresponding to a finite (thin) film. If we set h_0 to be the equilibrium precursor film height h_eq, the spreading coefficient is describing the same wetting situation as in the macroscopic case, see Eq. (2.10), e.g. partial - wetting, i.e. $\tilde{S} = S$. This energetic argument allows to bridge the two physical length scales via Eq. (2.11) and relate the equilibrium contact angle θ_{eq} to the equilibrium precursor film height h_{p} via the wetting / adhesion energy (disjoining pressure) as $\theta_{\text{eq}} = \sqrt{-2V(h_{\text{eq}})/\gamma}$. Note that h_{eq} is the film height where the Disjoining pressure is zero, i.e.

$$\Pi(h_{\text{eq}}) = 0. \tag{2.17}$$

Writing h_{eq} and θ_{eq} for our choice of $\Pi(h)$, see Eq. (2.15), in terms of the constants A and B, we have

$$h_{\text{eq}} = (B/A)^{1/3}, \tag{2.18}$$

and the equilibrium contact angle

$$\theta_{\text{eq}} = \sqrt{\frac{3}{5}\frac{A}{\gamma h_{\text{eq}}^2}} \tag{2.19}$$

respectively.

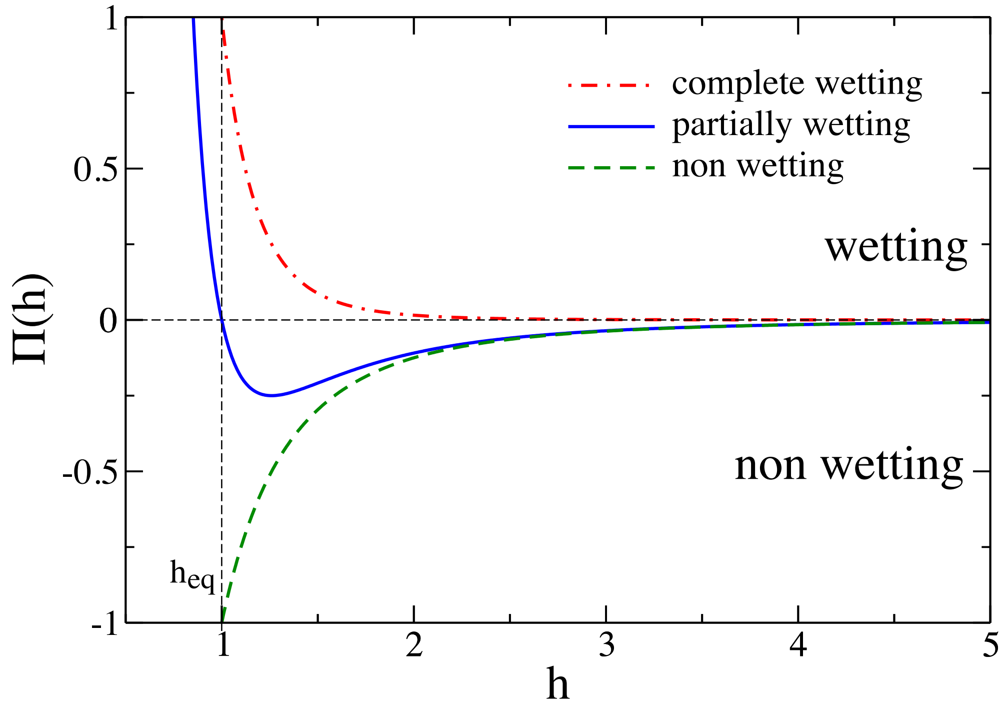

FIGURE 2.7: Shown are three different disjoining pressures for three wetting scenarios: complete wetting, partial–wetting and non–wetting. h_{eq} is the film height where the Disjoining pressure is zero, i.e. $\Pi(h_{\text{eq}}) = 0$ for $h_{\text{eq}} = 1$.

2.1.4 Non–dimensionalisation and long–wave approximation

Now, we can return to the long-wave approximation of the Navier–Stokes equations.

First we introduce non-dimensional variables and at a later stage we will take advantage of the difference in magnitude between the length scales parallel and normal to the substrate. For this purpose we first introduce a set of not-yet-specified scales (see Table 2.1), where l refers to some significant typical length of the system, such as mean film thickness, precursor film height, etc.; U_0 refers to a characteristic velocity and t_0 to a characteristic time-scale.

Dimensionless	Scale	Dimensional
$\tilde{z}$	l	$z = l\tilde{z}$
$\tilde{x}$	l	$x = l\tilde{x}$
$\tilde{t}$	$t_0 = l/U_0$	$t = t_0\tilde{t}$
$\vec{\tilde{v}}$	U_0	$\vec{v} = U_0\vec{\tilde{v}}$
$\tilde{P}$	$P_0 = \rho U_0^2$	$p = P_0\tilde{p}$

TABLE 2.1: Different Non-dimensional variables and scales

As an example, we introduce the particular body force $\vec{f} = \rho g(\sin\alpha, \cos\alpha)$, i.e. we look at a film on an inclined plate with gravity. The force is written in the components parallel and normal to the plate. Now, we introduce the aforementioned scales in Eq. (2.1) and obtain

$$
\begin{aligned}
\rho\frac{U_0^2}{l}(\partial_{\tilde{t}}\tilde{u} + \tilde{u}\partial_{\tilde{x}}\tilde{u} + \tilde{w}\partial_{\tilde{z}}\tilde{u}) &= -\rho\frac{U_0^2}{l}\partial_{\tilde{x}}\tilde{p} + \eta\frac{U_0^2}{l^2}(\partial_{\tilde{x}\tilde{x}}\tilde{u} + \partial_{\tilde{z}\tilde{z}}\tilde{u}) + \rho g\sin(\alpha) \\
\rho\frac{U_0^2}{l}(\partial_{\tilde{t}}\tilde{w} + \tilde{u}\partial_{\tilde{x}}\tilde{w} + \tilde{w}\partial_{\tilde{z}}\tilde{w}) &= -\rho\frac{U_0^2}{l}\partial_{\tilde{z}}\tilde{p} + \eta\frac{U_0^2}{l^2}(\partial_{\tilde{x}\tilde{x}}\tilde{w} + \partial_{\tilde{z}\tilde{z}}\tilde{w}) - \rho g\cos(\alpha)
\end{aligned}
\tag{2.20}
$$

for x and z components respectively. Using the definition of the dimensionless *Reynolds* number Re and the *Froude* number Fr,

$$
\begin{aligned}
\mathrm{Re} &= \frac{U_0 l\rho}{\eta} \\
\mathrm{Fr} &= \frac{U_0^2}{lg}.
\end{aligned}
$$

Eqs. (2.20) are re-expressed as (dropping the tilde for simplicity),

$$\begin{aligned} \partial_t u + u\partial_x u + w\partial_z u &= -\partial_x p + \frac{1}{\mathrm{Re}}\left(\partial_{xx}u + \partial_{zz}u\right) + \frac{\sin\alpha}{\mathrm{Fr}} \\ \partial_t w + u\partial_x w + w\partial_z w &= -\partial_z p + \frac{1}{\mathrm{Re}}\left(\partial_{xx}w + \partial_{zz}w\right) - \frac{\cos\alpha}{\mathrm{Fr}}. \end{aligned} \tag{2.21}$$

The Reynolds and Froude numbers stand for the ratio of the selected velocity scale and the viscose velocity scale and for the squared ratio of the selected velocity scale and the gravity velocity scale, respectively. The viscose scaling is defined specifying the velocity U_0 as $U_0 = \eta/\rho l$, so we have

$$\frac{1}{\mathrm{Re}} \to 1, \text{ and } \frac{1}{\mathrm{Fr}} \to \frac{g l^3 \rho^2}{\eta^2} =: G \tag{2.22}$$

where G is the *Gravitation* or *Galilei* number. Note that the scaling is always chosen for the specific problem so as to simplify the analysis without losing information. With Eq. (2.21) and the definition (2.22), it is possible to re-write the Navier-Stokes and continuity equations as well as the scalar boundary conditions (2.6), (2.7) as

$$\begin{aligned} \partial_t u + u\partial_x u + w\partial_z u &= -\partial_x p + \partial_{xx}u + \partial_{zz}u + G\sin\alpha \\ \partial_t w + u\partial_x w + w\partial_z w &= -\partial_z p + \partial_{xx}w + \partial_{zz}w - G\cos\alpha \\ \partial_x u + \partial_z w &= 0 \end{aligned} \tag{2.23}$$

and

$$\begin{aligned} \left(\partial_z u + \partial_x w\right)\left(1 - (\partial_x h)^2\right) + 2\left(\partial_z w - \partial_x u\right)\partial_x h &= -\mathrm{Ma}\Upsilon\left[(1 + (\partial_x h)^2\right]^{1/2} \\ p + \frac{2}{1 + (\partial_x h)^2}\left[-\partial_x u(\partial_x h)^2 - \partial_z w + \partial_x h\left(\partial_z u + \partial_x w\right)\right] &= -\frac{\gamma\partial_{xx}h}{[1 + (\partial_x h)^2]^{\frac{3}{2}}} - \Pi(h), \end{aligned} \tag{2.24}$$

respectively, where

$$\Upsilon = \partial_x T + \partial_x h \partial_z T.$$

Here, γ is the dimensionless surface tension, $\gamma = \gamma_0 l\rho/\eta^2$ and $\gamma_0 = \gamma(T_0)$ is the surface tension for temperature T_0 (γ may depend linearly on temperature, see page 13).

Note that the disjoining pressure can be non-dimensionalised via

$$\Pi(h) = \mathrm{K}\tilde{\Pi}, \tag{2.25}$$

with a dimensional constant $\mathrm{K} = A\rho l^2/\eta^2$, and $\tilde{\Pi}$ is the non-dimensional disjoining pressure (we have dropped the tildes in Eq. (2.23) and Eq. (2.24)).

At this stage, as mentioned before, we incorporate the long-wave scaling that simplifies the Navier–Stokes equations and its boundary conditions, preserving many of the important physical properties of the studied system. At this point it is important to take advantage of the different length scales between directions parallel and normal directions to the substrate: First, a smallness parameter ϵ is introduced, where $\epsilon = \frac{l}{L} \ll 1$, and L is for example the lateral drop size or the period of surface waves and l is some characteristic film height, like the precursor film height h_p or mean film thickness. The new length scale in x is introduced for z, for the velocities u and w and their derivatives. So, instead of using $x = l\tilde{x}$ and $z = l\tilde{z}$, we use

$$\begin{aligned} x = L\tilde{x} &= \frac{l}{\epsilon}\tilde{x} \\ z &= l\tilde{z}, \end{aligned} \tag{2.26}$$

and the new scaled velocities are,

$$\begin{aligned} u &= U_0\tilde{u} \\ w &= \epsilon U_0\tilde{w}, \end{aligned} \tag{2.27}$$

and the new scaled time is

$$t = \frac{L}{\epsilon U_0} = \frac{l}{\epsilon^2 U_0}\tilde{t}. \tag{2.28}$$

Finally, replacing (2.26), (2.27), (2.28) in Eq. (2.23) and Eq. (2.24), and dropping the tildes, we obtain the equations

$$\begin{aligned} \epsilon\left(\partial_t u + u\partial_x u + w\partial_z u\right) &= -\epsilon\partial_x p + \epsilon^2\partial_{xx}u + \partial_{zz}u + G\sin\alpha \\ \epsilon^2\left(\partial_t w + u\partial_x w + w\partial_z w\right) &= -\partial_z p + \epsilon^3\partial_{xx}w + \epsilon\partial_{zz}w - G\cos\alpha \\ \partial_x u + \partial_z w &= 0, \end{aligned} \tag{2.29}$$

and conditions,

$$
\begin{aligned}
\left(\partial_z u+\epsilon^2\partial_x w\right)\left(1-\epsilon^2(\partial_x h)^2\right)+2\epsilon^2\left(\partial_z w-\partial_x u\right)\partial_x h &= -\epsilon\mathrm{Ma}\Upsilon\left[(1+(\epsilon^2\partial_x h)^2\right]^{1/2}\\
p+\frac{2\left[-\epsilon^3\partial_x u(\partial_x h)^2-\epsilon\partial_z w+\epsilon\partial_x h\left(\partial_z u+\epsilon^2\partial_x w\right)\right]}{1+\epsilon^2(\partial_x h)^2} &= -\gamma\frac{\epsilon^2\partial_{xx}h}{[1+\epsilon^2(\partial_x h)^2]^{\frac{3}{2}}}-\Pi(h)\\
w &= \partial_t h+u\partial_x h. \qquad (2.30)
\end{aligned}
$$

in long–wave scaling, where

$$\Upsilon=\partial_x T+\partial_x h\partial_z T.$$

For small plate inclinations, i.e. for $\alpha \ll 1$, we introduce a new variable of order $O(1)$, $\tilde{\alpha}=\alpha/\epsilon$, i.e. $\sin\alpha\approx\epsilon\tilde{\alpha}$ and $\cos\alpha\approx 1-(\epsilon\tilde{\alpha})^2/2$. The choice of the scale for the surface tension, $\tilde{\gamma}=\gamma\epsilon^2$ is due to small inclination angles and where the velocities are small, so a new re-scaled velocity is introduced $\vec{\tilde{v}}=\frac{\vec{v}}{\epsilon}$. Note that we are interested here in the isothermal (non–thermal) case, i.e. $\Upsilon=0$ and $\mathrm{Ma}=0$. Now the equations are expressed in terms of powers of ϵ. The main interest is to study the low order expansions of ϵ; replacing the new scaled variables, dropping the tildes and dropping all terms of order $O(\epsilon^2)$ or higher, leads to a new set of non-dimensional equations and boundary conditions describing a thin film in the long-wave scaling:

$$\partial_{zz}u = \partial_x p - G\alpha \qquad (2.31)$$

$$\partial_z p = -G \qquad (2.32)$$

$$0 = \partial_x u+\partial_z w \qquad (2.33)$$

Now we are able to introduce the boundary conditions for the dragged-out plate depicted in Fig. 2.1. The transport equations are constrained by boundary conditions at the plate, $z=0$, and at the free surface, $z=h(x,t)$:

At the plate, $z=0$, the non–slip, non–penetration condition for the velocity field, recalling that there is no relative motion between the dragged plate and the liquid,

$$u(x,0)=-U \qquad (2.34)$$

and at the free surface, $z=h(x,t)$,

$$\partial_z u(x,h)= 0, \qquad (2.35)$$

the kinematic condition, i.e. the surface follows the the flow field,

$$w = \partial_t h + u\partial_x h \tag{2.36}$$

and the pressure at the free surface must satisfy,

$$p(h) = -\gamma\partial_{xx}h - \Pi(h) \tag{2.37}$$

where the integration constant is defined as

$$C_1(x) = Gh - \gamma\partial_{xx}h - \Pi(h). \tag{2.38}$$

Using the boundary conditions (2.37), (2.38) and integrating Eq. (2.33) in z,

$$p(x,z) = Gz + C_1(x) \tag{2.39}$$

it follows

$$p(x,z) = G(h-z) - \gamma\partial_{xx}h - \Pi(h) \tag{2.40}$$

Then, the derivative of p with respect to x is

$$\partial_x p = G\partial_x h - \partial_x\left[\gamma\partial_{xx}h + \Pi(h)\right]. \tag{2.41}$$

Integrating Eq. (2.32) twice and using the boundary conditions (2.34), (2.35) to determine the integration constants, one obtains for the velocity profile

$$u(x,z) = (\partial_x p - G\alpha)\left(\frac{z^2}{2} - hz\right) - U. \tag{2.42}$$

The kinematic boundary condition in combination with the continuity equation (2.33) gives

$$\partial_t h = -\partial_x \Gamma \tag{2.43}$$

where Γ is the flux in the laboratory frame. It is defined as

$$\Gamma = \int_0^{h(x,t)} u\mathrm{d}z. \tag{2.44}$$

Combining now Eqs. (2.42) and (2.40) and replacing in Eq. (2.43), we obtain the flux

$$\begin{aligned}\Gamma &= \int_0^{h(x)} \mathrm{d}z \left[(\partial_x p - G\alpha)\left(\frac{z^2}{2} - hz\right) - U\right] \\ &= -\frac{h^3}{3}(\partial_x p - G\alpha) - Uh. \end{aligned} \tag{2.45}$$

Finally we obtain the non-dimensional long-wave thin film evolution equation:

$$\partial_t h = -\partial_x \left(\frac{h^3}{3}\partial_x\left[\gamma\partial_{xx}h + \Pi(h)\right] - \frac{h^3}{3}G\left(\partial_x h - \alpha\right) - Uh\right) \tag{2.46}$$

We identify the different terms in Eq. (2.46) as the time–dependent term on the L. H. S., and on the R. H. S. the Laplace pressure term,

$$\begin{aligned}\underbrace{\partial_t h}_{\text{time dependent term}} &= -\partial_x(\underbrace{\frac{h^3}{3}}_{\text{Mobility factor}} \overbrace{\partial_x\left[\gamma\partial_{xx}h + \Pi(h)\right]}^{\text{Laplace and Derjaguin pressure}} \\ &\quad - \frac{h^3}{3} \underbrace{G\left(\partial_x h - \alpha\right)}_{\text{hydrostatic pressure and lateral gravity force}} - \underbrace{Uh}_{\text{drawing by substrate}})\end{aligned}$$

the Derjaguin / disjoining pressure term, the hydrostatic pressure term, the gravity term and the drawing term by the substrate. Note that the pre-factor $h^3/3$ multiplying the pressure terms and the hydrostatic - gravity term is called mobility factor, which represents the dynamic response of the medium towards the external perturbations. We simplify the expression by further rescaling by setting $\gamma = 1$, i.e. $l = \eta^2/(\epsilon^2\rho\gamma_0)$, and by absorbing the factor 1/3 from the mobilities h^3 into the scaled velocity U, i.e. $\tilde{U} = U/3$ and in the time derivative, i.e. $\partial_{\tilde{t}} = 3\partial_t$, and dropping the tildes, we have

$$\partial_t h = -\partial_x \left\{h^3\partial_x\left[\partial_{xx}h + \Pi(h)\right] - h^3 G\left(\partial_x h - \alpha\right) - Uh\right\}, \tag{2.47}$$

or explicitly,

$$\begin{aligned}\partial_t h = \; - \;& h^3\partial_{xxxx}h - h^2\partial_x h\partial_{xxx}h - h^3\left[\partial_{hh}\Pi(h)(\partial_x h)^2 + \partial_h\Pi(h)\partial_{xx}h)\right] \\ & -h^2\partial_x h\partial_h\Pi(h) + Gh^3\partial_{xx}h + Gh^2(\partial_x h)^2 - \alpha h^2\partial_x h + U\partial_x h.\end{aligned}$$

The first step in our analysis is to study steady-states of the equation, i.e. when $\partial_t h = 0$. For simplicity, we start from Eq. (2.47) and take $\partial_t h = 0$. We can now integrate once with respect to x, we obtain the steady-states equation:

$$h^3\left(\partial_{xxx}h + \partial_h\Pi(h)\partial_x h\right) - h^3 G\left(\partial_x h - \alpha\right) - Uh + J_0 = 0, \tag{2.48}$$

where the integration constant J_0 corresponds to the flux to the left. Note that Eq. (2.47) has been non-dimensionalised using $L = \sqrt{3/5}\, h_{\mathrm{eq}}/\theta_{\mathrm{eq}}$ as the length scale in the x-direction, h_{eq} as the length scale in the z-direction and $\tau{=}(9\eta h_{\mathrm{eq}})/(25\gamma\theta_{\mathrm{eq}}^4)$ as the time scale, where η is the viscosity of the liquid. With this non-dimensionalisation the dimensionless disjoining pressure has the form

$$\Pi(h) = \Pi_1(h) + \Pi_2(h) = -\frac{1}{h^3} + \frac{1}{h^6}. \tag{2.49}$$

The scaled velocity, gravity number and the inclination angle are given by

$$U = \frac{3\tau}{L}u, \quad G = \frac{\rho g h_{\mathrm{eq}}^4}{A}, \quad \alpha = \frac{L}{h_{\mathrm{eq}}}\tilde{\alpha}, \tag{2.50}$$

respectively, where ρ is the density of the liquid and g is the acceleration due to gravity and u and $\tilde{\alpha}$ are the dimensional plate velocity and the plate physical inclination angle, respectively.

2.1.5 Boundary conditions

The main part of the analysis is focused on the solution behaviour of the steady-state equation. Time simulations will only be used in a few cases. However, we introduce the boundary conditions for the general case to allow for a study of the time-dependent behaviour in the meniscus geometry with Eq. (2.47). In our open geometry we have to determine asymptotic boundary conditions at both ends of the finite computational domain. We assume that h tends to an undetermined constant value (*e.g.*, at equilibrium the precursor film thickness) as $x \to -\infty$ implying that its derivatives tend to zero as $x \to -\infty$, while at the side of the liquid bath we need to connect the meniscus to the bath via an asymptotic expansion, which will be explained in the following section. The use of asymptotic boundary conditions allows for a certain independence of our main results from the particular numerical domain size used.

Boundary conditions at the precursor film side

We are interested in solutions that for $h \to -\infty$ approach a constant film height h_∞. At this point it is necessary to recall a few definitions for the film thickness at the precursor film side to avoid confusion:

(i) h_{eq}, equilibrium precursor film height for $U = 0$ and $\alpha = 0$, i.e. $\Pi(h_{\mathrm{eq}}) = 0$.

(ii) h_{p}, precursor film height for $U = 0$ and $\alpha \neq 0$.

(iii) h_∞, coated film height for $U \neq 0$ and $\alpha \neq 0$, i.e. in a *non–equilibrium situation.*

(iv) h_0, any flat film.

For the steady thin film equation, Eq. (2.48), we already know that due to the partial-wetting disjoining pressure the substrate will always be coated by an adsorbed thin film, meaning that far away from the liquid bath, in an asymptotic limit, the film height in the precursor film model tends for $U = 0$ to the constant precursor film height h_{p}, therefore we impose that all derivatives of h vanish, i.e.

$$\partial_x h = \partial_{xx} h = 0 \text{ for } \ x \to -\infty. \tag{2.51}$$

Note that the film height on the precursor film side is kept free, i.e. it can take any value, but it has to be constant and flat.

Boundary conditions at the meniscus - liquid bath

To describe the behaviour of the film thickness profiles in the entrainment zone, i.e. in the region in the vicinity of the dragged plate where liquid is set into motion (see Fig. 2.1), and to connect the film with the bath, we use an ansatz that fulfils $\partial_x h = \alpha$ when $x \to \infty$, i.e. the film slope tends to α, or with other words the film surface profile approaches the horizontal surface of the semi-infinitely extended bath. To obtain the next order contributions we use the ansatz

$$h = \alpha x + \sum_{j=1}^{\infty} \frac{C_j}{x^j} = \alpha x + \frac{C_1}{x} + \frac{C_2}{x^2} + \frac{C_3}{x^3} + \frac{C_4}{x^4} + \dots \tag{2.52}$$

that gives consistent results. Consistent results are not obtained when employing other sequences used elsewhere for related equations, see for example [10, 30]. Appendix A shows how to derive Eq. (2.52) using centre manifold theory.

The first derivative is

$$\partial_x h = \alpha - \sum_{j=1}^{\infty} j \frac{C_j}{x^{j+1}} = \alpha - \frac{C_1}{x^2} - \frac{2C_2}{x^3} - \frac{3C_3}{x^4} - \frac{4C_4}{x^5} + \ldots . \tag{2.53}$$

Alternatively the free surface could approach a constant curvature meniscus, i.e. when the "bath" is confined between two parallel plates. In this case, the ansatz is

$$h = \kappa x^{1/2} + \frac{C_1}{x} + \frac{C_2}{x^2} + \ldots .$$

To calculate the values of the coefficients C_j, we introduce ansatz (2.52) into Eq. (2.48), and expand in powers of $1/x$ resulting in

$$\left(-U\alpha + G\alpha^3 C_1\right) x + \left(2\,G\alpha^3 C_2 + J_0\right) + \frac{3 - UC_1 + 3\,G\alpha^3 C_3 + 3\,G\alpha^2 {C_1}^2 - 6\,\alpha^3 C_1}{x} + \frac{4\,G\alpha^3 C_4 + 9\,G\alpha^2 C_1\,C_2 - UC_2 - 24\,\alpha^3 C_2}{x^2} + \ldots = 0, \tag{2.54}$$

that we consider order by order in x.

The coefficients of the x^i (for $i = 1, 0, -1, \ldots$) in Eq. (2.54) have to be zero, allowing us to determine the values of the C_j. The relations obtained from the first 4 coefficients are:

$\boldsymbol{i = 1}$: $G\alpha^3 C_1 - U\alpha = 0$

$\boldsymbol{i = 0}$: $J_0 + 2\,G\alpha^3 C_2 = 0$

$\boldsymbol{i = -1}$: $3 - UC_1 + 3\,G\alpha^3 C_3 + 3\,G\alpha^2 {C_1}^2 - 6\,\alpha^3 C_1 = 0$

$\boldsymbol{i = -2}$: $4\,G\alpha^3 C_4 + 9\,G\alpha^2 C_1\,C_2 - UC_2 - 24\,\alpha^3 C_2 = 0$

From the expressions above, we find

$$\begin{aligned} C_1 &= \frac{U}{\alpha^2 G} \\ C_2 &= -\frac{1}{2}\frac{J_0}{G\alpha^3} \\ C_3 &= -\frac{1}{3}\frac{3\alpha^2 G + 2U^2 - 6U\alpha^3}{\alpha^5 G^2} \\ C_4 &= J_0\frac{U-3\alpha^3}{G^2\alpha^6}. \end{aligned} \tag{2.55}$$

For our later calculations it turns out to be sufficiently exact to use the first three

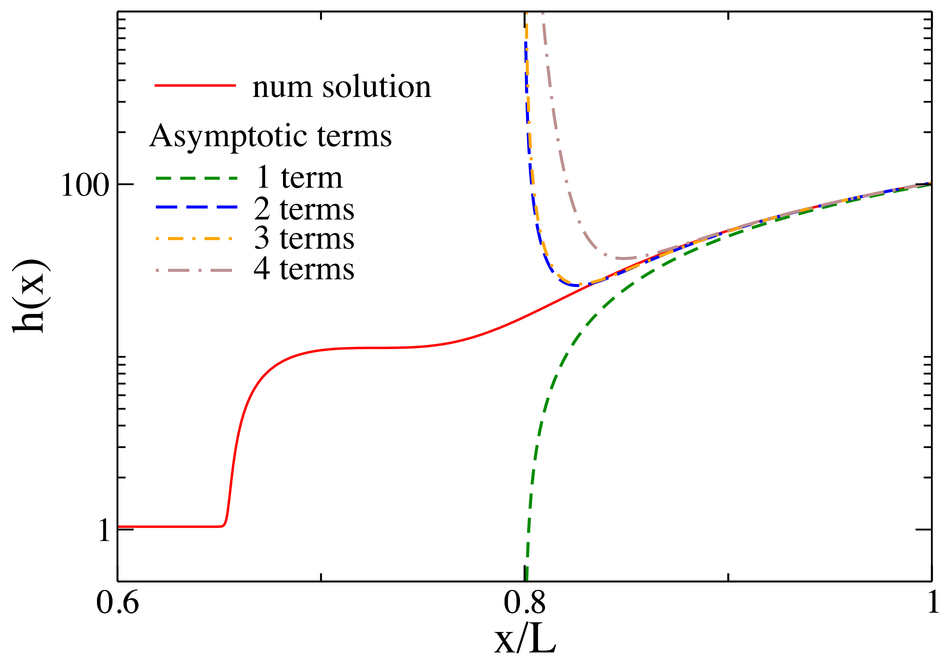

FIGURE 2.8: Shown is a log-normal plot with a comparison of a numerical solution for $\alpha = 0.5$ at $U = 0.083$ with asymptotic solutions with 1, 2, 3 and 4 terms in the series expansion, i.e. Eq. (2.53) with Eqs. (2.56). The domain size is $L = 1000$ and the position of the meniscus is at $x_M = 800$. The region of interest is where the meniscus connects to the bath. Line styles as shown in the legend.

terms of Eq. (2.52), i.e. the boundary conditions are, see Fig. 2.8:

$$\begin{aligned} h &\approx \alpha x + \frac{U}{\alpha^2 G x} - \frac{J_0}{2G\alpha^3 x^2}, \\ \partial_x h &\approx \alpha - \frac{U}{\alpha^2 G x^2} + \frac{J_0}{G\alpha^3 x^3}. \end{aligned} \tag{2.56}$$

Note that the connection between the plate and an idealised straight bath surface occurs at a fixed coordinate x_M (see Fig. 2.1), so that the boundary conditions (2.56) are valid for $\tilde{x} = x - x_M$. We can re-write the boundary conditions now including the position of the meniscus,

$$\begin{aligned} h &\approx \alpha(x - x_M) + \frac{U}{\alpha^2 G(x - x_M)} - \frac{J_0}{2G\alpha^3 (x - x_M)^2} \\ \partial_x h &\approx \alpha - \frac{U}{\alpha^2 G(x - x_M)^2} + \frac{J_0}{G\alpha^3 (x - x_M)^3}. \end{aligned} \tag{2.57}$$

In Fig. 2.8 we compare a numerical solution for $\alpha = 0.5$ at $U = 0.083$ with asymptotic solutions with 1, 2, 3 and 4 terms in the series expansion for a simulation $L = 1000$ and $x_M = 800$.

For simplicity we define the meniscus position as $x_M = 0$ and solve the equation on the domain $[-L_1, L_2]$. At $x = -L_1$, we impose the boundary conditions $h'(-L_1) = 0$ and $h''(-L_1) = 0$, see Eq. (2.51) and at $x = L_2$, we impose the boundary condition obtained by truncating the asymptotic expansion, see Eq. (2.56). Note that the flux J_0 will be obtained via a relation defined in Eq. (2.68), see Subsection 2.2.3.

2.2 Linear stability analysis

2.2.1 Linear stability analysis of a flat film

To analyse the linear stability in time of any flat film, i.e. $h(x,t) = h_0 \equiv const.$, we introduce a Fourier mode decomposition, $h(x,t) = h_0 + \epsilon e^{(\beta t + ikx)}$, with Re$[\beta]$ being the growth rate and k the wave number of the linear perturbation, while Im$[\beta]$ describes the phase velocity $C_{\text{phase}}(k)$ =Im$[\beta]/k$. The perturbation amplitude ϵ is small, i.e. $\epsilon \ll 1$. Note that

$$\partial_x^n h(x,t) = \epsilon (ik)^n e^{\beta t + ikx} \tag{2.58}$$

and

$$\partial_t h(x,t) = \epsilon \beta e^{\beta t + ikx}, \tag{2.59}$$

are the n–th spatial and the temporal derivatives, respectively. Introducing the ansatz, Eqs. (2.58), and (2.59), in Eq. (2.47) and linearising in ϵ, the dispersion relation

$$\beta(k) = -k^2 h_0^3 (k^2 - k_c^2) - ik \left(3G\alpha h_0^2 - U\right) \tag{2.60}$$

is obtained, where we introduced $k_c^2 = \partial_h \Pi(h_0) - G$.

The growth rate is (see Fig. 2.9),

$$\mathrm{Re}[\beta(k)] = -k^2 h_0^3 (k^2 - k_c^2) \tag{2.61}$$

and the imaginary part describes the phase velocity $C_{\mathrm{phase}}(k)$ of the mode via

$$\mathrm{Im}[\beta(k)]/k = C_{\mathrm{phase}} = -\left(3G\alpha h_0^2 - U\right). \tag{2.62}$$

The flat film is linearly unstable for $\mathrm{Re}[\beta(k)] > 0$. From Eq. (2.61) and Fig. 2.9 we see that an interval of unstable wave numbers k_u exists, $k_u \in [0, k_c]$, such that $\mathrm{Re}[\beta(0)] = \mathrm{Re}[\beta(k_c)] = 0$, where k_c is the critical wave number. Fig. 2.9 shows the growth rate $\mathrm{Re}[\beta(k)]$ for a flat film on an inclined plate. The unstable and linearly stable case are depicted as a solid line and a dashed line respectively.

2.2.2 Spatial linear stability analysis of flat films

We focus now on the spatial linear stability and start our analysis defining a spatial dependance of steady perturbations for the steady state equation Eq. (2.48),

$$h(x) = h_0 + \epsilon h_1(x) \tag{2.63}$$

where h_0 is any constant film height and $\epsilon \ll 1$ the small amplitude of the perturbation. After introducing the perturbation Eq. (2.63) into Eq. (2.48) and expanding

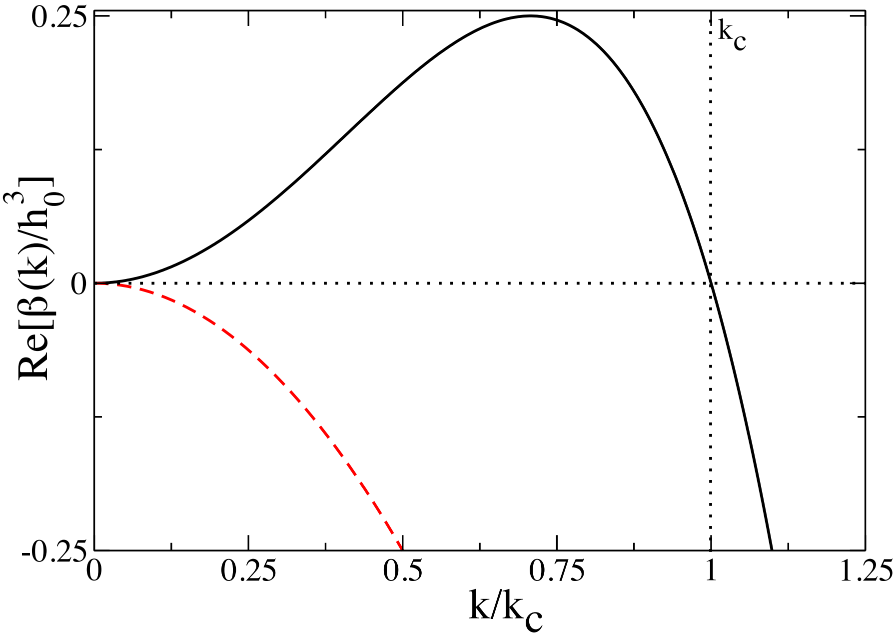

FIGURE 2.9: Dispersion relation (Growth rate Re[$\beta(k)$]) for a flat film on an inclined plate. Shown are the unstable (solid line) and linearly stable case (dashed line).

in ϵ one obtains at order O(1),

$$J_0 + G{h_0}^3\alpha - Uh_0 = 0 \tag{2.64}$$

and at O(ϵ),

$$\partial_{xxx}h_1(x) + \partial_x h_1(x)\left(\frac{3}{h_0^4} - \frac{6}{h_0^7} - G\right) + h_1(x)\frac{3G\alpha h_0^2 - U}{h_0^3} = 0. \tag{2.65}$$

The first equation is analysed in the following subsection. It tells us that for each given set of parameters U, α and J_0 there are three possible flat film heights h_0.

The second equation, Eq. (2.65) is a third order linear differential equation, that can be solved via standard methods [49]. As we are looking into spatial perturbations of an infinitely extended flat film, we decompose into Fourier modes

$$h_1(x) = Ae^{kx}, \tag{2.66}$$

introduce this into Eq. (2.65) and obtain the characteristic polynomial $P(k)$ in terms of the wave number k

$$k^3 + k\left(\frac{3}{h_0^4} - \frac{6}{h_0^7} - G\right) + \frac{3\,G\alpha\,h_0^2 - U}{h_0^3} = 0. \tag{2.67}$$

We are now able to solve the coupled system of equations, Eqs. (2.64) and (2.67): First we numerically solve Eq. (2.64) and for each physically meaningful solution for the flat film heights h_0, we solve Eq. (2.67) obtaining three possibly complex wave numbers k that will characterise how flat parts of the film profiles connect to other parts.

2.2.3 Flat films

We know already under which conditions a flat film will be unstable. We also know how to calculate the eigenvalues corresponding to spatial linear perturbations, which will give us valuable information about the film profile structure. Now we need to understand which flat films can be used for these calculations, i.e. the physically meaningful solutions, so we need to solve Eq. (2.64), which is a cubic polynomial relation in h_0,

$$G\alpha h_0^3 - U h_0 + J_0 = 0 \tag{2.68}$$

that relates the flux J_0 and height h_0 for given parameters α and U as shown in Fig. 2.10. Note that if we introduce the boundary conditions (2.51) in Eq. (2.48), we obtain the same relation, i.e. the value the film height takes at $x \to -\infty$ is one of the solutions. We are interested only in positive film heights, which are the physical meaningful solutions of the problem. Analysing Eq. (2.68) we find that there exists a range of values for h_0 that is a physical solution for the problem at hand where we impose $J_0 > 0$, in particular $h_0 \in [0, \sqrt{U/(G\alpha)}]$. The flux J_0 is constrained between zero and a maximum value $J_{\max} = \frac{2\sqrt{3}}{9} U^{2/3} \sqrt{1/G\alpha}$, that is obtained at $h_0 = \sqrt{U/3G\alpha}$ from Eq. (2.68). It is worth to point out, that the precursor film boundary condition, Eq. (2.68), determines a relation between the flux J_0 and the coating film height $h_0 = h_\infty$. A close inspection of the cubic equation results in a relation between the number of possible real positive solutions for flat film heights and a given flux J_0. The following cases are of interest:

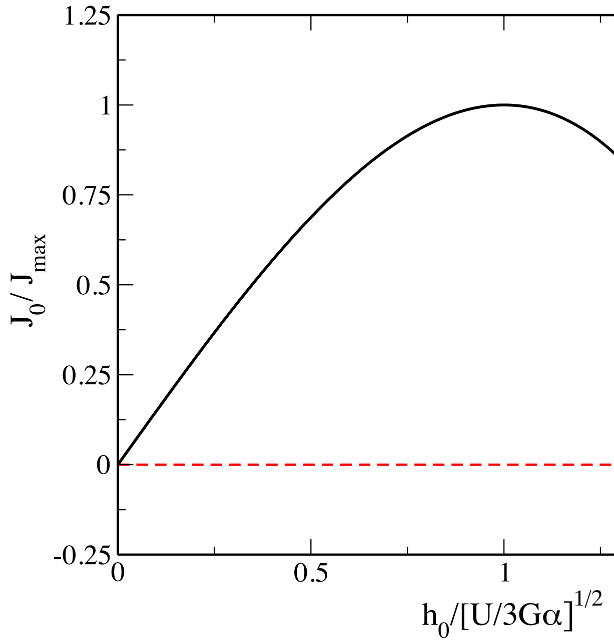

FIGURE 2.10: Flux - film height dependence. Shown is the flux $J_0/J_{\max}$ vs. $h_0/\sqrt{U/3G\alpha}$. For $\tilde{h}_0 = h_0/\sqrt{U/3G\alpha} \in \{0, \sqrt{3}\}$ the flux is zero. The maximum flux $J_{\max} = 2/3U\sqrt{U/(3G\alpha)}$ is obtained at $\tilde{h}_0 = 1$.

(i) no flat film solution

$$J_0 > J_{\max} = \frac{2}{3}U\sqrt{\frac{U}{3G\alpha}} \tag{2.69}$$

(ii) one flat film solution

$$J_0 = J_{\max} \tag{2.70}$$

(iii) two flat film solutions

$$0 \leq J_0 < J_{\max} \tag{2.71}$$

(iv) one flat film solution

$$J_0 < 0 \tag{2.72}$$

We do not consider the last case here as it can only result if additional liquid is supplied onto the plate at $x = -\infty$, (see however, discussion in [41]).

The case in Eq. (2.69) results in one negative real solution and two complex conjugate solutions, none of the three correspond to a physical film height, the relation in Eq. (2.70) results in three real solutions, where one is negative and the other two are double roots corresponding to one physical film height and case (2.71) results in three different real solutions with one being negative and the other two are physical film heights. As we will see in the next chapter, solutions in cases (2.70) and (2.71) are describing physically meaningful solutions, namely Landau–Levich films [8], *foot*–solutions / thick–film solutions [10, 14, 18] and ultra–thin coating layers close to precursor thickness.

This analysis gives us an insight of how many different film heights exist for fixed parameters indicating if steady solutions may exist that connect several flat film parts.

The information obtained via relations (2.69), (2.70) and (2.71) can be complemented by an additional condition to restrict the range of possible values of flat film heights $h_0 = h_\infty$ for the present case without source of liquid at $x \to -\infty$, see e.g. [29]. This is done by inspecting the expression for the velocity profile in the film Eq. (2.42), particulary analysing the sign of the velocity directly at the free surface. Requesting that the velocity $v(h_0) > 0$ gives an upper bound for h_0 through the condition $v(h_0) = 0$,

$$h_0^{\max} = \sqrt{\frac{2U}{G\alpha}} \tag{2.73}$$

with values of $h_0 > h_0^{\max}$ corresponding to films where an upper layer above $z = z_0 \leq h_0$ flows down the plate towards the bath of liquid. These solutions have no physical correspondence to the system we are studying as they need a liquid source at $x \to -\infty$.

2.3 Streamlines

To have a better understanding of the internal structure of the meniscus–, foot– and film solutions, it is instructive to see the changes of the velocity field inside the profiles. In the problem we are studying, we have a two dimensional incompressible flow, i.e. the velocity distribution of the moving fluid depends only on two coordinates, x and z, and is constrained to the $(x - z)$-plane. In this type of problem it is useful to introduce the *stream function* $\Psi(x, z)$ which depends on the velocity components $u(x, z)$ and $w(x, z)$. The contour lines of the stream function

$\Psi(x, z)$, i.e. lines on which $\Psi(x, z)$ = constant., represent the *streamlines*. The direction of the tangent vector of a streamlines at a given coordinate (x_i, z_i) is the direction of the fluid velocity at this given point.

The stream function $\Psi(x, z)$ can be calculated using the expression of the velocity components $u(x, z)$ and $w(x, z)$, see e.g. [50, 51], by means of

$$u(x, z) \quad = \quad \partial_z \Psi(x, z) \tag{2.74}$$

and

$$w(x, z) \quad = \quad -\partial_x \Psi(x, z). \tag{2.75}$$

We can easily construct the full expression of the x-component of the velocity $u(x, z)$ from the expression of the velocity component $u(x, z)$, Eq. (2.42), and the expression for the pressure, Eq. (2.41), i.e.

$$u(x, z) = \left(G(\partial_x h - \alpha) - \partial_{xxx} h - \partial_h \Pi(h) \partial_x h\right) \left(\frac{z^2}{2} - hz\right) - U. \tag{2.76}$$

On the other hand, in order to simplify this expression, we can use Eq. (2.47) to replace the higher order derivative $\partial_{xxx} h$ from the steady state equation, i.e.

$$-\partial_{xxx} h = \partial_h \Pi \partial_x h - G(\partial_x h - \alpha) - 3\left(\frac{U}{h^2} + \frac{J_0}{h^3}\right). \tag{2.77}$$

The x-component velocity $u(x, z)$ of the fluid is

$$u(x, z) = 3\left(-\frac{U}{h^2} + \frac{J_0}{h^3}\right)\left(\frac{z^2}{2} - hz\right) - U. \tag{2.78}$$

To construct the z-component velocity $w(x, z)$ we use the incompressibility relation, Eq. (2.33), i.e.

$$w(x, z) = -\int \mathrm{d}z \partial_x u(x, z). \tag{2.79}$$

From Eq. (2.78) $\partial_x u(x, z)$ is,

$$\partial_x u(x, z) = \partial_x h \left[\left(\frac{6U}{h^3} - \frac{9J_0}{h^4}\right)\left(\frac{z^2}{2} - hz\right) - 3\left(\frac{U}{h^2} - \frac{J_0}{h^3}\right) z\right] \tag{2.80}$$

and after a straightforward integration $w(x, z)$ results as

$$w(x,z) = -\partial_x h \left[\left(\frac{6U}{h^3} - \frac{9J_0}{h^4} \right) \left(\frac{z^3}{6} - \frac{hz^2}{2} \right) - \frac{3}{2} \left(\frac{U}{h^2} - \frac{J_0}{h^3} \right) z^2 \right] + \widetilde{C}(x). \quad (2.81)$$

To determine $\widetilde{C}(x)$, we apply the boundary conditions, see Eq. (2.34), at $z = 0$, i.e. no–slip and no–penetration, so that $\widetilde{C}(x) = 0$.

For a consistency check, we know that the velocity component $w(x, z)$ at $z = h(x)$ satisfies the kinematic condition Eq. (2.36), i.e.

$$w(x,h) - \partial_x h \, u(x,h) = 0 \quad (2.82)$$

which is fully satisfied.

Using Eq. (2.78) and Eq. (2.81) in combination with Eq. (2.74) and Eq. (2.75), we obtain two expressions for the stream function $\Psi(x, z)$

$$\Psi(x,z)_1 = \left(-\frac{U}{h^2} + \frac{J_0}{h^3} \right) \frac{z^3}{2} - \left(-\frac{U}{h} + \frac{J_0}{h^2} \right) \frac{3z^2}{2} - Uz + \widetilde{C_1}(x) \quad (2.83)$$

$$\Psi(x,z)_2 = \left(-\frac{U}{h^2} + \frac{J_0}{h^3} \right) \frac{z^3}{2} - \left(-\frac{U}{h} + \frac{J_0}{h^2} \right) \frac{3z^2}{2} + \widetilde{C_2}(z). \quad (2.84)$$

Both stream functions Ψ_1 and Ψ_2 should be the same, which leads to

$$\begin{aligned} \widetilde{C_1}(x) &= 0 \\ \widetilde{C_2}(z) &= -Uz. \end{aligned}$$

The stream function is given by

$$\Psi(x,z) = \left(-\frac{U}{h^2} + \frac{J_0}{h^3} \right) \frac{z^3}{2} - \left(-\frac{U}{h} + \frac{J_0}{h^2} \right) \frac{3z^2}{2} - Uz, \quad (2.85)$$

for $0 \le z \le h(x)$ and $\forall x \in [-L_1, L_2]$.

There are some points (x_{st}, z_{st}) where the fluid velocity $\vec{u}$ could be zero, i.e. $\vec{u}(x_{st}, z_{st}) = 0$. These points are known as *stagnation points* and they can occur on the free surface of the fluid, i.e. at $h(x)$, and also inside the film proflie, i.e. $0 \le z < h(x)$.

We calculate the coordinates of the stagnation points from the velocity components expressions, Eq. (2.78) and Eq. (2.81),

$$\begin{aligned} 3\left(-\frac{U}{h^2}+\frac{J_0}{h^3}\right)\left(\frac{z^2}{2}-hz\right)-U &= 0 \\ -\partial_x h\left[\left(\frac{6U}{h^3}-\frac{9J_0}{h^4}\right)\left(\frac{z^3}{6}-\frac{hz^2}{2}\right)-\frac{3}{2}\left(\frac{U}{h^2}-\frac{J_0}{h^3}\right)z^2\right] &= 0. \end{aligned}$$

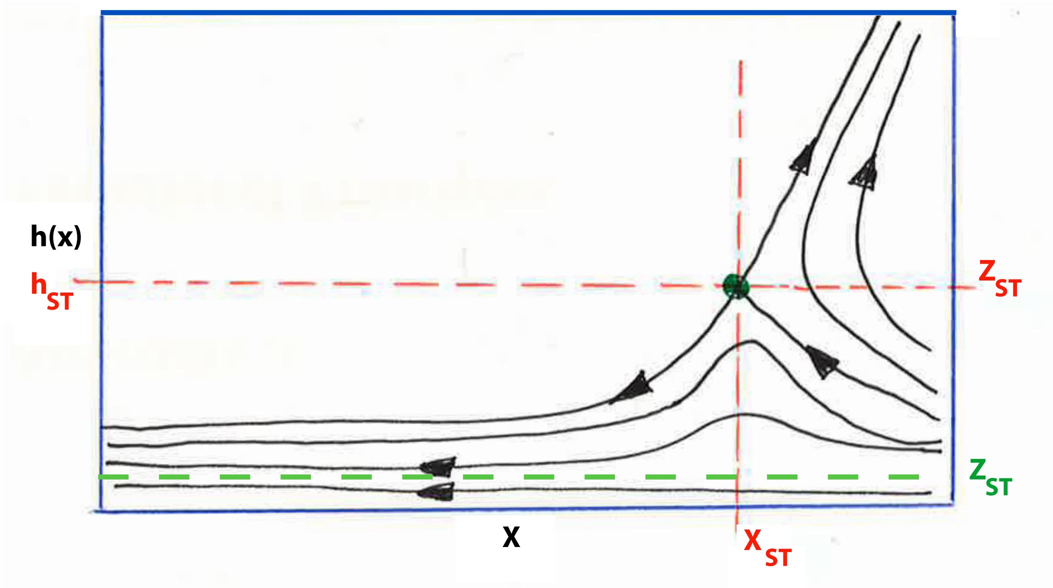

FIGURE 2.11: Sketch of a stagnation point located at the coordinates (x_{st}, z_{st}). As example is also shown a stagnation line (dashed green line). See text.

The stagnation points are located at

$$\begin{aligned} h_{st} &= 3\frac{J_0}{U} \\ z_{st} &= 3\frac{J_0}{U}. \end{aligned}$$

Note that $h_{st} = h(x_{st})$ and corresponds as well to the coordinate x_{st}, see Fig. 2.11. These solutions allow as well a stagnation line located at z_{st} and stagnation points at z_{st}, with $z_{st} < h(x)$.

Chapter 3

Behaviour of a drawn meniscus of non–volatile liquid

> “This is the job. Don’t wait for it to happen. Don’t even want it to happen. Just watch what does happen.”
>
> Jim Malone

In the previous chapters we have introduced the physical problem, the governing equations, the non-dimensional mathematical model in long-wave approximation as well as the necessary boundary conditions to solve it numerically. Here, we will describe important results pertaining the different behaviours of the system with particular focus on the triggering mechanisms responsible for the transitions leading from the deposition of (i) an ultrathin coating film at small plate velocities to (ii) a macroscopic film of thickness $h \propto U^{2/3}$ (corresponding to the classical Landau–Levich film). Depending on the plate inclination, four regimes are found for the change from case (i) to (ii). These different regimes and the transitions between them are analysed employing numerical continuation of steady states and of loci of saddle-node bifurcations as well as simulations in time. We also discuss the relation of our results to results obtained with a slip model, which will be discussed later on in the text.

3.1 Partially wetting liquid

The results presented here are obtained using continuation techniques [52, 53] bundled in the package AUTO (auto07p) [54]. This software package is based on the method of orthonormal collocation for discretising solutions, with an adaptive mesh to equidistribute the discretisation error. Starting from known solutions, AUTO searches nearby solutions for the discretised system using a combination of Newton and Chord iterative methods. When a solution converges, AUTO starts to follow the solution–path by a small step in the parameter space defined by the free continuation parameters and re-starts the iteration.

A description and examples of the application of numerical continuation techniques to thin film problems can be found in sect. 4b of the review in ref. [55], in sect. 2.10 of ref. [56], and in refs. [57–59]. These techniques are used for analysing Eq. (2.48) with the boundary conditions described in Eq. (2.51) and Eq. (2.56). This enables us to obtain steady solutions for a specific set of control parameters, e.g. plate inclination angle α, plate velocity U. These two control parameters are a natural choice, as they can be directly related to the parameters of the experimental setup. To investigate the influence of the domain size, we carried out test runs

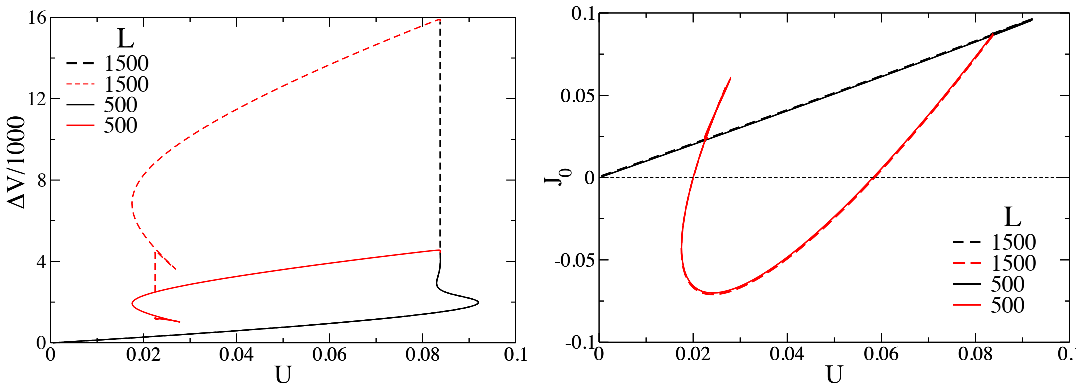

FIGURE 3.1: Domain size effects. Left panel: Solution measure ΔV versus plate velocity U for plate inclination angle $\alpha = 0.5$ and different system sizes $L = 500$ and $L = 1500$. Note that when the front reaches the domain end, the system jumps to a different solution branch (shown in red). Right panel: Flux versus drag velocity for plate inclination angle $\alpha = 0.5$ and different system sizes $L = 500$ and $L = 1500$. The physically meaningful solutions are those shown in black and for $J_0 > 0$. For more details, see text.

using different domain sizes, $L = 500$, 1000 and 1500 for different fixed plate inclination angles α. In Fig. 3.1 we compare a smaller domain size, $L = 500$, with a larger one, $L = 1500$. In the left panel we plot the effective volume measure ΔV

(see Appendix B , Eq. (B.1)), divided by 1000, versus plate velocity U for plate inclination angle $\alpha = 0.5$. When the solution profile front reaches the domain end, the system jumps to a different solution branch (shown in red in both panels). On the right panel, we plot flux J_0 versus plate velocity U for plate inclination angle $\alpha = 0.5$. The physically meaningful solutions are those shown in black and for $J_0 > 0$[1].

Finally, unless stated otherwise a domain size of $L = 1000$ is chosen to avoid finite domain effects. We use the dimensionless gravity number $G = 0.001$ for all numeric calculations.

3.1.1 Steady menisci at zero plate velocity and at small (scaled) angles

We start our numerical analysis by studying the behaviour at plate velocity $U = 0$ for different plate inclination angles. We observe for all angles that a meniscus rises up from the bath due to wettability and surface tension. In Fig. 3.2 a full range of different inclination angles is shown, note the inset in the left panel that zooms on the region around x_{M}. This range covers equidistant inclination angles, where α spans from $\alpha = 0.25$ to $\alpha = 10$ with an step increase of $\Delta\alpha = 0.25$. The semi-log scale is chosen to have a better representation of the whole range of inclination angles with a focus on the contact line region. We identify clearly the precursor (coating) film of height h_∞ preceding the meniscus. Note that as $U = 0$, $h_\infty = h_{\mathrm{p}} \approx h_{\mathrm{eq}}$ for all α.

We observe also how the curvature of h changes sign in the contact line region (around x_{M}) as the plate inclination angle α passes the value of the equilibrium angle θ_{eq}, see Fig. 3.3. There, we plot in the left panel the slope h_x for five equidistant inclination angles below and above the equilibrium contact angle $\theta_{\mathrm{eq}} = 0.775$, namely $\alpha = 0.25, 0.5, 0.75, 1.0$ and 1.25. The change of sign in the curvature occurs when the relative maximum of h_x crosses zero. Note how the slope of the profile approaches the plate inclination angle as x tends to L, i.e. $h_x \to \alpha$.

We will first focus on the behaviour at relatively small inclination angles, $\alpha \lesssim 1.0$. We continue our analysis by observing how the physical system behaves once it

[1] In our numerical calculations, the flux J_0 is a secondary continuation parameter which is left free and is related to the coating height h_∞ via Eq. (2.68)

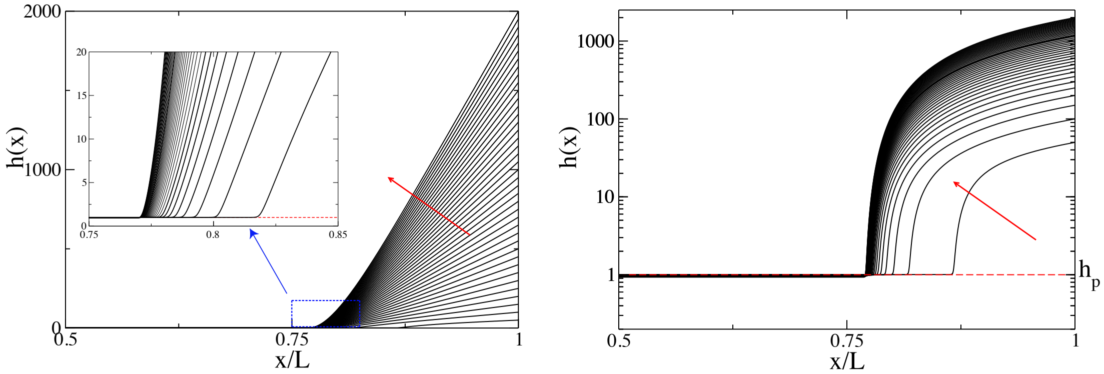

FIGURE 3.2: Steady menisci for zero plate velocity, $U = 0$, for different equidistant inclination angles, $\alpha \in [0.25,\ 10]$, increment $\Delta\alpha = 0.25$. The arrow indicates direction of increasing α. Detail in the inset as indicated. Left panel: Normal plot of film profiles. Right panel: Semi-log plot of film profiles. Note that in the semi-log plot the depiction of the precursor (coating) film of height h_∞ preceding the meniscus is clearer. The red dashed line indicates the equilibrium precursor film height $h_\mathrm{p} = 1$, see Eq. (2.18). Meniscus position is at $x_\mathrm{M} = 0.8$ and the domain size is $L = 1000$ in both panels.

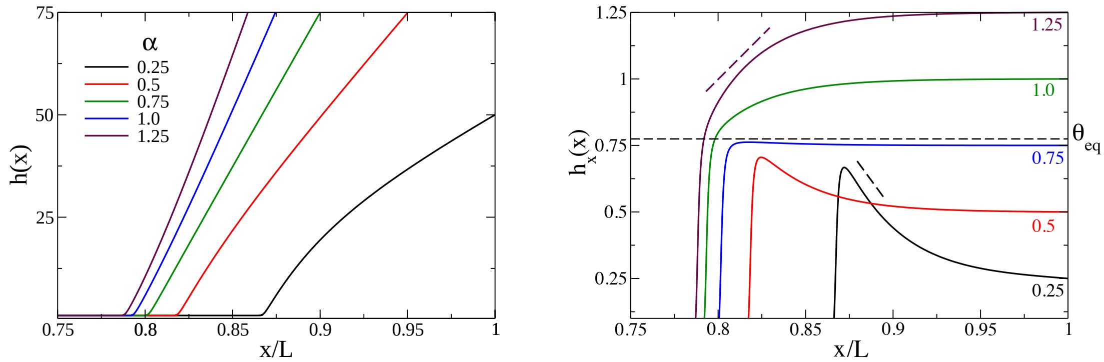

FIGURE 3.3: Left panel: Shown are five film profiles at $U = 0$ for different plate inclination angles as described in the legend. Note the change of curvature (see left panel) in the contact line region. Right panel: Shown is h_x at $U = 0$ for different plate inclination angles as indicated in the coloured legend. Note the change of slope as the the plate inclination approaches the equilibrium angle $\theta_\mathrm{eq} = 0.77459$ and how $h_x \to \alpha$ for $x \to L$.

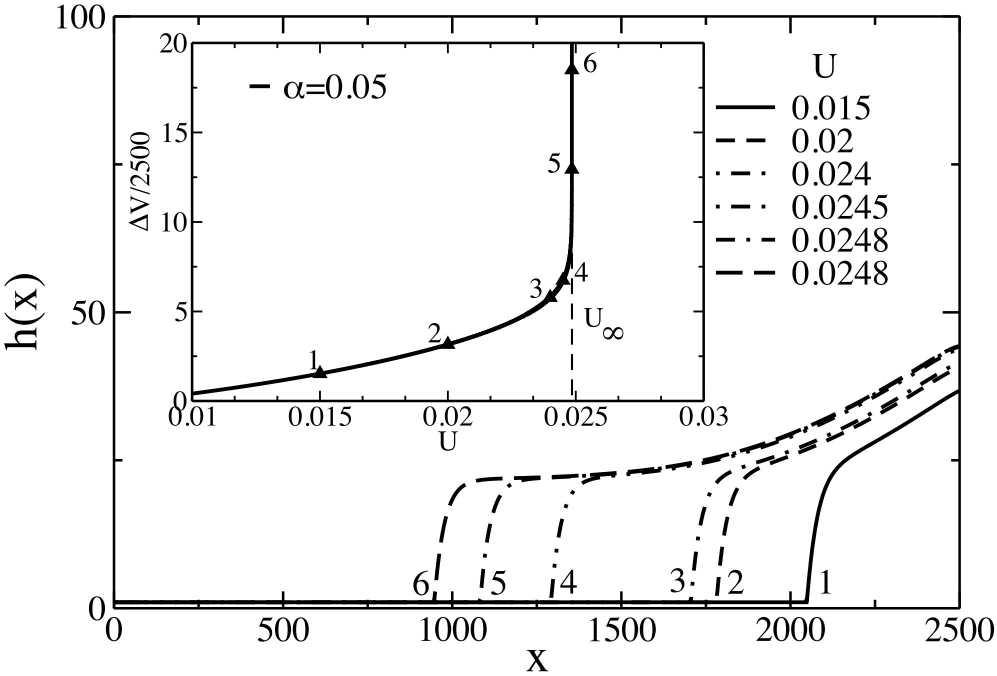

FIGURE 3.4: $\alpha = 0.05$: Film profiles for different drag-out velocities. As an inset effective volume ΔV in dependence of the plate velocity U. The numbers on the bifurcation diagram correspond to the depicted film profiles. The domain size is $L = 2500$.

starts to be driven by the moving plate at small angles, for example at $\alpha = 0.05$, see Fig. 3.4. In the inset, a bifurcation diagram in terms of the effective volume ΔV in dependence of plate velocity U is shown. We observe that, as the drag velocity U increases, the volume increases monotonically and approaches a vertical asymptote at some velocity value, that we define as U_∞.

Further on, the film profile solutions we observe as the plate velocity U increases, show that with increasing U the meniscus profile starts to grow in length and evolves into an *extended meniscus* or *foot solution*. These profiles are shown in Fig. 3.4, where the corresponding number on the bifurcation curve corresponds to the film profile in the main figure. Note how the foot solution emerges when the vertical asymptote at U_∞ is approached. The foot then increases its length at constant height, h_f. At U_∞, the foot length diverges. This foot is entirely flat and does not exhibit undulations on the free surface. We observe this behaviour for all values of α up to a critical inclination angle $\alpha = \alpha_1 \approx 0.1125$.

When the plate is inclined further, e.g. at $\alpha = 0.5$, see Fig. 3.5, we observe a different bifurcation diagram: Now, we detect pairs of saddle nodes in the bifurcation

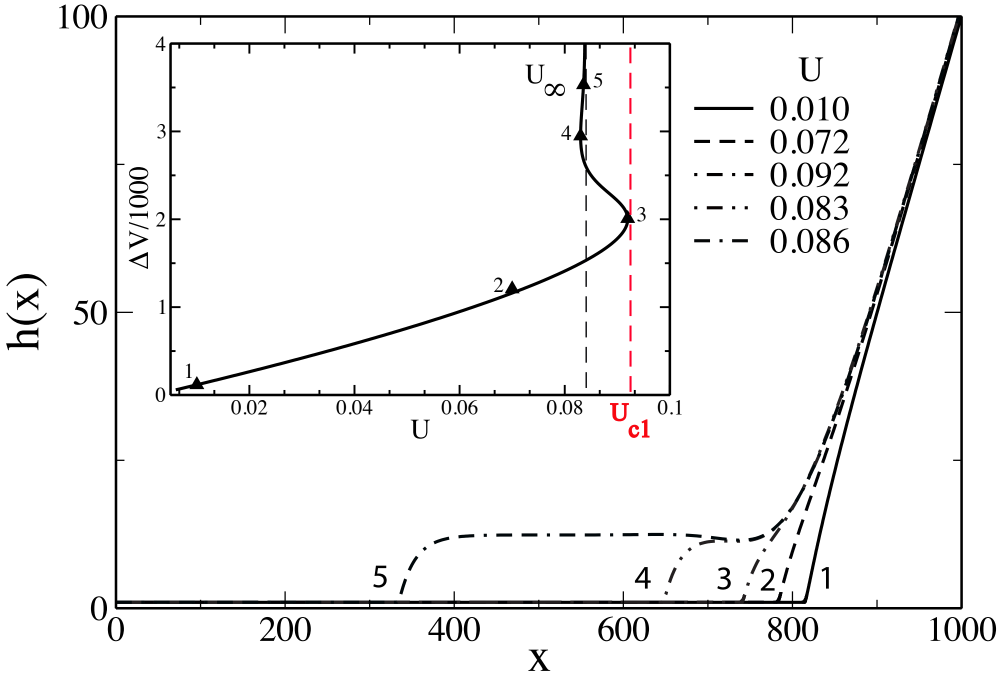

FIGURE 3.5: $\alpha = 0.5$: Film profiles for different drag-out velocities. As an inset effective volume in dependence of the drag velocity. Note the appearance of the characteristic *snaking* after U_{C1} when the bifurcation curve starts to fold back. The numbers on the bifurcation diagram correspond to the depicted film profiles. The domain size is $L = 1000$.

diagram. The first saddle node occurs at a critical velocity U_{C1}, where the bifurcation curve folds back and switches to an upper branch. Note that $U_{C1} > U_\infty$. The second saddle node occurs at $U = U_{C2}$, with $U_{C2} < U_\infty$. The bifurcation curve starts to exhibit a *snaking* behaviour, see sketch on left panel of Fig. 3.6: it oscillates around a vertical asymptote at $U = U_\infty$ with a decaying amplitude. Note that in this case there is an infinite but countable number of saddle nodes at which the slope of the bifurcation curve is vertical. The vertical asymptote U_∞ is different for every plate inclination angle α.

The film profile solutions we observe as the plate velocity U increases, show that the meniscus profile evolves again into an extended meniscus or foot solution. These profiles are shown in Fig. 3.5, where the corresponding numbers on the bifurcation curve corresponds to the numbered film profiles in the main figure. Note how the foot starts to emerge when the bifurcation first folds back at the critical velocity U_{C1} and how the foot monotonically increases its length at constant height as the plate velocity oscillates around U_∞. These foot solutions exhibit undulations on the free surface.

Summing up, in both cases, see Fig. 3.4 and Fig. 3.5, a clear description of how the meniscus foot is dragged out as the plate velocity changes emerges: For solutions (1) and (2), no foot like film profile exists yet — just a simple meniscus. Note that when the velocity approaches U_∞ [solution (3)], the film shape starts to change to the foot solution. Solutions (4) and (5) present clearly foot–like solutions, note, as previously described, that the thick film covers a larger region of the plate and that the foot height $h_\mathrm{f} \propto U_\infty^{1/2}$.

These foot-like solutions present two characteristic heights:

(a) (coating) precursor film height h_∞

(b) foot height h_f, where $h_\mathrm{f} \propto U_\infty^{1/2}$.

It is important for the sake of simplicity in our further analysis to define for these type of film profiles a solution measure which quantifies the foot length, ℓ_f, using the characteristic film heights h_∞ and h_f and the volume measure ΔV,

$$\ell_\mathrm{f} = \frac{\Delta V}{h_\mathrm{f} - h_\infty}. \tag{3.1}$$

A more detailed description of this solution measure can be found in Appendix C.

Although we have already defined a foot length measure ℓ_f, it is also useful to introduce an alternative measure for the foot length, L_F, which will be used as well. It is defined as the distance between the inflection point (change of concavity), i.e. $\partial_{xx}h|_{x_0} = 0$ at the matching between the (coating) precursor film height h_∞ and the plateau height h_f and at the matching between plateau and the bath, i.e. $\partial_x h|_{x_1} = 0$, see Fig 3.6,

$$L_\mathrm{F} = x_0 - x_1. \tag{3.2}$$

In Fig. 3.7 we present dependencies on plate velocity for various angles between $\alpha = 0.05$ and $\alpha = 1.0$, where we observe for all angles a vertical asymptote velocity U_∞. This asymptote at U_∞ is approached monotonically in U for smaller angles, e.g. $\alpha = 0.05$ and 0.1, and for larger angles, $\alpha = 0.33, 0.5, 0.75$ and 1.0, this approach is non-monotonic. As the angle is increased pairs of saddle nodes occur at corresponding critical velocities $U_{\mathrm{C}1}$, where the bifurcation curve starts to *snake* around U_∞.

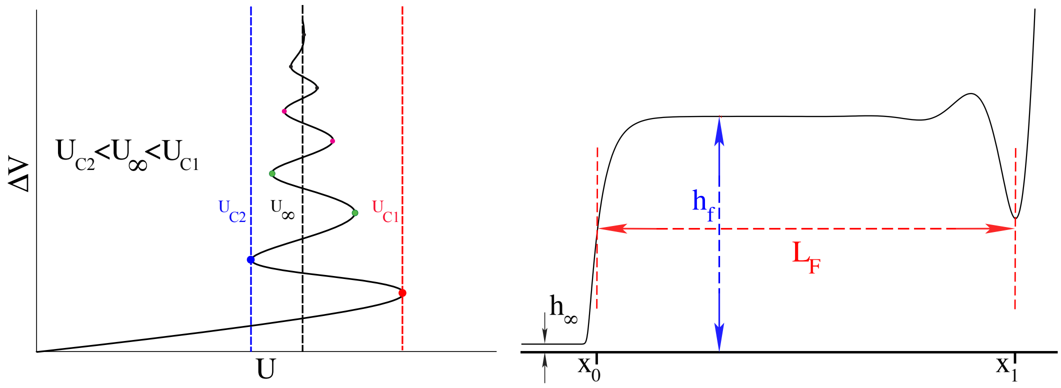

FIGURE 3.6: Left panel: Sketch of the *snaking* behaviour. Note the appearance of the first pair of saddle nodes at U_{C1} and U_{C2} respectively. The bifurcation curve then oscillates with an exponential decay around U_∞. Note the other pair of saddle nodes occurring, marked with coloured dots. Right panel: The foot length L_{F} is defined as the distance between the change of concavity, i.e. $\partial_{xx}h|_{x_0} = 0$ at the matching between the (coating) precursor film height h_∞ and the plateau height h_{f} and at the matching between plateau height h_{f} and the bath, i.e. $\partial_x h|_{x_1} = 0$. The foot or plateau height is the distance between the ground and the plateau. See text.

Note that the critical velocities where the first two saddle nodes are located, U_{C1} and U_{C2}, as well as U_∞ are different for each plate inclination angle. Representing these velocities as a function of the inclination angle, i.e. in a $(\alpha - U)$ phase diagram, is helpful to understand and characterise the behaviour of the system.

In Fig. 3.8 we compare film profiles for identical plate velocity at different inclination angles as indicated in the legends. The four chosen values of U are indicated in Fig. 3.7. In Fig. 3.8, panel (a) and panel (b) we observe how the foot structure starts to emerge for $\alpha = 0.33$ as the velocity is close to $U_\infty(\alpha = 0.33)$, while for the other inclination angles the film profile is a meniscus solution. In panel (b) we see that for $\alpha = 0.33$ the foot starts to grow (black and red-dashed solutions). Panel (c) focuses on $\alpha = 0.5$, where we observe a similar behaviour as for $\alpha = 0.33$. Panel (d) shows profiles at $U_\infty(\alpha = 0.75)$: we see clearly how the foot emerges and grows. For larger drag velocities ($U > U_{C1}$) no meniscus and foot profiles exist.

Finally, we show in Fig. 3.9 that the precursor film height (coating height) evolves towards a fixed point in the (U, h_∞)-plane for each angle α at the corresponding limiting velocity U_∞. Note that the flux J_0 is always positive, see Fig. 3.10 where we show J_0 in dependance on plate velocity U. This flux corresponds to physical film solutions.

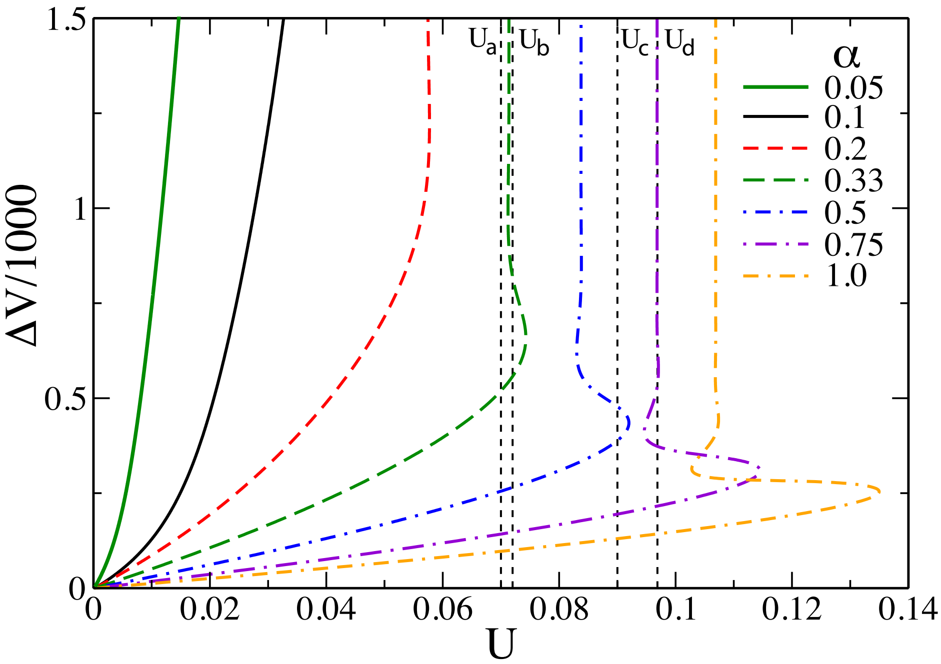

FIGURE 3.7: Bifurcation diagram in dependence of the plate velocity U for different inclination angles as indicated in the legend. Film profiles are shown in Fig. 3.8 at corresponding plate velocities U_{a}, U_{b}, U_{c} and U_{d}. Inclination angles as indicated in the legend.

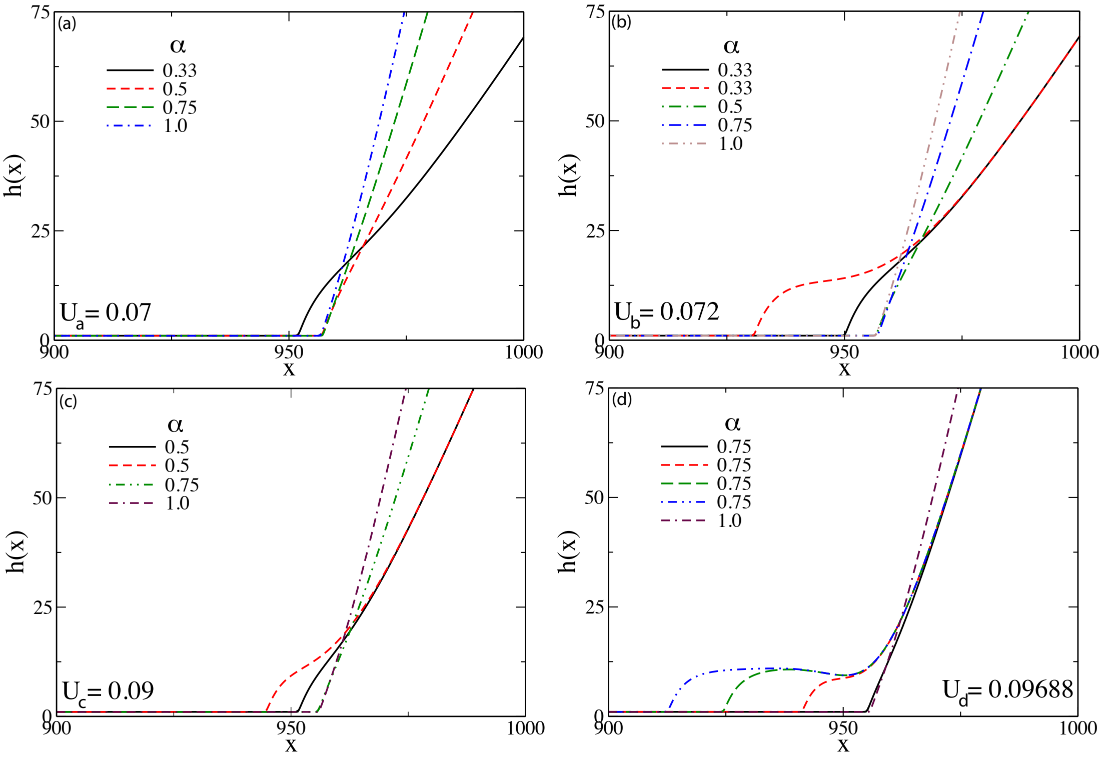

FIGURE 3.8: Film profiles for (a) $U_a = 0.07$, (b) $U_b = 0.072$, (c) $U_c = 0.09$ and (d) $U_d = 0.09688$ as marked in Fig. 3.7 by vertical dashed lines. In every panel inclination angles are indicated in the legend. Observe that for larger drag velocities no profiles exist for $\alpha = 0.33$ and $\alpha = 0.5$.

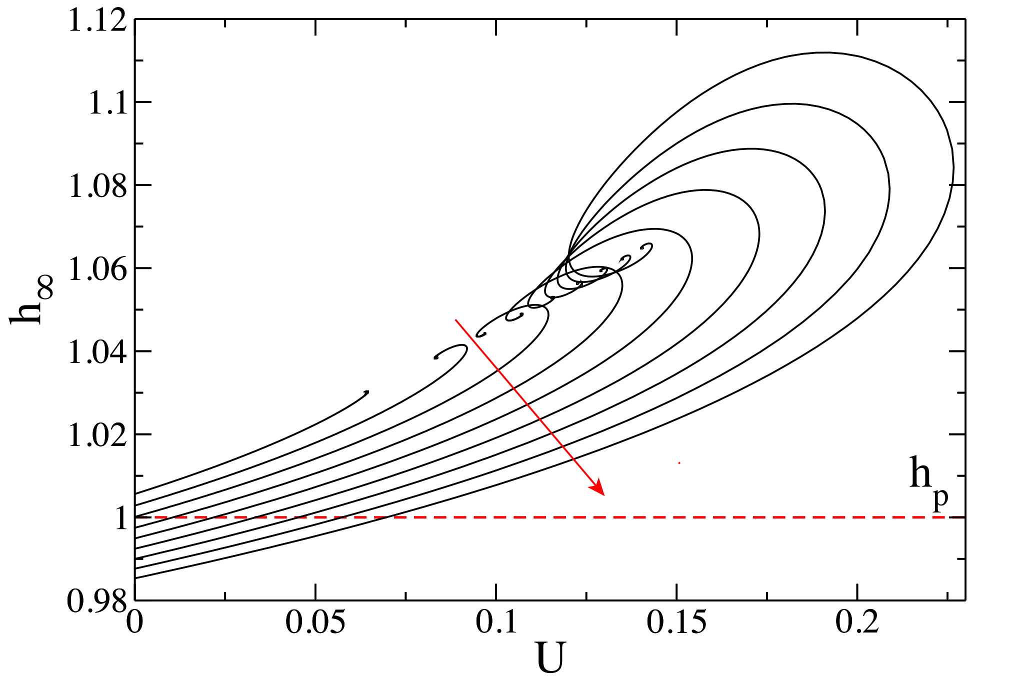

FIGURE 3.9: Coating film height at $x \to \infty$ vs. plate velocity U. Equidistant inclination angles with $\alpha \in [0.25, 2.25]$ and an increase $\Delta\alpha = 0.25$. Arrow indicates increasing plate angles: As U increases, the curve converges to a point in the (U, h_∞)-plane for each angle α. The red line corresponds to the equilibrium precursor $h_p = 1$ film height in a flat horizontal plate.

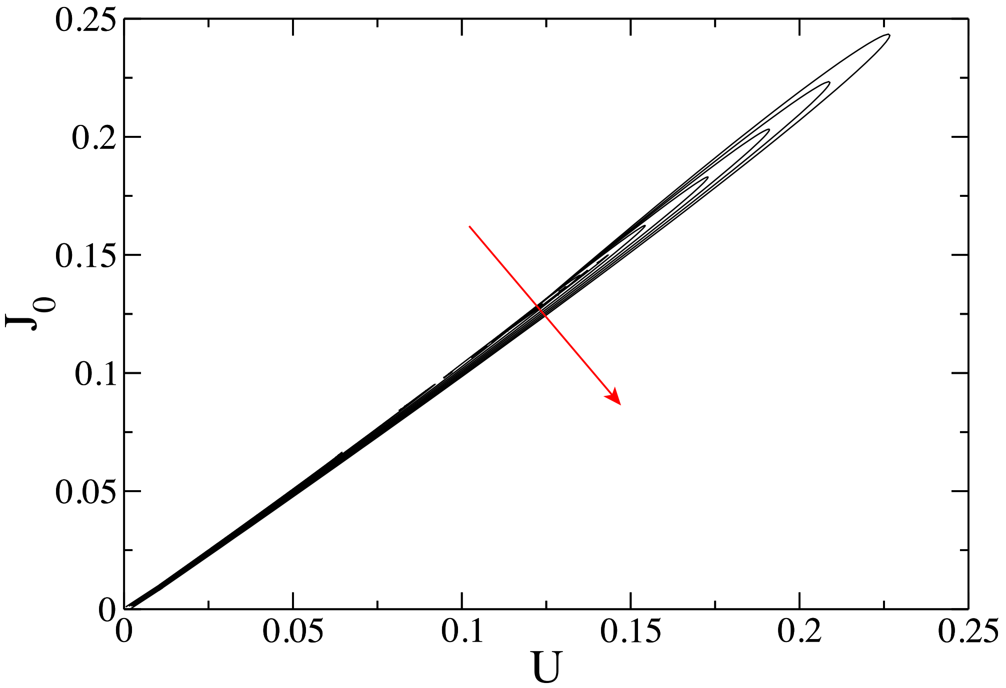

FIGURE 3.10: Flux J_0 vs. plate velocity U. Equidistant inclination angles with $\alpha \in [0.25, 2.25]$ and an increase $\Delta\alpha = 0.25$. Arrow indicates increasing plate angles: As U increases, the curve converges to a point in the (U, J_0)-plane for each angle α. Note that $J_0 > 0$ correspond to physical film solutions.

3.1.2 Transition at small angles

We will now analyse in detail the changes occurring at small inclination angles, $\alpha \lesssim 1$. As an example, we focus on $\alpha = 0.1$ and $\alpha = 0.5$. In Fig. 3.11 and Fig. 3.12, we present bifurcation diagrams showing the dependence of the solution measure quantifying the foot length l_f, on the plate velocity. As mentioned before, we observe that there is a critical inclination angle, $\alpha_1 \approx 0.11$, such that for $\alpha < \alpha_1$, the curve rises monotonically and approaches a vertical asymptote at some value of the velocity, which we denote by U_∞. This can be observed in the left panel of Fig. 3.11 for $\alpha = 0.1$. On the right panel of Fig. 3.11 when $\alpha = 0.5$, i.e. $\alpha > \alpha_1$, we observe a snaking behaviour where the bifurcation curve oscillates back and forth around a vertical asymptote at $U = U_\infty$ with decaying amplitude of oscillations. We note that in this case there is an infinitely but countable number of saddle-nodes bifurcations at which the slope of the bifurcation curve is vertical. Below, we will calculate the critical angle α_1 and explain why U_∞ is different for each inclination angle.

In order to illustrate the different behaviour for angles below and above α_1, we also show the foot length measure, l_f (see Eq. (3.4)), versus $|U - U_\infty|$ in a semi-log plot, see the left and right panels of Fig. 3.12 for $\alpha = 0.1$ and $\alpha = 0.5$, respectively. For $\alpha = 0.1$, it can be clearly seen that the bifurcation curve approaches the vertical asymptote exponentially with a rate which we denote by ν_s.

$$l_f \propto \nu_s \ln \frac{U_\infty}{|U - U_\infty|} \tag{3.3}$$

However, for $\alpha = 0.5$, we see that the approach of the vertical asymptote is exponential with the snaking wavelength tending to a constant value, which we denote by Λ_s, note that the foot–length l_f is

$$\exp\left(\mathrm{Re}[\nu_s] l_f\right) \sin(\mathrm{Im}[\nu_s] l_f) \propto \frac{U_\infty}{|U - U_\infty|}. \tag{3.4}$$

Figure 3.13 shows the snaking behaviour for $\alpha = 0.5$ in more detail. In the left panel, we see the bifurcation diagram where the red filled circles mark solutions at U_∞. In the chosen solution measure, the solutions are nearly equidistantly distributed, i.e. the difference in foot length between subsequent solutions at U_∞ is a constant, namely $\Lambda_s/2$. In the inset, the first five solutions are indicated and

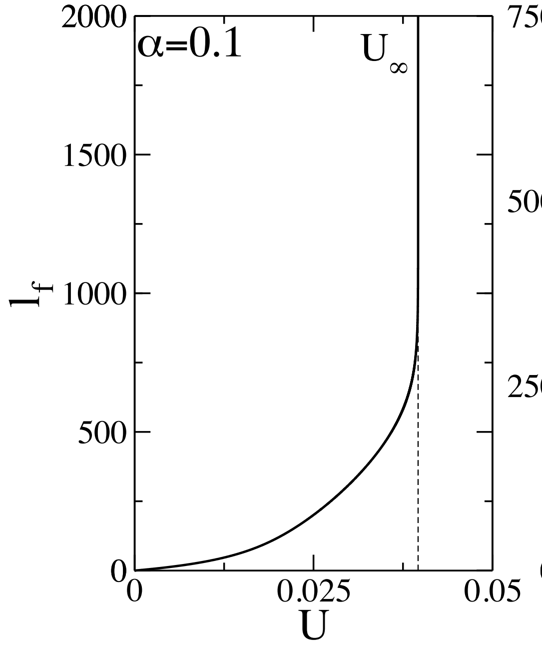

FIGURE 3.11: Left panel: Asymptotical monotonic growth of the pseudo-foot-length measure ℓ_f towards the vertical asymptote at $U = U_\infty$ as a function of the dragged velocity U for $\alpha = 0.1$, which is below α_1. Right panel: Snaking behaviour of the foot-length measure ℓ_f where the bifurcation curve oscillates around a vertical asymptote at $U = U_\infty$ with decaying amplitude of oscillations as a function of the dragged velocity U for $\alpha = 0.5$, which is above α_1.

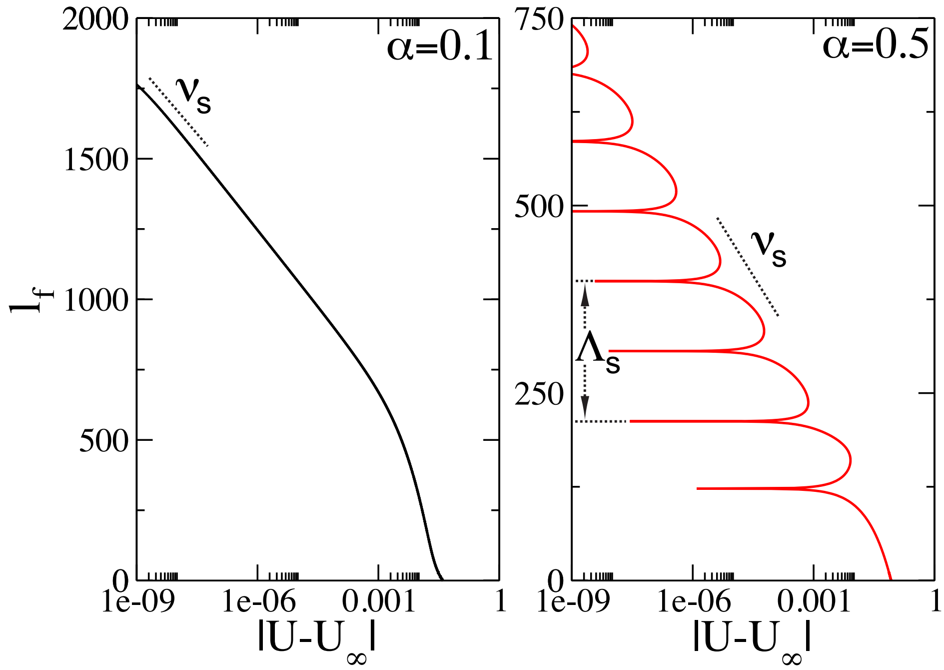

FIGURE 3.12: In order to illustrate the different behaviour for angles below and above α_1, we show the foot-length measure ℓ_f versus $|U - U_\infty|$ in a semi-log plot. Left panel: The semi-log plot shows an asymptotic monotonic growth in U. Right panel: An exponential – oscillating periodic decay is clearly shown. A periodic structure with a snaking wavelength Λ_s and an exponential decay rate ν_s appears after U_{C1} (bifurcation: appearance of the first saddle node).

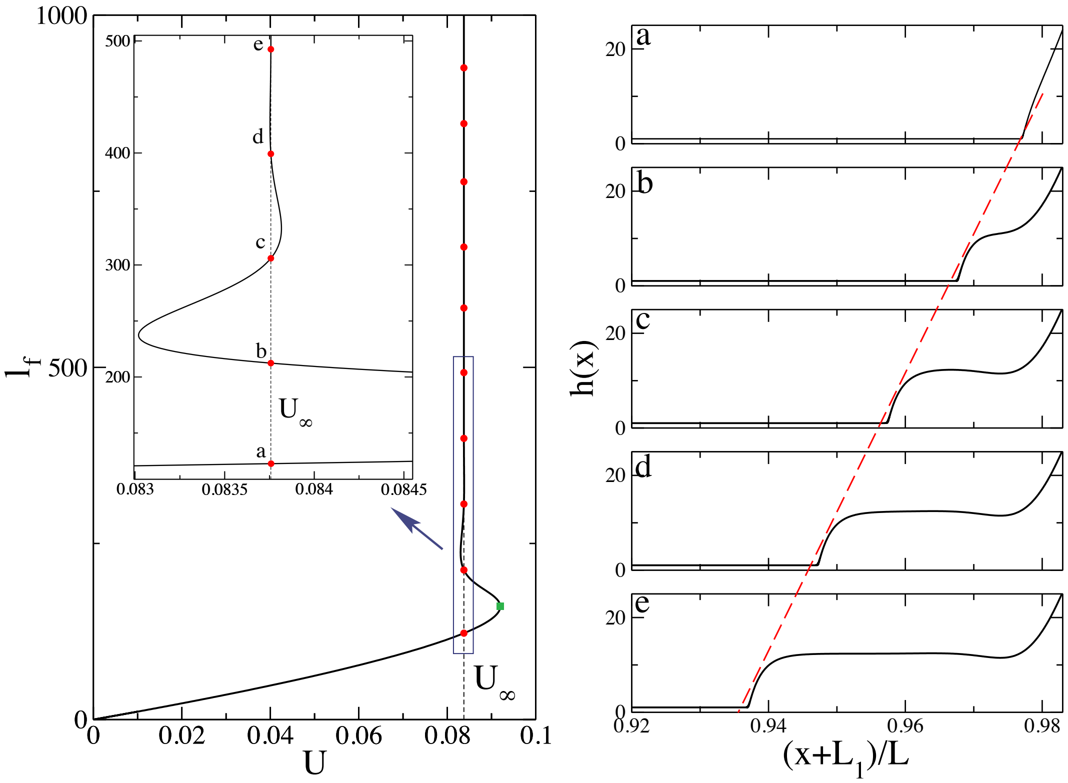

FIGURE 3.13: Film profiles at plate velocity U_∞ for $\alpha = 0.5$. Left panel: Bifurcation diagram. The red filled circles correspond to film solutions at plate velocity U_∞. The inset shows a blow-up of the region with the first five solutions. Note the appearance of a characteristic snaking behaviour around U_∞. The letters in the inset correspond to the film profiles depicted in the right panel. Note the appearance of undulations on top the foot-like part of the solution as the foot becomes longer. The numerical domain size used is $L = 10000$, $L_1 = 9800$. Note that the first profile (a) corresponds to a meniscus solution. It is located on the lowest branch before the bifurcation curve folds back at U_{C1} (the green square). The red dashed line indicates a linear increase in foot length.

labeled by (a)-(e). The corresponding film profiles are shown in the right panels. The dashed line that connects the front positions of all foot solutions in the right panels confirms the linear growth of the foot length.

The striking differences in film profiles for angles below and above α_1 is illustrated in Fig. 3.14. There we show solutions for velocities close to U_∞ for $\alpha = 0.1$ and at U_∞ for 0.5 by solid and dashed lines, respectively. In the left and the right panels, we compare solutions with short and long foot, respectively. The foot lenghts of the solutions in the same panel are similar. To emphasise the differences, we represent the profiles in a semi-log plot $\ln|h(x) - h_f|$ versus $(x + L_1)/L$ in the bottom panels. For $\alpha = 0.1$ we see no undulations – only exponential decays at a

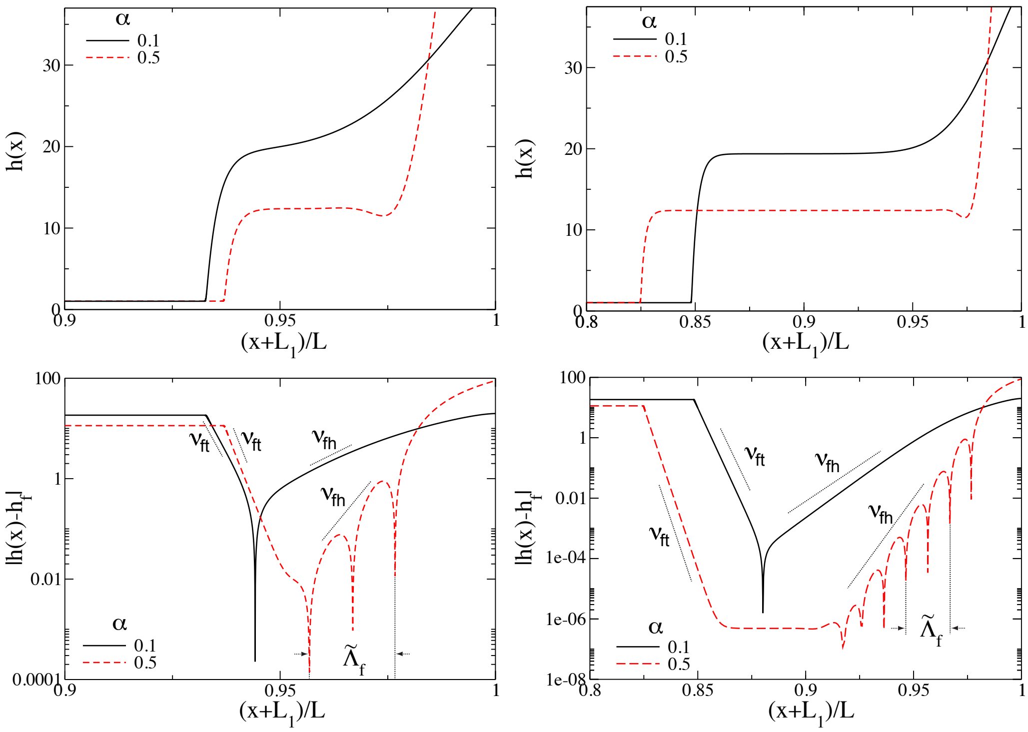

FIGURE 3.14: Film profiles above and below α_1 given as solid and dashed lines, respectively. Left panel: Shown are film profiles for $\alpha = 0.1$ close to U_∞ and for $\alpha = 0.5$ at U_∞. Right panel: In order to show the appearance of undulations on top of the foot above α_1, we represent in bottom panels $|h(x) - h_f|$ versus $(x + L_1)/L$ in a semi-log plot, where $L_1 = 9800$, $L = 10000$ is the numerical domain size and h_f is the characteristic foot height calculated for each inclination angle α by solving Eq. (2.48) for $h' = 0$, $h'' = 0$ and $h''' = 0$ (using the numerically obtained value of the flux J_0). Observe the exponential approach with rate ν_{fh} of the foot height from the bath side, and as well the exponential departure with rate ν_{ft} from the foot height towards the precursor film (see main text for details). Note that the measured foot wavelength is $\Lambda_f = \widetilde{\Lambda}_f L$.

rate denoted by ν_{fh} from the bath to the foot and at a rate denoted by ν_{ft} from the foot to the precursor. However, for $\alpha = 0.5$ we observe an oscillatory exponentially decaying behaviour at a rate denoted by ν_{fh} with a wavelength denoted by Λ_f in the region between the bath and the foot. In the region between the foot and the precursor film, we again observe a monotonic exponential decay.

Note that the precursor (coating height) film h_∞ and the foot height h_f correspond to fixed points of Eq. (2.48). The values of h_∞ and h_f at $U = U_\infty$ are shown in Fig. 3.15 as functions of α by dashed and solid lines, respectively. In Fig. 3.16, we show the dependence of the eigenvalues calculated from Eq. (2.67) at fixed points h_∞ and h_f at $U = U_\infty$ as functions of α. We note that for the precursor film all the eigenvalues are real, one of them is positive and two are negative independently of the angle, see Table 3.1. We denote these eigenvalues by $\lambda_{p,i}$, $i = 1, 2, 3$. However for the foot, the behaviour of the eigenvalues changes exactly

α	h_p	$\lambda_{p,1}$	$\lambda_{p,2}$	$\lambda_{p,3}$
0.1	1.0210	-0.0152	1.5659	-1.5507
0.5	1.0385	-0.0362	1.4418	-1.4056

TABLE 3.1: Eigenvalues at fixed point h_p for $\alpha = 0.1$ close to U_∞ and for $\alpha = 0.5$ at U_∞. Note that all the eigenvalues are real for $\alpha = 0.1$ and for $\alpha = 0.5$. See Fig. 3.16.

at the critical angle α_1 at which monotonic bifurcation diagrams change to snaking ones ,*i.e.*, at $\alpha_1 \approx 0.1125$. We observe that for $\alpha < \alpha_1$ all the eigenvalues for the foot are real – two are positive and denoted by $\lambda_{f,1}$ and $\lambda_{f,2}$ so that $\lambda_{f,1} < \lambda_{f,2}$ and one is negative and is denoted by $\lambda_{f,3}$. However, for $\alpha > \alpha_1$ there is a negative real eigenvalue, $\lambda_{f,3}$, and a pair of complex conjugate eigenvalues with positive real parts, $\lambda_{f,1}$ and $\lambda_{f,2}$. Table 3.2 shows the values of eigenvalues $\lambda_{f,i}$, $i = 1, 2, 3$, for $\alpha = 0.1$ and 0.5.

α	h_f	$\lambda_{f,1}$	$\lambda_{f,2}$	$\lambda_{f,3}$
0.1	19.3732	0.0173	0.0188	-0.0361
0.5	12.3922	0.0263 +0.0346 i	0.0263 −0.0346 i	-0.0525

TABLE 3.2: Eigenvalues at fixed point h_f for $\alpha = 0.1$ close to U_∞ and for $\alpha = 0.5$ at U_∞. Note that all the eigenvalues are real for $\alpha = 0.1$, whereas for $\alpha = 0.5$ one eigenvalue is real and negative and two are complex conjugates with positive real parts. See Fig. 3.16.

In Tables 3.3 and 3.4, we compare $\mathrm{Re}[\lambda_{f,3}]$ with the exponential rate ν_{ft} characterising the connection between the foot and the coating film, and $\mathrm{Re}[\lambda_{f,1}]$ with the exponential rate ν_{fh} characterising the connection between the foot and the bath. Table 3.3 corresponds to a short foot, while table 3.4 corresponds to a long foot. For $\alpha = 0.5$ the plate velocity is equal to U_∞, while for $\alpha = 0.1$ we choose a foot of approximately the same lengths as for $\alpha = 0.5$ and we note that for $\alpha = 0.1$ the

α	$\nu = \mathrm{Re}[\lambda_{f,3}]$	ν_{ft}	$\nu = \mathrm{Re}[\lambda_{f,1}]$	ν_{fh}
0.1	-0.0361	-0.0403	0.0173	0.0152
0.5	-0.0525	-0.0497	0.0263	0.0278

TABLE 3.3: Shown is for a short foot the comparison of the exponential decays ν_{ft}, ν_{fh} with the eigenvalue ν from the linear stability analysis for $\alpha = 0.1$ close to U_∞ and for $\alpha = 0.5$ at U_∞. See Fig. 3.14.

α	$\nu = \text{Re}[\lambda_{f,3}]$	ν_{ft}	$\nu = \text{Re}[\lambda_{f,1}]$	ν_{fh}
0.1	-0.0361	-0.0356	0.0173	0.0155
0.5	-0.0525	-0.0463	0.0263	0.0255

TABLE 3.4: Shown is for a long foot the comparison of the exponential decays ν_{ft}, ν_{fh} with the eigenvalue ν from the linear stability analysis for $\alpha = 0.1$ close to U_∞ and for $\alpha = 0.5$ at U_∞. See Fig. 3.14.

α	Λ=$2\pi/\text{Im}[\lambda_{f,1}]$	Λ_f (long)	Λ_f (short)	Λ_s
0.5	181.6987	202.6920	198.8801	184.7657

TABLE 3.5: Shown is the comparison of the wavelength of snaking Λ_s from the bifurcation diagram and wavelength of the undulations of the foot Λ_f from the foot-like profile with the wavelength Λ calculated from the eigenvalues $\lambda_{f,i}$ at U_∞ for $\alpha = 0.5$. Note the locking between $\Lambda \approx \Lambda_s \approx \Lambda_f$. See Fig. 3.12 and Fig. 3.14.

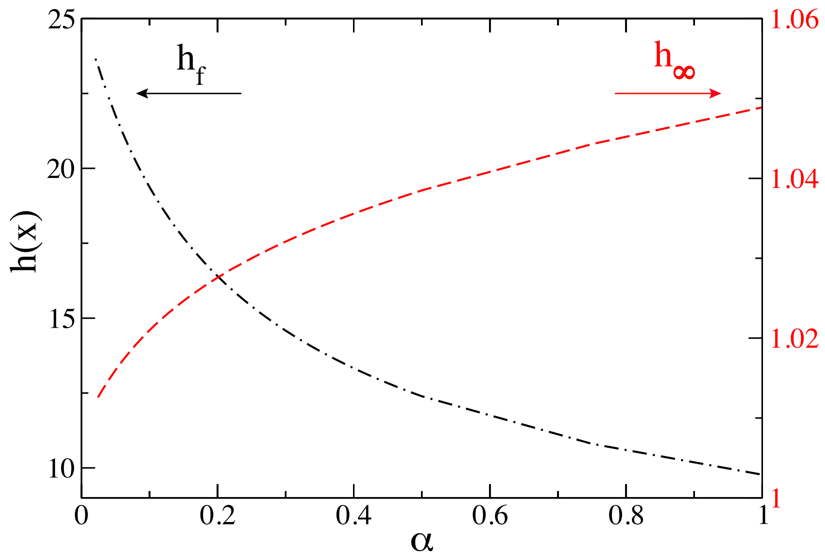

FIGURE 3.15: Film heights at fixed points for the coating film height, h_∞, and foot height, h_f, versus inclination angle α at U_∞ shown by dashed and solid lines, respectively, in a double entry plot. Note that the correct numerically obtained flux J_0 is needed at each α to determine the fixed points. The left side of the ordinate axis corresponds to the foot height, the right side corresponds to the coating height.

bifurcation curves do not reach U_∞, but for the chosen foot the velocities coincide with U_∞ up to at least seven significant digits. The results show that there is good agreement between $\text{Re}[\lambda_{f,3}]$ and ν_{ft} and between $\text{Re}[\lambda_{f,1}]$ and ν_{fh} for both values of α and for both foot lengths, with a maximal error below 12%.

In Table 3.5, we compare $\Lambda = 2\pi/\text{Im}[\lambda_{f,1}]$ with the wavelength of the oscillations on the foot, Λ_f, for a long and a short foot, and with the wavelength of oscillations

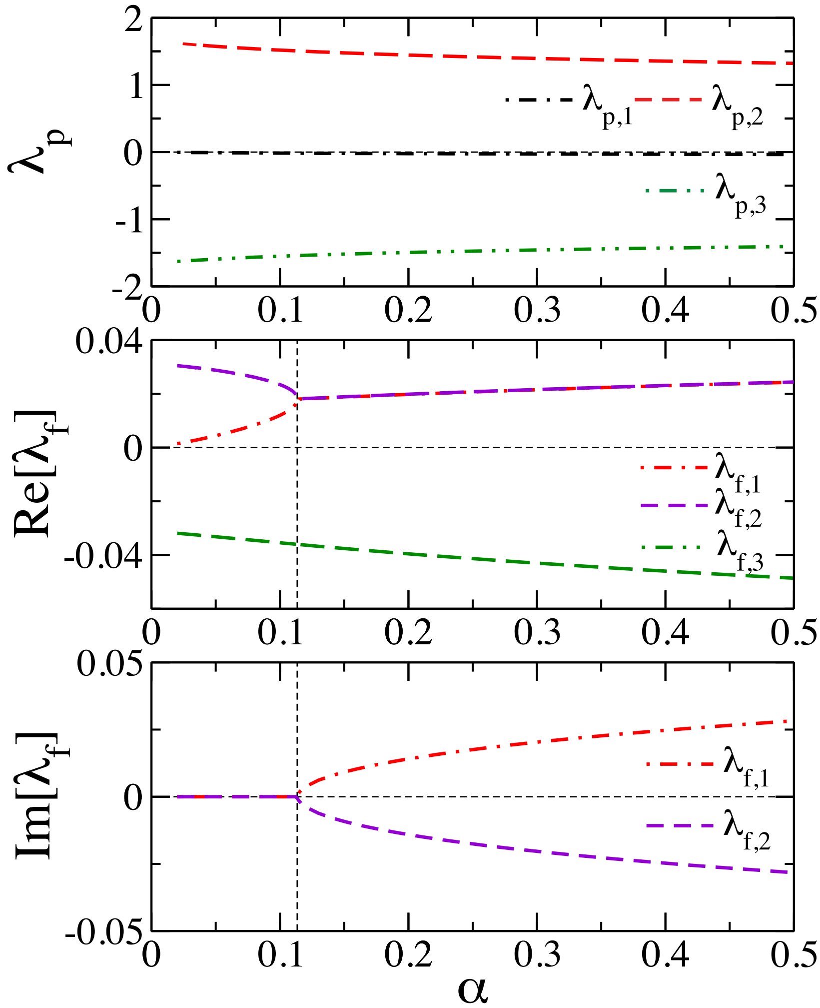

FIGURE 3.16: Eigenvalues of flat film solutions at the U_∞ that corresponds to each α. Upper panel: Shown are the three eigenvalues λ_p versus α for the fixed point corresponding to the precursor film. Note that all the eigenvalues are real. Middle and bottom panels: Shown are the real and the imaginary parts, respectively, of the three eigenvalues λ_f versus α for the foot height.

α	Re$[\lambda_{f,1}]$	$1/\nu_s$
0.1	0.0173	0.0151
0.5	0.0263	0.0284

TABLE 3.6: Shown is the comparison of the exponential decay constant $1/\nu_S$ from the bifurcation diagrams with the eigenvalues $\lambda_{f,i}$ calculated from the linear stability analysis for $\alpha = 0.1$ and $\alpha = 0.5$. See Fig. 3.12.

in snaking bifurcation diagrams, Λ_s, when $\alpha = 0.5$. The results show that there is good agreement between Λ and Λ_s – the error is below 2%, and between Λ and Λ_f for both foot lengths – the error is below 12%.

In table 3.6, we compare $\mathrm{Re}[\lambda_{f,1}]$ with the exponential rate $1/\nu_s$, where ν_s characterises the rate at which the bifurcation diagrams approach the vertical asymptotes. We again observe good agreement for both values of α, with an error up to 13%.

3.1.3 Heteroclinic snaking

In what follows, our aim is to explain the snaking behaviour observed in our numerical results, see right panels of Fig. 3.11, Fig. 3.12 and left panel of Fig. 3.13. Related exponential snaking behaviour has been analysed in systems involving either one fixed point [60, 61] or two fixed points [62]. Table 3.7 illustrates that

Author	*Description of scenario*	*#Fixed Points*
Shilnikov	infinite number of periodic orbits approaching a homocline	1 fixed point
Knobloch & Wagenknecht	infinite number of homoclines approaching a heteroclinic cycle	2 fixed points
Present study	infinite number of heteroclines approaching a heteroclinic chain	3 fixed points

Table 3.7: Hierarchy of systems exhibiting exponential snaking behaviour, Shilnikov [60], Knobloch & Wagenknecht [62].

our results form part of a hierarchy of such snaking behaviours: Shilnikov (see refs. [60, 61]) analyses homoclinic orbits to saddle-focus fixed points in three-dimensional dynamical systems that exist for some value β_0 of parameter β and demonstrated that if the fixed point has a one-dimensional unstable manifold and a two dimensional stable manifold, so that the eigenvalues of the Jacobian at this point are λ_1 and $-\lambda_2 \pm \mathrm{i}\,\omega$, where $\lambda_{1,2}$ and ω are positive real numbers, and if the saddle index $\delta \equiv \lambda_2/\lambda_1 < 1$, then in the neighbourhood of the primary homoclinic orbit there exists an infinite number of periodic orbits that pass near the fixed point several times. Moreover, the difference in the periods of these orbit tends asymptotically to π/ω. The perturbation of the structurally unstable homoclinic orbit leads to a snaking bifurcation diagram showing the dependence of the period of the orbit versus the bifurcation parameter β. This diagram has an infinitely countable number of turning points at which the periodic orbits vanish in saddle-node bifurcations. However, if the saddle index is greater than unity, then the bifurcation diagram is monotonic. Knobloch and Wagenknecht [62, 63] analyse symmetric heteroclinic cycles connecting saddle-focus equilibria in reversible four-dimensional dynamical systems that arise in a number of applications, *e.g.*, in models for water waves in horizontal water channels [64] and in the study of cellular buckling in structural mechanics [65]. In these systems the symmetric heteroclinic cycle organises the dynamics in an equivalent way to the homoclinic solution in Shilnikov's case. It is found that a necessary condition for exponential snaking in such four-dimensional systems is the requirement that one of the involved fixed points is a bi-focus [62]. Then there exists an infinite number of homoclines to the second involved fixed point that all pass a close neighbourhood of the bi-focus. We will show below that the presently studied case is equivalent to the cases of Shilnikov and of Knobloch and Wagenknecht, however, here a heteroclinic chain between three fixed points forms the organising centre of an infinite number of heteroclines.

First, following a proposal of ref. [10], we introduce variables $y_1 = 1/h$, $y_2 = h'$ and $y_3 = h''$, and convert the steady-state equation Eq. (2.48) into a three-dimensional dynamical system:

$$y_1' = -y_1^2 y_2, \tag{3.5}$$

$$y_2' = y_3, \tag{3.6}$$

$$y_3' = (6y_1^7 - 3y_1^4)y_2 + Gy_2 + Uy_1^2 - J_0 y_1^3 - G\alpha. \tag{3.7}$$

Note that the transformation $y_1 = 1/h$ is used to obtain a new fixed point corresponding to the bath, namely the point $\boldsymbol{y}_b = (0,\, \alpha,\, 0)$, beside other fixed points, two of which, $\boldsymbol{y}_f = (1/h_f,\, 0,\, 0)$ and $\boldsymbol{y}_p = (1/h_p,\, 0,\, 0)$, correspond to the foot and the precursor film, respectively. First, we consider fixed points of system (3.5)-(3.7) with $y_1 \neq 0$. For such fixed points, $y_2 = y_3 = 0$ and y_1 satisfies the equation

$$f(y_1) \equiv y_1^3 - \frac{U}{J_0} y_1^2 + \frac{G\alpha}{J_0} = 0. \tag{3.8}$$

It can be easily checked that this cubic polynomial has a local maximum at $y_1^a = 0$ and a local minimum at a positive point y_1^b. Moreover, $f(y_1^a) > 0$ implying that there is always a fixed point with a negative value of the y_1-coordinate. We disregard this point, since physically it would correspond to negative film thickness.

Also, assuming that $G\alpha < (4/27)(U^3/J_0^2)$, we obtain $f(y_1^b) < 0$, which implies that there are two positive roots a_1 and a_2 of the cubic polynomial satisfying $a_1 < a_2$. This implies that there are two more fixed points, $\boldsymbol{y}_f = (a_1, 0, 0)$ and $\boldsymbol{y}_p = (a_2, 0, 0)$. The point $\boldsymbol{y}_f$ corresponds to the foot and the point $\boldsymbol{y}_p$ corresponds to the precursor film.

To analyse stability of these fixed points, we compute the Jacobian at these points,

$$J_{\boldsymbol{y}_{f,p}} = \begin{pmatrix} 0 & -a_{1,2}^2 & 0 \\ 0 & 0 & 1 \\ 2Ua_{1,2} - 3J_0 a_{1,2}^2 & 6a_{1,2}^7 - 3a_{1,2}^4 + G & 0 \end{pmatrix}. \tag{3.9}$$

A simple calculation shows that for both, $\boldsymbol{y}_f$ and $\boldsymbol{y}_p$, all the eigenvalues have non-zero real parts implying that these points are hyperbolic. Point $\boldsymbol{y}_f$, corresponding to the foot, has a two-dimensional unstable manifold and one-dimensional stable manifold, while point $\boldsymbol{y}_p$, corresponding to the precursor film, has a one-dimensional unstable manifold and a two-dimensional stable manifold. Our numerical simulations presented in the previous section show that if α is sufficiently small, there exists a value of the plate speed, U_∞, and a value of the flux, $J_0 = J_\infty$, such that in the vicinity of these values there exist steady solutions for which the foot length can be arbitrarily long, see Fig. 3.11. We, therefore, conclude that at $U = U_\infty$ and $J_0 = J_\infty$, there exists a heteroclinic chain connecting the fixed points $\boldsymbol{y}_p$, $\boldsymbol{y}_f$ and $\boldsymbol{y}_b$, and the solutions of different foot lengths correspond to heteroclinic orbits in the vicinity of this chain connecting $\boldsymbol{y}_p$ to $\boldsymbol{y}_b$. As was discussed in the previous section, in the top panel of Fig. 3.16, we can observe that for point $\boldsymbol{y}_p$ all the eigenvalues are real at $U = U_\infty$ and $J_0 = J_\infty$ implying that this point is a saddle. The two bottom panels of Fig. 3.16 demonstrate that there is a critical inclination angle $\alpha_1 \approx 0.1125$ such that for $\alpha \leq \alpha_1$, all the eigenvalues for $\boldsymbol{y}_f$ are real, whereas for $\alpha > \alpha_1$, one eigenvalue is real and negative and there is a pair of complex conjugate eigenvalues with positive real parts. Therefore, for $\alpha \leq \alpha_1$, point $\boldsymbol{y}_f$ is a saddle, but for $\alpha > \alpha_1$, it is a saddle-focus. To understand the existence of these multiple heteroclinic orbits connecting two of the fixed points of a three dimensional dynamical system which has three fixed points connected by a heteroclinic chain, we present the following theorem, which corresponds to situation similar to the one that we analyse in the previous sections. Namely, we analytically prove that if $\boldsymbol{y}_f$ is a saddle-focus, there exists a countably infinite

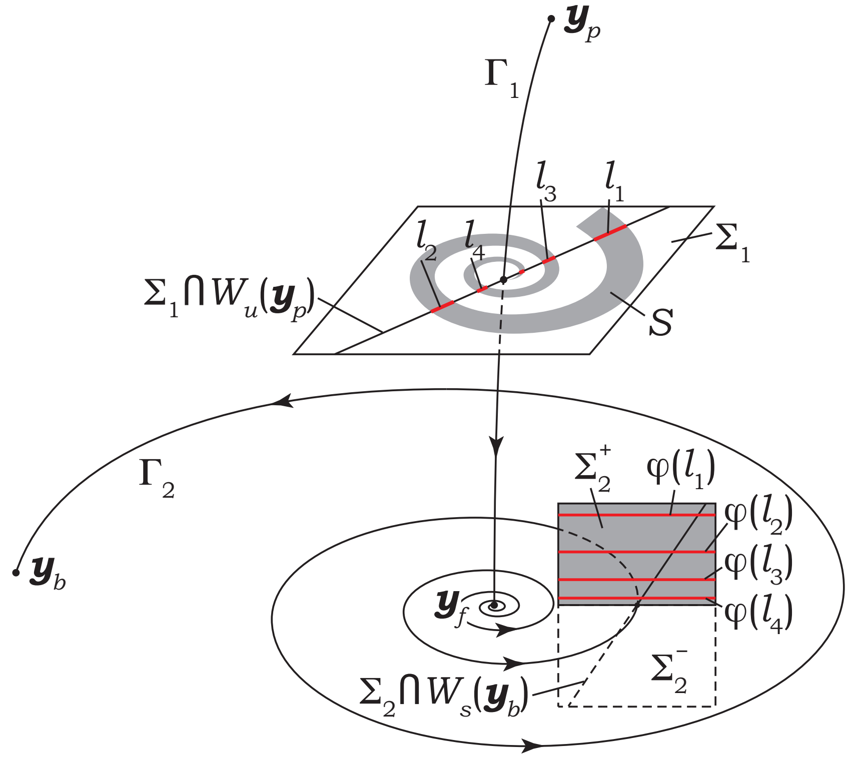

FIGURE 3.17: Schematic representation in the three-dimensional phase-space of the fixed points $\boldsymbol{y}_p$, $\boldsymbol{y}_f$ and $\boldsymbol{y}_b$ of system (3.10) when $\beta = \beta_0$. The fixed point $\boldsymbol{y}_p$ is a saddle point with two-dimensional unstable manifold, $W_u(\boldsymbol{y}_p)$, and a one-dimensional stable manifold. The fixed point is $\boldsymbol{y}_f$ is a saddle-focus with two-dimensional unstable manifold and a one-dimensional stable manifold. The fixed point $\boldsymbol{y}_b$ is a non-hyperbolic point having two-dimensional stable manifold, $W_s(\boldsymbol{y}_b)$. The fixed points $\boldsymbol{y}_p$ and $\boldsymbol{y}_f$ are connected by the heteroclinic orbit Γ_1 and the fixed points $\boldsymbol{y}_f$ and $\boldsymbol{y}_b$ are connected by the heteroclinic orbit Γ_2.

number of subsidiary heteroclinic orbits connecting $\boldsymbol{y}_p$ and $\boldsymbol{y}_b$ that lie in a sufficiently small neighbourhood of the heteroclinic chain connecting $\boldsymbol{y}_p$, $\boldsymbol{y}_f$ and $\boldsymbol{y}_b$. This result is closely related[2] to the existence of a countably infinite number of steady-state solutions having different foot lengths that we have analysed in the previous section, see the left panels of Fig. 3.11, Fig. 3.12 and Fig. 3.13.

Theorem. Consider a three-dimensional system

$$\boldsymbol{y}' = \boldsymbol{f}(\boldsymbol{y},\, \beta), \qquad \boldsymbol{y} \in \mathbb{R}^3, \tag{3.10}$$

[2]The precursor film fixed point $\boldsymbol{y}_p$ of the dynamical system analysed in the previous section has a one-dimensional unstable manifold $W_u(\boldsymbol{y}_p)$ and a two-dimensional stable manifold $W_s(\boldsymbol{y}_p)$, while for the system described in the following section, the precursor film fixed point $\boldsymbol{y}_p$ has a two-dimensional unstable manifold $W_u(\boldsymbol{y}_p)$ and a one-dimensional stable manifold $W_s(\boldsymbol{y}_p)$. This was not clearly laid out in [66].

where β denotes a parameter. We assume that there exist three fixed points, which we denote by $\boldsymbol{y}_p$, $\boldsymbol{y}_f$ and $\boldsymbol{y}_b$, when β is sufficiently close to a number β_0. We additionally assume that $\boldsymbol{y}_p$ and $\boldsymbol{y}_b$ have a two-dimensional unstable manifold $W_u(\boldsymbol{y}_p)$ and a two-dimensional stable manifold $W_s(\boldsymbol{y}_b)$, respectively, and that $\boldsymbol{y}_f$ is a saddle-focus fixed point with a one-dimensional stable manifold $W_s(\boldsymbol{y}_f)$ and a two-dimensional unstable manifold $W_u(\boldsymbol{y}_f)$ (*i.e.*, the eigenvalues of the Jacobian at $\boldsymbol{y}_f$ are $-\lambda_1$, $\lambda_2 \pm \mathrm{i}\,\omega$, where $\lambda_1 = \lambda_1(\beta)$, $\lambda_2 = \lambda_2(\beta)$ and $\omega = \omega(\beta)$ are positive real numbers when β is sufficiently close to β_0). Let us also assume that for $\beta = \beta_0$, there is a heteroclinic orbit $\Gamma_1 \in W_u(\boldsymbol{y}_p) \cap W_s(\boldsymbol{y}_f)$ connecting $\boldsymbol{y}_p$ and $\boldsymbol{y}_f$ and that the manifolds $W_u(\boldsymbol{y}_f)$ and $W_s(\boldsymbol{y}_b)$ intersect transversely so that there is a heteroclinic orbit $\Gamma_2 \in W_u(\boldsymbol{y}_f) \cap W_s(\boldsymbol{y}_b)$ connecting $\boldsymbol{y}_f$ and $\boldsymbol{y}_b$. Then for $\beta = \beta_0$ there is an infinite countable number of heteroclinic orbits connecting $\boldsymbol{y}_p$ and $\boldsymbol{y}_b$ and passing near $\boldsymbol{y}_f$. Moreover, the difference in 'transition times' from $\boldsymbol{y}_p$ to $\boldsymbol{y}_b$ tends asymptotically to π/ω (the meaning of a 'transition time' from $\boldsymbol{y}_p$ to $\boldsymbol{y}_b$ will be explained below).

Proof: After a suitable change of variables, the dynamical system $\boldsymbol{y}' = \boldsymbol{f}(\boldsymbol{y}, \beta)$ can be written in the form

$$\begin{aligned} y_1' &= \lambda_2 y_1 - \omega y_2 + \tilde{f}_1(\boldsymbol{y}, \beta), && (3.11)\\ y_2' &= \omega y_1 + \lambda_2 y_2 + \tilde{f}_2(\boldsymbol{y}, \beta), && (3.12)\\ y_3' &= -\lambda_1 y_3 + \tilde{f}_3(\boldsymbol{y}, \beta), && (3.13) \end{aligned}$$

where $\tilde{f}_i$, $i = 1, 2, 3$, are such that $\partial \tilde{f}_i / \partial y_j = 0$, i, $j = 1, 2, 3$, at $\boldsymbol{y} = \boldsymbol{y}_f$. After such a change of variables, the origin is a stationary point corresponding to $\boldsymbol{y}_f$ and sufficiently close to the origin, the terms $\tilde{f}_1(\boldsymbol{y}, \beta)$, $\tilde{f}_2(\boldsymbol{y}, \beta)$ and $\tilde{f}_3(\boldsymbol{y}, \beta)$ are negligibly small, so that near the origin the dynamical system can be approximated by the linearised system

$$\begin{aligned} y_1' &= \lambda_2 y_1 - \omega y_2, && (3.14)\\ y_2' &= \omega y_1 + \lambda_2 y_2, && (3.15)\\ y_3' &= -\lambda_1 y_3. && (3.16) \end{aligned}$$

Let Σ_1 be a plane normal to the stable manifold of $\boldsymbol{y}_f$, Γ_1, and located at a small distance ε_1 from $\boldsymbol{y}_f$, *i.e.*, locally Σ_1 is given by

$$\Sigma_1 = \{(y_1,\, y_2,\, \varepsilon_1) : \, y_1,\, y_2 \in \mathbb{R}\}. \tag{3.17}$$

Let Σ_2 be part of a plane transversal to the unstable manifold of $\boldsymbol{y}_f$, Γ_2, at some point near $\boldsymbol{y}_f$ and passing through $\boldsymbol{y}_f$ that is locally given by

$$\Sigma_2 = \{(y_1,\, 0,\, y_3) : \, |y_1 - r^*| \le \varepsilon_2,\, |y_3| \le \varepsilon_3\}. \tag{3.18}$$

Here $(r^*,\, 0,\, 0) \in \Gamma_1$ is sufficiently close to the origin and $\varepsilon_3 < \varepsilon_1$. We denote the upper half-plane of Σ_2, when $y_3 > 0$, by Σ_2^+, *i.e.*, $\Sigma_2^+ = \{\boldsymbol{y} \in \Sigma_2 : \, y_3 > 0\}$ and let $\Sigma_2^- = \Sigma_2 \backslash \Sigma_2^+$. We choose ε_2 to be sufficiently small so that each trajectory crosses Σ_2 only once. It can be shown that this condition is satisfied when $\varepsilon_2 < \tanh(\lambda_2 \pi/\omega)\, r^*$.

Using cylindrical polar coordinates $(r,\, \theta,\, z)$, such that $y_1 = r\cos\theta$, $y_2 = r\sin\theta$ and $y_3 = z$, the linearised dynamical system near the origin is given by

$$r' = \lambda_2 r, \tag{3.19}$$

$$\theta' = \omega, \tag{3.20}$$

$$z' = -\lambda_1 z. \tag{3.21}$$

The solution is given by

$$r = r_0 \mathrm{e}^{\lambda_2 x}, \tag{3.22}$$

$$\theta = \theta_0 + \omega x, \tag{3.23}$$

$$z = z_0 \mathrm{e}^{-\lambda_1 x}. \tag{3.24}$$

In the cylindrical polar coordinates, Σ_1 is given by $z = \varepsilon_1$ and Σ_2 is given by

$$\Sigma_2 = \{(r,\, 0,\, z) : \, |r - r^*| \le \varepsilon_2,\, |z| \le \varepsilon_3\}. \tag{3.25}$$

Let φ_x be the flow map for the linearised dynamical system. Also, let S be the set in Σ_1 given by

$$S = \{\boldsymbol{y} \in \Sigma_1 : \, \exists\, x \text{ such that } \varphi_x(\boldsymbol{y}) \in \Sigma_2\}. \tag{3.26}$$

Then we can define the map

$$\varphi : S \to \Sigma_2 : \; \boldsymbol{y} \mapsto \varphi_x(\boldsymbol{y}) \text{ for some } x > 0. \tag{3.27}$$

It can easily be checked that the image of φ is in fact Σ_2^+. Also, it can be easily seen that the set S is the so-called Shilnikov snake, a set bounded by two spirals, s_1 and s_2, given by

$$r = (r^* \pm \varepsilon_2)\mathrm{e}^{-\lambda_2 x}, \quad \theta = -\omega x, \quad z = \varepsilon_1, \tag{3.28}$$

respectively, where $x \in [(1/\lambda_1)\log(\varepsilon_1/\varepsilon_3),\, \infty)$, and the following segment of a straight line:

$$r \in \left[(r^* - \varepsilon_2)\left(\frac{\varepsilon_3}{\varepsilon_1}\right)^{\lambda_2/\lambda_1},\, (r^* + \varepsilon_2)\left(\frac{\varepsilon_3}{\varepsilon_1}\right)^{\lambda_2/\lambda_1}\right], \tag{3.29}$$

$$\theta = \frac{\omega}{\lambda_1}\log\left(\frac{\varepsilon_3}{\varepsilon_1}\right), \quad z = \varepsilon_1. \tag{3.30}$$

Let $l_p = \Sigma_1 \cap W_u(\boldsymbol{y}_p)$ be the intersection of the two-dimensional unstable manifold of $\boldsymbol{y}_p$ and the plane Σ_1, which is locally a straight line given for $\beta = \beta_0$ by the equations $\theta = \theta_p$ and $z = \varepsilon_1$, where θ_p is some constant. As $\theta_p \bmod \pi$ determines the direction of the line, we can choose without out loss of generality,

$$\theta_p \in (-\pi + (\omega/\lambda_1)\log(\varepsilon_3/\varepsilon_1),\, (\omega/\lambda_1)\log(\varepsilon_3/\varepsilon_1)]. \tag{3.31}$$

Next, let l_n, $n = 1, 2, \ldots$, be the intersections of the line l_p with set S such that $|l_1| > |l_2| > \cdots$, where $|l_n|$ denotes the length of the segment l_n, $n = 1, 2, \ldots$, see Fig. 3.17. We can see that l_n is given by

$$\begin{aligned} r \in [&(r^* - \varepsilon_2)\exp(-\lambda_2(\pi(n-1) - \theta_p)/\omega), \\ &(r^* + \varepsilon_2)\exp(-\lambda_2(\pi(n-1) - \theta_p)/\omega)], \end{aligned} \tag{3.32}$$

$$\theta = \theta_p - \pi(n-1) = \theta_p \bmod \pi, \quad z = \varepsilon_1. \tag{3.33}$$

Then, we find that $\varphi(l_n)$ is a segment of a line in Σ_2 given by

$$r \in [(r^* - \varepsilon_2),\, (r^* + \varepsilon_2)], \tag{3.34}$$

$$\theta = 0, \tag{3.35}$$

$$z = \varepsilon_1 \exp(-\lambda_1(\pi(n-1) - \theta_p)/\omega). \tag{3.36}$$

Let $l_b = \Sigma_2 \cap W_s(\boldsymbol{y}_b)$ be the intersection of the two-dimensional stable manifold of $\boldsymbol{y}_b$ and the plane Σ_2. Locally it is a segment of a straight line, and since manifolds $W_u(\boldsymbol{y}_f)$ and $W_u(\boldsymbol{y}_b)$ intersect transversely, this segment of the line is given for $\beta = \beta_0$ by parametric equations

$$r = r^* + as, \quad \theta = 0, \quad z = s, \tag{3.37}$$

where a is some constant and s is a parameter changing from $-\varepsilon_3$ to ε_3. Note that we can choose ε_3 to be smaller than $\varepsilon_2/|a|$ so that the line l_b intersects all the lines $\varphi(l_n)$, $n = 1, 2, \ldots$, and we denote such intersections points by $\boldsymbol{y}_{b,n}$, $n = 1, 2, \ldots$. Let us denote the preimages of these points with respect to map φ by $\boldsymbol{y}_{p,n}$, $n = 1, 2, \ldots$. Note that $\boldsymbol{y}_{p,n} \in l_n$, $n = 1, 2, \ldots$. Next, since for each $n = 1, 2, \ldots$, point $\boldsymbol{y}_{p,n}$ belongs to the unstable manifold of $\boldsymbol{y}_p$, there is an orbit $\Gamma_{p,n}$ connecting $\boldsymbol{y}_p$ and $\boldsymbol{y}_{p,n}$. Also, by definition of point $\boldsymbol{y}_{p,n}$, it is mapped by the flow map φ_x to point $\boldsymbol{y}_{b,n}$ and the 'transition time' from $\boldsymbol{y}_{p,n}$ to $\boldsymbol{y}_{b,n}$ is approximately equal to $x = t_{\text{tr}} = (\pi(n-1) - \theta_p)/\omega$. Note that the difference in 'transition times' from $\boldsymbol{y}_{p,n}$ to $\boldsymbol{y}_{b,n}$ and from $\boldsymbol{y}_{p,(n+1)}$ to $\boldsymbol{y}_{b,(n+1)}$ tends to π/ω as n increases. We denote the orbit connecting $\boldsymbol{y}_{p,n}$ with $\boldsymbol{y}_{b,n}$ by $\Gamma_{f,n}$. Finally, since $\boldsymbol{y}_{b,n}$ for each $n = 1, 2, \ldots$, point $\boldsymbol{y}_{p,n}$ belongs to the stable manifold of $\boldsymbol{y}_b$, there is an orbit $\Gamma_{b,n}$ connecting $\boldsymbol{y}_{b,n}$ and $\boldsymbol{y}_b$. We conclude that there is an infinite countable number of subsidiary heteroclinic orbits connecting points $\boldsymbol{y}_p$ and $\boldsymbol{y}_b$ that are given by $\Gamma_{s,n} = \Gamma_{p,n} \cup \Gamma_{f,n} \cup \Gamma_{b,n}$, $n = 1, 2, \ldots$. Moreover, the difference in 'transition times' for two successive orbits $\Gamma_{s,n}$ and $\Gamma_{s,(n+1)}$ taken to get from plane Σ_1 to plane Σ_2 tends to π/ω as $n \to \infty$. Q.E.D.

Remark 1. We would like to point out that snaking diagrams as those computed in the previous section are obtained by an unfolding of the structurally unstable heteroclinic chain connecting $\boldsymbol{y}_p$, $\boldsymbol{y}_f$ and $\boldsymbol{y}_b$. For β close to β_0 but not necessarily equal to β_0, line $l_p = \Sigma_1 \cap W_u(\boldsymbol{y}_p)$ is locally given by

$$y_2 = b(\beta) y_1 + c(\beta), \quad y_3 = \varepsilon_1, \tag{3.38}$$

where $c(\beta_0) = 0$ and $b(\beta_0) = \tan(\theta_p)$ (without loss of generality, we can assume that $\theta_p \neq \pi/2 + \pi n$ for any $n \in \mathbb{Z}$). This implies that in a small neighbourhood of point $(0, 0, \varepsilon_1)$, this line can be approximated by

$$y_2 = (b(\beta_0) + \Delta\beta\, b'(\beta_0)) y_1 + \Delta\beta\, c'(\beta_0), \quad y_3 = \varepsilon_1, \tag{3.39}$$

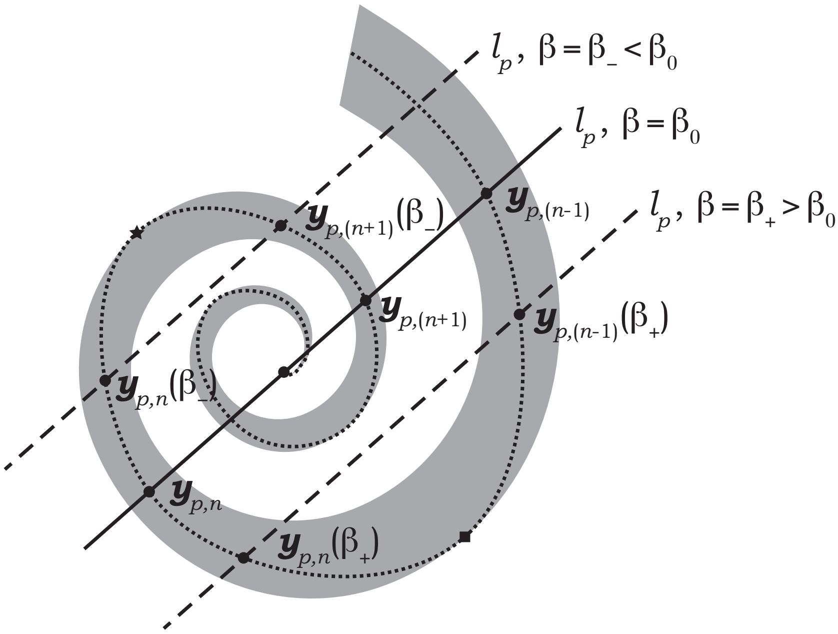

FIGURE 3.18: Schematic representation of the Shilnikov snake, S, in plane Σ_2. The solid line shows line l_p for $\beta = \beta_0$, the dashed lines show lines l_p for $\beta = \beta_+ > \beta_0$ and for $\beta = \beta_- < \beta_0$. The dotted line shows the locus of the points through which heteroclinic orbits connecting $\boldsymbol{y}_p$ and $\boldsymbol{y}_b$ pass for certain values of β near β_0. The black square corresponds to the value of β_+ at which line l_p is tangent to S and at which points $\boldsymbol{y}_{p,(n-1)}$ and $\boldsymbol{y}_{p,n}$ vanish in a saddle-node bifurcation. The star corresponds to the value of β_- at which line l_p is tangent to S and at which points $\boldsymbol{y}_{p,n}$ and $\boldsymbol{y}_{p,(n+1)}$ vanish in a saddle-node bifurcation.

where $\Delta\beta = \beta - \beta_0$. Assuming that $c'(\beta_0) \neq 0$, we obtain that for $\beta \neq \beta_0$ line l_p is shifted in plane Σ_2 and does not pass through point $(0, 0, \varepsilon_1)$, see Fig. 3.18. This implies that for $\beta \neq \beta_0$ line l_p intersects the Shilnikov snake, S, finitely many times. For sufficiently small $\Delta\beta$, we denote by $l_n(\beta)$ the intersection of l_p with S that is obtained by a small shift of l_n for $\beta = \beta_0$. By considerations similar to those in the proof of the previous theorem, it can be shown that in each of the line segments there is a point $\boldsymbol{y}_{p,n}(\beta)$ such that there is a heteroclinic orbit passing through this point and connecting $\boldsymbol{y}_p$ and $\boldsymbol{y}_b$. For $\beta \neq \beta_0$ there is only a finite number of such orbits. Figure 3.18 schematically shows l_p by a solid line for $\beta = \beta_0$ and by dashed lines for $\beta = \beta_+ > \beta_0$ and $\beta = \beta_- < \beta_0$. In addition, points $\boldsymbol{y}_{p,(n-1)}(\beta_+)$, $\boldsymbol{y}_{p,n}(\beta_+)$, $\boldsymbol{y}_{p,n}(\beta_-)$ and $\boldsymbol{y}_{p,(n+1)}(\beta_-)$ are shown. For certain value of β_+, points $\boldsymbol{y}_{p,(n-1)}(\beta_+)$, $\boldsymbol{y}_{p,n}(\beta_+)$ vanish in a saddle-node bifurcation. This point is indicated by a black square in the figure. At this point, line l_p is tangent to the boundary of S. Also, for certain value of β_-, points $\boldsymbol{y}_{p,n}(\beta_-)$, $\boldsymbol{y}_{p,(n+)}(\beta_-)$ vanish in a saddle-node bifurcation. This point is indicated by a star in the figure. At this point, line l_p is tangent to the boundary of S. The locus of the points through which heteroclinic orbits connecting $\boldsymbol{y}_p$ and $\boldsymbol{y}_b$ pass for certain values of β near β_0 is shown by a dotted line. It can be seen that this line is a spiral, s, that belongs to S, passes through points $\boldsymbol{y}_{p,n}$ and is tangent between transitions from $\boldsymbol{y}_{p,n}$ to $\boldsymbol{y}_{p,(n+1)}$, $n = 1, 2, \ldots$, to the boundary of S given by spiral s_1. It can therefore be concluded that the bifurcation diagram showing the 'transition time' for heteroclinic orbits connecting $\boldsymbol{y}_p$ and $\boldsymbol{y}_p$ versus parameter β is a snaking curve, shown schematically in Fig. 3.19, similar to the numerically obtained cases in figs. 3.11, 3.12 and 3.13 for $\alpha = 0.5$. There is an infinite number of such orbits in a neighbourhood of β_0 and there is an infinite countable number of saddle-node bifurcations that correspond to the points at which spiral s touches the boundary of the Shilnikov spiral, S.

We can find that the slope of the line tangent to spiral s_1 is

$$\frac{\mathrm{d}y_2}{\mathrm{d}y_1} = R\tan(\theta + \theta_0), \tag{3.40}$$

where $R = \sqrt{\lambda_2^2 + \omega^2}$ and $\theta_0 = \tan^{-1}(\omega/\lambda_2)$. Therefore, at the points where line l_p touches spiral s_1, we must have

$$R\tan(\theta_n + \theta_0) = b(\beta_0) + \Delta\beta_n b'(\beta_0), \tag{3.41}$$

where θ_n and $\Delta\beta_n$ are the values of θ and $\Delta\beta$ corresponding to the n^{th} saddle-node bifurcation. Thus, at these points

$$\theta_n = \tan^{-1}\left(\frac{b(\beta_0)}{R} + \Delta\beta_n \frac{b'(\beta_0)}{R}\right) - \theta_0 - \pi n, \tag{3.42}$$

for sufficiently large integer n. Equivalently,

$$x_n = -\frac{1}{\omega}\tan^{-1}\left(\frac{b(\beta_0)}{R} + \Delta\beta_n \frac{b'(\beta_0)}{R}\right) + \frac{\theta_0}{\omega} + \frac{\pi}{\omega}n. \tag{3.43}$$

From this formula, we clearly see that the difference in transition times between two saddle-node bifurcations tends to π/ω. Also, at the saddle-node bifurcations we must have

$$r_n \sin\theta_n = (b(\beta_0) + \Delta\beta_n b'(\beta_0)) r_n \cos\theta_n + \Delta\beta_n c'(\beta_0), \tag{3.44}$$

where $r_n = (r^* + \varepsilon_2)\mathrm{e}^{-\lambda_2 x_n}$, which implies

$$\Delta\beta_n = r_n \frac{\sin\theta_n - b(\beta_0)\cos\theta_n}{c'(\beta_0) + b'(\beta_0) r_n}. \tag{3.45}$$

From the latter expression, we can conclude that

$$|\Delta\beta_n| = O(r_n) = O(\mathrm{e}^{-\lambda_2 x_n}), \tag{3.46}$$

which shows that the snaking bifurcation diagram approaches the vertical asymptote at an exponential rate, which is similar to the results presented in the right panel of Fig. 3.12 and in table 3.6. Also, note that if $\boldsymbol{y}_f$ is a saddle, then the set S

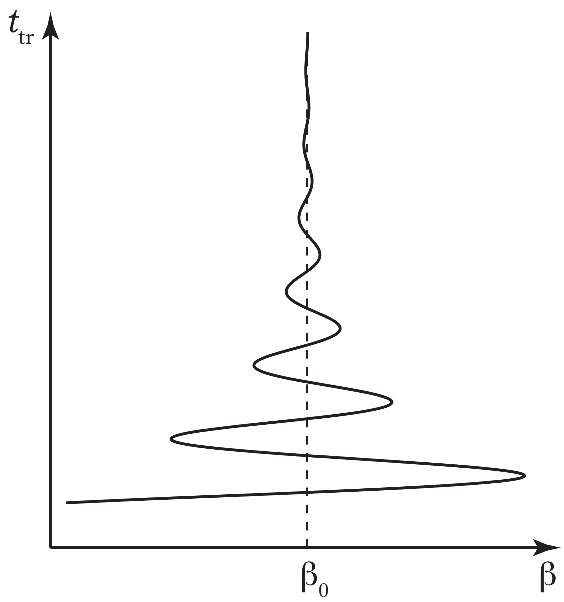

FIGURE 3.19: Bifurcation diagram for heteroclinic orbits connecting $\boldsymbol{y}_p$ and $\boldsymbol{y}_b$.

is not a spiral but is a wedge-shaped domain. The line l_p then passes through the vertex of this domain for $\beta = \beta_0$ and, generically, intersects it in the neighbourhood of the vertex only for $\beta < \beta_0$ but not for $\beta > \beta_0$ or vice versa. Then, the bifurcation diagram showing the 'transition time' for heteroclinic orbits connecting $\boldsymbol{y}_p$ and $\boldsymbol{y}_b$ versus parameter β is a monotonic curve instead of a snaking curve shown in Fig. 3.19, similarly to the case in Fig. 3.11 and Fig. 3.12 for $\alpha = 0.1$.

Note that in the dragged meniscus problem the 'transition time' is a measure of the length of the foot and is therefore equivalent to the measure l_f introduced in the previous section. Thus, the bifurcation diagrams obtained in figs. 3.11, 3.12 and 3.13 are explained by the results presented above.

Remark 2. Note that in the dragged meniscus problem, the unstable manifold of $\boldsymbol{y}_p$ is not two-dimensional, but one-dimensional. However, we notice that instead of having one parameter, β as is described in Theorem 3.1.3, we have now two parameters, the plate velocity U and the flux J_0. If U is fixed at $U = U_\infty$ and J_0 varies, the one–dimensional unstable manifold of $\boldsymbol{y}_p$ sweeps a two–dimensional surface which plays the role of $W_u(\boldsymbol{y}_p)$ discussed in the proof of Theorem 3.1.3.

3.1.4 Foot / snake locking

We have analysed in the last section the appearance of undulations on the free surface of the foot solutions and its connection to the collapsed snaking in the bifurcation diagram.

Here, we will analyse – using results from the linear stability analysis – the behaviour of the undulations during the evolution of the steady state profiles as the plate velocity changes for *all* plate velocities U (not only at U_∞ as was the case in the previous section) for a chosen angle above the first transition, $\alpha = 2.4175$. We show in the left panel of Fig. 3.20 a typical foot–film profile for the chosen angle with the characteristic undulation structure on the free surface, and in the

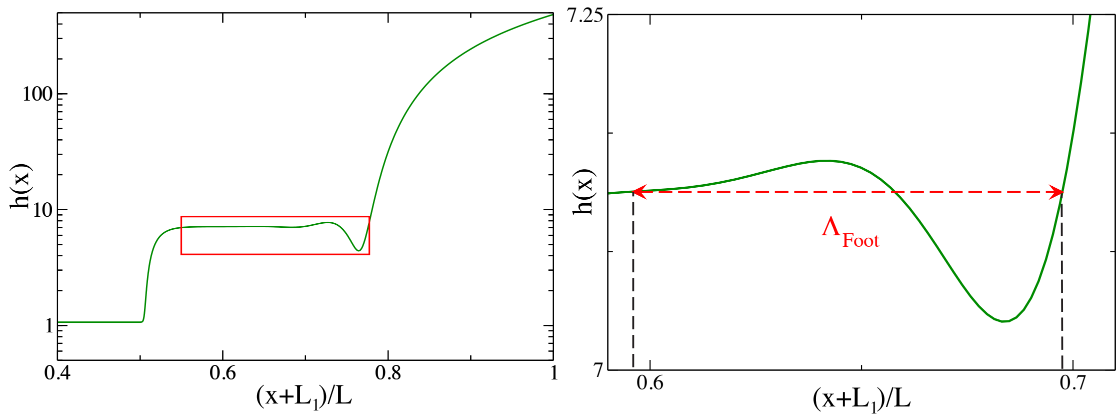

FIGURE 3.20: Left panel: We observe undulations on top of the profile along the foot. The red inset is depicted in the right panel. The example is for $\alpha = 2.4175$ and $U = 0.1441$. Right panel: Shown is a detail of the oscillation on the foot for the film profile shown in the left panel. The wave length $\Lambda_{Foot} = 0.084$ measured corresponds to one obtained by linear stability analysis, $\Lambda \simeq 0.083$.

right panel we show a blowup of the free surface. Note the wavelength Λ_{Foot} as indicated in the figure.

Employing the linear stability analysis discussed in Eq. (2.64) and Eq. (2.65), we can compute the wave numbers K via Eq. (2.67) for different film profiles for the given inclination angle $\alpha = 2.4175$ at different plate velocities.

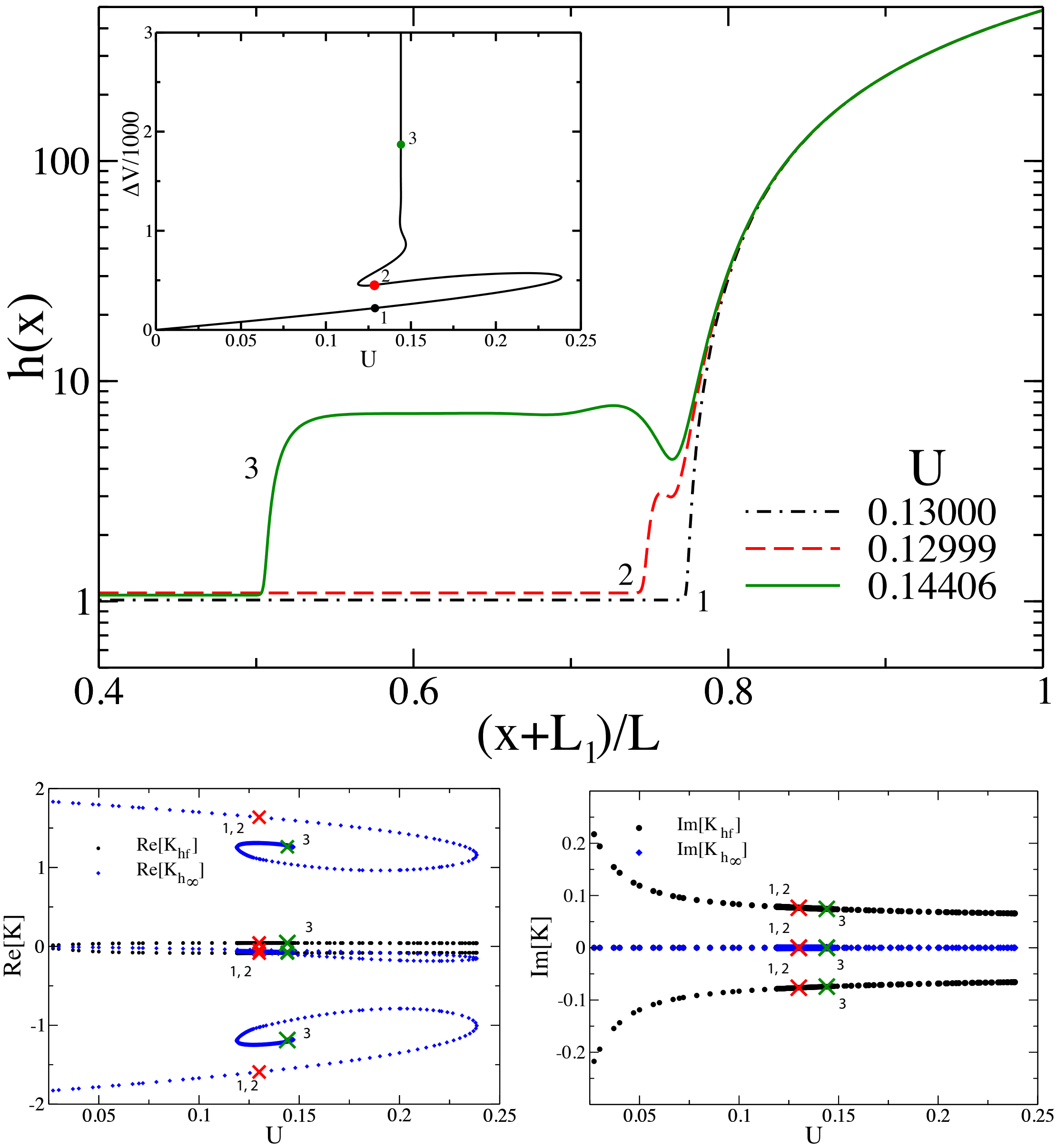

FIGURE 3.21: α=2.4175. Top panel: Film profiles for a fixed angle and different drag velocity U. As an inset bifurcation diagram with ΔV vs. U for the profiles (colour coded and numbered). Bottom panels, from left to right: Real part of the wave number K in black for foot height h_f, blue for the coating film height h_∞. Imaginary part of the wave number K in black for foot height h_f, blue for the coating film height h_∞. The crosses correspond in both panels to the profiles depicted above (colour and number code).

The solution of Eq. (2.65) for the film height is $h_1(x)$ is

$$h_1(x) = A_1 e^{(K_1 r + I K_1 i)x} + A_2 e^{(K_2 r + I K_2 i)x} + A_3 e^{(K_3 r + I K_3 i)x}. \tag{3.47}$$

From our numerical solution we can compare the values of the complex wave number K a see the correspondence to the coating film height h_∞ and the foot height h_f. We will analyse as an example solution 3 with parameter values of $\alpha = 2.4175$, $U = 0.14406$ and $\Delta V = 1.94133$ from Fig. 3.21:

The values of the two different heights are: $h_\infty = 1.067$ and $h_f = 7.131$, and the wave numbers are listed below:

Height	K_1	K_2	K_3
h_∞	$1.2619 + 0.0000I$	$-0.0747 + 0.0000I$	$-1.1872 + 0.0000I$
h_f	$0.0423 + 0.0743I$	$-0.0846 + 0.0000I$	$0.0423 - 0.0743I$

TABLE 3.8: Wave numbers of the two film heights for the film profile solution for $\alpha = 2.4175$, $U = 0.1441$, $\Delta V/1000 = 1.941$.

The solution of the coating film height shows pure real values of the wave number, i.e. there are no oscillations. The real part of the wave numbers show one positive K, i.e. $\mathrm{Re}[K] > 0$, and other two negative K, i.e. $\mathrm{Re}[K] < 0$. The first one allows the growing of the film to match the foot height as x grows, and diminishes as $x \to 0$, while the other two diminish approaching the foot height, allowing the matching.

$$h_\infty(x) = \underbrace{A_1 e^{1.2619x}}_{\text{grows to match the foot, diminishes } x \to 0} + \underbrace{A_2 e^{-0.0747x} + A_3 e^{-1.1872x}}_{\text{diminishes towards the foot}} \tag{3.48}$$

On the other hand, the solution for the foot height has two complex conjugate wave numbers with positive real part, and one pure real negative wave number. These two complex conjugated wave numbers introduce exponential growing oscillations that will match the bath as x gets larger, while the pure real negative K decays to match the coating film solution.

$$h_f(x) = \underbrace{A_1 e^{(0.0423+0.0743I)x} + A_2 e^{(0.0423-0.0743I)x}}_{\text{oscillations and grow towards to match the bath}} + \underbrace{A_3 e^{-0.0846x}}_{\text{diminishes to match the coating film}} \tag{3.49}$$

We also observe that the wavelength of the oscillation (scaled over the simulation domain L=1000) is $\Lambda = 2\pi/\mathrm{Im}[K] \approx 0.083$. This value is in accordance with the one measured on the profile, see Fig. 3.20, $\Lambda_{Foot} = 0.0845$.

In Fig. 3.22 we plot the foot length L_{F} defined in Eq. (3.2), for selected angles as shown in the legend. We observe how as the foot gets longer, the foot wavelength tends to a constant value Λ_F, coinciding with calculated Λ_f from the linear stability analysis.

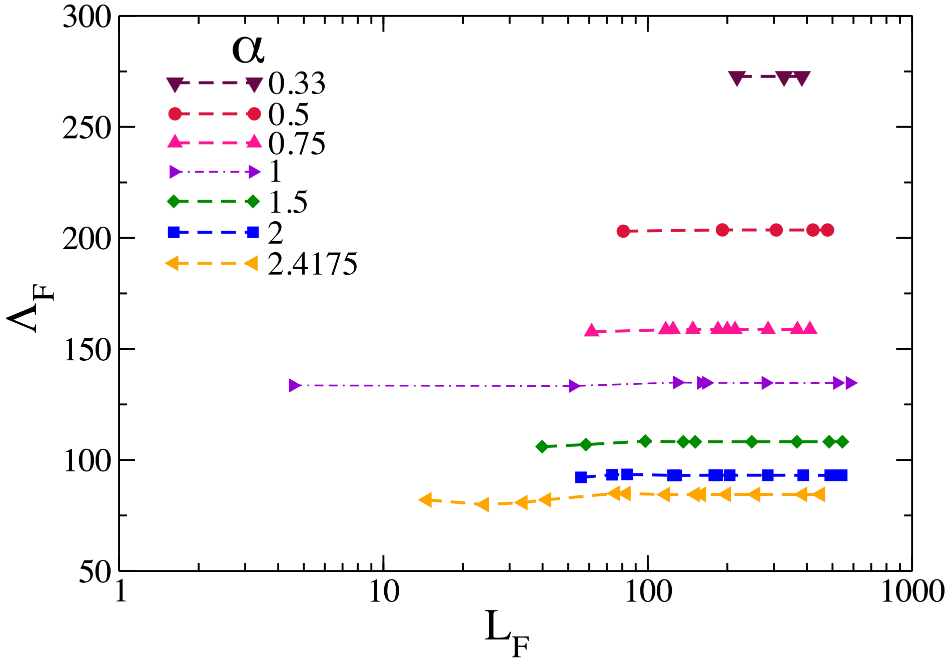

FIGURE 3.22: Shown is the foot length L_f for different inclination angles α as indicated in the legend versus the wavelength Λ_{Foot} of the undulations observed on the foot. As the foot length becomes larger, the wavelength tends to Λ_∞.

In Fig. 3.23 we compare in a log-log-plot the calculated wavelengths from the linear stability analysis Λ_{foot} (blue dots and orange circles) with the measured wavelength Λ_{F} (lila squares) at corresponding U_∞^α as function of $\breve{\alpha} = \alpha - \alpha_1$, where α is the inclination angle and $\alpha_1 \approx 0.1125$ is the critical angle where the wavelength of the foot diverges (i.e. the imaginary part of the spatial eigenvalue for the foot height $K_i \to 0$). α_1 is the inclination angle where the first described transition occurs. We have also include the measured snaking wavelength Λ_s (red and orange diamonds) with the error bar form the measurements, with a maximal error below 15%. Note that there exists a *locking* between the snaking wavelength Λ_s and the foot wavelength Λ_f, i.e. $\Lambda_s \approx \Lambda_f$ for angles with a collapsed snaking bifurcation diagram, i.e. for $\alpha > \alpha_1$. Note that we have included solutions (orange colour code) which will be discussed in later sections of the text.

Note that wavelengths Λ, Λ_s, Λ_F at U_∞ scale following a power-law with exponent $\nu = -1/2$,

$$\Lambda \propto (\alpha - \alpha_1)^{-\frac{1}{2}}.$$

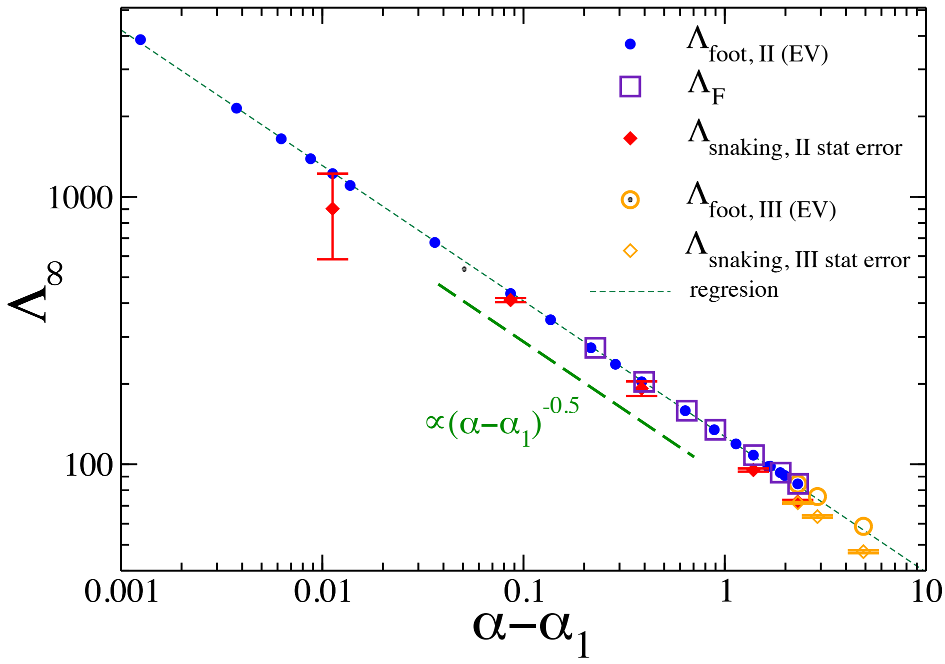

FIGURE 3.23: Shown is a Log-Log-plot of the wavelength of the foot Λ_f and of the snaking Λ_s at U_∞ versus $\breve{\alpha}$. $\breve{\alpha} = \alpha - \alpha_1$, where α is the inclination angle and α_1 is the critical angle where the wavelength of the foot diverges (i.e. the imaginary part of the spatial eigenvalue for the foot height $K_i \to 0$). α_1 is the inclination angle where the first transition occurs: the appearance of undulations on the foot. Note that the relation between Λ_{foot} , Λ_s and $\breve{\alpha}$ follows a power-law with and exponent $\nu = -1/2$

In a green dashed line we also plot a regression curve which follows the power-law $(\alpha - \alpha_1)^{-\frac{1}{2}}$.

3.1.5 Limiting velocity U_∞: Relation between the dragged plate and a sliding droplet

The limiting velocity U_∞ and foot height h_f can be connected to the problem of a large flat sliding droplet on an incline, see Fig. 3.24. This problem has been studied by several authors, see e.g. [67, 68]. In the co-moving frame of the sliding droplet, the non-dimensional long-wave equation modelling the sliding droplet on an incline is *exactly* the same as Eq. (2.47) describing the drawn meniscus problem, although the boundary conditions are different. For this particular case, the boundary conditions are $h' = h'' = 0$ at both simulation domain ends. In the lower panel

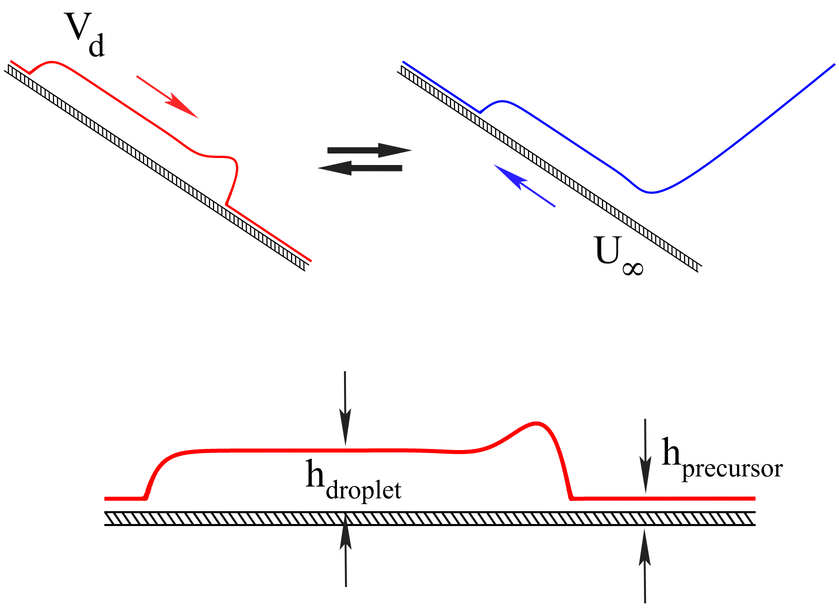

FIGURE 3.24: Comparison and relation between sliding droplet and dragged plate

of Fig. 3.24 we identify the droplet height h_d and the precursor film height h_p for a typical sliding droplet. Note the precursor film wetting the substrate in front and behind the drop due to the use of a partial wetting disjoining pressure. The limiting velocity U_∞ in the dragged-out plate problem then corresponds to the droplet sliding velocity V_d for the same inclination angle α. In the left panel of Fig. 3.25 we show the computed sliding droplet velocity V_d as a function of inclination angle α, and we superpose the results of U_∞ for the drawn meniscus problem as a function of α. On the right panel we plot the height h_d of the sliding drop and the foot height h_f at U_∞ as a function of the inclination angle α. Note that the blue dots in both panels correspond to a family of foot solutions that

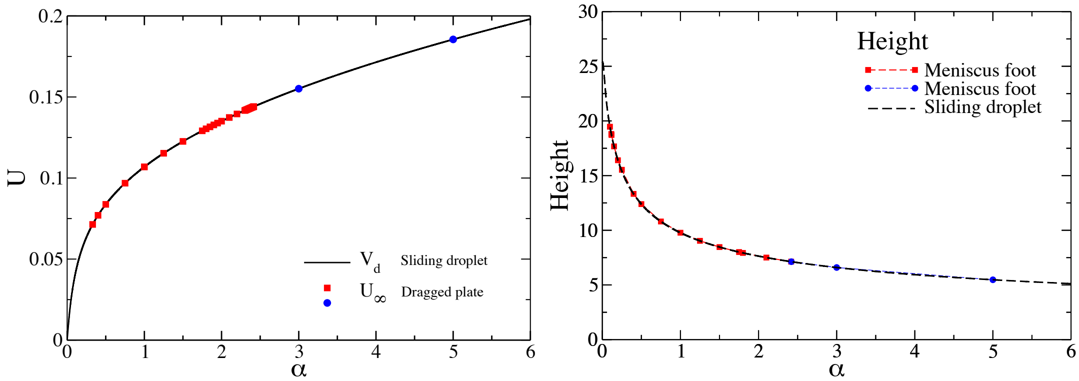

FIGURE 3.25: Comparison and relation between sliding droplet and dragged plate. Left panel: Droplet sliding velocity V_d versus inclination angle α, superposed U_∞ for foot solutions versus inclination α. Right panel: Droplet sliding height h_d versus inclination angle α, superposed film height h_f at U_∞ for foot solutions versus inclination α.

will be addressed later on in this chapter. To see the connection between the two problems, we move to the co-moving frame. For a system with an infinitely large droplet, when looking at the tail, the solution structure is the same as the tip of the foot for the dragged plate problem.

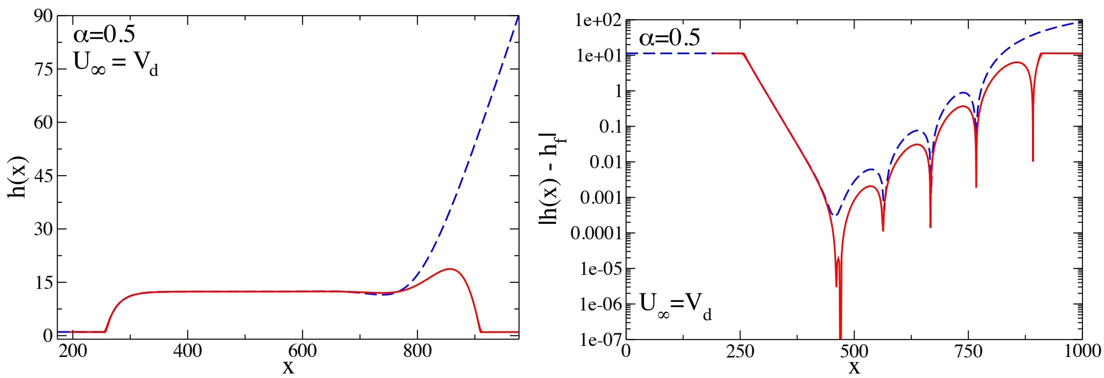

FIGURE 3.26: Film profile structures. Left panel: Superposition of sliding droplet profile and drawn meniscus foot solution at $V_d = U_\infty$ and same inclination angle $\alpha = 0.5$ for a same droplet / foot length. Right panel: $|h(x) - h_f|$ versus x. Note the identical undulated structure of the free surface of the superposed profiles. The blue dots in both panels correspond to a family of foot solutions that will be addressed later on in this chapter.

In Fig. 3.26 we show a sliding droplet profile (red line) and a foot solution for the drawn plate (dashed blue line) at $V_d = U_\infty$ and same inclination angle $\alpha = 0.5$ for identical droplet / foot length. On the left panel we note the similar structure and profile, with special focus on the tail of the droplet / tip of the foot. This characteristic can be seen clearer in the right panel where we plot $|h(x) - h_f|$ versus

x and the undulations on the free surface can be identified. Note the identical undulated structure of the free surface of the superposed profiles, especially at the tail.

3.1.6 Time dependent behaviour

The stability of the steady states solutions is determined via arguments of bifurcation theory [69] and is checked employing time simulations. For the time dependent calculations, Eq. (2.47) is solved numerically using a second order upwind finite difference scheme in space, while for the time integration, we used a variable-order and variable-step backward differentiation formulae algorithm. For all systems sizes a grid spacing of $\Delta x = 1$ was used and for all calculations, we applied following boundary conditions:

$$
\begin{aligned}
x \to L_1 &\Longrightarrow \begin{cases} h_x \to 0 \\ h_{xx} \to 0 \end{cases} \\
x \to L_2 &\Longrightarrow \begin{cases} h \to \alpha x \\ h_x \to \alpha. \end{cases}
\end{aligned}
\tag{3.50}
$$

As initial conditions, we used steady state solutions obtained with AUTO or profiles obtained with our time dependent code. We perturbed the plate velocity U of those solutions in $\Delta = |\delta U|$, and the new plate velocity resulted $\hat{U} = U \pm \delta U$. The behaviour can be observed in the $(\alpha,\, U)$ – phase diagram, see left panel of Fig. 3.27. The phase diagram is constructed based on the values of U_{C1}, U_{C2} and U_∞ for each inclination angle α and the behaviour of the time evolution of the selected profiles. Three different zones can be distinguished:

Region (1): Below U_∞, i.e. $U < U_\infty$
Region (2): Between U_∞ and U_{C2}, i.e. $U_{C2} < U < U_\infty$
Region (3): Above U_{C1}, i.e. $U > U_{C1}$

On the right panel of Fig. 3.27 we sketch the stability of the branches: black solid lines denote *stable branches* and red dashed lines denote *unstable branches.* Solutions from region (1) are steady menisci, while solutions in region (3) evolve

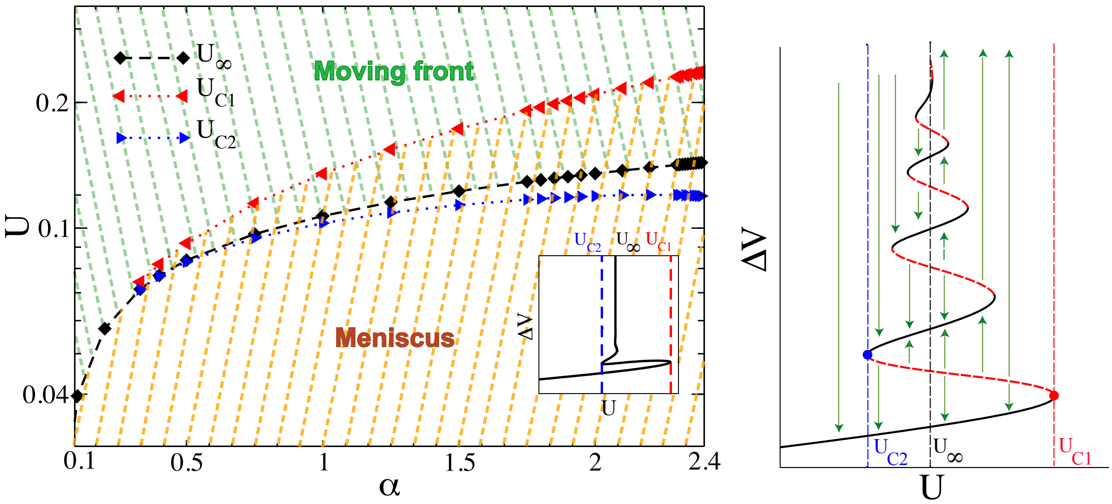

FIGURE 3.27: Left panel: Phase diagram in $(\alpha,\, U)$ – plane. Three different regions can be identified: (1) Below U_∞ a steady meniscus shape exists, (2) between U_∞ and U_{C2}, where steady menisci and menisci with moving front coexist and (3) above U_{C1} where solutions with moving front exist. The moving front solutions are unstable solutions that evolve to stable ones in (1). Right panel: Sketch of the stability behaviour: black solid lines denote *stable branches* and red dashed lines denote *unstable branches*.

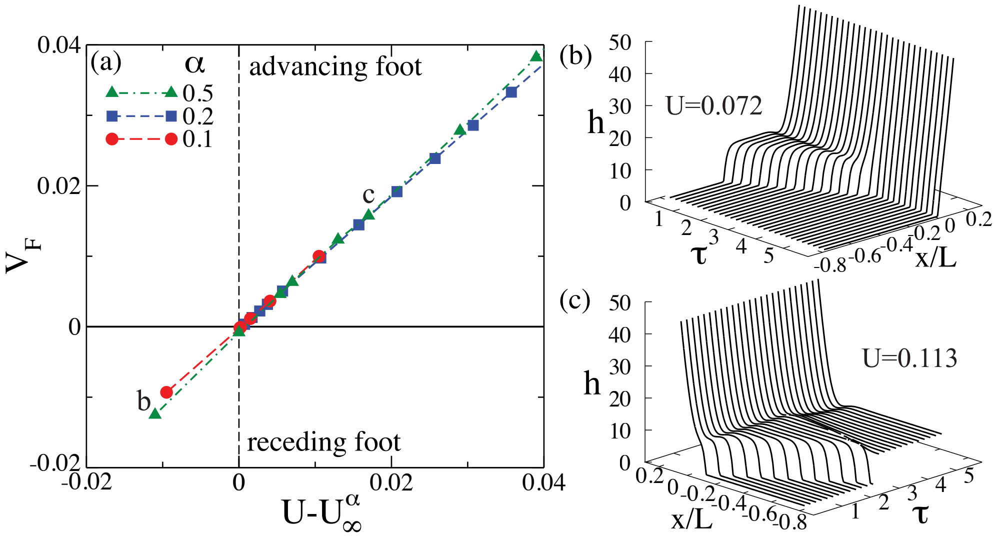

FIGURE 3.28: (a) Advancing and receding foot-like structures are characterized by the dependence of the velocity V_F of the front that connects the ultrathin coating layer of thickness h_∞ with the foot plateau of height h_foot on the velocity difference $U - U_\infty^\alpha$ where U_∞^α changes with the plate inclination α. Note that the curves for various α as given in the legend collapse onto a master curve, indeed $V_\mathrm{F} \approx U - U_\infty^\alpha$. Panels (b) and (c) give for $\alpha = 0.5$ space-time plots representing the time evolution[3] of a receding and an advancing foot, respectively, at values of U indicated by small letters in panel (a). The evolution in (b) converges to a steady simple meniscus, while in (c) the foot advances with constant speed until its tip reaches the domain boundary. Then at $\tau \approx 4$ the foot transforms into a Landau–Levich film of a different thickness via a fast shallow backwards-moving front.

towards a steady solution. These film profiles have a moving front with a front velocity V_F. As an example in the left panel of Fig. 3.28 are shown the front velocities for the unstable solutions for $\alpha = 0.1$, $\alpha = 02.$ and α=0.5. Region (2) is a multi-stable region where stable and unstable solutions coexist. Note that the curves for various α as given in the legend collapse onto a master curve, indeed $V_{\mathrm{F}} \approx U - U_\infty^\alpha$. Panels (b) and (c) of Fig. 3.28 give for $\alpha = 0.5$ space-time plots representing the time evolution of a receding and an advancing foot, respectively, at values of U indicated by small letters in panel (a). The evolution in (b) converges to a steady simple meniscus, while in (c) the foot advances with constant speed until its tip reaches the domain boundary. Then at $\tau \approx 4$ the foot transforms into a Landau–Levich film of a different thickness via a fast shallow backwards-moving front, these solutions will be discussed in the next section.

3.1.7 Behaviour at large (scaled) angles

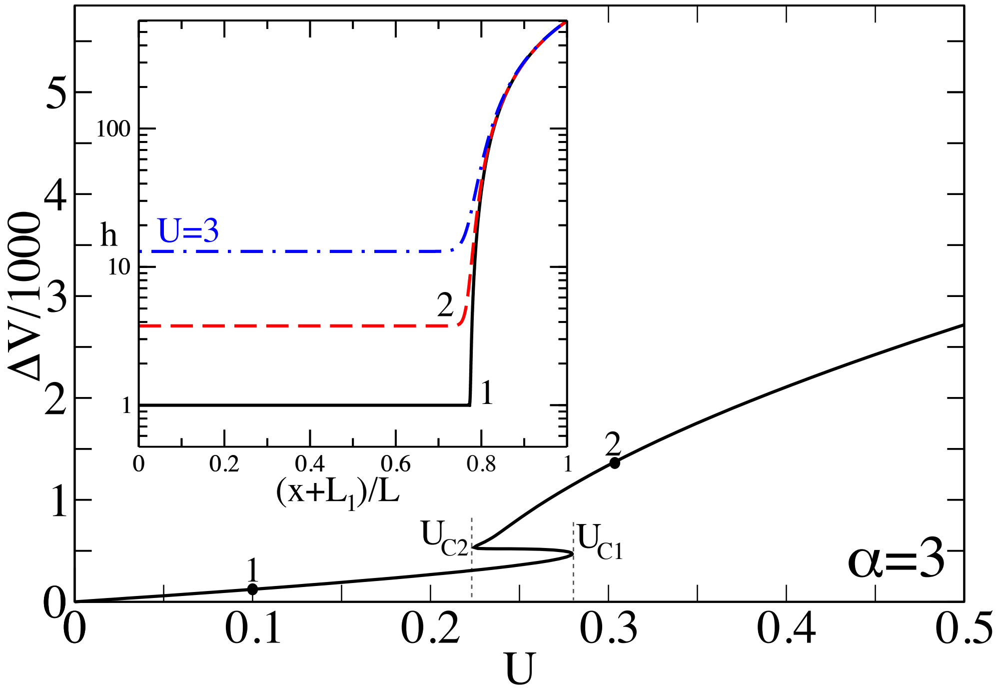

FIGURE 3.29: $\alpha = 3$: Effective volume ΔV in dependence of the plate velocity U. The numbers on the bifurcation diagram correspond to the depicted film profiles in the inset. Additionally a film profile at $U = 3$ is shown. The domain size is $L = 1000$.

At large inclination angles, i.e. for $\alpha \gtrsim 3$, the system shows a qualitatively different behaviour: In Fig. 3.29 we observe that as the plate velocity U increases, the volume ΔV increases monotonically up to a critical velocity $U = U_{C1}$, where the the first of only two saddle node bifurcations occurs. Here the bifurcation curve folds back and switches to an upper branch. The second saddle node occurs at a critical plate velocity $U = U_{C2}$, where the curve folds back again. Note, that in this velocity interval, $U \in [U_{C1}, U_{C2}]$, the effective volume ΔV always increases with a non-monotonic U exhibiting an *hysteretic* behaviour. Then, the bifurcation curve growths monotonically as the plate velocity U is increased. We observe now, in clear contrast to the previous described small angle cases, that there is no limiting velocity U_∞.

An observation of the steady film profiles as the plate velocity U increases, see Fig. 3.29, shows that the meniscus profile starts to grow in length [Solution(1)], but as the velocity $U \gtrsim U_{C1}$ the coating film height h_∞ starts to thicken [Solution(2) and Solution(3)], with $h_\infty >> h_p$ coating *completely* the plate with a thick macroscopic film.

We will investigate the behaviour in the hysteretic region further along the text.

At larger inclination angles, e. g. for $\alpha \gtrsim 10$, the system shows again a qualitatively different behaviour: In Fig. 3.30 we observe now for $\alpha = 10$ that as the plate velocity U increases, the volume ΔV increases monotonically – no occurrence of saddle nodes is observed – and no limiting velocity U_∞ is present. The saddle node annihilation occurs at $\alpha = \alpha_3 \approx 5.92$. The film profile solutions as the plate

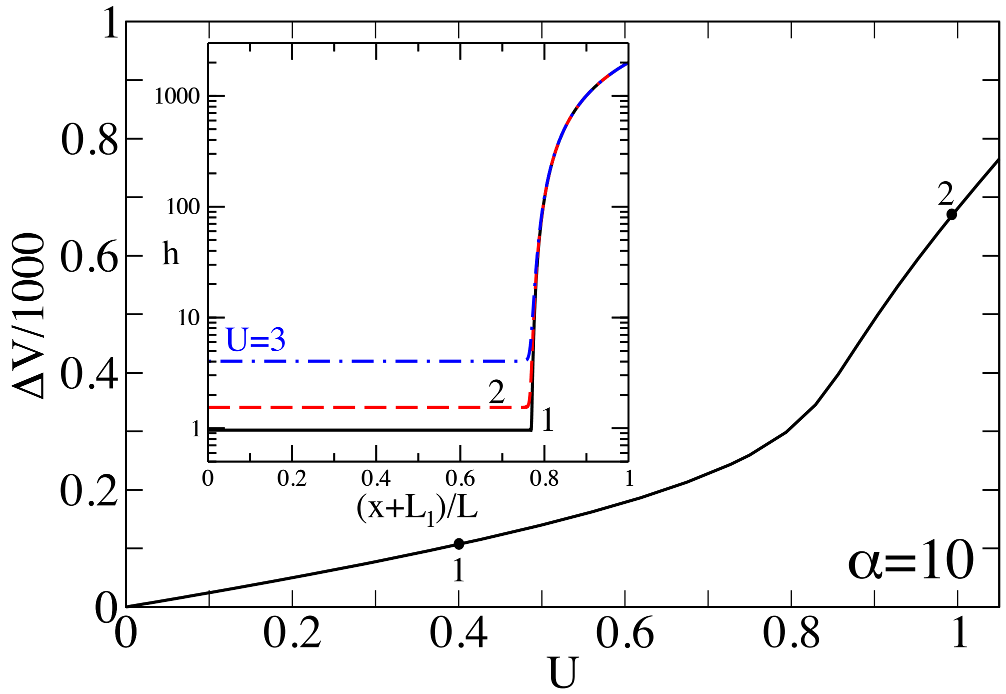

FIGURE 3.30: $\alpha = 10$: Effective volume ΔV in dependence of the plate velocity U. The numbers on the bifurcation diagram correspond to the depicted film profiles in the inset. Additionally a film profile at $U = 3$ is shown. The domain size is $L = 1000$.

velocity U increases, see Fig. 3.30, show that the meniscus profile starts to grow in length [Solution(1)] up to a certain transient velocity U_t, which will be investigated in the next paragraph, where the ultrathin film unbinds from the substrate and the coating film height h_∞ starts to increase [Solution(2) and Solution(3)], with $h_\infty >> h_p$ *completely* coating the plate with a thick macroscopic film. We observe in the last two cases that the coating film height h_∞ becomes a macroscopic film for plate velocities $U \gtrsim U_t$ (in these described cases with plate inclination angle up to $\alpha \approx 10$ and $U_t \gtrsim 1$). In Fig. 3.31 we see that the coating film height h_∞ scales like the Landau– Levich coating law [8], i.e.

$$h_\infty \propto U^{2/3}, \tag{3.51}$$

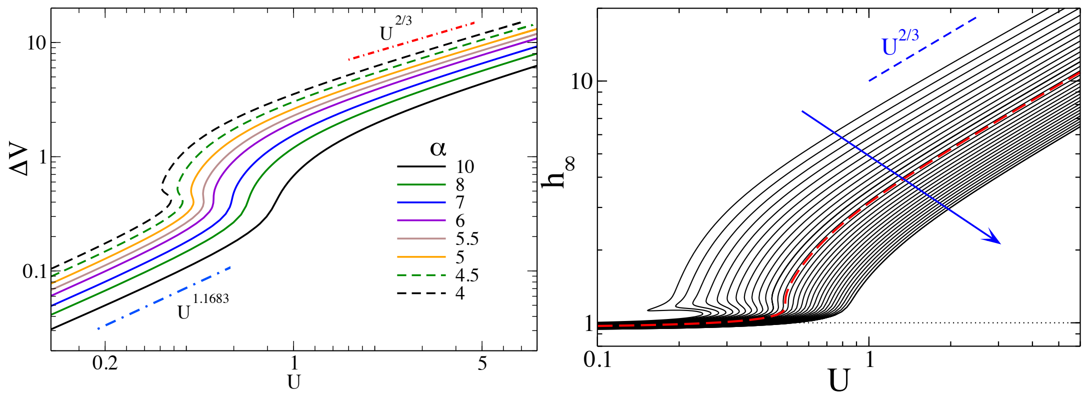

FIGURE 3.31: Left panel: Effective volume vs plate velocity U in a Log–Log-plot. For larger velocities $U \gtrsim 1$, the volume follows a Landau–Levich scaling. For plate velocities $U \lesssim 1$ a power law of 1.1683 dominates the effective volume. Angles as shown in colour coded legend. Right panel: The coating film height follows the Landau – Levich coating law, i.e. $h_\infty \propto U^{2/3}$ for velocities above $U \gtrsim 1$. Equidistant inclination angles with $\alpha \in [2.42,\ 10]$ and $\Delta\alpha = 0.25$. Red dashed line indicates the transition occurring at α_3 (see text). The arrow indicates increasing inclination angle α.

for plate velocities $U > U_t$, where U_t ($U_t \gtrsim 1$) is the transient velocity. To estimate the transient plate velocity U_t as a function of the plate inclination angle α for large angles we drive the plate velocity up to large values, see Fig. 3.32: On the left panel we see in a log–log-plot the coating film height h_∞ as function of the plate velocity U up to $U = 1000$ for different angles up to $\alpha = 1000$, with $\alpha \in [10, 20, 30...100, 150, 200, 250...1000]$ (the arrow indicates increasing inclination angle). We clearly see that as the angle α increases, the transient velocity U_t where the film starts to scale with the Landau–Levich law becomes larger, and as previously mentioned, the coating height follows the Landau–Levich scaling law. To identify the transient or threshold velocity U_t, we plot for selected velocities as indicated with the dashed vertical lines, the coating film height h_∞, see right panel. The scaling law reads,

$$h_\infty \propto \frac{1}{\alpha}. \tag{3.52}$$

We see that for smaller velocities, e.g. $U = 1$ and $U = 5$ (see right panel of Fig. 3.32), the coating film height starts to deviate form the scaling law, i.e. those values do not correspond to a Landau–Levich macroscopic film. We are now able to estimate a scaling law for the transient velocity U_t using Eq. 3.51 and Eq. 3.52 and assuming that the transition to a macroscopic coating height occurs at $h_\infty \gtrsim 1$,

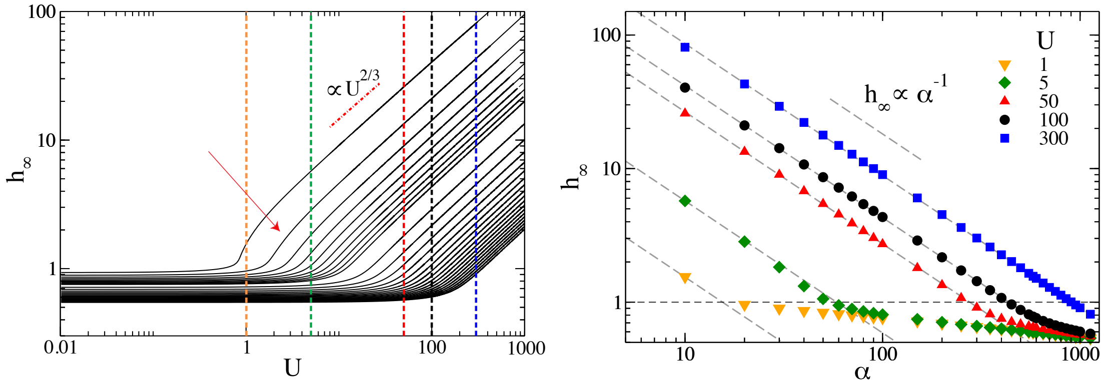

FIGURE 3.32: Right panel: Log-log plot for the coating film height h_∞ as function of plate velocity U for $\alpha \in [10, 20, 30...100, 150, 200, 250...1000]$ (the arrow indicates increasing inclination angle). Dashed colour lines correspond to selected velocities: $U = 1$ (orange), $U = 5$ (green), $U = 50$ (red), $U = 100$ (black) and $U = 300$ (blue), which will be used to represent $h_\infty(\alpha)$ in the left panel. Left panel: Log-log plot of the coating height as a function of the inclination angle, $h_\infty(\alpha)$ for selected velocities (see right panel, same colour code). Note the scaling law for macroscopic films, $h_\infty \propto 1/\alpha$. The dashed black at $h_\infty = h_p = 1$ indicates the equilibrium coating height.

via a straightforward calculation, the scaling reads

$$U_t \propto \alpha^{\frac{3}{2}}. \tag{3.53}$$

We can now easily evaluate the threshold / transient velocity U_t for a given large plate inclination angle α, where a macroscopic Landau–Levich film will emerge.

In the aforementioned hysteretic region, i.e. for $U \in [U_{C2}, U_{C1}]$ corresponding to the occurrence of the pair of saddle nodes at the extrema of the interval, it is expected to see a foot-like solution behaviour close / after the first saddle node bifurcation. The closest angle exhibiting the hysteretic behaviour is $\alpha \approx 2.42$, see Fig. 3.33. For this range of angles close after the transition and below α_3, i.e. below the angle where the saddle nodes annihilate, multiple film solutions coexist. An example is shown for $\alpha = 2.42$ in Fig. 3.33: On the left panel we plot the the effective volume ΔV as a function of the plate velocity U indicating selected velocities. On the right panel, we plot the selected 7 solutions as indicated in the figure: solution (1), for $U < U_{C1}$ corresponds to a meniscus solution; solution (3) for $U = U_{C1}$ corresponds to a meniscus solution, while solutions (2), (4) and (6) for a plate velocity $U = 0.2$, $U \in (U_{C2}, U_{C1})$, correspond to a meniscus solution, an emerging foot solution and a film like solution respectively. Note that solution

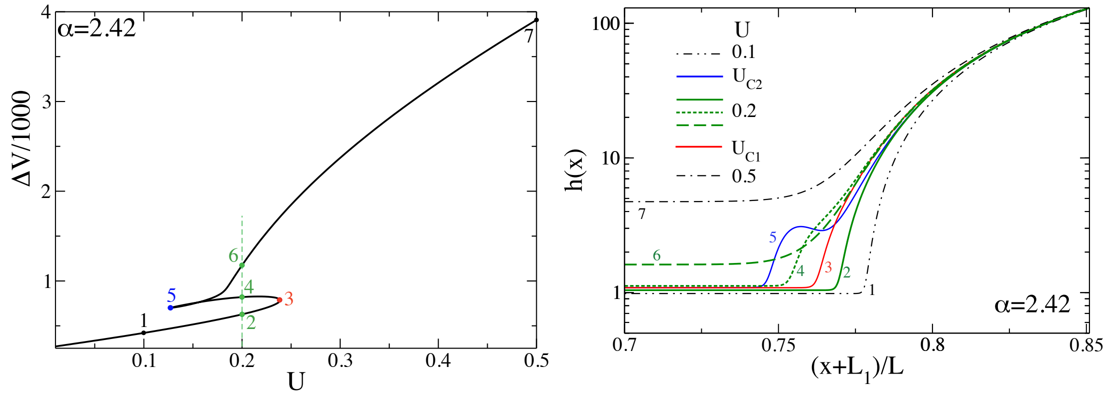

FIGURE 3.33: Right panel: Effective volume ΔV versus of plate velocity U for α=2.42. Indicated are plate velocities for selected film-profile solutions. Left panel: Film profiles for $\alpha = 2.42$: Three different solution types are depicted: (1), (2) and (3) meniscus like solutions – low velocities; (4), (5) foot-like solutions and (6), (7) film like solutions (Landau–Levich type solutions). Note the coexistence of solution families in the hysteretic region: solutions (2), (4) and (6) (colour code green), for same plate velocity U; solutions (3) and (5) for U_{C1} and U_{C2} in red and blue respectively. Domain size is $L = 1000$.

(5) for $U = U_{C2}$ is a fully developed foot solution. Finally, solution (7) at $U = 0.5$ is a Landau–Levich type solution.

3.1.8 Transition from small to larger angles

We have described in the previous sections the behaviour for smaller angles, $\alpha < 2.42$, and larger angles, $\alpha > 3$, and the two occurring transitions: the creation and annihilation of saddle nodes at $\alpha = \alpha_1 \approx 0.1025$ and $\alpha = \alpha_3 \approx 5.92$ respectively and the important changes in behaviour. Here, we will emphasise in the transition occurring between $\alpha \in (2.41, 2.42)$.

In the left panel of Fig. 3.34 a sequence of bifurcation diagrams (effective volume ΔV versus plate velocity U) is given for $\alpha = 2.41$, 3, 5 and 10. We observe that for $\alpha = 2.41$ a vertical asymptote U_∞ still exists, but for larger values of α not anymore, as we have described thoroughly in the previous sections. On the right panel, we see a detailed depiction of the transition occurring between $\alpha = 2.4175$ and $\alpha = 2.42$. We set for convenience the transition angle $\alpha = \alpha_2 \approx 2.4175$.

The transition is highlighted for the coating height h_∞ as a function of the plate velocity U in Fig. 3.35 for equidistant inclination angles $\alpha \in [0.25, 10]$ with a step of $\Delta\alpha = 0.25$, i.e. for angles below and above the second transition at α_2. The change of behaviour is observed when the curve does not converges anymore to a

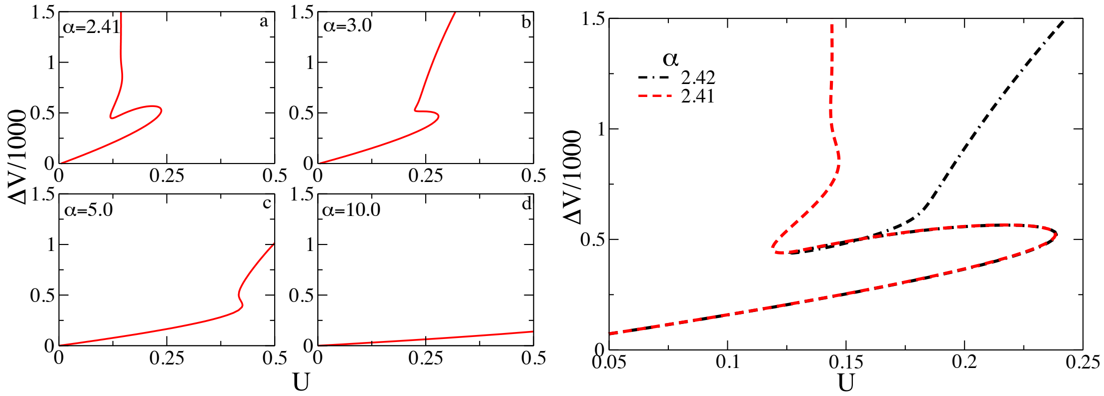

FIGURE 3.34: Left panel: effective volume ΔV in dependence of the drag velocity for different inclination angles as indicated in the figure: (a) α=2.41, (b) α=3.0, (c) α=5.0, (d) α=10. A change of behaviour occurs above $\alpha = 2.41$.; Right panel: Detail of the transition: effective volume ΔV in dependence of the drag velocity for an inclination angle below transition, α=2.41, and above, α=2.42. Domain size $L = 1000$.

fixed point in the (U, h_∞)–plane, i.e. a fixed coating film height h_∞. We highlight the angles just before and just after the occurrence of the transition using a red solid line at $\alpha_B = 2.4175$, and a dashed blue line at $\alpha_A = 2.42$ respectively.

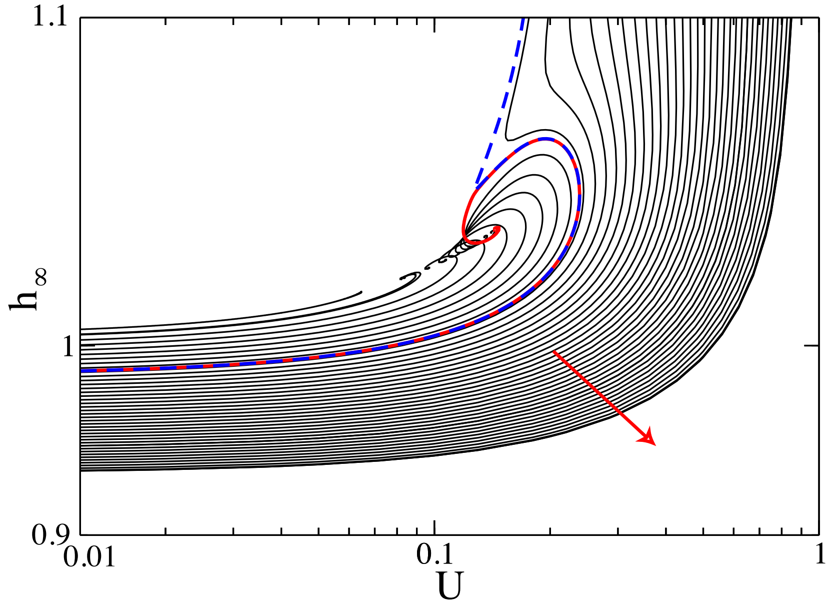

FIGURE 3.35: h_∞ in dependence of the plate velocity U for different, equidistant inclination angles (α = [0.25, 10], $\Delta\alpha$ = 0.25), arrow indicates increasing inclination angle α. Highlighted are the transition curves at α_B=2.4175, before the transition, and α_A=2.42, after the transition, in solid red and dashed blue respectively. Note that the curves before the transition at $\alpha = \alpha_2$ converge to a fixed point in the (U, h_∞)–plane. Red arrow indicates increasing α.

We have now a complete bifurcation diagram gathering the two solution families – meniscus, foot solutions and Landau–Levich films as shown in Fig. 3.36. There, we observe that for angles below α_2, a new family branch of solutions appears (black dashed line). This new branch is *not* bounded to a limiting velocity U_∞ for large values of U, but has a vertical asymptote coinciding with U_∞ (see panels (a) and (b)). For angles above α_2, another new branch appears that *has* a vertical asymptote at a given plate velocity U_∞ (solid red line). We observe in panels (a), (b), (c) and (d) the detail of the transition.

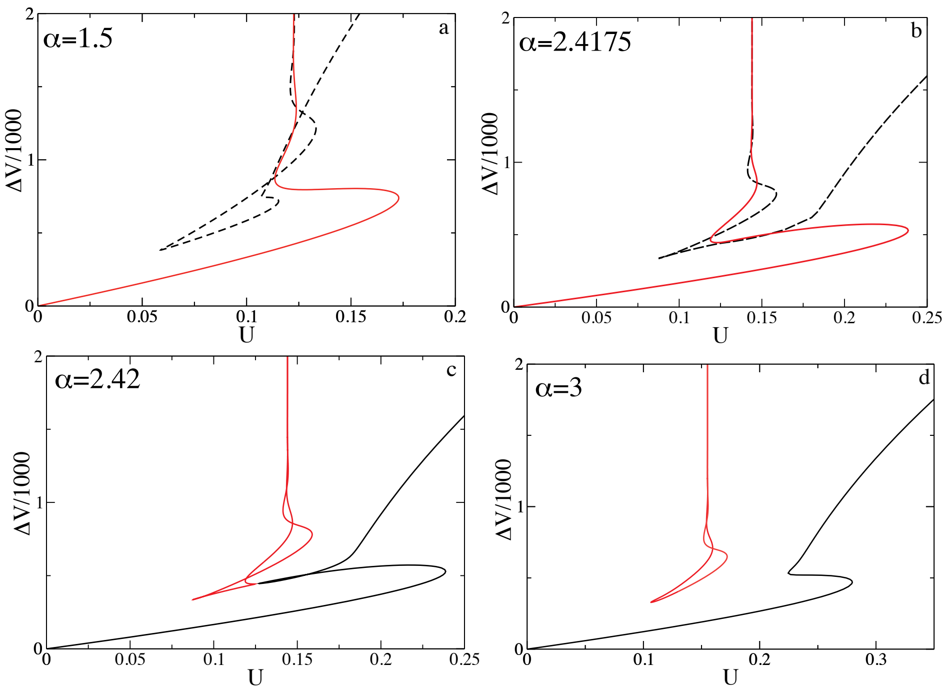

FIGURE 3.36: Detail of the transition and full bifurcation diagram effective volume ΔV as a function of plate velocity U gathering the two families of solutions for different plate inclination angles as shown in the figure. The domain size is $L = 1000$.

These new solution branches for $\alpha < \alpha_2$ have for larger velocities a 2/3-power law behaviour for the coating film height, i.e. a Landau–Levich film, as an example in Fig. 3.37 we show two (h_∞, U)–diagrams for $\alpha = 1.5$ and $\alpha = 2.4175$ respectively.

The reconnection and transition mechanism of the two solution branches is clearly detailed in the sequence shown in Fig. 3.38 for the coating film height h_∞ as a function of plate velocity U for selected angles. Note that in every panel both families of solutions are shown. Panel (a) shows $\alpha = 1.0$, in red the meniscus and foot solutions and in black film solutions for larger values of U, this new branch

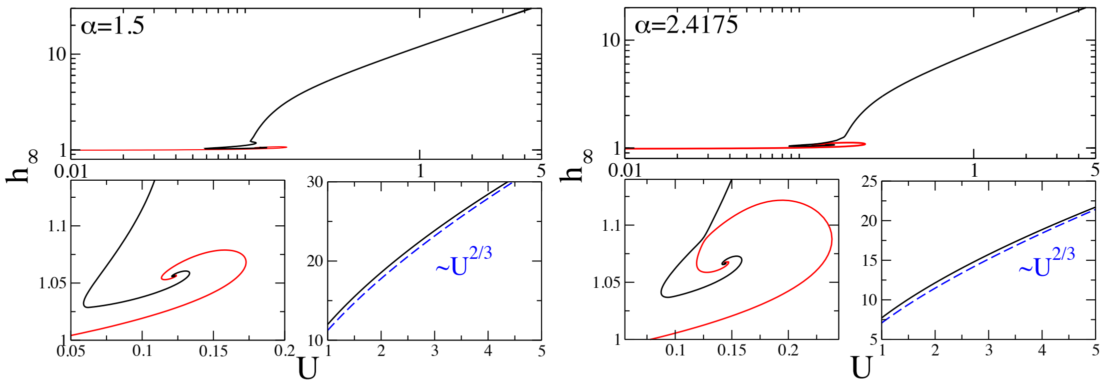

FIGURE 3.37: h_∞ in dependence of the drag velocity for different inclination angles below α_2, α =1.5 and 2.4175. In the lower panels a blow-up of the low and high velocity regions are shown. The film height in the high velocity region scales with the 2/3-power law.

has a lower different limiting velocity, i.e. a vertical asymptote at $U_\infty^L \neq U_\infty$, and no bounded upper velocity. Panel (b) shows $\alpha = 1.5$, with both limiting velocities U_∞ coinciding. For large plate velocities solutions scale like Landau–Levich films. In panels (c) $\alpha = 2.4175$ and (d) $\alpha = 2.42$, we observe first the strangling of the branches and then the reconnection. Finally, in panels (e), $\alpha = 3$, and (f) the new family branch of foot solutions is shown in red. Note the limiting velocity point in the (h_∞, U)–diagram and the *isola* type structure (in red).

In Fig. 3.39 we show the new film solutions, focusing on solutions before, $\alpha = 2.4175$, and after the transition, $\alpha = 2.42$. In the upper panel we show for $\alpha = 2.4175$ new foot solutions in red, solutions 1 and 2. This foot now is *"detached"* from the bath and it resembles a droplet sliding on an incline as we have seen in a previous section. Note that the foot increases its length as it approaches U_∞, coating the plate. In blue, the Landau–Levich type of solutions are shown, solutions 3, 4 and 5, see Fig. 3.37. In the lower panel we present new film profiles for $\alpha = 2.42$. Note that we can distinguish three solution branches: in black, solutions a, b, c show a foot like structure. Red film solutions 1–4 correspond to the red branch of *"detached"* foot solutions that increase their length while approaching the vertical asymptote at U_∞. Finally, blue solutions 1–4 correspond to the blue branch and present the same behaviour as foot solutions described in previous sections.

The transition and reconnection occurs via a *reverse necking bifurcation* at $\alpha = \alpha_2 = 2.4174$. The normal form of this codimension-2 bifurcation is given in [70][4]

[4] When $\epsilon < 0$ the solutions form two hyperbolas $a = \pm\sqrt{\lambda - \epsilon}$ separated by $2\sqrt{-\epsilon}$ in a. When $\epsilon = 0$ the two hyperbolas pinch together at the origin forming two straight lines, $a = \pm\lambda$.

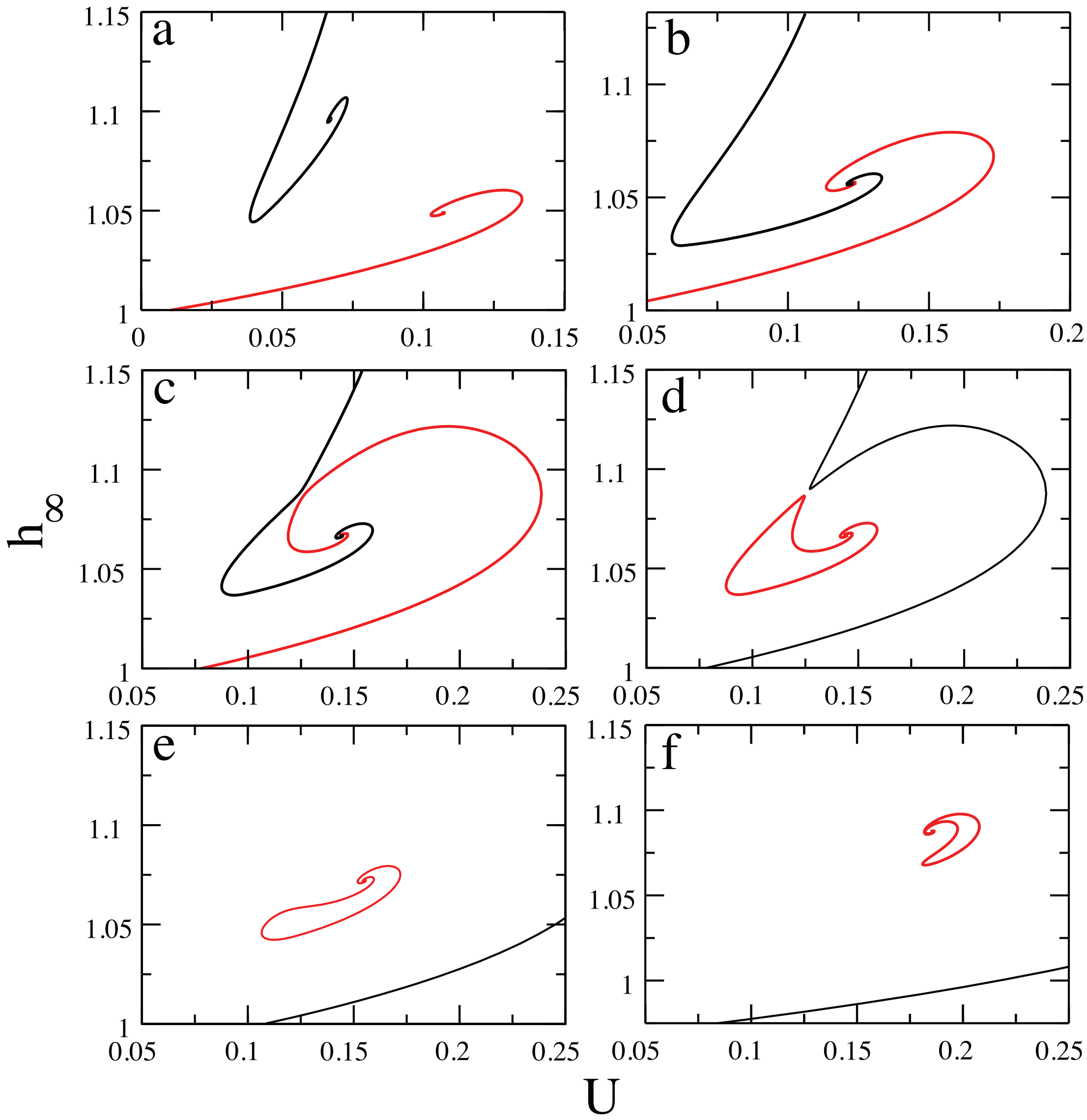

FIGURE 3.38: h_∞ versus plate velocity U for different inclination angles and both families of solutions: (a) $\alpha = 1.0$, (b) $\alpha = 1.5$, (c) $\alpha = 2.4175$, (d) $\alpha = 2.42$, (e)$\alpha = 3.0$ and (f) $\alpha = 5.0$. The transition mechanism is via a reverse necking bifurcation, shown middle panels (c) and (d). See main text.

as

$$a^2 + \lambda^2 - \epsilon = 0, \tag{3.54}$$

where a is an amplitude that corresponds to the chosen solution measure, i.e. the volume or L_2-norm, λ is the bifurcation parameter which corresponds to the plate velocity U and ϵ is the unfolding parameter that corresponds to the plate inclination angle α.

For $\epsilon > 0$ these reconnect forming two hyperbolas separated by $2\sqrt{\epsilon}$ in λ and introducing two saddle-node bifurcations.

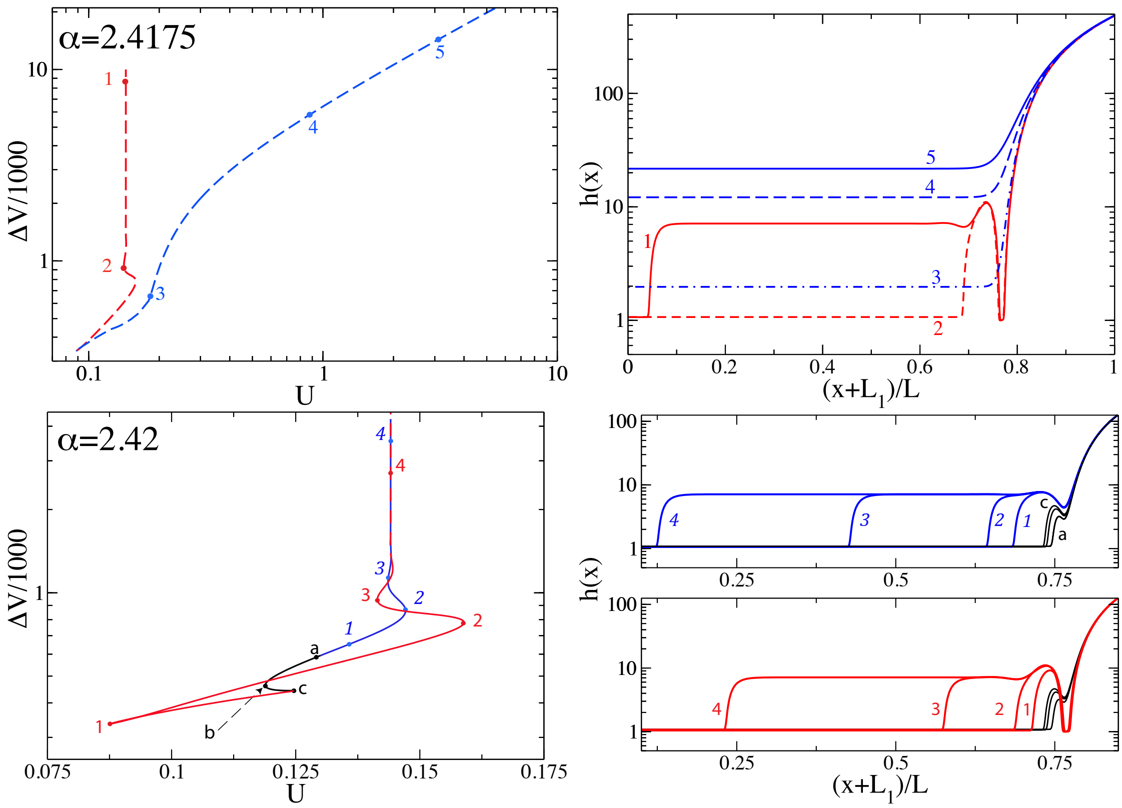

FIGURE 3.39: Left panels show effective volume ΔV vs. plate velocity U bifurcation diagrams. Numbers colour coded correspond to the solutions show in the right panel. Right panels show new solutions, numbered and colour coded as in the bifurcation diagrams. Higher panels correspond to $\alpha = 2.4175$, lower panels to $\alpha = 2.42$. Note the new *detached* foot solution.

To understand qualitatively the stability of these new solutions and how the reconnection affects the stability, we have perturbed the solutions and performed time simulations as we have done in Subsection 3.1.6. In Fig. 3.40 we show a complete bifurcation diagram for $\alpha = 2.4175$ and $\alpha = 2.42$, left and right panel respectively. We indicate used solutions with dots on both panels, colour-coded and labeled accordingly to their behaviour.

In the lower panel we depict the different observed behaviours of the perturbed film profiles, showing the *"starting profile solution"*, the *"intermediate profile solution"* (only in some cases), and the *"final profile solution"*, below we enumerate a short description,

P1: starts from a foot solution and recedes to a meniscus solution.

P2: starts from a longer foot solution and recedes to a shorter foot. In **P2d**, it starts from a *detached* longer foot and it recedes to a shorter foot.

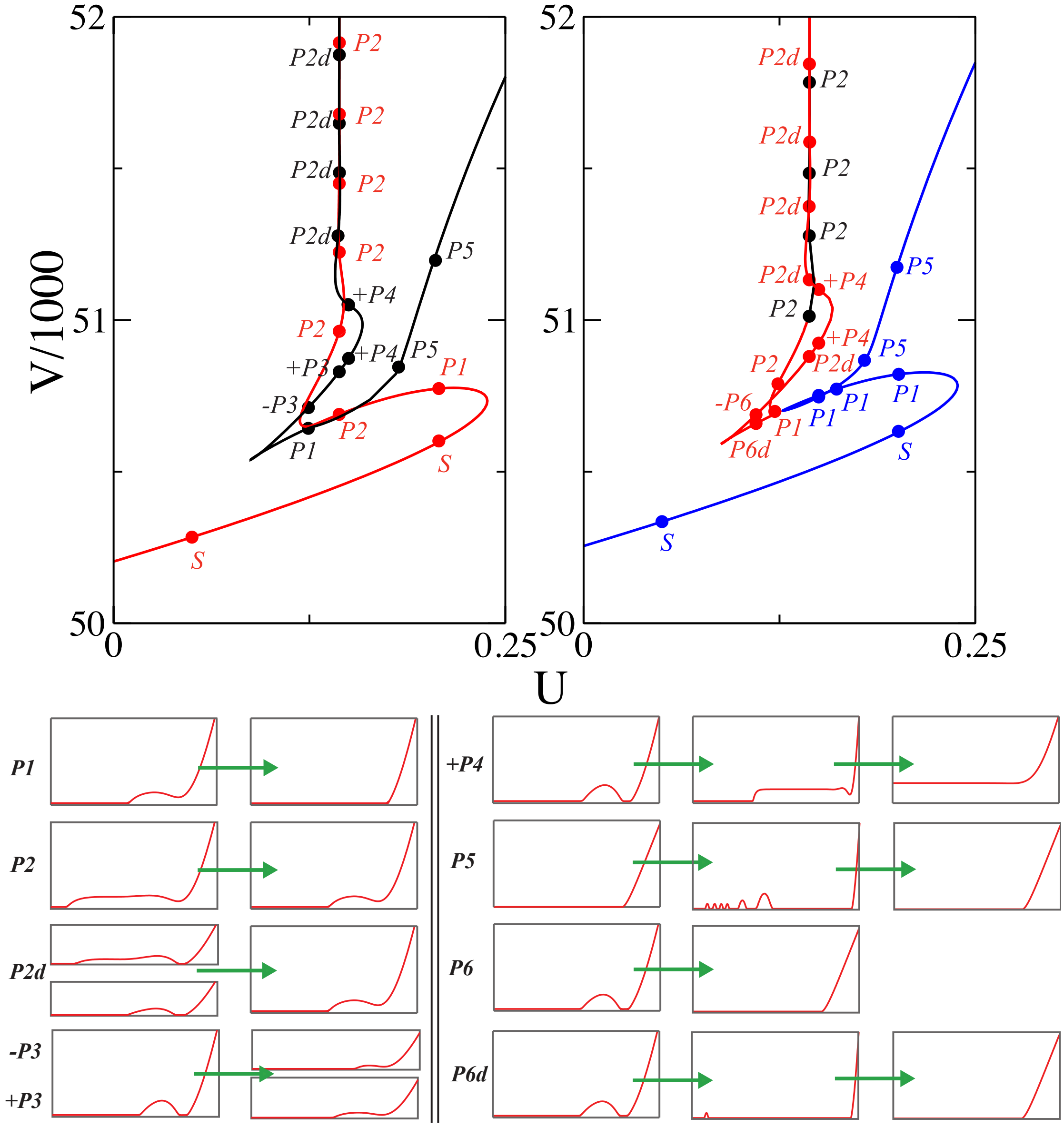

FIGURE 3.40: Upper panel: Complete family for $\alpha = 2.4175$ and $\alpha = 2.42$, left and right panels respectively. Indicated solutions with dots on both panels were perturbed and time evolution was performed to study their evolution. Labels correspond to the type of evolution. These labels are explained in the lower panels and in the main text.

P3: starts from a *detached foot* and evolves into either + a long, higher foot or - a shorter, lowerfoot.

P4: starts from a longer *detached foot*, evolves into a longer foot and finally into a Landau–Levich film.

P5: starts form a meniscus film, an undulated travelling structure towards $-L_1$ emerges and then decreases its height into a meniscus.

P6: starts from a short *detached foot* and recedes into a meniscus. In **P6d**, while receding, a detached droplet / rim moves towards $-L_1$ and finally recedes to a meniscus.

The solutions labeled with **S** are stable. Although not shown in Fig. 3.40, Landau–Levich solutions at larger values of U are stable to perturbations.

We note that the stability behaviour in the reconnected branches is similar, conserving the stable behaviour / unstable behaviour.

3.1.9 Scaled flux and scaled coating film height

In Chapter 2 we derived the equation that relates the flux J_0 and film height h_0, see Eq. (2.68) and Fig. 2.10, for the scaled flux, $J_0^* = J_0/J_{\max}$ as a function of the scaled height $h_0^* = h_0/\sqrt{U/(G\alpha)}$[5]. Here, we compare the theoretical derived relation from the linear stability analysis with our numerical results.

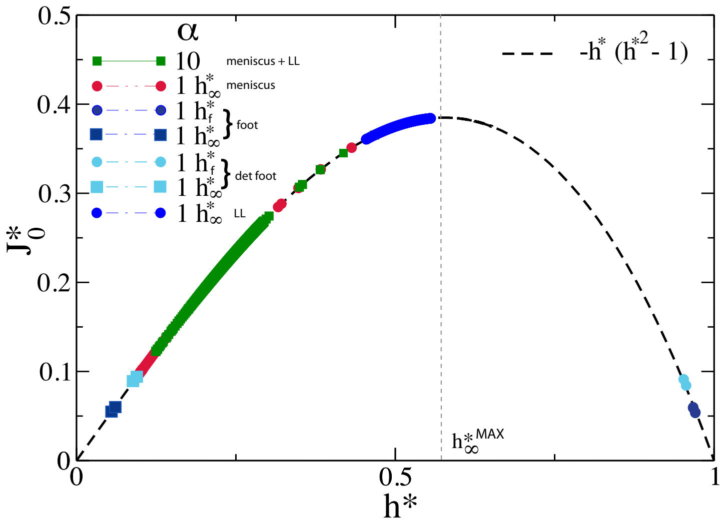

FIGURE 3.41: Shown is a comparison of the theoretical curve (dashed line) and the numerical results for the scaled flux J_0^* as a function of the scaled coating height h_∞^* for $\alpha = 1$. Different families of solutions for $\alpha = 1$ are depicted: red dots correspond to meniscus, blue squares and dots correspond to foot solutions (precursor height and foot height, respectively), light blue correspond to detached foot solutions (precursor height and foot height, see legend) and navy blue dots to solutions scaling with $h_\infty \propto U^{2/3}$. In green squares solutions for $\alpha = 10$ are shown, which correspond to $h_\infty \propto U^{2/3}$ for $h_\infty^* < h_\infty^{*,MAX}$.

[5]Note that for the sake of simplicity, we have used here the flat film relation derived from Eq. (2.46), i.e. $1/3G\alpha h_0^3 - Uh_0 + J_0 = 0$ without affecting the results.

In Fig. 3.41 we superpose the theoretical calculated curve (black dashed lined) with our numerical results for selected inclination angles $\alpha = 1$ – for both solution families, i.e. meniscus and foot solutions and Landau–Levich film solutions (see legends) – and for $\alpha = 10$, i.e. menisucs + Landau–Levich (green squares). Note the agreement between the results and as well, the evolution of the scaled film height h_∞^*: for a meniscus coating height it starts at $h_\infty^* \approx 1$ and then evolves *decreasing* up to a critical value which corresponds either to the occurrence of the first saddle node or to the transition velocity in the Landau–Levich film solutions, depending on the inclination angle of the plate. The scaled variables can be used

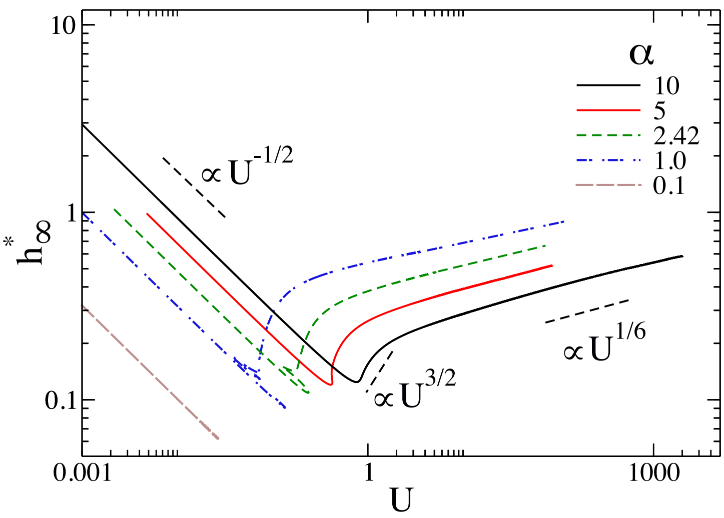

FIGURE 3.42: Scaled coating height h_∞^* as a function of plate velocity U. Note different power laws for menisci solutions and Landau–Levich solutions.

for plotting the coating height h_∞^* as a function of the plate velocity U for selected angles. In Fig. 3.42 we show a log-log plot where one can distinguish clearly the three different power-law regimes: for a meniscus solution, $h_\infty^* \propto U^{-1/2}$; transition regime, $h_\infty^* \propto U^{3/2}$ and Landau – Levich films; $h_\infty^* \propto U^{1/6}$.

These numerical results are in agreement with the theoretical approximation assuming the known results for different coating heights (see below) and replacing them into $h_\infty^* = h_\infty / \sqrt{U/(G\alpha)}$, namely

(i) for a meniscus type solution, $h_\infty \approx$ constant $\longrightarrow h_\infty^* \propto U^{-1/2}$, and

(ii) for a Landau–Levich film solution, $h_\infty \approx U^{2/3} \longrightarrow h_\infty^* \propto U^{1/6}$.

3.1.10 The complete transitions scenario

Let us summarise the qualitatively different behaviours of the system that we have seen in the preceedings sections:

(a) for very small angles, $\alpha < \alpha_1 \approx 0.1125$ there is a monotonic increase of the effective volume ΔV with increasing U towards a vertical asymptote at U_∞, no saddle node bifurcations appear, film solutions are menisci and foot solutions with increasing foot length as $|U - U_\infty| \to 0$ without undulations on the free surface of the foot, see Fig. 3.4 and Fig. 3.7,

(b) for angles $\alpha_1 < \alpha < \alpha_2 = 2.4175$, the effective volume ΔV increases, while U first increases, then changes non–monotonically and the $\Delta(U)$ dependence approaches a vertical asymptote at U_∞, pairs of saddle nodes appears at $\alpha = \alpha_1$ and we observe *collapsed snaking*. Film solutions are menisci and undulated foot solutions with increasing foot length as $|U - U_\infty| \to 0$, see Fig. 3.5 and Fig. 3.7,

(c) for angles $\alpha_2 < \alpha < \alpha_3 \approx 5.92$ only a *pair* of saddle nodes still exists, the primary curve ΔV vs U exhibits an hysteresis region, no vertical asymptote in U, solutions are menisci, foot solutions in the hysteretic velocity interval and Landau–Levich films at large plate velocities, see Fig. 3.29 and Fig. 3.31, and

(d) for $\alpha > \alpha_3$ we observe a monotonic growth of the effective volume ΔV in U, no vertical asymptote in U, solutions are menisci and Landau–Levich films, see Fig. 3.30 and Fig. 3.31.

We can construct a phase diagram in the plane spanned by plate velocity U and inclination angle α to explain in detail the occurring transitions.

Via a fold continuation in the aforementioned phase space of the control parameters α and U, we obtain the phase diagram depicted in Fig. 3.43. The fold continuation technique consists in tracking a known saddle node in the control parameter space, in these case we have chosen the first pair of saddle nodes occurring at U_{C1} and U_{C2} (black solid line).

In the figure we can accurately identify the occurring three transitions at α_1, α_2 und α_3: we see the creation of the pair of saddle nodes at $\alpha_1 \approx 0.1125$, where we observe how the two loci of folds bifurcate – each line corresponding to one of the velocities U_{C1} and U_{C2}, with $U_{C1} > U_{C2}$ for α up to $\alpha_3 \approx 5.92$ where the two lines rejoin and the pair of saddle nodes annihilate in a hysteresis transition. At $\alpha_2 = 2.4175$ we observe a *cusp*, where the *reverse necking* bifurcation and reconnection to new solutions occur.

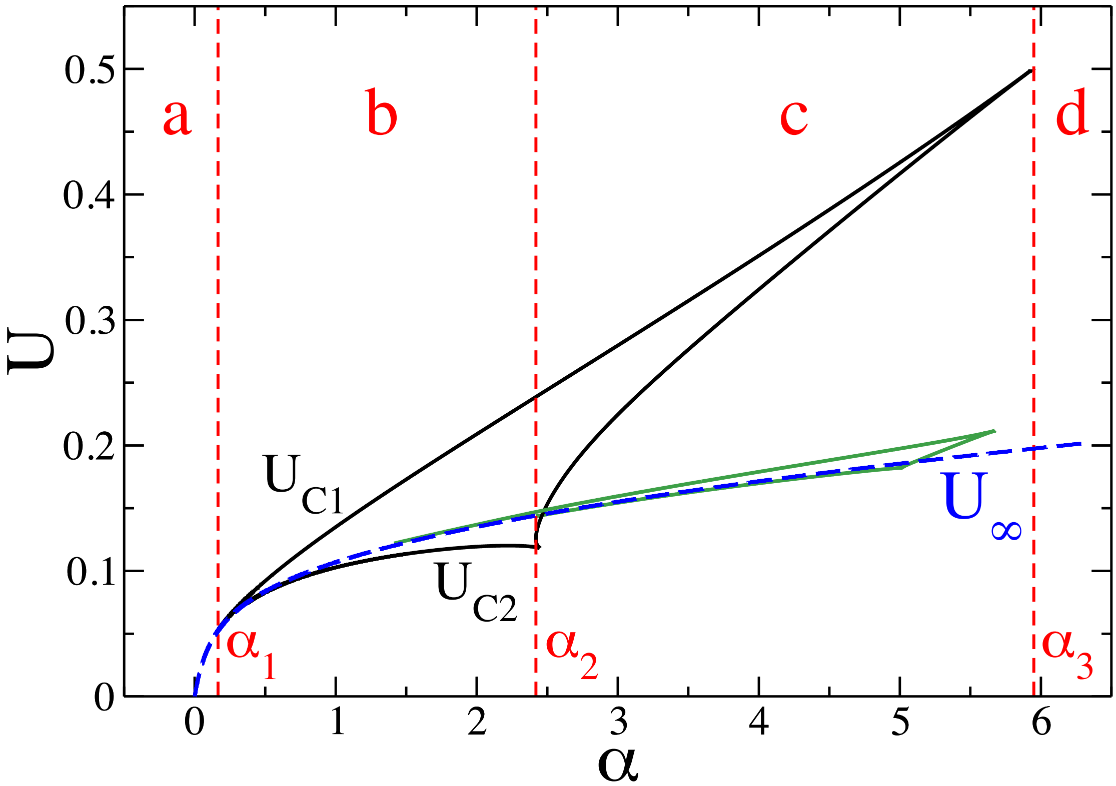

FIGURE 3.43: $(U - \alpha)$ phase diagram: we can identify four different regions as defined in the text: (a) $\alpha < \alpha_1$, (b) $\alpha_1 < \alpha < \alpha_2$, (c) $\alpha_2 < \alpha < \alpha_3$ and (d) $\alpha > \alpha_3$.

Note that in Fig. 3.43 we have also included the loci (green solid line) of the second pair of saddle nodes (see left panel of Fig. 3.6, labeled with green dots), and this curve indicates as well the reconnection and crossover to the new family of solutions for $\alpha > \alpha_2$, see region (c). Also included is the limiting velocity U_∞ in its dependance on α (blue dashed line).

Note that a richer behaviour is described when we track other pairs of saddle nodes, see Fig. 3.44. We see the in the upper panels bifurcation diagrams including different families of solutions for two different angles, $\alpha = 0.5$ and 3. For $\alpha = 0.5$ we have included in a dashed black line a new family of solutions which will be investigated in the future. The coloured circles correspond to the folds that are being tracked in the $(\alpha - U)$–space (see lower panel), each line of fold loci with the corresponding colour. In the lower panel we see the rich behaviour in the

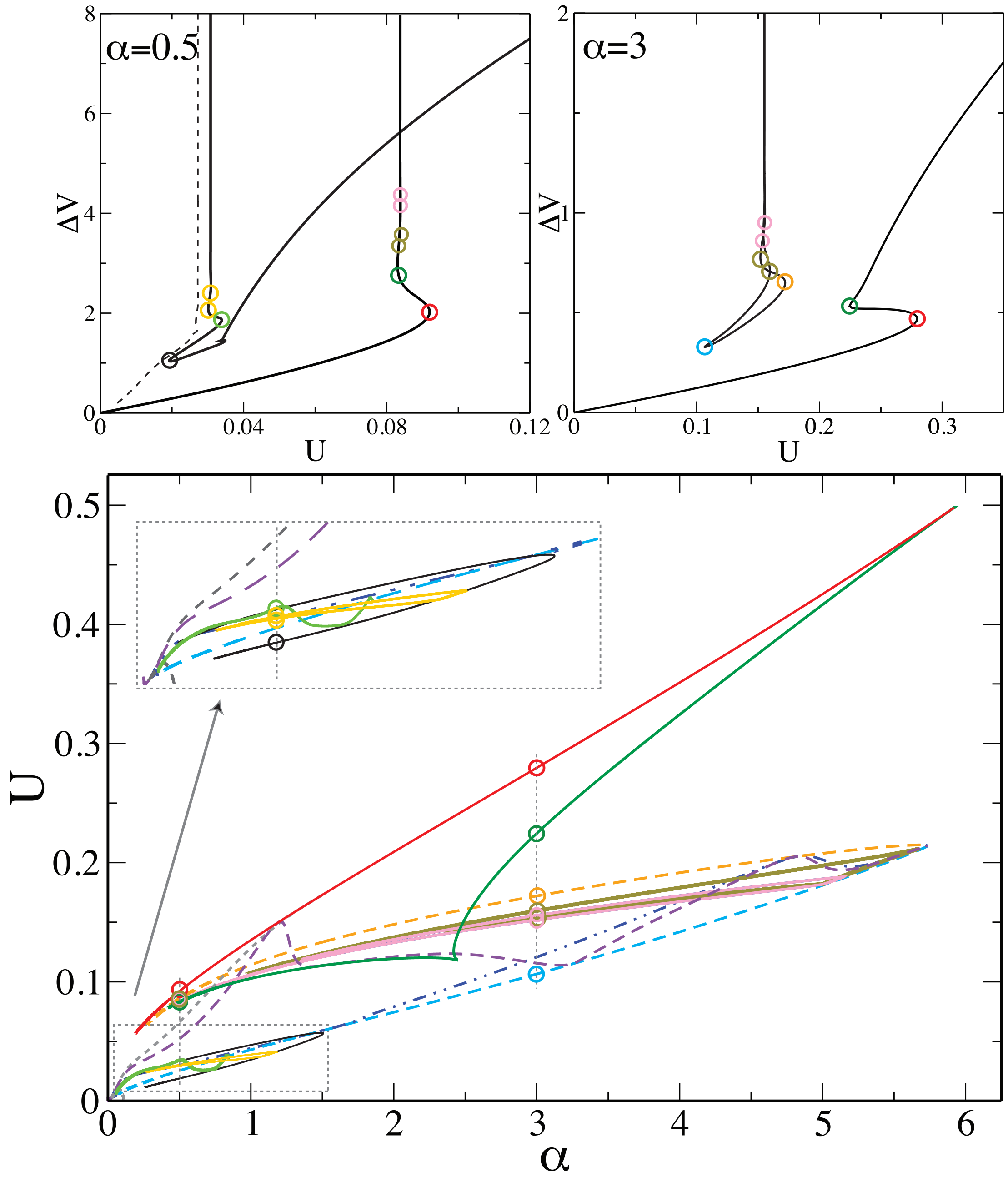

FIGURE 3.44: Fold continuation. Upper panels show for two different angles, $\alpha = 0.5$ and 3, the bifurcation diagram for different families of solutions, the coloured circles correspond to the folds that are being tracked in the $(\alpha - U)$–space in the lower panel, each branch with the corresponding colour code. Lower panel shows the rich behaviour in the $(\alpha - U)$–space. In the inset, a detail of the phase space for smaller angles (e.g. see $\alpha = 0.5$).

$(\alpha - U)$—space. In the inset, a detail of the phase space for the fold continuation for the solution families for $\alpha \lesssim 1.5$. Note that this is an incomplete picture of the fold loci, as there are more families of solutions, which have not been included here.

3.1.11 Streamlines

To have an insight into the internal flow within the meniscus–, foot– and film solutions, we plot the streamlines using the stream function $\Psi(x, z)$, see Eq. (2.85), for different film profiles using our previous results. First, we present in the left panel of Fig. 3.45 for an inclination angle $\alpha = 1.5$ streamlines for zero plate velocity (the flux $J_0 < 0$), where we can see a small back flow to the bath due to the action of gravity towards the bath. On the right panel we present the typical streamlines for a Landau–Levich film (shown is $\alpha = 3$ at $U = 5$), where due to the drawn plate the fluid is pulled out of the bath coating the plate with a layer of a height scaling like $h_\infty \propto U^{2/3}$. Note the stagnation point on the free surface (green dot). As an example for all types of film profiles we have discussed, we

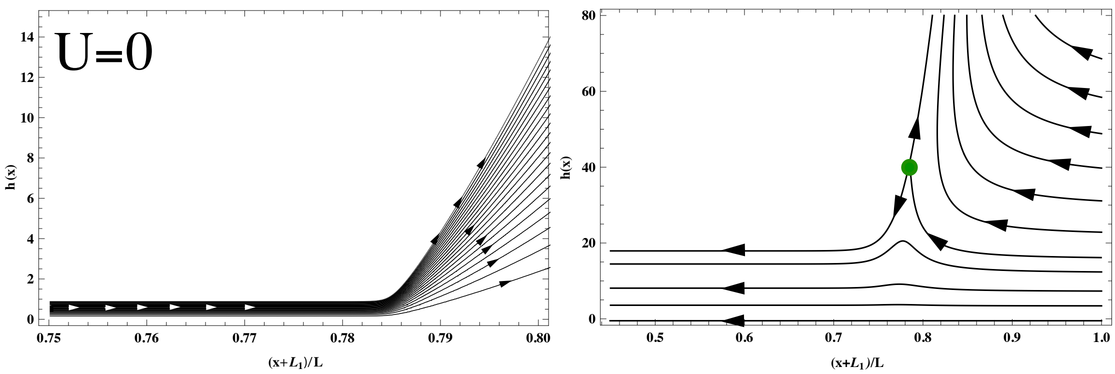

Figure 3.45: Left panel: Streamlines for a meniscus solution at an inclination angle $\alpha = 1.5$ and plate velocity $U = 0$. Right panel: Streamlines for a Landau–Levich film for an inclination angle $\alpha = 3$ at plate velocity $U = 5$. There is a stagnation point present at the free surface marked with the green dot.

focus on a single inclination angle $\alpha = 1.5$. In Fig. 3.46, panel **(h)** we present the bifurcation diagram as a function of the plate velocity U. The labels correspond to the profiles shown in the other panels at given plate velocities: (a), (b) and (d) $U = 0.1$; (c) $U = 0.058$; (e), (f) $U = U_\infty = 0.1225$ and (g) $U = 3.0$. The streamlines correspond to equidistant values of the stream function.

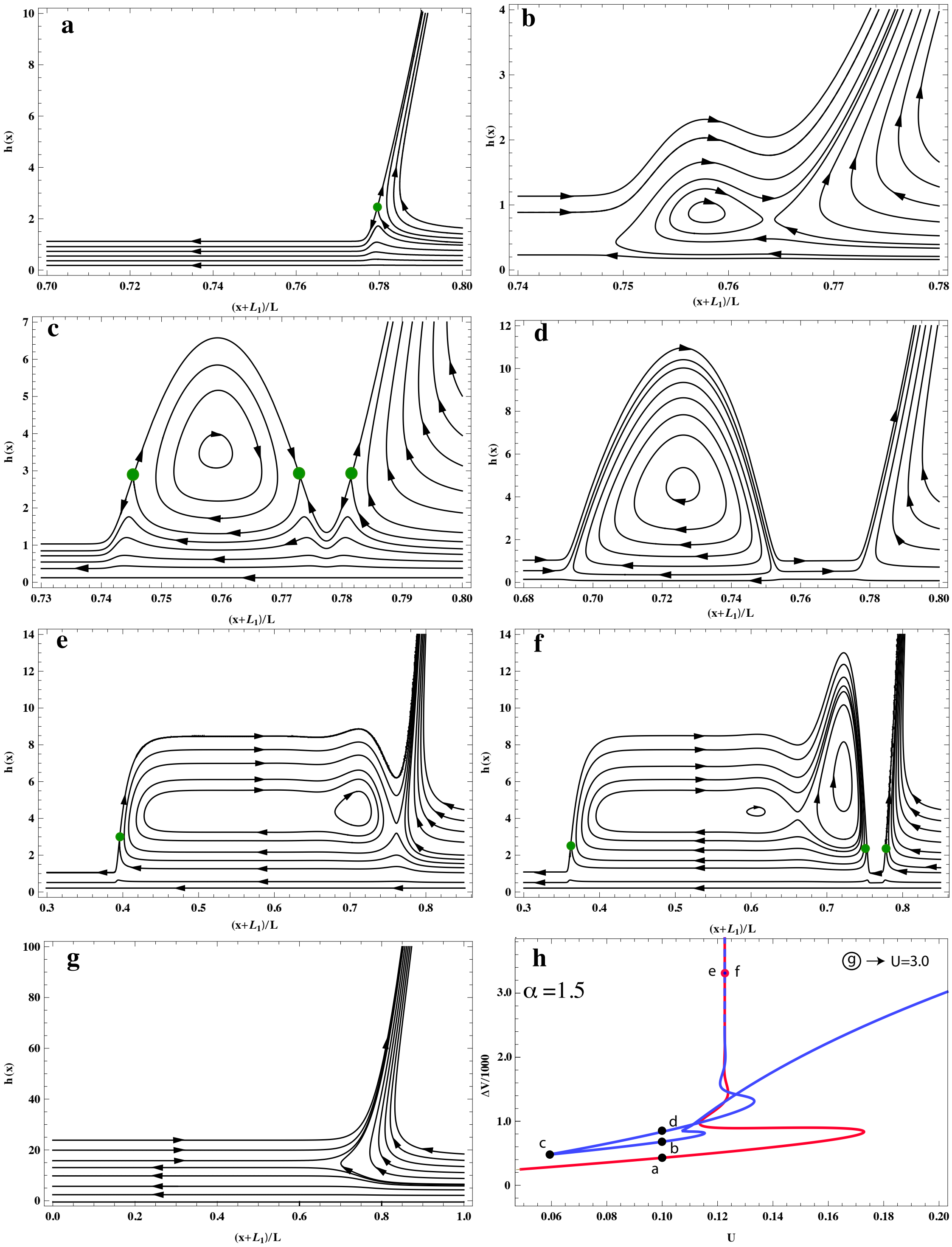

FIGURE 3.46: Streamlines for film profiles for $\alpha = 1.5$. The labels on the profiles shown in the panels at given plate velocities: (a), (b) and (d) $U = 0.1$; (c) $U = 0.058$; (e), (f) $U = U_\infty = 0.1225$ and (g) $U = 3.0$ correspond to the bifurcation diagram ΔV as a function of plate velocity U shown in (h). The arrows indicate the direction of the local fluid velocity $\vec{u}$. Green dots indicate stagnation points in the profiles.

3.2 Completely wetting liquid

So far we have been investigating the drawn meniscus for a partially wetting liquid. Here instead, we focus on the behaviour for the same experimental setting but using a complete wetting liquid defined by an appropriate disjoining pressure $\Pi(h)$. The dimensional disjoining pressure for the completely wetting liquid is defined via a long-range destabilising van der Waals interaction with $A' < 0$, see Subsection 2.1.3 and Fig. 2.7, as

$$\Pi(h) = -\frac{A'}{h^3}. \tag{3.55}$$

The dimensional equation modelling the drawn meniscus for a complete wetting liquid reads,

$$\partial_t h \; = \; -\partial_x \left\{ \frac{h^3}{3\eta} \, \partial_x \, \left[\gamma \partial_{xx} h + \Pi(h) \right] - \frac{h^3}{3\eta} \rho g \left(\partial_x h - \alpha \right) - U h \right\}. \tag{3.56}$$

Although we could introduce a new scaling where the inclination angle of the plate α could be absorbed into the new scales and non-dimensional variables, this would not allow to compare with earlier findings in previous sections. Therefore, we use a non-specified height h_{w} as a scale for h. The non-dimensionalisation follows the procedure of Subsection 2.1.4, and the scales here are given by

$$x = L\tilde{x} \qquad t = \beta\tilde{t} \qquad h = h_{\mathrm{w}}\tilde{h} \tag{3.57}$$

where

$$L = \sqrt{\frac{\gamma}{A'}} h_{\mathrm{w}}^2 \qquad \beta = \frac{3\eta\gamma h_{\mathrm{w}}^5}{A'^2}, \tag{3.58}$$

with A' being the Hamaker constant and γ, ρ and η the surface tension, the density and the dynamic viscosity of the liquid respectively. Eq. (3.56) is non–dimesionalised and re-written with the new scales as (dropping the tildes),

$$\partial_t h \; = \; -\partial_x \left\{ h^3 \, \partial_x \, \left[\partial_{xx} h + \frac{1}{h^3} \right] - h^3 G \left(\partial_x h - \alpha \right) - U h \right\}, \tag{3.59}$$

and the steady state equation reads,

$$h^3 \partial_{xxx} h - \frac{3}{h} \partial_x h - h^3 G \left(\partial_x h - \alpha \right) - U h + J_0 = 0, \tag{3.60}$$

where J_0 is the flux to the right and $\tilde{U} = U/(3L/\beta)$. The boundary conditions for the numerical calculations follow Subsection 2.1.5 and are defined as in Eq. 2.56. In the far–field, i.e. for $x \to -\infty$ ($x \to -L_1$)

$$\partial_x h = \partial_{xx} h = 0, \tag{3.61}$$

and at the bath side, i.e. for $x \to \infty$ ($x \to L_2$),

$$\begin{aligned} h &\approx \alpha x + \frac{U}{\alpha^2 G x} - \frac{J_0}{2G\alpha^3 x^2}, \\ \partial_x h &\approx \alpha - \frac{U}{\alpha^2 G x^2} + \frac{J_0}{G\alpha^3 x^3}. \end{aligned} \tag{3.62}$$

We note that in the case of a complete wetting liquid there are no *foot* like

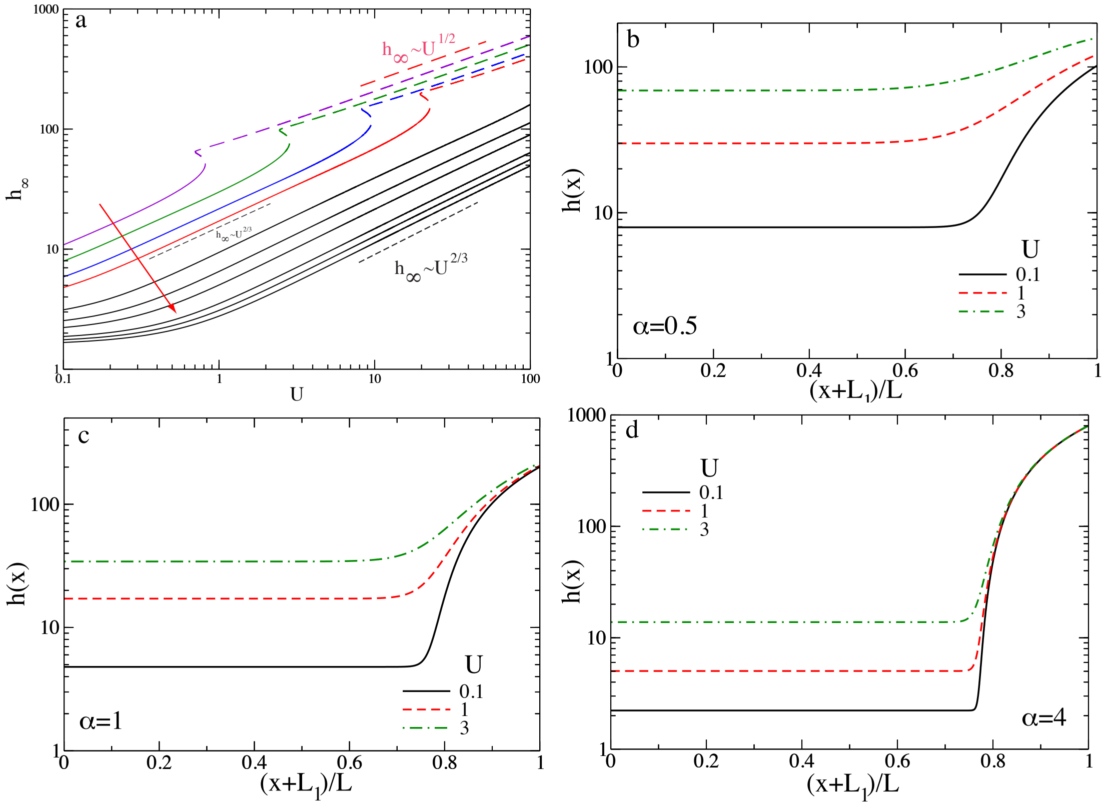

FIGURE 3.47: h_∞ in dependence on the plate velocity U for different inclination angles as indicated in the figure. (a) Log-log plot with (i) Landau–Levich velocity scaling for $U \gtrsim 0.1$ for all angles and (ii) thick-film scaling, i.e. $h_\infty \propto U^{1/2}$ for angles $\alpha \leq 1$ (dashed lines). Red arrow indicates direction of increasing α, i.e. $\alpha \in [0.33, 0.5, 0.75, 1, 2, ..., 8]$. In (b), (c) and (d) are shown film profiles for inclination angles $\alpha = 0.5, 1$ and 4 respectively for different plate velocities U as indicated in the legends. The domain is L=1000.

structures. In panel (a) of Fig. 3.47 we plot coating height h_∞ in dependance of plate velocity U. For a completely wetting liquid, we see clearly a drawn (drag) and wetting dominated regime with a continous and smooth transition to a Landau–Levich film independently of the inclination angle α, where the red arrow indicates direction of increasing α, i.e. $\alpha \in [0.33, 0.5, 0.75, 1, 2, ..., 8]$. Note that for angles $\alpha \leq 1$, the front reaches the domain end and the system jumps to a different solution branch, namely to a thick-film regime, i.e. $U \propto U^{1/2}$. This is shown with dashed–lines in Fig. 3.47. In panels (b), (c) and (d) we show corresponding film profiles for inclination angles $\alpha = 0.5, 1$ and 4 respectively for different plate velocities U as indicated in the legends.

3.3 Drawn meniscus in a slip length model

In Subsection 2.1.2 we have mentioned the problem arising for a dynamic contact line in the hydrodynamical description if the free surface truly continues to the substrate. The no–slip condition results in the divergence of the viscous dissipation at the contact line, implying that contact line motion is not possible under these conditions. In order to *relieve* this singularity, several mechanisms and solutions were proposed, e.g. a mesoscopic precursor film [38], surface roughness [71, 72] and Navier slip [41] to name a few (a more complete list can be found in [73]).

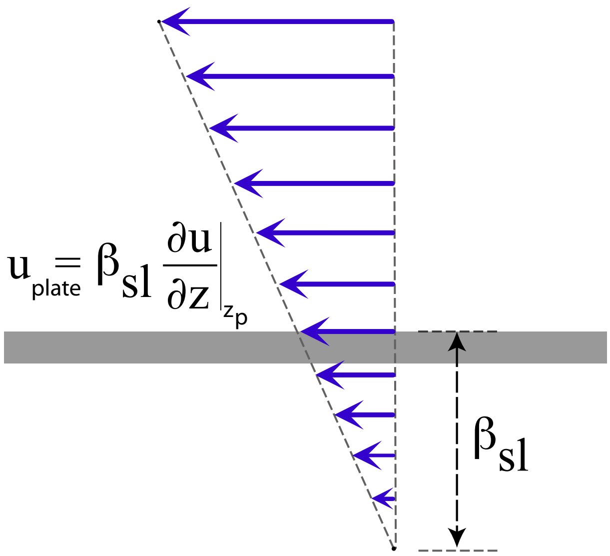

FIGURE 3.48: Sketch illustrating the Navier slip boundary condition and of the slip length. Note that u_{plate} is the tangent component of the velocity.

Here, we compare our results for film solutions obtained with the precursor film model with a Navier slip model for different orders of magnitude for the slip length β_{sl}. The slip length β_{sl} is an offset length such that the fluid velocity at the solid surface, i.e. at the drawn plate at $z = z_p = 0$, is the slip length times the normal derivative of the velocity [74], see sketch in Fig. 3.48. The Navier slip boundary condition is

$$u_{\text{plate}} = \beta_{sl} \frac{\partial u}{\partial z}\bigg|_{z=0} . \tag{3.63}$$

Note that u_{plate} is the tangent component of the fluid velocity at the plate. The non - dimensional long–wave time evolution equation with the Navier slip boundary condition and slip length β_{sl} for the drawn meniscus reads

$$\partial_t h = -\partial_x \left\{ Q(h)\, \partial_{xxx} h - Q(h) G \left(\partial_x h - \alpha \right) - U h \right\}, \tag{3.64}$$

and the steady–state equation, after integration in x, is

$$Q(h)\, \partial_{xxx} h - Q(h) G \left(\partial_x h - \alpha \right) - U h + J_0 = 0, \tag{3.65}$$

where J_0 is the flux to the right and $Q(h)$ in the mobility factor which includes the slip length β_{sl},

$$Q(h) = h^2 (h + \beta_{sl}). \tag{3.66}$$

Note that the corresponding boundary conditions for numerically solving Eq. (3.65) have been obtained in the same fashion as described in Subsection 2.1.5. In the far–field, i.e. for $x \to -\infty$ ($x \to -L_1$)

$$\partial_x h = \partial_{xx} h = 0, \tag{3.67}$$

and at the bath side, i.e. for $x \to \infty$ ($x \to L_2$),

$$\begin{aligned} h &\approx \alpha x + \frac{U}{\alpha^2 G x} - \frac{J_0 + \beta_{sl} U}{2 G \alpha^3 x^2}, \\ \partial_x h &\approx \alpha - \frac{U}{\alpha^2 G x^2} + \frac{J_0 + \beta_{sl} U}{G \alpha^3 x^3}. \end{aligned} \tag{3.68}$$

In Fig. 3.49 and Fig. 3.50 we show the coating film thickness h_∞ over the plate velocity U comparing results of the disjoining pressure model and of the slip length model. Fig. 3.49 corresponds to a plate inclination angle of $\alpha = 1$ and Fig. 3.50

is for $\alpha = 10$. We start our analysis from a Landau–Levich film and gradually decrease the plate velocity U. We note, that for the slip length model (solid red line) the film height decreases monotonically as the plate velocity decreases and approaches zero as the plate velocity goes to zero, see Fig. 3.50. For the disjoining pressure model (for $\alpha = 1$ green solid line in Fig. 3.49 – foot and meniscus film solutions – and dashed blue line – Landau–Levich film solutions– and for $\alpha = 10$ green solid line in Fig. 3.50), the film thickness approaches a constant finite coating height as the velocity decreases. Note that in the slip model, the region where the foot solutions exist are not accessed in our calculations.

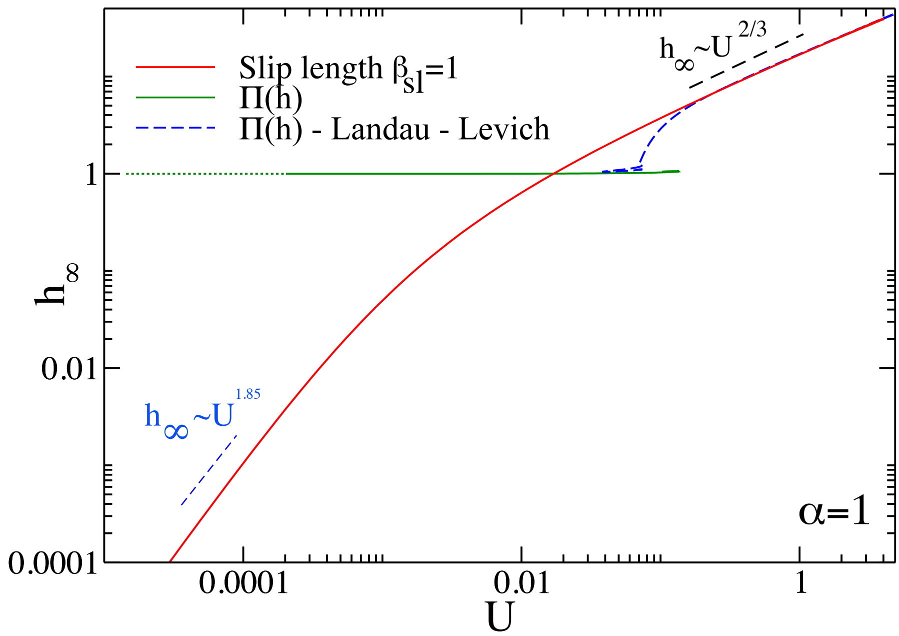

FIGURE 3.49: Shown in log-log plot is a comparison between the precursor film model (green solid line and blue dashed line) and the slip model (red solid line) for an angle $\alpha = 1$.

Previous works use a slip model that allows the film height to go to zero at the contact line, see e.g. [18, 75]. Although a slip model allows for a *quantitative* study of meniscus solutions and Landau–Levich films it is not able to describe transitions between them, as in a slip model they are topologically different, namely, for meniscus and foot solutions the film height goes exactly to zero at a certain point, whereas for film solutions the film thickness approaches a constant value at infinity. Therefore, such solutions are characterised by different boundary conditions and there is no way to continuously transform a foot or meniscus solution into a film solution. This concerns the actual transition dynamics as well as the description of transitions in dependence of control parameters such as the plate speed U and

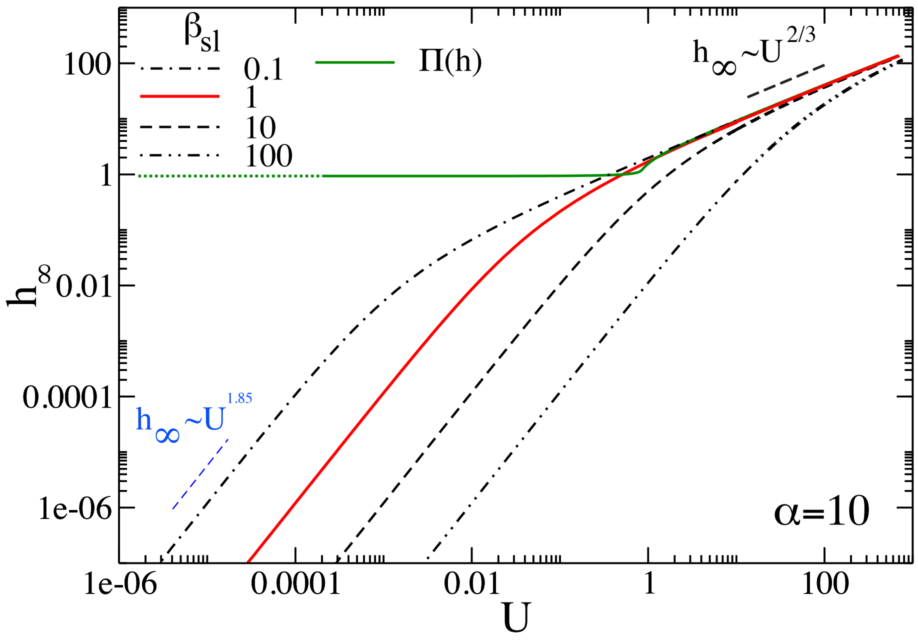

FIGURE 3.50: Shown in log-log plot is a comparison between the precursor film model (green solid line) and the slip length model for an angle $\alpha = 10$ for different slip lengths as indicated in the legend (dashed black lines and solid red line). Note that via the slip-length model it is not possible to access the meniscus / foot solution region from the Landau–Levich film region.

plate inclination angle α. Note that far from the transition regions, the predictions of precursor and slip models agree very well and can be quantitatively mapped [76], this is shown for the case of the Landau–Levich film solutions in Fig. 3.49 where slip and precursor model coincide for values of plate velocity $U \gtrsim 0.9$ and strongly differ at smaller U. Fig. 3.50 indicates how the begin of the region of agreement shifts to larger U when increasing the slip length β_{sl}.

3.4 Continuous and discontinuous dynamic unbinding transitions

We have summarised qualitatively our findings in Subsubsection 3.1.10, where we represent the changes in a phase diagram spanned by the plate velocity U and inclination angle α, see Fig. 3.43. Here, we use these results to describe these changes within the framework of dynamic unbinding transitions. First, we make a brief introduction to contextualise these new description.

The equilibrium and non–equilibrium behaviour of mesoscopic and macroscopic drops, menisci and films of liquid in contact with static or moving solid substrates is not only of fundamental interest but also crucial for a large number of modern technologies. On the one hand, the equilibrium behaviour of films, drops and menisci is studied by means of statistical physics. A rich substrate-induced phase transition behaviour is described even for simple liquids, e.g., related to wetting and emptying transitions - both represent unbinding transitions well studied at equilibrium. In a wetting transition the thickness of an adsorption layer of liquid diverges continuously or discontinuously at a critical temperature or strength of substrate-liquid interaction, i.e., the liquid-gas interface of the film unbinds from the liquid-solid interface [73]. In an emptying transition a macroscopic meniscus in a tilted slit capillary develops a tongue (or foot) along the lower wall. The foot length diverges logarithmically at a critical slit width, i.e., the tip of the foot unbinds from the meniscus and the capillary is emptied [77].

The hydrodynamic long-wave model that we have developed, Eq. (2.47) with Eq. (2.49), corresponds directly to a gradient dynamics of an underlying interface Hamiltonian (or free energy) $F[h] = \int[\xi\gamma + f(h)]dx$ as often used to study the above introduced equilibrium unbinding transitions. Here, $\xi dx \approx (1/2)[1 + (\partial_x h)^2]ds$ is the surface area element in long-wave approximation and $f(h)$ is an appropriately defined energy containing terms related to wettability and gravity. Note that in the wetting literature $F[h]$ is called "Hamiltonian" as it may be derived from a microscopic Hamiltonian. However, thermodynamically it is a free energy [78], while mathematically it represents a Lyapunov functional [79]. This equivalence allows for a natural understanding of the various occuring transitions as non-equilibrium (or dynamic) unbinding transitions.

A previous analysis of the changes that steady menisci undergo with increasing plate speed U shows that four qualitatively different cases exist depending on the plate inclination angle α, see Subsection 3.1.10. Each case is now related to a distinguished *non-equilibrium unbinding transition* as illustrated in Fig. 3.51:

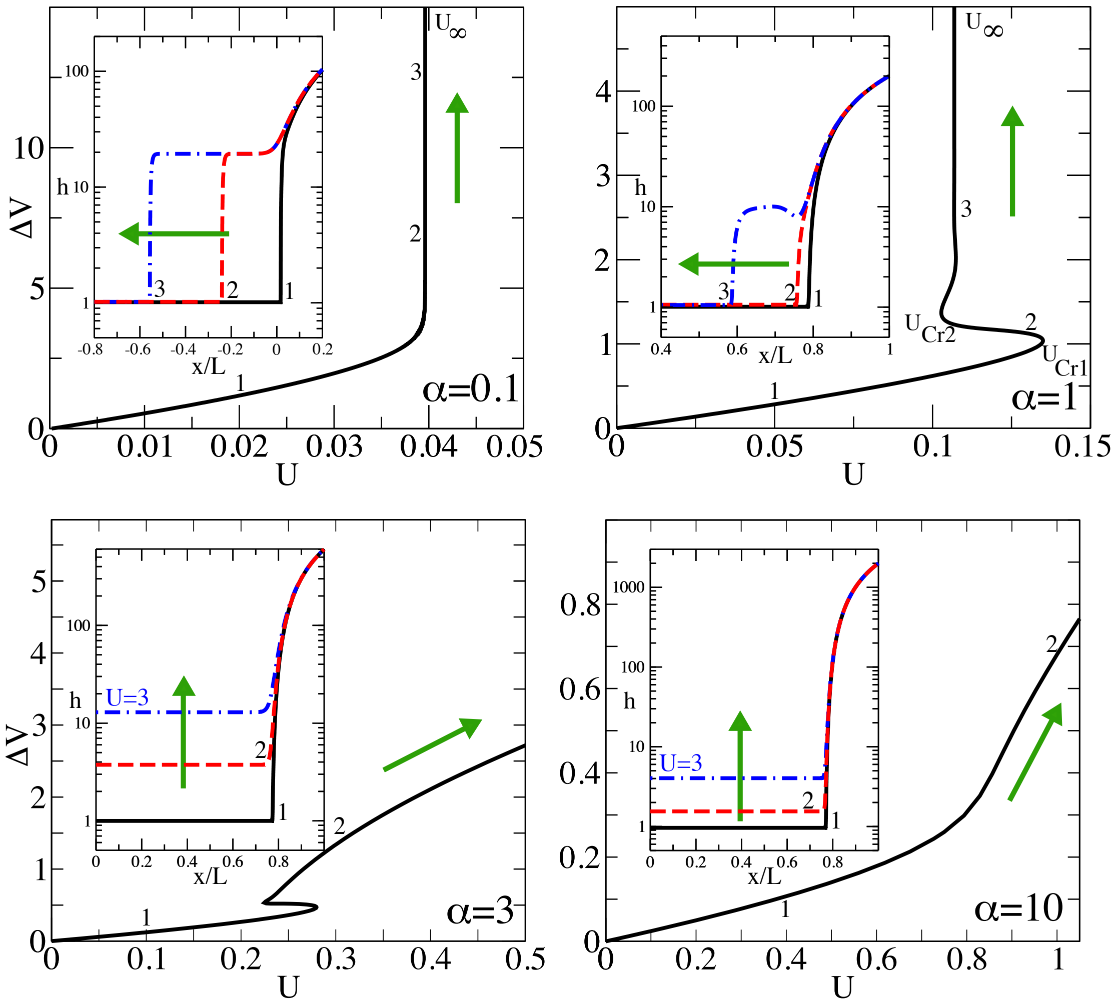

FIGURE 3.51: Bifurcation curves indicating the occurence of qualitatively different behaviour with increasing plate inclination angles (a) $\alpha = 0.1$, (b) $\alpha = 1$, (c) $\alpha = 3$, and (d) $\alpha = 10$. The main panels shown the excess volume ΔV over domain size L (see main text) in dependence of the plate velocity U, while the respective insets give Log-normal representations of steady film profiles at selected plate velocities as indicated by corresponding labels at the profiles and at the bifurcation curves. Additionally, panels (c) and (d) give a film profile at $U = 3$. The domain size is $L = 1000$. Arrows indicate how the profiles change as one moves along the bifurcation curves.

(a) At small α, the volume ΔV monotonically increases: first slowly, then faster until it diverges at $U_\infty \approx 0.04$ [Fig. 3.51(a)]. The corresponding simple meniscus profiles first deform only slightly due to viscous bending before a distinguished foot-like protrusion of a height $h_\mathrm{f} \approx 10$ develops whose length L_f diverges $\propto \ln\left[(U_\infty - U)/U_\infty\right]^{-1}$. This corresponds to a ***continuous dynamic emptying transition***, a non-equilibrium analogue of the equilibrium transition discussed above (cf. Ref. [77]). In other words, at U_∞ the tip of the foot unbinds from the meniscus and the bath is emptied. For $U > U_\infty$ the foot advances with a constant velocity $V_F \approx (U - U_\infty)$ as shown in Fig. 3.28, in a finite system, ultimatly resulting in a Landau–Levich film state.

(b) Above a first critical $\alpha = \alpha_1 \approx 0.11$, the transition changes its character and becomes a ***discontinuous dynamic emptying transition*** that has no analogue at equilibrium. As shown in Fig. 3.51(b), ΔV increases first monotonically with U until a saddle-node bifurcation is reached at U_1 where the curve folds back. Following the curve further, one finds that it folds again at U_2. This back and forth folding infinitely continues at loci that exponentially approach U_∞ from both sides and that separate linearly stable and unstable parts of the solution branch. This exponential (or collapsed) snaking [80] results in foot length with $\left[(U_\infty - U)/U_\infty\right]^{-1} \propto \exp(\mathrm{Re}[\nu]L_\mathrm{f})\sin(\mathrm{Im}[\nu]L_\mathrm{f})$ where ν is a linear eigenvalue whose real and imaginary part determine the exponential approach and the period of the snaking, respectively [66]. Note that for $U > U_\infty$ one can always find a critical foot length beyond which the foot advances with a constant velocity $V_F \approx (U - U_\infty)$, ultimately resulting in a film state. In contrast, for $U < U_\infty$ there is always a critical length above which a foot recedes. *Advancing* and *receding* fronts, are illustrated in Fig. 3.28(a) for $\alpha = 0.1, 0.2$ and 0.5. Panels (b) and (c) show for $\alpha = 0.5$ the time evolution of a receding and an advancing foot, respectively. In both previously described regions, (a) and (b), one finds that $h_\mathrm{f} \propto U^{1/2}$. The limiting velocity U_∞^α coincides with the velocity of a large flat drop (pancake-like drop) sliding down a resting plate of inclination α [68]. This allows one to calculate U_∞ by continuation (see Fig. 3.43 below). Note that the found relation for the front velocity $V_\mathrm{F} \approx U - U_\infty^\alpha$ [Fig. 3.28(a)] is a direct consequence of the Galilean invariance of the motion of a drop down an incline.

(c) At a second critical $\alpha = \alpha_2 \approx 2.42$, the bifurcation diagram dramatically changes. Above α_2 the family of steady menisci that is connected to $U = 0$ does not diverge anymore at a limiting velocity U_∞. Instead of a protruding foot of increasing length that unbinds from the meniscus one finds a hysteretic transition [in Fig. 3.51(c) between $U = 0.1$ and 0.3] towards a coating layer whose thickness

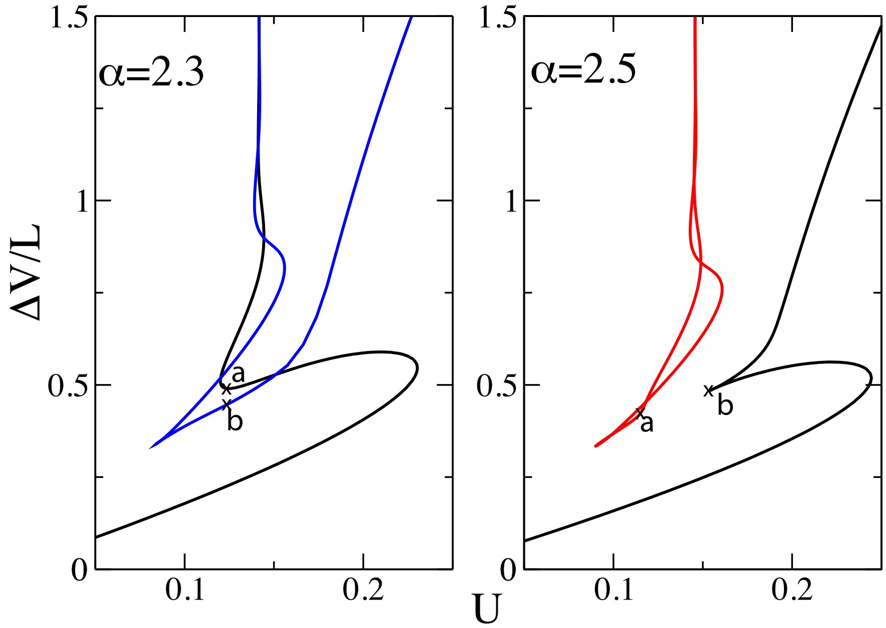

FIGURE 3.52: Detail of the transition from case (b) to (c) and full bifurcation diagram gathering the two families of solutions. One observes that the transition occurs via a reverse–necking bifurcation at $\alpha = \alpha_2$ and that Landau–Levich films are present below α_2.

homogeneously increases with increasing U, i.e., the layer surface unbinds from the substrate in an ***discontinuous dynamic wetting transition***.

(d) With increasing α the hysteresis of the discontinuous transition becomes smaller until at a third critical $\alpha = \alpha_3 \approx 5.92$ the two saddle-node bifurcations annihilate in a hysteresis bifurcation (as illustrated in the right panel of Fig. 3.31). For all $\alpha > \alpha_3$ one finds a ***continuous dynamic wetting transition***. As in cases (c) and (d), at large U the coating layer thickness follows the power law $h_\infty \propto U^{2/3}$, we identify these unbinding states as Landau–Levich films [8]. The critical velocity where the transition between the microscopic and macroscopic layer occurs, scales as $\alpha^{3/2}$.

Finally, we highlight and recall some further important facts:

The crossover between regions (a) and (b) at $\alpha = \alpha_1$ can be understood in terms of a change of the character of the spatial eigenvalues (EV) of a flat film of a height that corresponds to the foot height [20, 66]: In region (a) all EV are real while in region (b) only one is real and the other two are a pair of complex conjugate EV. The crossover between regions (c) and (d) at $\alpha = \alpha_3$ results from a hysteresis bifurcation where two saddle-node bifurcations annihilate. However, the crossover between regions (b) and (c) at $\alpha = \alpha_2$ that results in the strongest qualitative change, namely, from a dynamic emptying to a dynamic wetting transition cannot be understood by analysing a single family of steady profiles. As illustrated in Fig. 3.52 the crossover results from a reconnection (reverse necking bifurcation) at $\alpha = \alpha_2$ that involves two solution families. Both continue to exist on both sides of α_2. This results in intricate behaviour in certain small bands of the (U, α) plane and, in particular, around α_2 that will be studied in more depth elsewhere. For instance, in the fine grey band around U_∞ in region (c) [Fig. 3.43], there exist various stable extended meniscus profiles. They correspond to the left branch in Fig. 3.52(b). Experimentally, they might only be obtained through a careful control of the set-up at specific initial conditions.

To conclude this Chapter, we have shown that a long-wave mesoscopic hydrodynamic description of the coating problem for a plate that is drawn from a bath allows one to identify several qualitative transitions if wettability is modelled via a Derjaguin pressure. As a result we have distinguished four ***dynamic unbinding transitions***, namely ***continuous*** and ***discontinuous dynamic emptying transitions*** and ***discontinuous*** and ***continuous dynamic wetting transitions***. These dynamic transitions are out-of-equilibrium equivalents of well known equilibrium emptying and wetting transitions. Beside features known from equilibrium, our analysis has uncovered important features that have no equivalents at equilibrium. A future study of the influence of fluctuations might allow one to answer the question which surface profile is selected in the multistable regions.

Chapter 4

Evaporating drop with influx on substrate with a corner

"Weil der Kreis das Wesen aller Dinge ist. Alle mächtigen und wichtigen Dinge sind rund. Denk' mal nach: die Erdkugel, die Sonne, der Mond, der Tropfen..."

Alois Drahoslav Drichlik

Das Geheimnis des großen Lehrmeisters

In this Chapter we consider a well known problem: the pinning of droplets at sharp corners. In particular, we focus on the pinning of a completely wetting, volatile liquid droplet at a sharp corner. It is known, that during the spreading of a non-volatile liquid, the contact line can stay pinned at sharp edges of the substrate unless the apparent contact angle exceeds a critical value derived from properties of the corners and the equilibrium contact angle. This is known as the Gibbs–criterion. However, here we show that for volatile liquids there also exists a dynamically produced critical angle for depinning, which increases with the evaporation rate and results in a modified Gibbs–criterion. The proposed model and numerical simulations reproduce the experimental results presented in [81].

4.1 Motivation

Geometrical features on the surface of a rigid substrate, such as small-scale posts, grooves or other defects, pose an energy barrier hindering the movement of droplets or liquid films [82]. In particular, equilibrium thermodynamics explains why advancing contact lines will stay pinned at sharp edges until a certain equilibrium angle is exceeded [84]. The nature of contact line pinning (or depinning) has been

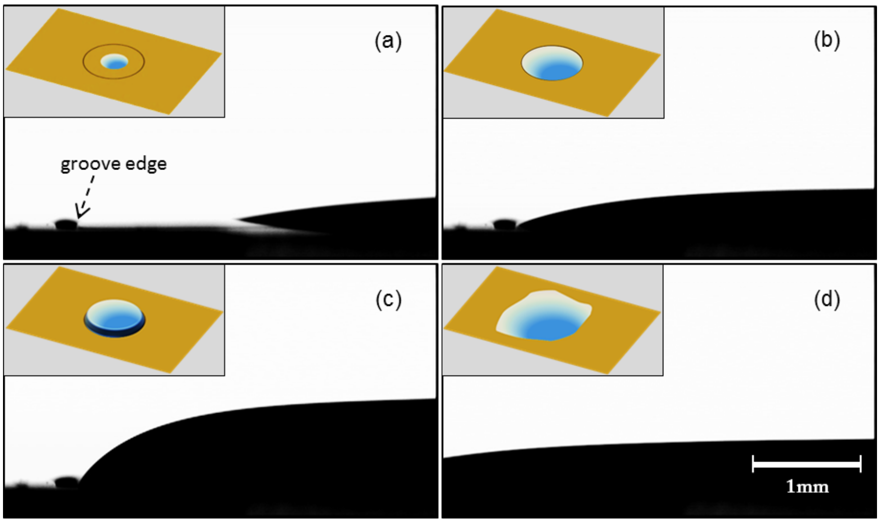

FIGURE 4.1: Side view images of the drop evolution, together with schematic representations; (a) advancing, (b) and (c) pinned at the groove's edge and (d) depinned contact line above a certain apparent contact angle. Fig. 1 of [81]. Courtesy of Y. Tsoumpas.

studied extensively [85–88], as it deeply affects many applications ranging from liquid transportation through microfluidic configurations [89, 90] and flows on surfaces patterned by posts or chemical features [91–93] to the suspension of water drops from pillars [94], not to mention its relation with contact angle hysteresis (for a review see [95]). In general, Gibbs' criterion (or inequality) is considered as a simple static relation, which reflects on a range of equilibrium angles that the contact line can adopt at a sharp edge,

$$\theta_{\text{eq}} \leq \theta_{\text{app}} \leq (\pi - \alpha) + \theta_{\text{eq}}. \tag{4.1}$$

Note that θ_{eq} is the equilibrium contact angle (or Young's angle) and α measures the downward slope of the surface discontinuity, see Fig. 4.2. There, we sketch the apparent pinning process of the contact line region on an edge: (1) the Young condition stipulates that the droplet has a contact angle θ_{eq}, and as it advances, (2) it meets the edge with the same contact angle θ_{eq}. (3) At the edge, when the droplet is pinned, the apparent contact angle θ_{app} can take any value, see Eq. (4.1), and in particular, depinning occurs when the apparent contact angle exceeds a critical value θ_{cr},

$$\theta_{\mathrm{cr}} = \theta_{\mathrm{eq}} + (\pi - \alpha), \tag{4.2}$$

i.e. when $\theta_{\mathrm{app}} > \theta_{\mathrm{cr}}$. (4) After depinning, the droplet creeps down the slope with the equilibrium angle θ_{eq}.

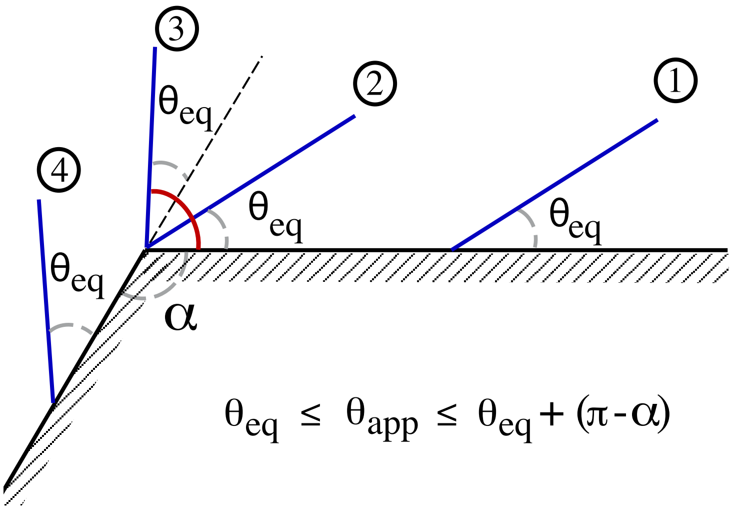

FIGURE 4.2: Sketch of the Gibbs' criterion.

Dynamic cases have been studied as well in terms of contact line relaxation concerning post-depinning times [96]. Evaporation, for instance, has been shown experimentally to trigger significant apparent contact angles, even for quasi-static drops of completely wetting liquids [97]. From the theoretical point of view, evaporation-induced contact angles have also been predicted on the basis of lubrication-type models [98–100]. In what follows, we present a model of how this evaporation-induced angle can affect the critical angle for depinning, corroborate the experimental findings and provide a simple generalization of the Gibbs' criterion, Eq. (4.1), that holds out of equilibrium.

4.2 Model and numerical approach

We start first describing how to model a substrate. One approach to real (i.e., non-idealized) substrates is to consider the limit of random heterogeneities [101–105].

Another approach focuses on the effect of individual well-defined defects [104, 106–108]. Recently, the latter approach was extended to study the depinning dynamics of drops on substrates with a periodic array of precisely specified chemical defects [109–111]. The approach employs a thin film evolution equation with a spatially modulated disjoining pressure and enables one to (i) study the depinning transition employing tools from dynamical systems theory and bifurcation theory, and (ii) investigate the dynamics of the stick-slip motion that occurs after depinning on substrates with many defects.

4.2.1 Lubrication equation

The partial differential equation governing the time evolution of the profile of a thin film of non-volatile liquid on a chemically structured substrate was discussed in depth in the 2d case in refs. [57, 109] and adapted to the 3d case in ref. [111, 112].

In the literature one finds two different ways of counting spatial dimensions in the problem at hand. On the one hand, focusing on the mathematical structure of Eq. (4.3) one distinguishes between one-dimensional (h depends on x only) and two-dimensional (h depends on x and y) cases. On the other hand, one may count the physical dimensions and refer to the situation where the film thickness depends only on x [depends on (x, y)] as the two-dimensional (2d) case [three-dimensional (3d) case]. Here we follow the latter convention.

The treatment of evaporating films and drops is reviewed in [113]. Here we combine the two approaches with the technique of studying steady evaporating droplets by imposing an influx that equals the loss by evaporation [114].

Briefly, we consider a layer or drop of volatile partially wetting (with a small equilibrium contact angle) or wetting liquid on a modulated two-dimensional solid substrate (see sketch in Fig. 4.3). The height of the film surface $h(x, t)$ and the substrate profile are both measured from $z = 0$. This implies that the local film thickness is $\phi(x, t) = h(x, t) - \xi(x) \geq 0$, i.e., it corresponds to the difference between local absolute height of the free surface h and the absolute substrate position ξ. The dynamical model is written in terms of $\phi(x, t)$.

Long-wave theory allows us to derive an evolution equation for the layer thickness profile $\phi(x, t)$ directly from the Navier-Stokes and continuity equations [34, 39]. We use no-slip and no penetration boundary conditions at the substrate, and the

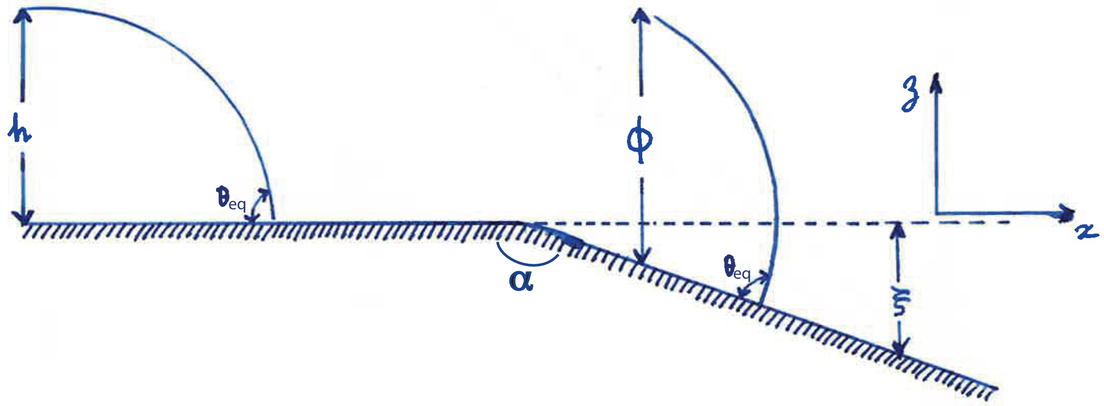

FIGURE 4.3: Sketch of the problem: $\theta_{\rm eq}$ is the contact angle, ϕ the layer thickness, $h(x)$ the film profile height, ξ the absolute substrate position and α the inclination angle.

equilibrium of tangential and normal stresses at the free surface. The wettability properties are incorporated as a disjoining pressure [38, 39]. Without lateral body force in the x-direction we obtain the non-dimensional equation

$$\partial_t\phi = -\partial_x\left\{Q\partial_x\left(\partial_{xx}(\phi+\xi)+\Pi\right)\right\} + \frac{E}{K+\phi}\left\{\partial_{xx}(\phi+\xi)+\Pi+\mu\right\} + q(x), \quad (4.3)$$

where we used $\phi(x,t) = h(x,t) - \xi(x)$[1]. The overall form of Eq. (4.3) corresponds to a combination of equations used in refs. [116] (substrate topography), [114] (voltile liquid with influx), and [117–119] (evaporation models). The mobility function $Q(\phi) \equiv \phi^3/3$ corresponds to a parabolic velocity profile in a no-slip model (Poiseuille flow). Capillarity is represented by $\partial_{xx}h = \partial_{xx}(\phi+\xi)$ (Laplace pressure). The substrate topography is incorporated via a z-independent modulation in order to focus on groove-like defects. Of the different functional forms for Π found in the literature [38, 120], many allow for the presence of a precursor film of thickness 1-10 nm on a 'dry' substrate and these are used to describe partial wetting. In this way 'true' film rupture in dewetting and the stress singularity at the moving contact line are avoided. We first look at a wetting situation and

[1]The scaling is based on the Hamaker constant A quantifying the effective attraction of liquid molecules by the substrate, and on the superheat ΔT driving evaporation, see [99] for details. The vertical (i.e. film thickness) scale is defined by the thickness of the ultra-thin film in equilibrium with the vapour, i.e. $h_f = (AT_{\rm sat}/\rho\mathcal{L}\Delta T)^{1/3}$, where $T_{\rm sat}$ is the saturation temperature, ρ is the liquid density, and $\mathcal{L}$ is the latent heat. Defining a molecular length scale by $a = \sqrt{A/\gamma}$, in which γ is the surface tension, the horizontal length scale is given by $[x] = \epsilon^{-1}h_f$, where $\epsilon = \sqrt{3}a/h_f \ll 1$ is a parameter whose smallness underlies both the lubrication approximation and the continuum assumption. E and K are the evaporation number and the dimensionless kinetic resistance, defined by $E = \nu\,\lambda T_{\rm sat}/3(a\,\mathcal{L}\,\rho)^2$ and $K = \lambda T_{\rm sat}^2/L_{ww}\,\mathcal{L}^2 h_f$, where ν stands for the liquid dynamic viscosity, λ for its thermal conductivity, and L_{ww} a phenomenological coefficient usually estimated by kinetic theory (see e.g. [115]).

only incorporate destabilizing long-range apolar van der Waals interactions, in a setting similar to [114] (cf. [38]), leading to the dimensionless disjoining pressure

$$\Pi(\phi) = -\frac{A}{\phi^3} \tag{4.4}$$

where the parameter $A < 0$ is set to one, i.e., is absorbed into the scaling. A option for partially wetting liquid that we might use, is the combination of $-1/\phi^3$ and $1/\phi^6$ terms.

For the influx $q(x)$ we use a normalised Gaussian

$$q(x) = q_0 \frac{2}{\sigma\sqrt{\pi}} \exp\left[-\frac{x^2}{\sigma^2}\right] \tag{4.5}$$

with $q_0 = \int_0^\infty q(x)dx$ being the total influx through the substrate. If the droplet size is large as compared to the width σ, the results do not depend on the particular choice of σ.

Here, the substrate modulation corresponds to a 'smooth' corner, i.e., part of a groove. It is described by a profile

$$\partial_x \xi = \frac{\alpha}{2}\left[1 + \tanh\left(\frac{x-c}{\omega}\right)\right] \tag{4.6}$$

where c is the position of the step measured from the centre of the drop. We take the domain size D sufficiently large to avoid interactions of the drop and the wall. The resulting profiles $\xi(x)$ are shown for an angle $\alpha < 0$ [$\alpha > 0$] indicates a downwards bend (groove) [upwards bend (ridge)], see Fig. 4.4. The bend is 'smooth' on a typical length scale ω. The resulting substrate variation must take place on length scales much larger than the physical film thickness for consistency with the long-wave approximation [121]. Note that the chemical potential in the evaporative flux is μ and that the long-wave scaling used here implies that the dimensionless contact angle and chemical potential μ may be of order one, i.e. $\mu = -1$.

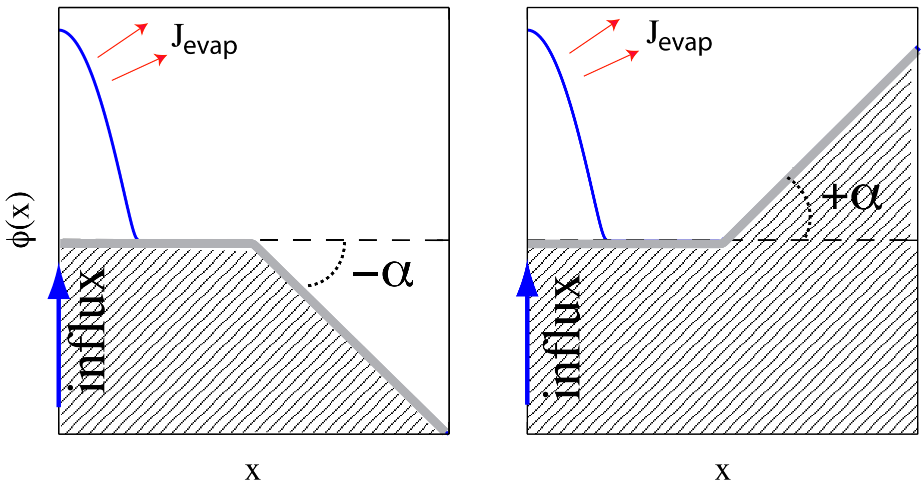

FIGURE 4.4: Sketch of a droplet sitting on an groove, left panel, and ridge, right panel. Note the liquid influx at the centre of the droplet to balance the evaporation.

4.2.2 Numerical schemes and parameters

For the continuation it is beneficial to use $\phi = h - \xi$ as the field to be calculated. We employ Eq. (4.3) i.e., the steady states in 1-d are given by

$$0 = -\partial_x \left\{ Q \partial_x \left(\partial_{xx}(\phi + \xi) + \Pi \right) \right\} + \frac{E}{K + \phi} \left\{ \partial_{xx}(\phi + \xi) + \Pi + \mu \right\} + q(x) \tag{4.7}$$

i.e.,

$$\begin{aligned} \partial_{xxxx}\phi = -\frac{\partial_x Q}{Q} \partial_{xxx}\phi - \frac{1}{Q} \partial_x \left\{ Q \partial_{xxx}\xi \right\} - \frac{1}{Q} \partial_x \left\{ Q \partial_x \Pi \right\} + \\ + \frac{E}{Q(K + \phi)} \left\{ \partial_{xx}(\phi + \xi) + \Pi + \mu \right\} + \frac{q(x)}{Q}. \end{aligned} \tag{4.8}$$

The chosen boundary conditions are,

symmetry at $x = 0$, i.e.

$$\phi_x(0) = 0 \tag{4.9}$$

$$\phi_{xxx}(0) = 0, \tag{4.10}$$

while at $x = D \gg c$, we impose a flat equilibrium microfilm, i.e.

$$\phi(D) = 1 \tag{4.11}$$

$$\phi_x(D) = 0. \tag{4.12}$$

This 4-th order problem is solved using the previously described continuation techniques in Section 3.1, using typical values $E = 0.124$, $K = 5.74$ and $\mu = -1$ as a reference case [99]. Some typical results are presented in Fig. 4.5 for $\alpha = -0.5$ and -5. There we see on panel (a) the solution L_2-norm of the layer thickness

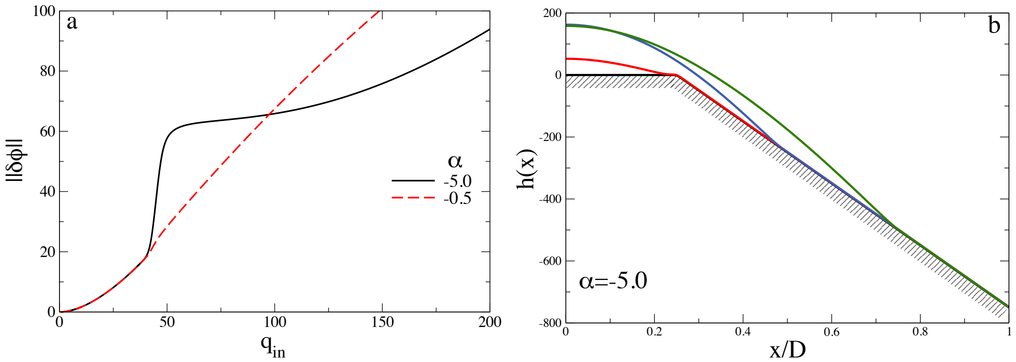

FIGURE 4.5: Shown are drop characteristics for steady droplets of volatile completely wetting liquids with influx q_{in} that sit on a chemically homogeneous substrate with a negative bend at $x = c = 50$ (overall domain $D = 200$, bend width $\omega = 1.0$, source width $\sigma = 0.1$) (a) L_2-norm of layer thickness $\phi(x)$ in dependence of q_{in}. (b) Selected steady film height profiles (see text) for various influxes on the substrate with a bend (solid black line).

$\phi(x)$ in dependence of the influx q_{in} for $\alpha = -0.5$ and -5.0. On panel (b) we show selected steady film height profiles (solid colour lines) for various influxes [$q_{\text{in}} =$ 25 (red solid line), 50 (blue solid line) and 75 (green solid line)] on the substrate with a bend (solid black line).

4.3 Results

Next we study a drop of volatile liquid on a smooth solid substrate that has a single bend of angle α for three cases $\alpha = 0$, $\alpha < 0$ and $\alpha > 0$. Using the overall influx as a control parameter we find following results:

4.3.1 Drop interacting with a flat horizontal plate $\alpha = 0$

For a horizontal substrate, i.e. $\alpha = 0$, we see that when the influx q_{in} increases, the L_2-norm of the layer thickness $\phi(x)$ and the volume increase monotonously, see Fig. 4.6. This case has been studied thoroughly in e.g. [114].

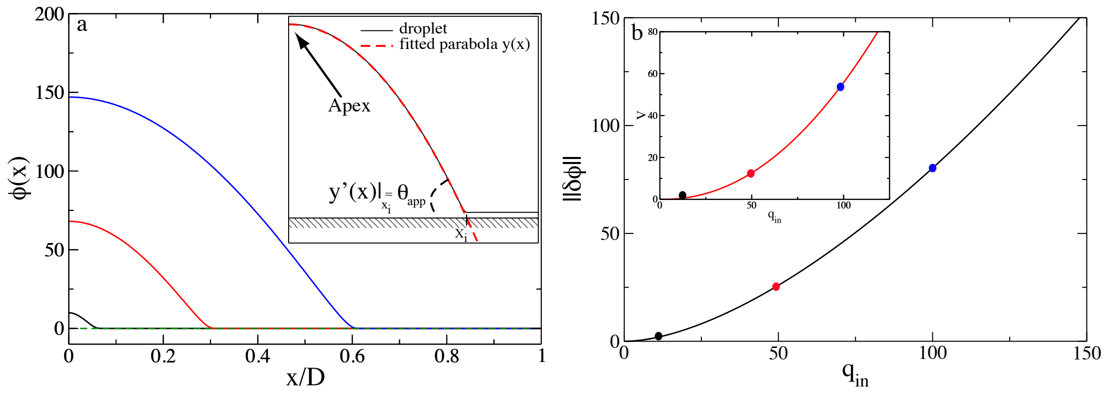

FIGURE 4.6: In the left panel are shown three steady droplets for different influxes $q_{\text{in}} = 10, 50$ and 100. In the inset a sketch of the apparent contact angle θ_{app}. On the right panel we show the solution L_2-norm of the layer thickness $\phi(x)$ in dependence of the influx q_{in}. In the inset we show droplet volume V in dependence of the influx q_{in}. The coloured dots indicate the influx for the droplets shown in the left panel.

The apparent contact angle θ_{app} is defined as $\theta_{\text{app}} = y'(x_i)$, where $y'(x)$ is the slope of the parabola used to fit the droplet shape by using the apex curvature – $h''(0)$ and $h(0)$ – and x_i is the intersection: (a) with the substrate $\xi(x)$ at $x_i = x_s$ and / or (b) with the horizontal line $y = 0$ at $x_i = x_0$, see inset in panel (a) of Fig. 4.6.

4.3.2 Drop interacting with a single substrate bend $\alpha < 0$

We now study the substrate with a bend, i.e. for $\alpha < 0$. In the left panel of Fig. 4.7 we show the L_2-norm of the layer thickness $\phi(x)$ in dependence of the influx for $\alpha = -5.0$ (black solid line) and for $\alpha = 0.0$ (red dashed line). For small influx, there are small drops with the contact line region left of the bend. The drop volume changes monotonously with influx, similar to the case without bend described before, see Fig. 4.6. When the contact line region reaches the bend region, the norm increases strongly for nearly constant influx q_c (blue dashed line), what indicates that the contact line is pinned. We also see that for the case of $\alpha = 0$, the norm continues increasing smoothly (red dashed line). Further increase of q_{in} results again in a slower increase of the norm as the contact line region is again depinned and creeps down the slope. The numbers correspond to the depicted droplets in the right panel. There we show four different droplet profiles for $q_{\text{in}} = 25, 50, 75$ and 100, respectively.

In Fig. 4.8 we show apparent contact angles θ_{app} for different inclination angles α, $\alpha \in [0, -0.01, -0.1, -0.5, -0.75, -1.0, -2.0]$, as a function of the contact line

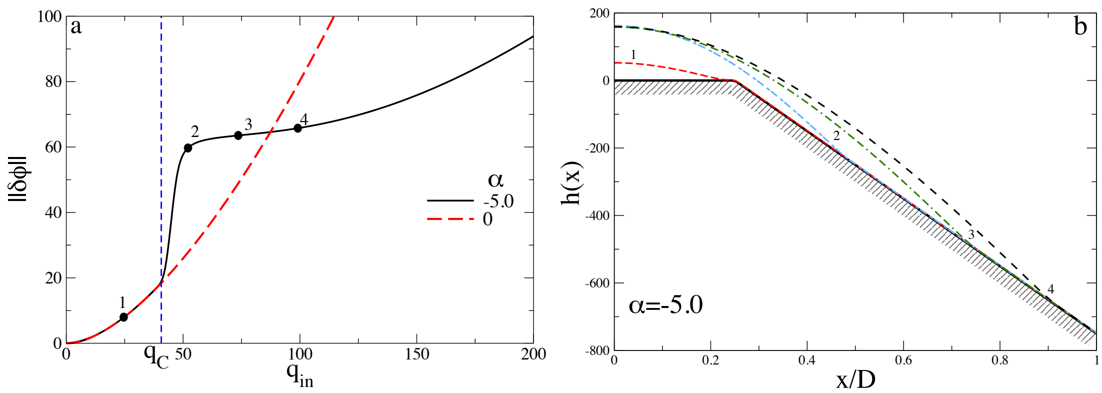

FIGURE 4.7: Left panel: Shown is the L_2-norm of the layer thickness $\phi(x)$ in dependence of the influx for $\alpha = -5.0$ (black solid line) and for $\alpha = 0.0$ (red dashed line). Numbers correspond to the shown profiles in the right panel. Note the strong increase of the L_2-norm at q_c when the contact line region reaches the bend and it gets pinned. Right panel: droplet profiles for $q_{\text{in}} = 25$ (1) ,50 (2) ,75 (3) and 100 (4).

position x_0. x_0 is the intersection of the substrate $\xi(x)$ and the parabola used to fit the droplet shape by using the apex curvature. We observe that as the droplet edge reaches the bend region and starts to interact with it, it gets pinned and the apparent contact angle θ_{app} increases. In panel (a) we see the apparent contact angle with respect to $y = 0$, while on panel (b), θ_{app} is shown with respect to the substrate $\xi(x)$. In the latter, it is clearly shown how θ_{app} increases at the bend region and then, after depinning, θ_{app} tends back to the previous value. Note that the apparent contact angle increases as the bend angle gets larger.

We also investigate how the smoothness of the bend affects the apparent contact angle θ_{app}. In Fig. 4.9 we plot for a fixed bend angle of $\alpha = -1.0$ the apparent contact angle for different values of w, with $w \in [3.5, 4, 5, 7, 8, 10]$. We observe that for larger values of the width of the bend region w, the transition is smoother and that the apparent contact angle decreases, see panels (a) and (b). We infer that the pinning is not as strong at the corner as the width of the bend region w increases (or becomes smoother), see left panel of Fig. 4.10, where we plot the apparent contact angle with respect to the substrate for three different bend widths, $w = [5, 50, 100]$. Note how the apparent contact angle strongly decreases for larger values of w. In the right panel, we plot the slope of the substrate ξ' (same colour code as in left panel). We see that, the larger the width w, the smoother the slope of $\xi(x)$ becomes. This translates in less pinnng of the contact line region of the droplet, and therefore a smaller apparent contact angle.

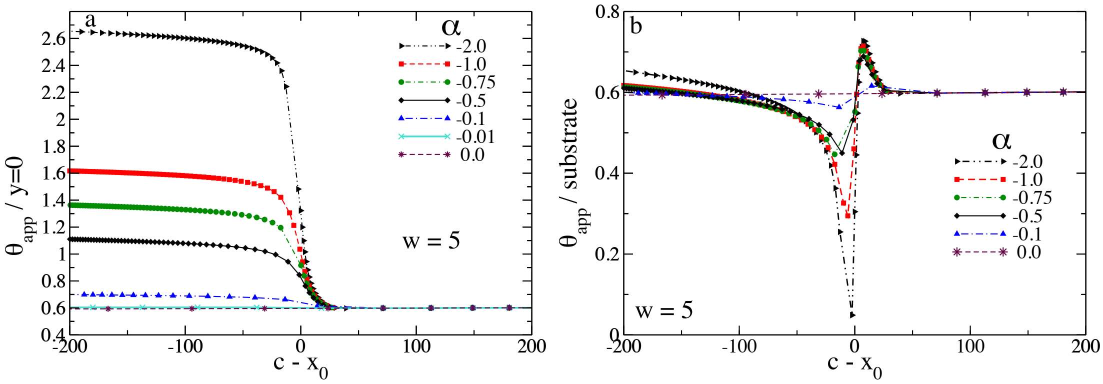

FIGURE 4.8: Shown are apparent contact angles θ_{app} for different inclination angles α as shown in the legend as a function of the contact line position x_0 (x_0 is the intersection of the substrate $\xi(x)$ and the parabola used to fit the droplet shape by using the apex curvature). Overall domain $D = 1000$, bend located at $c = 400$, bend width $w = 5.0$, source width $\sigma = 10$, plot respect to bend position c. (a) θ_{app} respect to the horizontal, i.e. $y = 0$. As the drop approaches the bend, θ_{app} increases. (b) θ_{app} respect to the substrate, i.e. $y = \xi(x)$. As the drop approaches the bend, θ_{app} increases and once passing the transition width, it tends to the apparent contact angle before the bend.

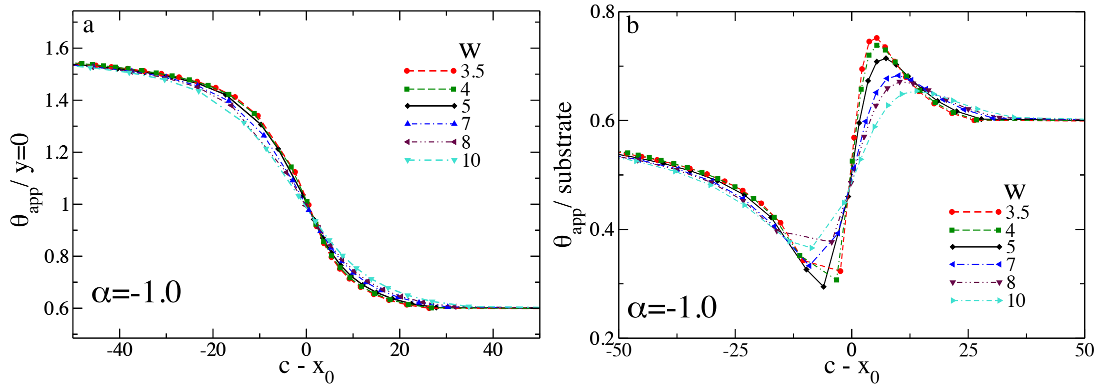

FIGURE 4.9: Shown are apparent contact angles θ_{app} for a fixed inclination angle $\alpha = -1.0$ for different bend widths w as shown in the legends for the contact line position x_0 (x_0 is the intersection of the substrate $\xi(x)$ and the parabola used to fit the droplet shape by using the apex curvature). Overall domain $D = 1000$, bend located at $c = 400$, source width $\sigma = 10$, plot respect to bend position c. (a) θ_{app} respect to the horizontal, i.e. $y = 0$. (b) θ_{app} respect to the substrate, i.e. $y = \xi(x)$.

To investigate changes in the system, e.g. how the apparent contact angle θ_{app} for a fixed inclination angle α changes, we perform continuation on the evaporation number E and the kinetic resistance K, see Fig. 4.11 and Fig. 4.12.

In the left panel of Fig. 4.11 we plot droplet volume V over influx $f = q_{\text{in}}/\sigma\sqrt{2/\pi}$. It is shown how as the evaporation number E increases, more influx $f = q_{\text{in}}/\sigma\sqrt{2/\pi}$ is needed to generate a sufficient large droplet which can reach the bend region

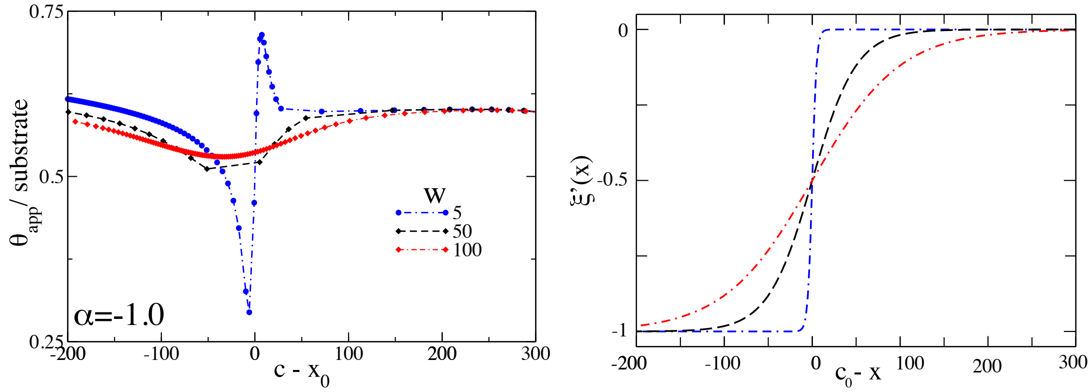

FIGURE 4.10: Shown are: (a) Apparent contact angles θ_{app} for a fixed inclination angle $\alpha = -1.0$ for different bend widths $w = 5, 50$ and 100, for the contact line position x_0 (x_0 is the intersection of the substrate $\xi(x)$ and the parabola used to fit the droplet by using the apex curvature). (b) Slope of $\xi(x)$ - same colour coding as in panel (a). Overall domain $D = 1000$, bend located at $c = 400$, source width $\sigma = 10$, plot respect to bend position c.

and get pinned, when the volume starts to increase strongly. In the right panel we plot droplet volume V over the kinetic resistance number K. Here, as K increases, the droplet reaches the bend region for a smaller influx $f = q_{\text{in}}/\sigma\sqrt{2/\pi}$.

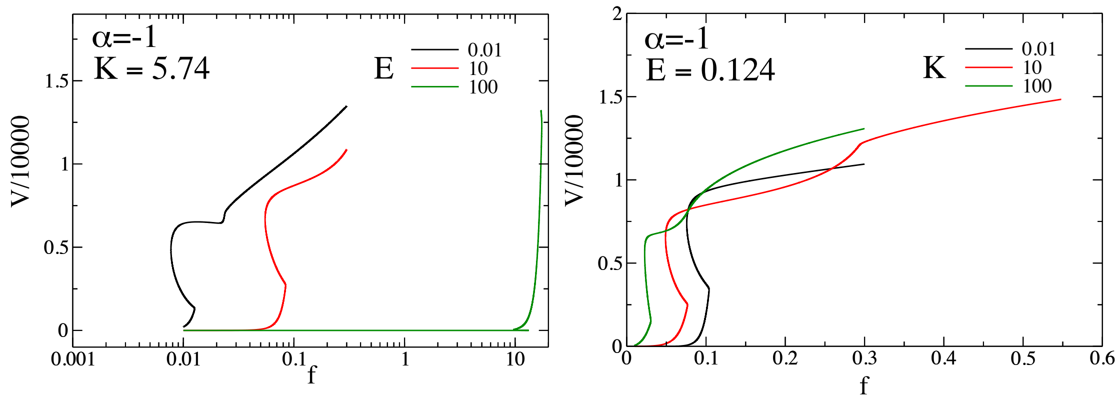

FIGURE 4.11: Shown is drop volume V over influx $f = q_{\text{in}}/\sigma\sqrt{2/\pi}$ for (left) different evaporation numbers $E = 0.01, 10, 100$ and kinetic resistance number $K = 5.74$, and (right) different kinetic resistance numbers $K = 0.01, 10, 100$ and evaporation number $E = 0.124$. In both cases one has overall domain $D = 1000$, bend position at $c = 400$, bend width $\omega = 5.0$, source width $\sigma = 10$.

In Fig. 4.12, left panel, we observe the influence of evaporation on the apparent contact angle θ_{app}. We plot the apparent contact angle as a function of the contact line position for 5 different values of E spanning 4 orders of magnitude, i.e. for $E = [0.01, 0.1.1, 10, 100]$ and a fixed kinetic resistance number $K = 5.74$ for a fixed bend angle $\alpha = -1.0$. We see, that as E increases, the apparent contact angle increases as well. In the right panel of Fig. 4.12 we plot the values of θ_{app}

for the evaporation numbers used, i.e. $E = [0.01, 0.1.1, 10, 100]$. We see that the apparent contact angle increases following a power law of $\theta_{\text{app}} \propto E^{1/4}$. We also

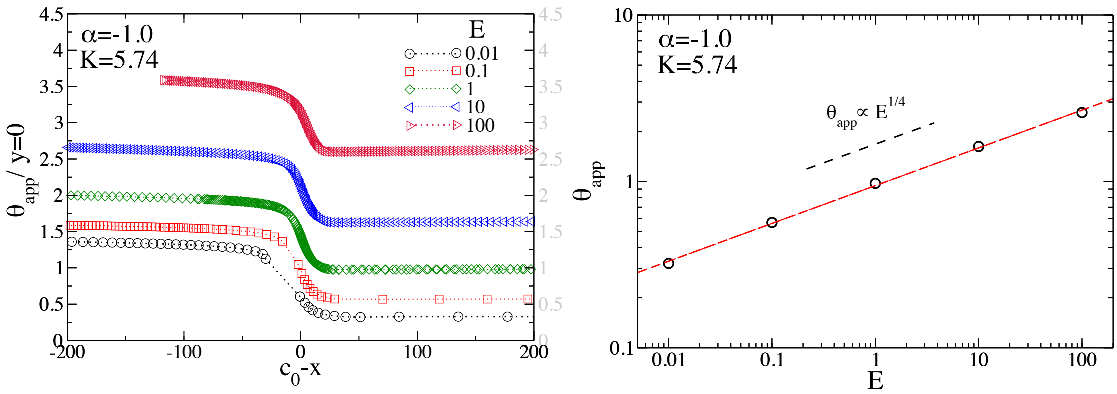

FIGURE 4.12: Left panel: Shown are apparent contact angles θ_{app} for a fixed inclination angle $\alpha = -1.0$ with respect to the horizontal $y = 0$ for the contact line position $\Delta x = c - x_0$ for different evaporation numbers E = 0.01, 0.1, 1, 10 and 100 as shown in the legend. Overall domain $D = 1000$, bend position at $c = 400$, bend width $\omega = 5.0$, source width $\sigma = 10$ and kinetic resistance number $K = 5.74$. Right panel: Shown is θ_{app} vs. E for $\alpha = -1$ and $K = 5.74$. As the evaporation number E increases, the apparent contact angle increases following a power law of $\theta_{\text{app}} \propto E^{1/4}$.

observe the occurrence of a pair of saddle nodes for different values of evaporation number E (fixed kinetic resistance number K) and for different kinetic number K (fixed evaporation number E), in order to investigate the saddle nodes, we re-write Eq. (4.8) to :

$$0 = -\partial_x \left\{ Q\partial_x \left(\gamma\partial_{xx}(\phi + \xi) + \Pi \right) \right\} + \frac{\beta}{1 + \frac{\phi}{K}} \left(\gamma\partial_{xx}(\phi + \xi) + \Pi + \mu \right) + q(x), \quad (4.13)$$

where $\beta = E/K$ for the sake of comparison with the model for $K \to \infty$, see Eq. (4.8). Now we have two independent parameters, β and K. We are able to compute a fold-continuation to generate a phase diagram spanned in the $(K - q_{\text{in}})$—space for a fixed value of $\beta = 0.02$, and varying K and the the inlfux $f = q_{\text{in}}/\sigma\sqrt{2/\pi}$, see Fig. 4.13.

We observe in the phase space, see left panel of Fig. 4.13, that as the kinetic resistance number K increases the pair of saddle nodes annihilate for values of K larger than 3000 and for values of K smaller than 0.0001. A clear hysteresis is present. In the limit of large K, after the annihilation of the saddle nodes, the model proposed by [114] is retrieved, see Fig. 4.8. On the right panel, we plot the apex over $f = q_{\text{in}}/\sigma\sqrt{2/\pi}$ for different kinetic resistance numbers K as show in the legend. Note that for $K = 1.10\text{x}10^6$ no saddle nodes are present anymore.

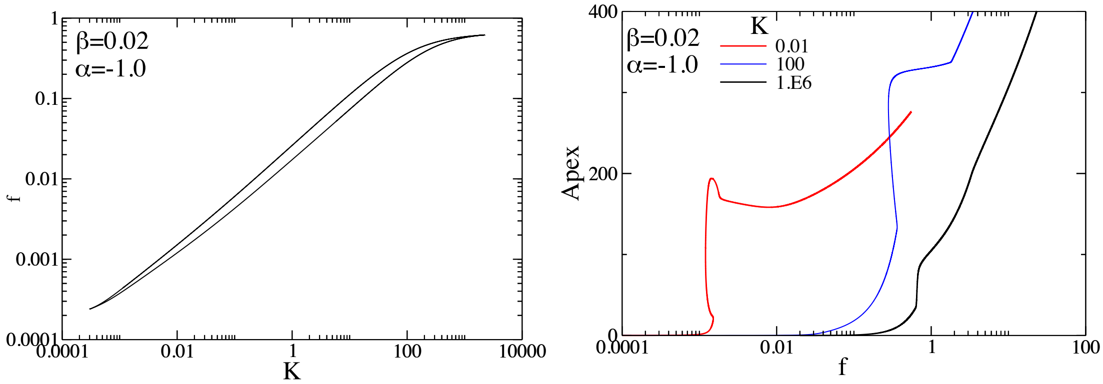

FIGURE 4.13: Shown is: Left panel $f = q_{\text{in}}/\sigma\sqrt{2/\pi}$ vs. kinetic resistance number K diagram for fixed $\beta = 0.02$ (which is E/K, for $E = 0.124$ and $K = 5.74$) and fixed bend inclination angle $\alpha = -1.0$ As K increases the pair of saddle nodes annihilate for values of K larger than 3000 and for values of K smaller than 0.0001. A clear hysteresis is present. Right panel: Apex over $f = q_{\text{in}}/\sigma\sqrt{2/\pi}$ for different kinectic resistance numbers as show in the legend. Note that for $K = 1.10\text{x}10^6$ no more saddle nodes are present.

Next, we investigate the pinning process, i.e. when the contact line region and the bend region start to interact. In panel (a) Fig. 4.14 we present the results for the apex of the droplet versus the influx $f = q_{\text{in}}/\sigma\sqrt{2/\pi}$ for different values of E, instead of the volume V as we have seen in panel (a) of Fig. 4.12. As it was expected, we see that as E increases, more influx is needed to generate a sufficiently large droplet which can reach the bend region and get pinned, where the apex increases strongly. Instead of the volume, we will use the apex of the droplet. We will focus on the case of a fixed evaporation number $E = 0.01$, fixed kinetic resistance number $K = 5.74$ and fixed bend inclination angle $\alpha = -1$. Panel (a) shows the L_2-norm as a function of the influx $f = q_{\text{in}}/\sigma\sqrt{2/\pi}$. In panel (b) we plot the droplet apex in dependence of the influx q_{in}. We observe that there are multivalued solutions for a fixed values of the influx, e.g. $f = q_{\text{in}}/\sigma\sqrt{2/\pi} = 0.0125$. These three profiles correspond to: (1) a droplet before the bend region, (2) a droplet pinned at the sharp edge and (3) a droplet after the bend region creeping down the slope. In panel (c) we plot these three profiles overlapped with the corresponding evaporation profiles. In panels (d), (e) and (f) we show them individually. We observe that the evaporation rises close to the contact line position, i.e. where the film is of the order of the precursor film height. In panel (f), where the droplet passed over the bend region and creeps down the slope, a "shoulder"-like structure is observed in the evaporation at the bend position $c = 400$. Note, that as the influx $f = q_{\text{in}}/\sigma\sqrt{2/\pi}$ is the same for the three cases, the integrals of the evaporation flux J_{evap} over the domain size D coincide.

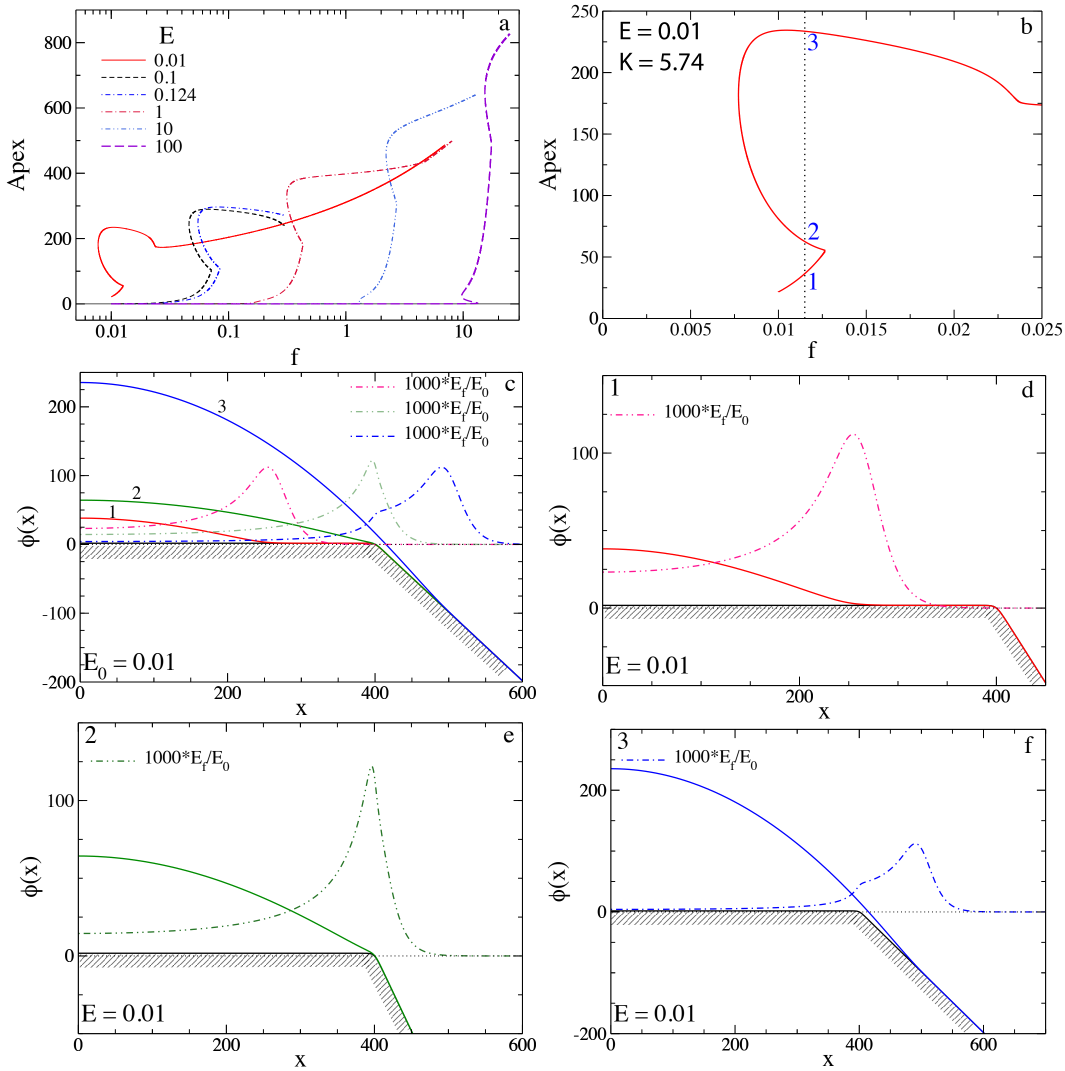

FIGURE 4.14: Shown are: (a) Apex over $f = q_{\text{in}}/\sigma\sqrt{2/\pi}$ for different evaporation numbers $E = 0.01, 0.1, 0.124, 1, 10, 100$ with overall domain $D = 1000$, bend position at $c = 400$, bend width $\omega = 5.0$, source width $\sigma = 10$, kinetic resistance number $K = 5.74$ and bend inclination $\alpha = -1.0$. (b) Apex over $f = q_{\text{in}}/\sigma\sqrt{2/\pi}$ for fixed evaporation number $E = 0.01$, kinetic resistance number $K = 5.74$ and bend inclination angle $\alpha = -1.0$. Numbers 1, 2 and 3 indicate multivalued solutions for a fixed $f = q_{\text{in}}/\sigma\sqrt{2/\pi} = 0.0125$. The corresponding droplet profiles and evaporation profiles are depicted in panel (c) overlapped, and in (d), (e) and (f) individually. Note that the evaporation is scaled in order by a factor 1000 to be visible in the graph. The evaporation rises close to the contact line position, i.e. where the film is of the order of the precursor film height. In panel (f), where the droplet passed over the bend, a "shoulder"-like structure is observed in the evaporation at the bend position $c = 400$.

We have previously introduced the depinning condition, i.e. when the apparent angle θ_{app} is larger then θ_{cr} depinning occurs. In the previous sections we have seen, that there exists an evaporation induced angle θ_{ev} adding up to the geometrical bend angle α. This suggests that a simple modification can be introduced to Gibbs' criterion, where the equilibrium angle θ_{eq} (in the case of a complete wetting liquid $\theta_{\text{eq}} = 0$, as we have been studying) is replaced by the evaporation induced angle θ_{ev}, i.e. the new critical angle is

$$\theta_{\text{cr}} = \theta_{\text{ev}} + \pi - \alpha. \tag{4.14}$$

This is consistent with the experimental results and proposed Gibbs' criterion modification for complete wetting liquid presented in [81].

4.3.3 Drop interacting with a single substrate bend $\alpha > 0$

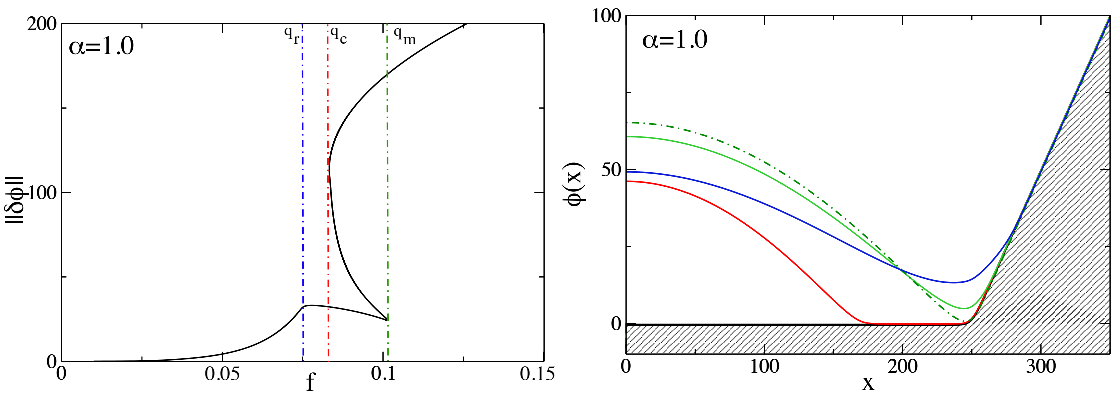

FIGURE 4.15: Left panel: Shown is the L_2-norm of the layer thickness ϕ over influx $f = q_{\text{in}}/\sigma\sqrt{2/\pi}$ for fixed evaporation number $E = 0.01$, kinetic resistance number $K = 5.74$ and ridge inclination angle $\alpha = 1.0$. Ridge is located at $c = 250$ and ridge width is $w = 5$. The Domain size is D = 500. Right panel: layer thickness profiles for different influxes: 0.06 (red solid line), 0.075 (dashed green line) – corresponds to the start of the ridge, 0.08 (solid green line) and 0.086 (solid blue line).

We now study the substrate with a ridge, i.e. for $\alpha > 0$. In the left panel of Fig. 4.15 we show the L_2-norm of the layer thickness $\phi(x)$ in dependence of the influx for $\alpha = 1$ (black solid line). For small influx, there are small drops with the contact line region left of the ridge. The drop norm (volume) changes monotonously with influx, similar to the case without bend and for a negative bend angle described before, see Fig. 4.6 and Fig. 4.8. When the contact line region reaches the ridge region, i.e. at $f = q_r$, the norm starts to decrease monotonously until q_m. Then it starts to increase strongly for nearly constant influx q_c (red dashed line). Further increase of f results again in a slower increase of the norm as the contact line region creeping up the slope. In the right panel of Fig. 4.15 we show layer thickness profiles for different influxes: at $f = 0.06$ (red solid line) for a thickness profile left of the ridge, at $f = 0.075$ (dashed green line), which corresponds to a profile at the start of the ridge. We notice that a further increase in the influx, results in a smaller L_2-norm of the droplet: the profile at influx $f = 0.08$ has a smaller apex (solid green line) and the contact line region starts to creep up the slope. A further increase in the influx $f = 0.086$ (solid blue line) results in a lower apex and the droplet creeping up the slope.

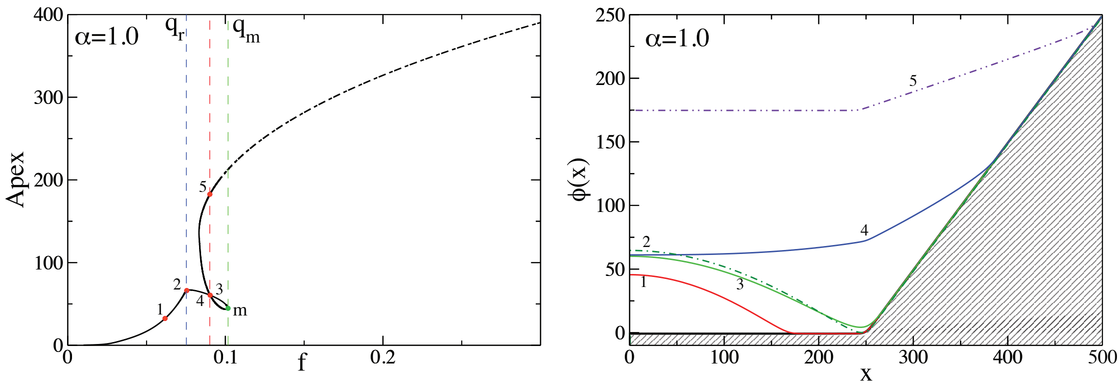

FIGURE 4.16: Left panel: Shown is the apex of the droplet over influx $f = q_{\text{in}}/\sigma\sqrt{2/\pi}$ for fixed evaporation number $E = 0.01$, kinetic resistance number $K = 5.74$ and ridge inclination angle $\alpha = 1.0$. Ridge is located at $c = 250$ and ridge width is $w = 5$. The numbers correspond to the profiles shown in the right panel. Note that the physical meaning solution is the solid black line (more details in the text).The Domain size is D = 500. Right panel: layer thickness profiles for different influxes as shown in the left panel.

In the left panel of Fig. 4.16 we plot the apex of the droplet in dependence of influx f. The behaviour is similar to the one described in Fig. 4.15, but plotting the apex gives us a better picture of what happens to the droplet: as the influx increases, the droplet is still left of the ridge (solution 1), and a further increase in f leads to the contact line region reaching the ridge region. As pointed out before, this is the same behaviour described for $\alpha < 0$. However in this case, the apex height starts to decrease while the contact line region starts to creep up the slope. We observe in Fig. 4.16 that the apex height reaches a minimum value and increases again. The region between q_r and q_m is multivalued in both quantities, i.e. in the influx f and in the apex height. We observe this multivalued region in the influx, e.g. solution numbers 3, 4 and 5 for $f = 0.09$, where solutions 3 and 4 have the same apex value. Note that solution 5 has reached the domain boundary and corresponds to another physical problem. Solution labeled m corresponds to the influx value q_m as indicated in the figure and is discussed in the next paragraph.

In Fig. 4.17 we detail solutions 2,3 and 4 and overlapped we plot the evaporative flux j_{evap}. We include additionally in panel (c) the thickness profile for the influx

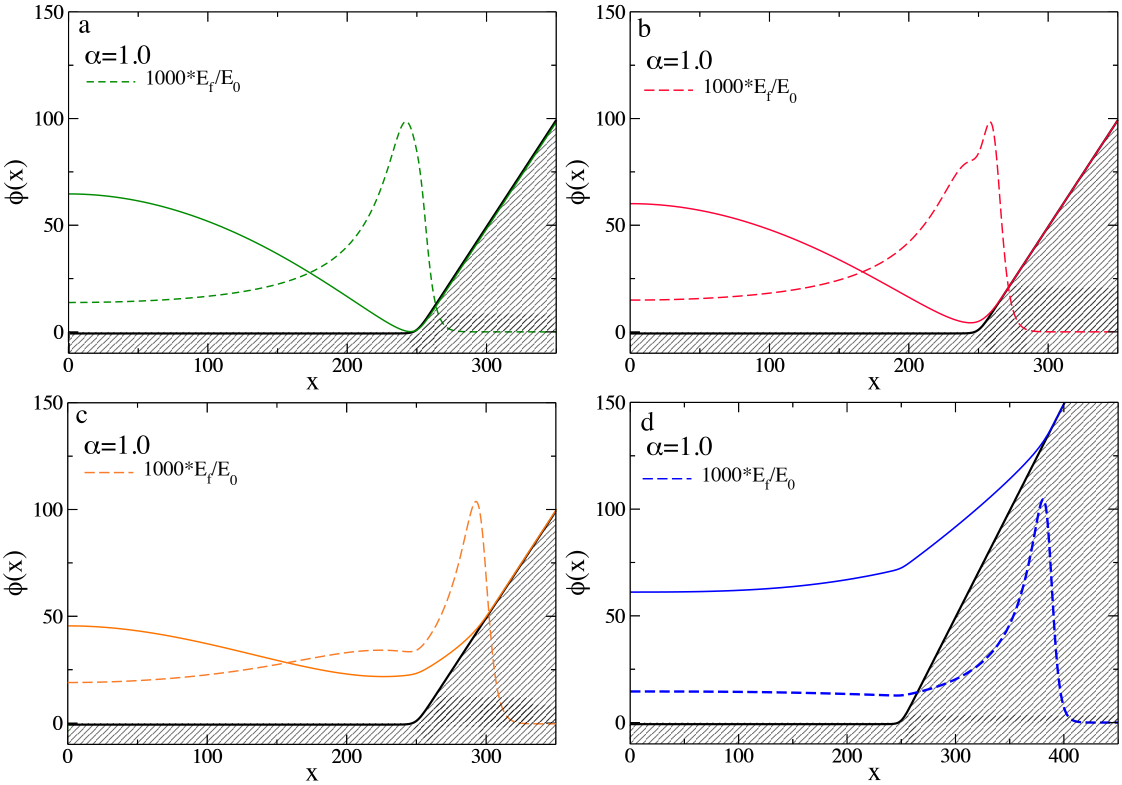

FIGURE 4.17: Shown are film thickness profiles and evaporation profiles for fixed evaporation number $E = 0.01$, kinetic resistance number $K = 5.74$, ridge inclination angle $\alpha = 1.0$ and ridge located at $c = 250$. Domain size is $D = 500$. Panel (a) corresponds to an influx value of $f = q_r \approx 0.075$ where the contact line region reaches the ridge. In panel (b) we show for $f = 0.09$ a thickness profile creeping up the slope. Note the "shoulder"-like structure in the evaporation flux at the bend position $c = 250$. Panel (c) corresponds to an influx value q_m (see Fig. 4.16). Note that the "shoulder"-like structure decreases but it is still present at the ridge position $c = 250$. Panel (d) shows a thickness profile for $f = 0.09$ and same apex height as panel (b). Note that the film creeps further up the slope and that the evaporation profile has no "shoulder"-structure anymore, as the thickness has an almost constant, thick height left of the ridge. Note that the evaporation is scaled in order by a factor 1000 to be visible in the graph. The evaporation rises close to the contact line position, i.e. where the film is of the order of the precursor film height.

q_m. Panel (a) corresponds to an influx value of $f = q_r \approx 0.075$ where the contact line region reaches the ridge. In panel (b) we show for $f = 0.09$ a thickness profile creeping up the slope. Note the "shoulder"-like structure in the evaporation flux at the bend position $c = 250$. Panel (c) corresponds to an influx value q_m (see Fig. 4.16). Note that the "shoulder"-like structure decreases but it is still present at the ridge position $c = 250$. Finally, panel (d) shows a thickness profile for $f = 0.09$ and same apex height of the thickness profile as panel (b). Note that the film creeps further up the slope and that the evaporation profile has no "shoulder"-structure anymore, as the thickness has an almost constant, thick height left of the ridge. Note that the evaporation is scaled in order by a factor 1000 to be visible in the graph. The evaporation rises close to the contact line position, i.e. where the film is of the order of the precursor film height.

Chapter 5

Conclusions and outlook

> "All except one thing. There's something you should know before you leave."
>
> Rick Blaine

In the present Thesis we have on the one hand studied free surface driven liquid films, principally focusing on drawn menisci, where we have uncovered several interesting features. On the other hand, we have also addressed the pinning of volatile droplets of completely wetting liquids at sharp edges. In what follows, we summarise the main results:

In the first Chapters we have analysed a liquid film that is deposited from a liquid bath onto a flat moving plate that is inclined at a fixed angle α to the horizontal and is removed from the bath at a constant speed U. We have analysed a two-dimensional situation with a long-wave equation that is valid for small inclination angles of the plate and under the assumption that the longitudinal length scale of variations in the film thickness is much larger than the typical film thickness. The model equation used in most parts of our work includes the terms due to surface tension, the disjoining (or Derjaguin) pressure modelling wettability, the hydrostatic pressure and the lateral driving force due to gravity, and the dragging by the moving plate. To further illustrate a particular finding we have also considered the situation where an additional lateral Marangoni shear stress results from a linear temperature gradient along the substrate direction. Our main goal has been to analyse selected steady-state film thickness profiles that are related to collapsed or exponential snaking.

First, we have used centre manifold theory to rigorously derive the asymptotic boundary conditions on the side of the bath. In particular, we have obtained asymptotic expansions of solutions in the bath region, when $x \to \infty$. We found that in the absence of the temperature gradient, the asymptotic expansion for the film thickness, h, has the form $h \sim \sum_{n=-1}^{\infty} D_n x^{-n}$, where without loss of generality D_0 can be chosen to be zero (fixing the value of D_0 corresponds to breaking the translational invariance of solutions and allows selecting a unique solution from the infinite family of solutions that are obtained from each other by a shift along the x-axis). In the presence of the temperature gradient, this asymptotic expansion is not valid, but instead consists of terms proportional to x, $\log x$ and $x^{-m} \log^n x$, where m and n is a positive and a non-negative integer, respectively. Note that our systematically obtained sequence differs in part from the one employed in ref. [10].

Next, we have obtained numerical solutions of the steady-state equation and have analysed the behaviour of selected solutions as the plate velocity and the temperature gradient are changed. When changing the plate velocity, we observe that the bifurcation curves exhibit collapsed heteroclinic snaking when the plate inclination angle is larger than a certain critical value, namely, they oscillate around a certain limiting velocity value, U_∞, with an exponentially decreasing oscillation amplitude and a period that tends to some constant value. In contrast, when the plate inclination angle is smaller than the critical value, the bifurcation curve is monotonic and the velocity tends monotonically to U_∞. The solutions along these bifurcation curves are characterised by a foot-like structure that emerges from the meniscus and is preceded by a very thin precursor film further up the plate. The length of the foot increases continuously as one follows the bifurcation curve as it approaches U_∞. It is important to note that these solutions of diverging foot length do not converge to the Landau–Levich film solution at the same $U = U_\infty$. Indeed, the foot height at $U_\infty(\alpha)$ scales as $U^{1/2}$ while the Landau–Levich films scale as $U^{2/3}$. As expected, the results for the bifurcation curves that we here obtained with a precursor film model are similar to results obtained for such situations employing a slip model [18, 20]. The protruding foot structure has been observed in experiments, *e.g.*, in refs. [18, 19, 122] where even an unstable part of the snaking curve was tracked. However, the particular transition described here has not yet been experimentally studied. This is in part due to the fact that in an experiment with a transversal extension (fully three-dimensional system) transversal meniscus and contact line instabilities set in before the foot length can diverge. We believe that experiments in transversally confined geometries may allow one to approach the transition more closely. Experiments with driving temperature gradients exist as well but focus on other aspects of the solution structure like, for instance, various types of advancing shocks (travelling fronts) and transversal instabilities [123]. We are not aware of studies of static foot-like structures in systems with temperature gradients.

We further note that the described monotonic and non-monotonic divergence of foot length with increasing plate velocity may be seen as a dynamic equivalent of the equilibrium emptying transition described in ref. [77]. There, a meniscus in a tilted slit capillary develops a tongue (or foot) along the lower wall. Its length diverges at a critical slit width. In our case, the length of the foot diverges at a critical plate speed – monotonically below and oscillatory above a critical inclination angle. The former case may be seen as a continuous dynamic emptying transition with a close equilibrium equivalent. The latter may be seen as a discontinuous dynamic emptying transition that has no analogue at equilibrium. This is further analysed in ref. [124].

Finally, we have shown for a particular described scenario that in an appropriate three-dimensional phase space, the three regions of the film profile, *i.e.*, the precursor film, the foot and the bath, correspond to three fixed points, $\boldsymbol{y}_p$, $\boldsymbol{y}_f$ and $\boldsymbol{y}_b$, respectively, of a suitable dynamical system. We have explained that the snaking behaviour of the bifurcation curves is caused by the existence of a heteroclinic chain that connects $\boldsymbol{y}_p$ with $\boldsymbol{y}_f$ and $\boldsymbol{y}_f$ with $\boldsymbol{y}_b$ at certain parameter values h_∞ and J_∞. To understand the existence of these multiple heteroclinic orbits connecting two of the fixed points of a three dimensional dynamical system which has three fixed points connected by a heteroclinic chain we have proved a general result that implies that if the fixed points corresponding to the foot and to the bath have two-dimensional unstable and two-dimensional stable manifolds, respectively, and the fixed point corresponding to the foot is a saddle-focus so that the Jacobian at this point has the eigenvalues $-\lambda_1$, $\lambda_2 \pm \mathrm{i}\,\omega$, where $\lambda_{1,2}$ and ω are positive real numbers, then in the neighbourhood of the heteroclinic chain there is an infinite but countable number of heteroclinic orbits connecting the fixed point for the precursor film with the fixed point for the bath. These heteroclinic orbits correspond to solutions with feet of different lengths. Moreover, these solutions can be ordered so that the difference in the foot lengths tends to π/ω. We have also explained that in this case the bifurcation curve shows a snaking behaviour. Otherwise, if the fixed point corresponding to the foot is a saddle, the Jacobian at this point has three real non-zero eigenvalues, and the bifurcation curve is monotonic.

The presented study is by no means exhaustive. It has focused on obtaining asymptotic expansions of the solutions in the bath region using rigorous centre manifold theory and on analysing the collapsed heteroclinic snaking behaviour associated with the dragged meniscus problems. However, the system has a much richer solution structure. Beside the studied solutions one may obtain Landau–Levich films and investigate their coexistence with the discussed foot and mensicus solutions. For other solutions the bath connects directly to a precursor-type film which then connects to a thicker 'foot-like' film which then goes back to the precursor-type film that continues along the drawn plate. We have addressed these solutions and their relation to the ones studied here briefly and it is now being part of ongoing work, which will be presented elsewhere. We have also shown that a long-wave mesoscopic hydrodynamic description of the coating problem for a drawn inclined plate from a bath allows one to identify several qualitative transitions if wettability is modelled via a Derjaguin pressure. As a result we have distinguished four dynamic unbinding transitions, namely continuous and discontinuous dynamic emptying transitions and discontinuous and continuous dynamic wetting transitions. These dynamic transitions are out-of-equilibrium equivalents of well known equilibrium emptying and wetting transitions. Beside features known from equilibrium, our analysis has uncovered important features that have no equivalents at equilibrium. A future study of the influence of fluctuations might allow one to answer the question which surface profile is selected in the multistable regions.

In the final part, we have studied a proposed generalisation of Gibbs' pinning criterion accounting for the non-equilibrium effect of evaporation, which explains the experimental results described in ref. [81]. The apparent angle entering the modified criterion is determined within a so-called microstructure of the contact line, corresponding to the macroscopic limit of a droplet, much larger than the relevant microscales. In this respect, we note that the corresponding theory of evaporation-induced contact angles for an atmosphere containing air is not quite developed yet, even though the existing studies (see e.g. [115]) show a weak dependence upon a single macroscopic length scale.

Other potential future work is to study Marangoni stress driven menisci in similar geometries for different complex liquids, such as colloidal suspensions, liquid crystals or non-newtonian liquids with particular interest towards the description of static and dynamic contact lines, their shape, motion and instabilities. The study will be extended by incorporating evaporation and/or external electrodynamic fields.

Understanding the spreading mechanisms of complex liquids on topographical substrates and other geometrical structures are of particular interest in designing surfaces, like antimicrobial surfaces and superhydrophobic surfaces. The study might be extended towards active liquids relevant for several biological systems.

Appendix A

Asymptotic behaviour of solutions at infinity

In what follows, we will analyse steady-state solutions of a more general equation including the temperature gradient Ω,

$$\partial_t h \;=\; -\partial_x\left(\frac{h^3}{3}\partial_x[\partial_x^2 h + \Pi(h)] - \frac{h^3}{3}G(\partial_x h - \alpha) - \frac{\Omega}{3}h^2 - \frac{U}{3}h\right), \quad \text{(A.1)}$$

i.e. solutions that satisfy the equation

$$h^3[h'' + \Pi(h)]' - Gh^3(h' - \alpha) - \Omega h^2 - Uh + J_0 = 0, \quad \text{(A.2)}$$

where now h is a function of x only and primes denote differentiation with respect to x. Here, J_0 is a constant of integration and represents the flux. Note that J_0 is in fact not an independent parameter but is determined as part of the solution of the boundary-value problem consisting of eq. (A.2) and four boundary conditions that will be discussed in the next section.

Following a proposal of ref. [10], we introduce variables $y_1 = 1/h$, $y_2 = h'$ and $y_3 = h''$, and convert the steady-state equation (A.2) into a three-dimensional dynamical system:

$$y_1' = -y_1^2 y_2, \quad \text{(A.3)}$$

$$y_2' = y_3, \quad \text{(A.4)}$$

$$\begin{aligned} y_3' &= (6y_1^7 - 3y_1^4)y_2 + Gy_2 + Uy_1^2 \\ &\quad + \Omega y_1 - J_0 y_1^3 - G\alpha. \end{aligned} \quad \text{(A.5)}$$

Note that the transformation $y_1 = 1/h$ is used to obtain a new fixed point corresponding to the bath, namely the point $\boldsymbol{y}_b = (0,\, \alpha,\, 0)$, beside other fixed points, two of which, $\boldsymbol{y}_f = (1/h_f,\, 0,\, 0)$ and $\boldsymbol{y}_p = (1/h_p,\, 0,\, 0)$, correspond to the foot and the precursor film, respectively.

To analyse the stability of the fixed point $\boldsymbol{y_b}$, we first compute the Jacobian at this point:

$$\boldsymbol{J}_{\boldsymbol{y}_b} = \begin{pmatrix} 0 & 0 & 0 \\ 0 & 0 & 1 \\ \Omega & G & 0 \end{pmatrix}. \tag{A.6}$$

The eigenvalues are 0, $\pm G^{1/2}$ and the corresponding eigenvectors are $(G,\, -\Omega,\, 0)$, $(0,\, \pm G^{-1/2},\, 1)$. So there is a one-dimensional centre (or critical) eigenspace, a one-dimensional stable eigenspace and a one-dimensional unstable eigenspace given by

$$\begin{aligned} T^c_{\boldsymbol{y}_b} &= \operatorname{span}\{(G,\, -\Omega,\, 0)\}, & \text{(A.7)} \\ T^s_{\boldsymbol{y}_b} &= \operatorname{span}\{(0,\, -G^{-1/2},\, 1)\}, & \text{(A.8)} \\ T^u_{\boldsymbol{y}_b} &= \operatorname{span}\{(0,\, G^{-1/2},\, 1)\}, & \text{(A.9)} \end{aligned}$$

respectively.

To determine the asymptotic behaviour of h as $x \to \infty$, we analyse the centre manifold of $\boldsymbol{y}_b$, which we denote by $W^c_{\boldsymbol{y}_b}$. This is an invariant manifold whose tangent space at $\boldsymbol{y}_b$ is $T^c_{\boldsymbol{y}_b}$. The existence of a centre manifold is provided by the centre manifold theorem (see, *e.g.*, theorem 1, p. 4 in ref. [125], theorem 5.1, p. 152 in ref. [69]). For simplicity, we use the substitution $z_1 = y_1$, $z_2 = y_2 - \alpha$, $z_3 = y_3$. In vector notation, the dynamical system takes the form

$$\boldsymbol{z}' = \boldsymbol{f}(\boldsymbol{z}), \tag{A.10}$$

where $\boldsymbol{f}(\boldsymbol{z}) = (f_1(\boldsymbol{z}),\, f_2(\boldsymbol{z}),\, f_3(\boldsymbol{z}))^T$ and

$$\begin{aligned} f_1(\boldsymbol{z}) = f_1(z_1,\, z_2,\, z_3) &= -z_1^2(z_2 + \alpha), & \text{(A.11)} \\ f_2(\boldsymbol{z}) = f_2(z_1,\, z_2,\, z_3) &= z_3, & \text{(A.12)} \\ f_3(\boldsymbol{z}) = f_3(z_1,\, z_2,\, z_3) &= (6z_1^7 - 3z_1^4)(z_2 + \alpha) + Gz_2 \\ &\quad + Uz_1^2 + \Omega z_1 - J_0 z_1^3. & \text{(A.13)} \end{aligned}$$

The fixed point corresponding to the bath is then $\boldsymbol{z}_b = (0,\, 0,\, 0)$. Next, we rewrite the system of ordinary differential equations (A.10) in its eigenbasis at $\boldsymbol{z}_b$, *i.e.*, we use the change of variables $\boldsymbol{u} = \boldsymbol{B}^{-1}\boldsymbol{z}$, where $\boldsymbol{B}$ is the matrix having the eigenvectors of the Jacobian as its columns,

$$\boldsymbol{B} = \begin{pmatrix} G & 0 & 0 \\ -\Omega & G^{-1/2} & -G^{-1/2} \\ 0 & 1 & 1 \end{pmatrix}, \tag{A.14}$$

and obtain the system

$$\boldsymbol{u}' = \boldsymbol{g}(\boldsymbol{u}) \equiv \boldsymbol{B}^{-1}\boldsymbol{f}(\boldsymbol{B}\boldsymbol{u}), \tag{A.15}$$

which can be written in the form

$$\xi' = \psi(\xi, \boldsymbol{\eta}), \tag{A.16}$$

$$\boldsymbol{\eta}' = \boldsymbol{C}\boldsymbol{\eta} + \boldsymbol{\varphi}(\xi, \boldsymbol{\eta}), \tag{A.17}$$

where ξ denotes the first component of $\boldsymbol{u}$ and $\boldsymbol{\eta} = (\eta_1, \eta_2)^T$ consist of the second and the third components of $\boldsymbol{u}$ (*i.e.*, $\xi \equiv u_1$, $\eta_1 \equiv u_2$ and $\eta_2 \equiv u_3$), ψ and $\boldsymbol{\varphi}$ have Taylor expansions that start with quadratic or even higher order terms and $\boldsymbol{C}$ is the matrix

$$\boldsymbol{C} = \begin{pmatrix} G^{1/2} & 0 \\ 0 & -G^{1/2} \end{pmatrix}. \tag{A.18}$$

After some algebra, we find

$$\begin{aligned}
\psi(\xi,\boldsymbol{\eta}) &= G\Omega\xi^3 - G\alpha\xi^2 - G^{1/2}\xi^2\eta_1 + G^{1/2}\xi^2\eta_2, && \text{(A.19)}\\
\varphi_1(\xi,\boldsymbol{\eta}) &= -3\,G^7\Omega\,\xi^8 + 3\,G^7\alpha\,\xi^7 + 3\,G^{13/2}\xi^7\eta_1 \\
&\quad -3\,G^{13/2}\xi^7\eta_2 + \frac{3}{2}\,G^4\Omega\,\xi^5 - \frac{3}{2}\,G^4\alpha\,\xi^4 \\
&\quad -\frac{3}{2}\,G^{7/2}\xi^4\eta_1 + \frac{3}{2}\,G^{7/2}\xi^4\eta_2 - \frac{1}{2}\,J_0\,G^3\xi^3 \\
&\quad +\frac{1}{2}\,G^{3/2}\Omega^2\xi^3 - \frac{1}{2}\,G^{3/2}\Omega\,\alpha\,\xi^2 + \frac{1}{2}\,UG^2\xi^2 \\
&\quad -\frac{1}{2}\,G\Omega\,\xi^2\eta_1 + \frac{1}{2}\,G\Omega\,\xi^2\eta_2, && \text{(A.20)}\\
\varphi_2(\xi,\boldsymbol{\eta}) &= -G^{1/2}\eta_2 - 3\,G^7\Omega\,\xi^8 + 3\,G^7\alpha\,\xi^7 \\
&\quad +3\,G^{13/2}\xi^7\eta_1 - 3\,G^{13/2}\xi^7\eta_2 + \frac{3}{2}\,G^4\Omega\,\xi^5 \\
&\quad -\frac{3}{2}\,G^4\alpha\,\xi^4 - \frac{3}{2}\,G^{7/2}\xi^4\eta_1 + \frac{3}{2}\,G^{7/2}\xi^4\eta_2 \\
&\quad -\frac{1}{2}\,J_0\,G^3\xi^3 - \frac{1}{2}\,G^{3/2}\Omega^2\xi^3 + \frac{1}{2}\,G^{3/2}\Omega\,\alpha\,\xi^2 \\
&\quad +\frac{1}{2}\,UG^2\xi^2 + \frac{1}{2}\,G\Omega\,\xi^2\eta_1 - \frac{1}{2}\,G\Omega\,\xi^2\eta_2. && \text{(A.21)}
\end{aligned}$$

Near the origin, $\boldsymbol{z_b}$, when $|\xi| < \delta$ for some positive δ, the centre manifold in the (ξ,η_1,η_2)-space can be represented by the equations $\eta_1 = g_1(\xi)$, $\eta_2 = g_2(\xi)$, where g_1 and g_2 are in C^2. Moreover, near the origin system (A.16), (A.17) is topologically equivalent to the system

$$\xi' = \psi(\xi,\boldsymbol{g}(\xi)), \qquad \text{(A.22)}$$

$$\boldsymbol{\eta}' = \boldsymbol{C}\boldsymbol{\eta}. \qquad \text{(A.23)}$$

where the first equation represents the restriction of the flow to its centre manifold (see, *e.g.*, theorem 1, p. 4 in ref. [125], theorem 5.2, p. 155 in ref. [69]).

The centre manifold can be approximated to any degree of accuracy. According to theorem 3, p. 5 in ref. [125], 'test' functions ϕ_1 and ϕ_2 approximate the centre manifold with accuracy $O(|\xi|^q)$, namely,

$$|g_1(\xi) - \phi_1(\xi)| = O(|\xi|^q), \quad |g_2(\xi) - \phi_2(\xi)| = O(|\xi|^q) \qquad \text{(A.24)}$$

as $\xi \to 0$, provided that $\phi_i(0) = 0$, $\phi_i'(0) = 0$, $i = 1, 2$ and $\boldsymbol{M}[\boldsymbol{\phi}](\xi) = O(|\xi|^q)$ as $\xi \to 0$, where $\boldsymbol{M}$ is the operator defined by

$$\boldsymbol{M}[\boldsymbol{\phi}](\xi) = \boldsymbol{\phi}'(\xi)\psi(\xi,\, \boldsymbol{\phi}(\xi)) - \boldsymbol{C}\boldsymbol{\phi}(\xi) - \boldsymbol{\varphi}(\xi,\, \boldsymbol{\phi}(\xi)). \tag{A.25}$$

The centre manifold can now be obtained by seeking for $\phi_1(\xi)$ and $\phi_2(\xi)$ in the form of polynomials in ξ and requiring that the coefficients of the expansion of $\boldsymbol{M}[\boldsymbol{\phi}](\xi)$ in Taylor series vanish at zeroth order, first order, second order, etc. Using this procedure, we can find the Taylor series expansions of g_1 and g_2:

$$\begin{aligned} g_1(\xi) \;=\; & \left(\frac{1}{2}\, G\Omega\,\alpha - \frac{1}{2}\, G^{3/2} U\right)\xi^2 \\ & + \left(G^2 U\alpha - G^{3/2}\Omega\,\alpha^2 - \frac{1}{2}\, G\Omega^2 + \frac{1}{2}\, G^{5/2} J_0\right)\xi^3 \\ & - \left(\frac{3}{2}\, G^3\alpha\, J_0 - 3\, G^2\alpha^3\Omega + \frac{3}{2}\, G^2\Omega\, U - 3\, G^{5/2}\alpha^2 U \right. \\ & \qquad \left. - \frac{3}{2}\, G^{7/2}\alpha - \frac{5}{2}\, G^{3/2}\alpha\,\Omega^2\right)\xi^4 + \cdots\,, \end{aligned} \tag{A.26}$$

$$\begin{aligned} g_2(\xi) \;=\; & \left(\frac{1}{2}\, G\Omega\,\alpha + \frac{1}{2}\, G^{3/2} U\right)\xi^2 \\ & + \left(G^2 U\alpha + G^{3/2}\Omega\,\alpha^2 - \frac{1}{2}\, G\Omega^2 - \frac{1}{2}\, G^{5/2} J_0\right)\xi^3 \\ & - \left(\frac{3}{2}\, G^3\alpha\, J_0 - 3\, G^2\alpha^3\Omega - 3\, G^{5/2}\alpha^2 U + \frac{3}{2}\, G^2\Omega\, U \right. \\ & \qquad \left. + \frac{3}{2}\, G^{7/2}\alpha + \frac{5}{2}\, G^{3/2}\alpha\,\Omega^2\right)\xi^4 + \cdots\,. \end{aligned} \tag{A.27}$$

Let $g_i^{(k)}(\xi)$, $i = 1, 2$, be the Taylor polynomial for $g_i(\xi)$ of degree k. Then $g_i(\xi) = g_i^{(k)}(\xi) + O(|\xi|^{k+1})$, $i = 1, 2$, and $\boldsymbol{M}[\boldsymbol{g}^{(k)}](\xi) = O(|\xi|^{k+1})$ as $\xi \to 0$. The dynamics on the centre manifold is therefore governed by the equation

$$\begin{aligned} \xi' \;&=\; \psi(\xi, \boldsymbol{g}^{(k)}(\xi)) + O(|\xi|^{k+3}) \\ &=\; G\Omega\xi^3 - G\alpha\xi^2 - G^{1/2}\xi^2 g_1^{(k)}(\xi) \\ &\qquad + G^{1/2}\xi^2 g_2^{(k)}(\xi) + O(|\xi|^{k+3}). \end{aligned} \tag{A.28}$$

Substituting eq. (A.26) and eq. (A.27) into eq. (A.28), we find

$$\begin{aligned} \xi' \;=\; & -G\alpha\xi^2 + G\Omega\xi^3 + UG^2\xi^4 - (J_0 G^3 - 2G^2\Omega\alpha^2)\xi^5 \\ & + (6G^3 U\alpha^2 - 3G^4\alpha - 5G^2\Omega^2\alpha)\xi^6 + \cdots\,. \end{aligned} \tag{A.29}$$

Taking into account the fact that $\xi = z_1/G$, we obtain

$$\begin{aligned} z_1' &= -\alpha z_1^2 + \frac{\Omega}{G} z_1^3 + \frac{U}{G} z_1^4 - \left(\frac{J_0}{G} - \frac{2\Omega\alpha^2}{G^2}\right) z_1^5 \\ &\quad + \left(\frac{6U\alpha^2}{G^2} - \frac{3\alpha}{G} - \frac{5\Omega^2\alpha}{G^3}\right) z_1^6 + \cdots . \end{aligned} \tag{A.30}$$

Rewriting this in terms of h, we get

$$\begin{aligned} h' &= \alpha - \frac{\Omega}{G} h^{-1} - \frac{U}{G} h^{-2} + \left(\frac{J_0}{G} - \frac{2\Omega\alpha^2}{G^2}\right) h^{-3} \\ &\quad - \left(\frac{6U\alpha^2}{G^2} - \frac{3\alpha}{G} - \frac{5\Omega^2\alpha}{G^3}\right) h^{-4} + \cdots \end{aligned} \tag{A.31}$$

as $h \to \infty$.

We seek for a solution for h whose slope approaches that of the line corresponding to the horizontal direction as $x \to \infty$. In the chosen system of coordinates, the line corresponding to the horizontal direction has the slope α. So we seek for a solution satisfying $h'(x) = \alpha + o(1)$ as $x \to \infty$. This can also be written in the form

$$h(x) = \alpha x + o(x) \quad \text{as} \quad x \to \infty. \tag{A.32}$$

Substituting eq. (A.32) into eq. (A.31), we obtain

$$h' = \alpha - \frac{\Omega}{\alpha G} x^{-1} + o(x^{-1}), \tag{A.33}$$

which implies

$$h = \alpha x - \frac{\Omega}{\alpha G} \log x + o(\log x). \tag{A.34}$$

Substituting eq. (A.34) into eq. (A.31), we find

$$h' = \alpha - \frac{\Omega}{\alpha G} x^{-1} - \frac{\Omega^2}{\alpha^3 G^2} x^{-2} \log x + o(x^{-2}\log x), \tag{A.35}$$

which implies

$$h = \alpha x - \frac{\Omega}{\alpha G} \log x + \frac{\Omega^2}{\alpha^3 G^2} x^{-1} \log x + o(x^{-1}\log x). \tag{A.36}$$

In principle, any constant of integration can be added to this expression, and this reflects the fact that there is translational invariance in the problem, *i.e.*, if $h(x)$ is a solution of eq. (A.2), then a profile obtained by shifting $h(x)$ along the x-axis is

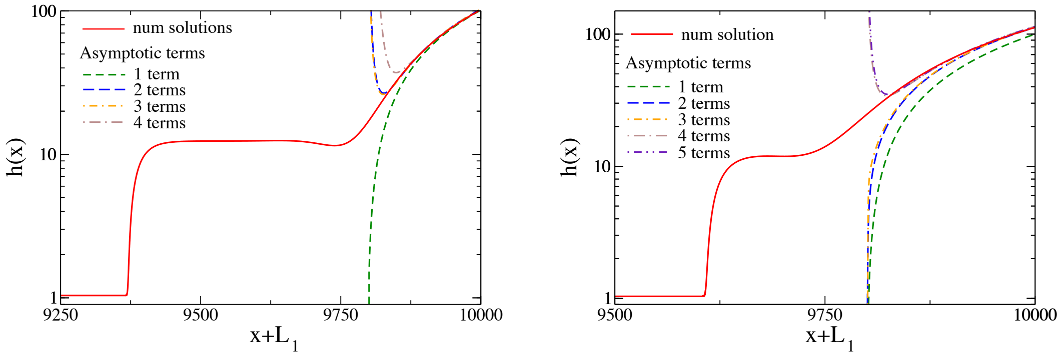

FIGURE A.1: Left panel: Comparison between a numerical solution for $\Omega = 0$ when $\alpha = 0.5$ and $U = 0.084$ and the expansion for $h(x)$ given by eq. (2.52) with 1-4 terms. Right panel: Comparison between a numerical solution for $\Omega = 0.001$ when $\alpha = 0.5$ at $U = 0.076$ and the expansion for $h(x)$ given by eq. (A.38) with 1-5 terms. $L_1 = 9800$, $L_2 = 200$.

also a solution of this equation. Without loss of generality, we choose the constant of integration to be zero, which breaks this translational invariance and allows selecting a unique solution from the infinite set of solutions.

Substituting eq. (A.36) into eq. (A.31), we find

$$\begin{aligned} h' &= \alpha - \frac{\Omega}{\alpha G}x^{-1} - \frac{\Omega^2}{\alpha^3 G^2}x^{-2}\log x \\ &\quad -\frac{U}{\alpha^2 G}x^{-2} - \frac{\Omega^3}{\alpha^5 G^3}x^{-3}\log^2 x \\ &\quad +\frac{\Omega^3}{\alpha^5 G^3}x^{-3}\log x + o(x^{-3}\log x), \end{aligned} \tag{A.37}$$

which implies

$$h = \alpha x - \frac{\Omega}{\alpha G}\log x + \frac{\Omega^2}{\alpha^3 G^2}x^{-1}\log x \tag{A.38}$$

$$\begin{aligned} &+\left(\frac{\Omega^2}{\alpha^3 G^2} + \frac{U}{\alpha^2 G}\right)x^{-1} \\ &-\frac{\Omega^3}{2\alpha^5 G^3}x^{-2}\log^2 x + o(x^{-2}\log x). \end{aligned} \tag{A.39}$$

The procedure described above can be continued to obtain more terms in the asymptotic expansion of h as $x \to \infty$. Note that all the terms in this expansion, except the first two, will be of the form $x^{-m}\log^n x$, where m is a positive integer and n is a non-negative integer. It should also be noted that the presence of the logarithmic terms in the asymptotic expansion of h is wholly due to the quadratic contribution to the flux in eq. (A.1) that here results from a lateral temperature gradient. Without this term, *i.e.*, for $\Omega = 0$, the expansion (A.31) for h' does not contain the term proportional to h^{-1}. This implies that after substituting $h(x) = \alpha x + o(x)$ in this expansion, no term proportional to x^{-1} will appear, and, therefore, integration will not lead to the appearance of a logarithmic term. In fact, it is straightforward to see that for $\Omega = 0$ an appropriate ansatz for h is

$$h \sim \alpha x + D_1 x^{-1} + D_2 x^{-2} + D_3 x^{-3} + \cdots\,, \tag{A.40}$$

implying that

$$\begin{aligned} D_1 &= \frac{U}{\alpha^2 G}, \qquad D_2 = -\frac{J_0}{2\alpha^3 G}, \\ D_3 &= -\frac{1}{3}\left(\frac{2U^2}{\alpha^5 G} + \frac{3}{\alpha^3 G} - \frac{6U}{\alpha^2 G^2}\right), \;\ldots\,. \end{aligned} \tag{A.41}$$

Note that the presence of a logarithmic term in the asymptotic behaviour of h was also observed by Münch and Evans [10] in a related problem of a liquid film driven out of a meniscus by a thermally induced Marangoni shear stress onto a nearly horizontal fixed plane. They find the following asymptotic behaviour of the solution, given with our definition of the coordinate system:

$$h(x) \sim h_0(x) + D_0 + D_1 \exp(-D^{1/2} x) \quad \text{as} \quad x \to \infty, \tag{A.42}$$

where $h_0 = x/D - \log x + o(1)$, D is the parameter measuring the relative importance of the normal component of gravity and D_0 and D_1 are arbitrary constants. The constant D_0 reflects the fact that there is translational invariance in the problem and it can be set to zero without loss of generality. An analysis performed along the lines indicated above shows that a more complete expansion has the form

$$\begin{aligned} h(x) \sim \frac{x}{D} - \log x + D\, x^{-1} \log x + D x^{-1} \\ + \frac{D^2}{2} x^{-2} \log^2 x + \cdots\,. \end{aligned} \tag{A.43}$$

Note that there is no need to include the exponentially small term as it is asymptotically smaller than all the other terms of the expansion.

Appendix B

Solution Measures

In what follows, we will introduce different useful solution measures to quantify the bifurcation diagrams:

A numerical finite domain L allows us to calculate, for example, the volume of the film profile. This solution measure will be of practical importance for the analysis of the extended meniscus (foot) solutions and correlate it to the foot length as we will describe later in this Appendix. We will define following solution measures, see Fig. B.1 and Fig. B.2:

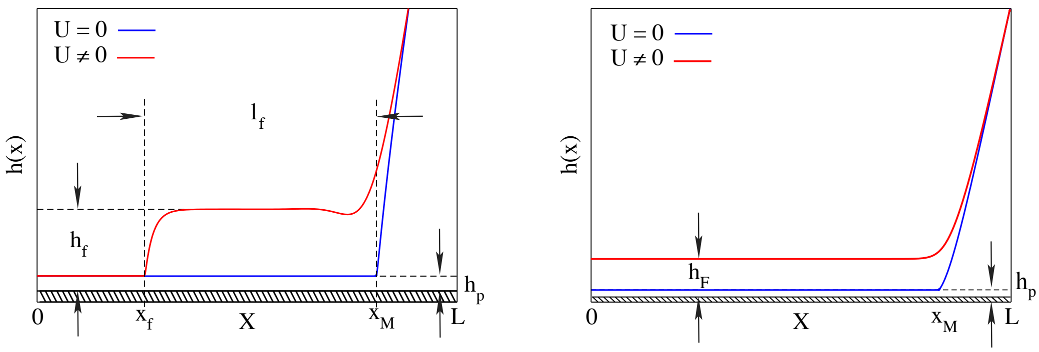

Figure B.1: Sketch of different solutions: Meniscus, foot-like structure and film. Left panel: Shown is the sketch of a meniscus at $U = 0$ and a foot solution for $U \neq 0$ for the same angle. We identify the foot height h_{f}, the precursor film height h_{p}, the position of the start of the foot x_{f} and the the position of the meniscus (and where the film profile connects to the bath) x_{M}. We define a length proportional to the foot length, the pseudo-foot length as $l_{\mathrm{f}} = x_{\mathrm{M}} - x_{\mathrm{f}}$. Right panel: Film type solutions. Shown is the sketch of a meniscus at $U = 0$ and a film solution for $U \neq 0$ for the same angle. We identify the film height h_{F}, the precursor film height h_{p}, and the position of the meniscus x_{M}. See text for more details.

(a) Effective volume measure ΔV: This solution measures the difference between a profile volume V at $U \neq 0$ and the volume V_0 at $U = 0$ for a fixed angle, i.e.

$$\Delta V = V - V_0. \tag{B.1}$$

We identify following three solution measures for the three different film profiles:

(i) Meniscus profile:

$$\begin{aligned} V &= \int_0^L h(x)\mathrm{d}x = \int_0^{x_\mathrm{M}} h_\mathrm{p}\mathrm{d}x + \delta V_M \\ &= x_\mathrm{M} h_\mathrm{p} + \delta V_M, \end{aligned} \tag{B.2}$$

where

$$\delta V_M = \int_{x_\mathrm{M}}^L h(x)\mathrm{d}x \tag{B.3}$$

is the volume of the profile for $x \in [x_M, L]$. x_M is the position where the film profile connects to the bath, see Fig. B.1.

The volume at $U = 0$ is equal to

$$V_0 = \int_0^L h(x)\mathrm{d}x = \int_0^{x_{\mathrm{M}'}} h_\mathrm{p}\mathrm{d}x + \delta V_M' = x_{\mathrm{M}'} h_\mathrm{p} + \delta V_M', \tag{B.4}$$

with $\delta V_M'$ defined as above. We assume $x_\mathrm{M} \approx x_{\mathrm{M}'}$. Finally, we have

$$\Delta V \approx 0. \tag{B.5}$$

(ii) For foot solutions we identify the foot height h_f, the coating film height h_∞, the position of the start of the foot x_f and the the position of the meniscus (and where the film profile connects to the bath) x_M, see Fig. B.1,

$$\begin{aligned} V &= \int_0^L h(x)\mathrm{d}x = \int_0^{x_\mathrm{f}} h_\mathrm{p}\mathrm{d}x + \int_{x_\mathrm{f}}^{x_\mathrm{M}} h_\mathrm{f}\mathrm{d}x \quad + \delta V_M \\ &= x_\mathrm{f} h_\mathrm{p} + (x_\mathrm{M} - x_\mathrm{f}) h_\mathrm{f} + \delta V_M, \end{aligned} \tag{B.6}$$

where

$$\delta V_M \quad = \quad \int_{x_\mathrm{M}}^{L} h(x)\mathrm{d}x \tag{B.7}$$

is the volume of the profile for $x \in [x_M, L]$. The volume at $U = 0$ is equal to

$$V_0 \quad = \quad \int_0^L h(x)\mathrm{d}x = \int_0^{x_\mathrm{M}} h_\mathrm{p}\mathrm{d}x + \delta V_M = x_\mathrm{M} h_\mathrm{p} + \delta V_M \tag{B.8}$$

with δV_M defined as above. Finally, we have

$$\Delta V = (x_\mathrm{M} - x_\mathrm{f})(h_\mathrm{f} - h_\mathrm{p}). \tag{B.9}$$

(iii) Film solutions

$$\begin{aligned} V \quad &= \quad \int_0^L h(x)\mathrm{d}x = \int_0^{x_\mathrm{M}} h_\mathrm{F}\mathrm{d}x + \delta V_M \qquad \text{(B.10)} \\ &= \quad x_\mathrm{M} h_\mathrm{F} + \delta V_M, \end{aligned}$$

where

$$\delta V_M \quad = \quad \int_{x_\mathrm{M}}^{L} h(x)\mathrm{d}x \tag{B.11}$$

is the volume of the profile for $x \in [x_M, L]$. The volume at $U = 0$ is equal to

$$V_0 \quad = \quad \int_0^L h(x)\mathrm{d}x = \int_0^{x_\mathrm{M}} h_\mathrm{p}\mathrm{d}x + \delta V_M = x_\mathrm{M} h_\mathrm{p} + \delta V_M \tag{B.12}$$

with δV_M defined as above. Finally, we have

$$\Delta V = x_\mathrm{M}(h_\mathrm{F} - h_\mathrm{p}). \tag{B.13}$$

(b) Volume measure $\Delta\tilde{V}$: This solution measure is the difference between a profile volume V at $U \neq 0$ and the volume V_0 at $U = 0$ for a fixed angle subtracting the volume V_p of the precursor film height. Note that

$$\Delta\tilde{V} = \Delta V. \tag{B.14}$$

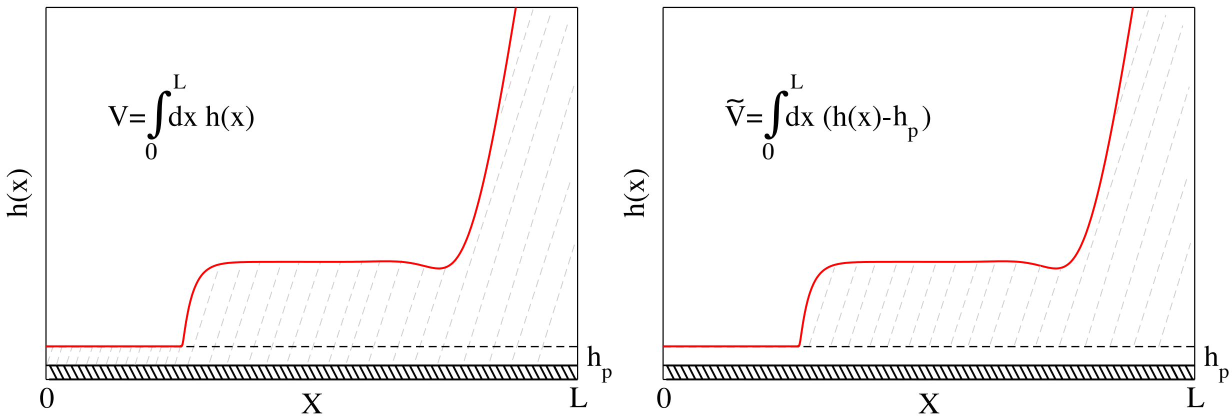

FIGURE B.2: Volume measures. Left panel: Effective volume measure, see text for more details. Right panel: Volume measure.

(c) Pseudo-foot length l_f: If we assume that the volume δV_M is invariant (or has small changes), we can define for foot structure solutions, the following solution measure from Eq. (B.13) for the foot length,

$$l_f \approx x_{\mathrm{M}} - x_{\mathrm{f}} = \frac{\Delta V}{h_{\mathrm{f}} - h_{\mathrm{p}}} \tag{B.15}$$

Note that the coating film height h_∞ and foot height h_{f} are obtained from the linear stability analysis.

Bibliography

> "Books are not made to be believed, but to be subjected to enquiry."
>
> William of Baskerville

[1] A. M. Rijke. Wettability and phylogenetic development of feather structure in water birds. *Journal of Experimental Biology*, 52(2):469–479, 1970.

[2] H. E. Huppert. Flow and instability of a viscous current down a slope. *Nature*, 300:427–429, 1982.

[3] N. J. Balmforth, RV Craster, and R Sassi. Dynamics of cooling viscoplastic domes. *J. Fluid. Mech.*, 499:149–182, 2004.

[4] A. Sharma and E. Ruckenstein. Mechanism of tear film rupture and formation of dry spots on cornea. *J. Colloid Interface Sci.*, 106:12–27, 1985.

[5] A. Gnanappa, E. Gogolides, F. Evangelista, and M. Riepen. Contact line dynamics of a superhydrophobic surface: application for immersion lithography. *Microfluidics and Nanofluidics*, 10(6):1351–1357, 2011.

[6] P. Nanetti. *Coatings from A to Z: A Concise Compilation of Technical Terms.* Coatings compendia. Vincentz Network, 2006.

[7] B. Derjaguin. On the thickness of the liquid film adhering to the walls of a vessel after emptying. *Acta Physicochim. USSR*, 39(-1):1316, 1943.

[8] L. Landau and B. Levich. Dragging of a liquid by a moving plane. *Acta Physicochimica U.R.S.S.*, 17, 1942. reprint in [126].

[9] S. D. R. Wilson. The drag-out problem in film coating theory. *Journal of Engineering Mathematics*, 16:209–221, 1982. 10.1007/BF00042717.

[10] A. Münch and P. L. Evans. Marangoni-driven liquid films rising out of a meniscus onto a nearly-horizontal substrate. *Physica D: Nonlinear Phenomena*, 209(1-4):164 – 177, 2005. Non-linear Dynamics of Thin Films and Fluid Interfaces.

[11] F. C. Morey. Thickness of a liquid film adhering to a surface slowly withdrawn from the liquid. *J. Res. Nat. Bur. Stand.*, 25:385, 1940.

[12] M. Maleki, M. Reyssat, F. Restagno, D. Quéré, and C. Clanet. Landau-levich menisci. *Journal of Colloid and Interface Science*, 354(1):359 – 363, 2011.

[13] D. A. White and J. A. Tallmadge. Theory of drag out of liquids on flat plates. *Chemical Engineering Science*, 20(1):33 – 37, 1965.

[14] J. H. Snoeijer, J. Ziegler, B. Andreotti, M. Fermigier, and J. Eggers. Thick films of viscous fluid coating a plate withdrawn from a liquid reservoir. *Phys. Rev. Lett.*, 100(24):244502, Jun 2008.

[15] P. Groenveld. High capillary number withdrawal from viscous newtonian liquids by flat plates. *Chemical Engineering Science*, 25(1):33 – 40, 1970.

[16] R. M. Cook. A supplementary note on meniskoi. *The Journal of Hellenic Studies*, 96:153–154, 1976.

[17] C. Clanet and D. Quéré. Onset of menisci. *Journal of Fluid Mechanics*, 460:131–149, 2002.

[18] J. H. Snoeijer, B. Andreotti, G. Delon, and M. Fermigier. Relaxation of a dewetting contact line. part 1. a full-scale hydrodynamic calculation. *Journal of Fluid Mechanics*, 579(-1):63–83, 2007.

[19] G. Delon, M. Fermigier, J. H. Snoeijer, and B. Andreotti. Relaxation of a dewetting contact line. part 2. experiments. *Journal of Fluid Mechanics*, 604(-1):55–75, 2008.

[20] J. Ziegler, J. H. Snoeijer, and J. Eggers. Film transitions of receding contact lines. *Eur. Phys. J. Special Topics*, 166:177–180, 2009.

[21] B. Jin, A. Acrivos, and A. Münch. The drag-out problem in film coating. *Physics of Fluids*, 17(10), 2005.

[22] F. S. Goucher and H. Ward. A problem in viscosity: The thickness of liquid films formed on solid surfaces under dynamic conditions. *Philosophical Magazine*, 44:1002 –1014, 1922.

[23] S. J. Weinstein and K. J. Ruschak. Coating flows. *Annu. Rev. Fluid Mech.*, 36:29–53, 2004.

[24] J. J. Rossum. Viscous lifting and drainage of liquids. *Applied Scientific Research, Section A*, 7:121–144, 1958.

[25] B. V. Derjaguin and M. Levis. *Film Coating Theory.* Focal Press, 1964.

[26] C. Gutfinger and J. A. Tallmadge. Some remarks on the problem of drainage of fluids on vertical surfaces. *AIChE Journal*, 10(5):774–780, 1964.

[27] B. V. Derjaguin and A. S. Titievskaya. *DAN URSS*, 50:307, 1945.

[28] L. M. Hocking. Meniscus draw-up and draining. *European Journal of Applied Mathematics*, 12(03):195–208, 2001.

[29] E. S. Benilov and V. S. Zubkov. On the drag-out problem in liquid film theory. *Journal of Fluid Mechanics*, 617(-1):283–299, 2008.

[30] E. S. Benilov, S. J. Chapman, J. B. McLeod, J. R. Ockendon, and V. S. Zubkov. On liquid films on an inclined plate. *Journal of Fluid Mechanics*, FirstView:1–17, 2010.

[31] A. Münch. The thickness of a marangoni-driven thin liquid film emerging from a meniscus. *SIAM Journal on Applied Mathematics*, 62(6):2045–2063, 2002.

[32] G. K. Batchelor. *An Introduction to Fluid Dynamics.* Cambridge University Press, 2000.

[33] D. J. Acheson. *Elementary Fluid Dynamics.* Clarendon Press, Oxford, 1990.

[34] S. Kalliadasis and U. Thiele, editors. *Thin Films of Soft Matter.* Springer, Wien / New York, 2007. CISM 490.

[35] T. Young. An essay on the cohesion of fluids. *Phil. Trans. R. Soc.*, 95:65–87, 1805.

[36] P. S. Marquis de Laplace. *Supplément au dixième livre du Traité de Mécanique Céleste*, volume Traité de Mécanique Céleste, 4. Chez Courcier, Imprimeur - Libraire pour les Mathématiques, quai des Agustines, n^{o}71, Paris, France, 1805.

[37] *La libertà è un uccello, che vola in felicità*
La libertà è vedere, un bambino che corre col suo aquilone
La libertà è una fiamma sempre accesa.
Davide Spina

[38] P.-G. de Gennes. Wetting: Statics and dynamics. *Rev. Mod. Phys.*, 57:827–863, 1985.

[39] A. Oron, S. H. Davis, and S. G. Bankoff. Long-scale evolution of thin liquid films. *Rev. Mod. Phys.*, 69:931–980, 1997.

[40] S. R. Friedman, M. Khalil, and P. Taborek. Wetting transition in water. *Phys. Rev. Lett.*, 111:226101, Nov 2013.

[41] C. Huh and L. E. Scriven. Hydrodynamic model of steady movement of a solid / liquid / fluid contact line. *J. Colloid Interface Sci.*, 35:85–101, 1971.

[42] E. B. Dussan. On the spreading of liquids on solid surfaces: Static and dynamic contact lines. *Ann. Rev. Fluid Mech.*, 11:371–400, 1979.

[43] B. V. Deryagin and N. V. Churaev. Structural component of disjoining pressure. *J. Colloid Interf. Sci.*, 49:249, 1974.

[44] B. V. Derjaguin, N. V. Churaev, and V. M. Muller. *Surface Forces*. Consultants Bureau, New York, 1987.

[45] M. N. Popescu, G. Oshanin, S. Dietrich, and A. M. Cazabat. Precursor films in wetting phenomena. *Journal of physics. Condensed matter : an Institute of Physics journal*, 24(24):243102, June 2012.

[46] C. Iwamoto and S. Tanaka. Atomic morphology and chemical reactions of the reactive wetting front. *Acta Mater.*, 50:749–755, 2002.

[47] F. Heslot, N. Fraysse, and A. M. Cazabat. Molecular layering in the spreading of wetting liquid drops. *Nature*, 338(6217):640–642, 1989.

[48] V. M. Starov and M. G.. Velarde. Surface forces and wetting phenomena. *Journal of Physics: Condensed Matter*, 21(46):464121, 2009.

[49] E. Zauderer. *Partial Differential Equations of Applied Mathematics*. Pure and Applied Mathematics: A Wiley Series of Texts, Monographs and Tracts. Wiley, 2011.

[50] F. R. S. Batchelor. *An Introduction to Fluid Dynamics*. University Press, Cambridge, 2000.

[51] L. D. Landau and E. M. Lifshitz. *Fluid Mechanics, Second Edition: Volume 6 (Course of Theoretical Physics)*. Course of theoretical physics / by L. D. Landau and E. M. Lifshitz, Vol. 6. Butterworth-Heinemann, 2 edition, 1987.

[52] E. Doedel, H. B. Keller, and J. P. Kernevez. Numerical analysis and control of bifurcation problems (I) Bifurcation in finite dimensions. *Int. J. Bifurcation Chaos*, 1:493–520, 1991.

[53] E. Doedel, H. B. Keller, and J. P. Kernevez. Numerical analysis and control of bifurcation problems (II) Bifurcation in infinite dimensions. *Int. J. Bifurcation Chaos*, 1:745–72, 1991.

[54] E. J. Doedel, R. C. Paffenroth, A. R. Champneys, T. F. Fairgrieve, Y. A. Kuznetsov, B. E. Oldeman, B. Sandstede, and X. J. Wang. *AUTO2000: Continuation and bifurcation software for ordinary differential equations*. Concordia University, Montreal, 1997.

[55] A. Dijkstra, F.W. Wubs, A.K. Cliffe, E. Doedel, I.F. Dragomirescu, B. Eckhart, A.Y. Gelfgat, A. Hazel, V. Lucarini, A.G. Salinger, E.T. Phipps, J. Sanchez-Umbria, H. Schuttelaars, L.S. Tuckerman, and U. Thiele. Numerical bifurcation methods and their application to fluid dynamics: Analysis beyond simulation. *Commun. Comput. Phys.*, 2013. (at press).

[56] U. Thiele. Structure formation in thin liquid films. In S. Kalliadasis and U. Thiele, editors, *Thin Films of Soft Matter*, pages 25–93, Wien, 2007. Springer.

[57] U. Thiele, L. Brusch, M. Bestehorn, and M. Bär. Modelling thin-film dewetting on structured substrates and templates: Bifurcation analysis and numerical simulations. *Eur. Phys. J. E*, 11:255–271, 2003.

[58] P. Beltrame and U. Thiele. Time integration and steady-state continuation method for lubrication equations. *SIAM J. Appl. Dyn. Syst.*, 9:484–518, 2010.

[59] D. Tseluiko, J. Baxter, and U. Thiele. A homotopy continuation approach for analysing finite-time singularities in thin liquid films. *IMA J. Appl. Math.*, 2013. (online).

[60] L. P. Shilnikov. A case of the existence of a countable number of periodic motions. *Sov. Math. Dokl.*, 6:163166, 1965.

[61] L. P. Shilnikov. The existence of a denumerable set of periodic motions in four-dimensional space in an extended neighborhood of a saddle-focus. *Sov. Math. Dokl.*, 8(1):5458, 1967.

[62] J. Knobloch and T. Wagenknecht. Homoclinic snaking near a heteroclinic cycle in reversible systems. *Phys. D (Amsterdam, Neth.)*, 206(12):82 – 93, 2005.

[63] J. Knobloch and T. Wagenknecht. Snaking of multiple homoclinic orbits in reversible systems. *SIAM Journal on Applied Dynamical Systems*, 7(4):1397–1420, 2008.

[64] M. Chen. Solitary-wave and multi-pulsed traveling-wave solutions of boussinesq systems. *Applicable Analysis*, 75(1-2):213–240, 2000.

[65] G.W. Hunt, M.A. Peletier, A.R. Champneys, P.D. Woods, M. Ahmer Wadee, C.J. Budd, and G.J. Lord. Cellular buckling in long structures. *Nonlinear Dyn.*, 21(1):3–29, 2000.

[66] D. Tseluiko, M. Galvagno, and U. Thiele. Collapsed heteroclinic snaking near a heteroclinic chain in dragged meniscus problems. *Eur. Phys. J. E*, 2013.

[67] U. Thiele, M. G. Velarde, K. Neuffer, M. Bestehorn, and Y. Pomeau. Sliding drops in the diffuse interface model coupled to hydrodynamics. *Phys. Rev. E*, 64:061601, 2001.

[68] U. Thiele, K. Neuffer, M. Bestehorn, Y. Pomeau, and M. G. Velarde. Sliding drops on an inclined plane. *Colloid Surf. A*, 206:87–104, 2002.

[69] I.U.A. Kuznetsov. *Elements of Applied Bifurcation Theory*. Number vol. 112 in Applied Mathematical Sciences. Springer, New York, 1998.

[70] U. Thiele and E. Knobloch. Thin liquid films on a slightly inclined heated plate. *Physica D*, 190:213–248, 2004.

[71] L. M. Hocking. A moving fluid interface on a rough surface. *Journal of Fluid Mechanics*, 76:801–817, 8 1976.

[72] L. M. Hocking. A moving fluid interface. II. The removal of the force singularity by a slip flow. *J. Fluid Mech.*, 79:209–229, 1977.

[73] D. Bonn, J. Eggers, J. Indekeu, J. Meunier, and E. Rolley. Wetting and spreading. *Rev. Mod. Phys.*, 81:739–805, 2009.

[74] A. Münch, B.A. Wagner, and T.P. Witelski. Lubrication models with small to large slip lengths. *Journal of Engineering Mathematics*, 53(3-4):359–383, 2005.

[75] J. Eggers. Hydrodynamic theory of forced dewetting. *Phys. Rev. Lett.*, 93:094502, 2004.

[76] N. Savva and S. Kalliadasis. Dynamics of moving contact lines: A comparison between slip and precursor film models. *Europhys. Lett.*, 94:64004, 2011.

[77] A. O. Parry, C. Rascon, E. A. G. Jamie, and D. G. A. L. Aarts. Capillary emptying and short-range wetting. *Phys. Rev. Lett.*, 108:246101, 2012.

[78] A. Oron and P. Rosenau. Formation of patterns induced by thermocapillarity and gravity. *J. Physique II France*, 2:131–146, 1992.

[79] V. S. Mitlin. Dewetting of solid surface: Analogy with spinodal decomposition. *J. Colloid Interface Sci.*, 156:491–497, 1993.

[80] Y. P. Ma, J. Burke, and E. Knobloch. Defect-mediated snaking: A new growth mechanism for localized structures. *Physica D*, 239:1867–1883, 2010.

[81] Y. Tsoumpas, S. Dehaeck, M. Galvagno, A. Rednikov, H. Ottevaere, U. Thiele, and P. Colinet. Nonequilibrium Gibbs Criterion for Competely Wetting Volatile Liquids. *Langmuir*, 30(40), 2014.

[82] R. E. Johnson and H. Dettre. Contact angle hysteresis. iii. study of an idealized heterogeneous surface. *J. Phys. Chem.*, 68:1744–1750, 1964.

[83] *Der Menschheit Würde ist in eure Hand gegeben;*
Bewahret sie!
Sie sinkt mit euch;
mit euch wird sie sich heben!
Friedrich von Schiller

[84] J. W. Gibbs. Scientific papers. *Scientific Papers vol. 1, Dover Publications, Inc. New York*, 1906/1961.

[85] J. F. Oliver, C. Huh, and S. G. Mason. Resistance to spreading of liquids by sharp edges. *J. Colloid and Interface Sci.*, 59:568–581, 1977.

[86] Y. H. Mori, T. G. M. van de Ven, and S. G. Mason. Resistance to spreading of liquids by sharp edged microsteps. *Colloids and Surfaces*, 4:1–15, 1982.

[87] T. Ondarçuhu and A. Piednoir. Pinning of a contact line on nanometric steps during the dewetting of a terraced substrate. *Nano Lett.*, 5:1744–1750, 2005.

[88] G. Fang and A. Amirfazli. Understanding the edge effect in wetting: A thermodynamic approach. *Langmuir*, 28:9421–9430, 2012.

[89] J. C. Baret, M. Decré, S. Herminghaus, and R. Seemann. Transport dynamics in open microfluidic grooves. *Langmuir*, 23:5200–5204, 2007.

[90] S. Herminghaus, M. Brinkmann, and R. Seemann. Wetting and dewetting of complex surface geometries. *Annu. Rev. Mater. Res.*, 38:101–121, 2008.

[91] M. L. Blow, H. Kusumaatmaja, and J. M. Yeomans. Imbibition through an array of triangular posts. *J. Phys.*, 21:464125, 2009.

[92] N. Savva, S. Kalliadasis, and G. A. Pavliotis. Two-dimensional droplet spreading over random topographical substrates. *Phys. Rev. Lett.*, 104:084501, 2010.

[93] R. Vellingiri, N. Savva, and S. Kalliadasis. Droplet spreading on chemically heterogeneous substrates. *Phys. Rev. E*, 84:036305, 2011.

[94] T. Tóth, D. Ferraro, E. Chiarello, M. Pierno, G. Mistura, G. Bissacco, and C. Semprebon. Suspension of water droplets on individual pillars. *Langmuir*, 27:4742–4748, 2011.

[95] D. Quéré. Wetting and roughness. *Annu. Rev. Mater. Res.*, 38:71–99, 2008.

[96] J. A. Marsh and A. M. Cazabat. Dynamics of contact line depinning from a single defect. *Phys. Rev. Lett.*, 71:2433–2436, 1993.

[97] C. Poulard, O. Bénichou, and A. M. Cazabat. Freely receding evaporating droplets. *Langmuir*, 19:8828–8834, 2003.

[98] S. J. S. Morris. Contact angles for evaporating liquids predicted and compared with existing experiments. *J. Fluid Mech.*, 432:1–30, 2001.

[99] P. Colinet, S. Rossomme, and A. Rednikov. Steady microstructure of a contact line for a liquid on a heated surface overlaid with its pure vapor: parametric study for a classical model. *Multiphase Science and Technology*, 21:213–248, 2009.

[100] D. Todorova, U. Thiele, and L. M. Pismen. The relation of steady evaporating drops fed by an influx and freely evaporating drops. *J. Eng. Math.*, 73:17–30, 2012.

[101] M. O. Robbins and J. F. Joanny. Contact angle hysteresis on random surfaces. *Europhys. Lett.*, 3:729–735, 1987.

[102] D. Ertas and M. Kardar. Critical dynamics of contact line depinning. *Phys. Rev. E*, 49:R2532–R2535, 1994.

[103] R. Golestanian and E. Raphaël. Relaxation of a moving contact line and the Landau-Levich effect. *Europhys. Lett.*, 55:228–234, 2001.

[104] S. Moulinet, C. Guthmann, and E. Rolley. Dissipation in the dynamics of a moving contact line: effect of the substrate disorder. *Eur. Phys. J. B*, 37:127–136, 2004.

[105] P. Le Doussal, K. J. Wiese, E. Raphaël, and R. Golestanian. Can nonlinear elasticity explain contact-line roughness at depinning? *Phys. Rev. Lett.*, 96:015702, 2006.

[106] J. F. Joanny and P.-G. de Gennes. A model for contact angle hysteresis. *J. Chem. Phys.*, 81:552–562, 1984.

[107] E. Raphaël and P. G. de Gennes. Dynamics of wetting with nonideal surfaces - the single defect problem. *J. Chem. Phys.*, 90:7577–7584, 1989.

[108] J. A. Marsh and A. M. Cazabat. Dynamics of contact line depinning from a single defect. *Phys. Rev. Lett.*, 71:2433–2436, 1993.

[109] U. Thiele and E. Knobloch. On the depinning of a driven drop on a heterogeneous substrate. *New J. Phys.*, 8:313, 1–37, 2006.

[110] U. Thiele and E. Knobloch. Driven drops on heterogeneous substrates: Onset of sliding motion. *Phys. Rev. Lett.*, 97:204501, 2006.

[111] P. Beltrame, P. Hänggi, and U. Thiele. Depinning of three-dimensional drops from wettability defects. *Europhys. Lett.*, 86:24006, 2009.

[112] P. Beltrame, E. Knobloch, P. Hänggi, and U. Thiele. Rayleigh and depinning instabilities of forced liquid ridges on heterogeneous substrates. *Phys. Rev. E*, 83:016305, 2011.

[113] U. Thiele. Thin film evolution equations from (evaporating) dewetting liquid layers to epitaxial growth. *J. Phys.-Cond. Mat.*, 22:084019, 2010.

[114] D. Todorova, U. Thiele, and L. M. Pismen. The relation of steady evaporating drops fed by an influx and freely evaporating drops. *J. Eng. Math.*, 73:17–30, 2012.

[115] P. Colinet and A. Rednikov. On integrable singularities and apparent contact angles within a classical paradigm. *Eur. Phys. J. Special Topics*, 197:89–113, 2011.

[116] K. Kargupta and A. Sharma. Creation of ordered patterns by dewetting of thin films on homogeneous and heterogeneous substrates. *J. Colloid Interface Sci.*, 245:99–115, 2002.

[117] A. V. Lyushnin, A. A. Golovin, and L. M. Pismen. Fingering instability of thin evaporating liquid films. *Phys. Rev. E*, 65:021602, 2002.

[118] V. S. Ajaev. Evolution of dry patches in evaporating liquid films. *Phys. Rev. E*, 72:031605, 2005.

[119] A. Rednikov and P. Colinet. Vapor-liquid steady meniscus at a superheated wall: asymptotics in an intermediate zone near the contact line. *Microgravity Science and Technology*, 22:249–255, 2010.

[120] G. F. Teletzke, H. T. Davis, and L. E. Scriven. Wetting hydrodynamics. *Rev. Phys. Appl.*, 23:989–1007, 1988.

[121] U. Thiele. Open questions and promising new fields in dewetting. *Eur. Phys. J. E*, 12:409–416, 2003.

[122] J. H. Snoeijer, J. Ziegler, B. Andreotti, M. Fermigier, and J. Eggers. Thick films of viscous fluid coating a plate withdrawn from a liquid reservoir. *Phys. Rev. Lett.*, 100:244502, Jun 2008.

[123] A. L. Bertozzi, A. Münch, X. Fanton, and A. M. Cazabat. Contact line stability and "undercompressive shocks" in driven thin film flow. *Phys. Rev. Lett.*, 81:5169–5173, 1998.

[124] M. Galvagno, D. Tseluiko, H. Lopez, and U. Thiele. Continuous and discontinuous dynamic unbinding transitions in drawn film flow. *Phys. Rev. Lett.*, 112, 2014.

[125] J. Carr. *Applications of Centre Manifold Theory.* Applied Mathematical Sciences, Vol. 35. Springer-Verlag, Berlin / New York, 1981.

[126] Pierre Pelce, editor. *Dynamics of curved fronts.* Academic Press, London, 1. edition, 1988.

[127] *War der Tag nicht dein Freund, so war er doch dein Lehrer!*